DISTINCTIVE 2017

3rd Annual Meeting, York, 5th - 6th April

Book of Summaries

DISTINCTIVE
Decommissioning,
Immobilisation and
Storage soluTIons for
NuClear wasTe InVEntories

A university consortium funded
by the Research Councils
UK Energy programme

Research Councils UK
Energy
For a Low Carbon Future

UNIVERSITY OF SURREY

UNIVERSITY OF LEEDS

UNIVERSITY OF BIRMINGHAM

University of BRISTOL

Imperial College London

Loughborough University

Lancaster University

MANCHESTER 1824
The University of Manchester

The University Of Sheffield.

University of Strathclyde Glasgow

UCL

Master Project List

Theme	Title	Leading Institution	Researcher	Type
1	An Investigation of Wasteform Evolution During Wet-recovery and Drying of SNF	Bristol	Dr. James E Darnbrough Dr. Leila Costelle	PDRA
1	UO_2 Surface Reactivity and Alteration – a Fundamental Study of Photocatalytic and Structural Effects Related to Long Term Storage of SNF	Bristol	Sophie Rennie	PhD
1	Options for Exotic Carbide Fuels	Imperial	Claudia Gasparrini	PhD
1	The Behaviour of Used Nuclear Fuel in Wet Storage	Lancaster	Elizabeth Howett	PhD
1	Determination of Optimum Drying Conditions for AGR fuels	Leeds	James Goode	PhD
1	Grain Boundary Damage Mechanisms in Strained AGR Cladding Under Irradiation	Manchester	Chiara Barcellini	PhD
1	A Life Cycle Approach as a Decision Tool for Nuclear Waste Management and Decommissioning of Existing and Future Plants	UCL	Andrea Paulillo	PhD
2	Computational Modelling of PuO_2 Ageing and Fuel Residues	Birmingham	Nathan Palmer	PhD
2	In-situ Characterisation of Heavily-Contaminated Plutonium Finishing Environments	Lancaster	-	PhD
2	Real-time Fast Neutron Plutonium Assay for Plutonium Storage and Ageing Applications	Lancaster	Rashed Sarwar	PhD
2	Understanding the Interfacial Interactions of Plutonium Dioxide with Water	Lancaster	Dr. Dominic Laventine	PDRA
2	Investigation of Anomalous Hydrogen Production from Water Adsorbed on Oxides	Manchester	Jamie Southworth	PhD
2	Modelling the Surface Chemistry of PuO_2 at the Molecular Level	Manchester	Dr. Bengt Tegner	PDRA
2	Simulation of Low-energy Electron Radiolysis of Water Adsorbed on Oxides	Manchester	Marisa Smith	PhD
2	Understanding Surface Species and Interactions Between Adsorbed Chloride and Water on Stored PuO_2	Manchester	Sophie Sutherland-Harper	PhD
2	Understanding the Interfacial Interactions of Plutonium Dioxide with Water	Manchester	Dr. Luke Jones Dr Thomas Donoclift	PDRA
2	Ceramic Materials for Actinide Disposition	Sheffield	Dr. Shi-Kuan Sun	PDRA

2	Development of Glass-ceramics for Pu Disposition using Hot Isostatic Pressing	Sheffield	Stephanie Thornber	PhD
2	Understanding Actinide Sorption and Binding to Cement Materials for Radioactive Waste Management	Sheffield	Antonia Yorkshire	PhD
2	The Interaction of Water with PuO_2 Surfaces	UCL	Joseph Wellington	PhD
3	New Ion Exchange Materials For Effluent Clean-up	Birmingham	Ryan George	PhD
3	Novel Ceramic Wasteforms for Cs and Sr Encapsulation	Birmingham	George Day	PhD
3	Novel Ion Exchange Materials	Birmingham	Dr. Evin (Tzu-Yu) Chen	PDRA
3	Corrosion of Uranium in Water and Hydrogen	Bristol	Antonis Banos	PhD
3	Development of Raman Spectroscopy Techniques for the Remote Analysis of Nuclear Wastes in Storage	Bristol	Kate Wyness	PhD
3	The Evolution of Grouted Waste Forms Containing Uranium	Bristol	Haris Paraskevoulakos	PhD
3	Durability of Heterogeneous ILW Glass/Ceramic Wasteforms from Complex Wastestreams	Imperial	Dr. Paul Fossati	PDRA
3	Glass Composite Materials for Fukushima ILW Immobilisation	Imperial	Dimitri Pletser	PhD
3	Glass Composite Materials for Sellafield LP&S ILW Immobilisation	Imperial	Charles Hutchison	PhD
3	Magnetic Nanoparticles for Waste Separation or Sequestration	Imperial	Eleonora Cali	PhD
3	Computational Simulations of Storage Pond Sludge Disturbance	Lancaster	Olivia Lynes	PhD
3	Characterisation of Flocculated Waste Suspensions with Acoustic Backscatter	Leeds	Alastair Tonge	PhD
3	Gas Retention and Release from Nuclear Legacy Waste	Leeds	Michael Johnson	PhD
3	Measurement and Modelling of Sludge Mobilisation and Transport	Leeds	Dr. Derrick Njobuenwu/Dr. Hugh Rice	PDRA
3	The Development of Characterisation Techniques for Intermediate Level Waste Sludges	Leeds	Andre Botha	PhD
3	Enhanced Shear Micro- and Ultra-Filtration Without Recycle Pumping	Loughborough	Keith Schou	PhD

3	Autonomous Systems for Nuclear Decommissioning in Extreme Radiation Environments	Manchester	Olusola Ayoola	PhD
3	Irradiated Sludges - Experimental	QUB	Mel O'Leary	PhD
3	Modelling Hydrogen Generation from Radioactive Sludges	QUB	Conrad Johnston	PhD
3	Thermal Treatment of PCM and ILW	Sheffield	Luke Boast	PhD
3	The Interaction of Brucite Surfaces with Uranium and its Fission Products	UCL	Eszter Makkos	PhD
4	Production of Real-time Segmented as-built CAD Models for the Planning and Execution of Remote and Human Intervention Tasks	Birmingham	Henry (Cheng) Zhao	PhD
4	The Impact of Recycled Concrete Fines on the Engineering Performance of Cementitious Infill	Leeds	Toby Lord	PhD
4	Simulating Radiation Damage in Cement	QUB	Ryan Kavanagh	PhD
4	Crack Sealing and Water Transport	Strathclyde	Riccardo Maddalena	PhD
4	Development of Novel, Low Cost Biomineral Permeable Reactive Barriers for Radionuclide Remediation	Strathclyde	Tom Mullan	PhD
4	In-situ Ground Contaminant Containment (Physical barrier)	Strathclyde	Christopher Wong	PhD
4	In-situ Ground Contaminant Containment (Physical barrier)	Strathclyde	Dr. Matteo Pedrotti	PDRA
4	Integrated Sensors for Infrastructure	Strathclyde	-	PhD
4	Nano-cracking of Cement Phases: Reactivity and Dissolution	Strathclyde	Luca Rizzo	PhD
4	Smart cements for chloride and moisture sensing in nuclear concrete assets	Strathclyde	Lorena Biondi	PhD
4	Impacts of colloidal silica based grout injection on geo-mechanical and geochemical properties of soil and radioactive wastes	Strathclyde	Dr Pieter Bots	

Radiation Driven Reactions at the Surface of Uranium Dioxide

S. Rennie*[1], J. E Darnbrough[1], E. Lawrence Bright[1], J. Sutcliffe[1], I. Griffiths[1], , L. Costelle[1], J. Rawle[2], R. Gwilliam[3], C. Jeynes[3], T. B. Scott[1], and G. H. Lander[4], R. S. Springell[1]

*Email: Sophie.rennie@bristol.ac.uk

[1] Interface Analysis Centre, University of Bristol (Bristol BS2 8BS, UK)
[2] Diamond Light Source (Harwell Science and Innovation Campus, Harwell OX11 0DE, UK)
[3] Nodus Lab, University of Surrey (Guildford, Surrey, GU2 7XH, UK)
[4] European Commission, JRC, Institute for Transuranium Elements (Postfach 2340, D-76125 Karlsruhe, Germany)

Abstract

In order to ensure resilient, long-term storage for nuclear material it is critical to have a thorough understanding of the reactions occurring at the surface of stored uranium oxides. This project aims to explore this topic in further detail through studying radiation induced oxidative *dissolution of uranium dioxide thin films*. Building on our previously developed experimental technique, we have expanded upon our initial measurements to investigate the effect of crystal orientation on the dissolution of UO_2. These measurements were conducted on the I07 beamline at the Diamond Light Source in March 2016 and a full analysis of the experimental results is currently underway. However, preliminary analysis has shown crystal orientation to significantly affect the rate of UO_2 dissolution, with the [111] film appearing far more resilient to radiation induced corrosion than either the [001] or [110] orientations.

Introduction

With the ever increasing demand for energy and the need for a more sustainable future, providing improved energy solutions has become a pressing challenge for nations across the world [1]. With nuclear power presenting a reliable, carbon-free solution, many countries have chosen to invest heavily in nuclear technology, resulting in high level waste (HLW) increasing globally, by around 12,000 tonnes each year [2]. With uranium oxides comprising the vast majority of HLW generated by modern society, it is critical that a safe and efficient storage strategy is developed for these materials. Despite the recent advancement in HLW containment systems, eventual failure will expose the surface of nuclear material to reactive environments, which may lead to degradation and corrosion of the fuel surface, releasing harmful radionuclides in to the environment [3]. It is therefore crucial that we acquire a fundamental understanding of the reactions occurring within a failed storage environment in order to develop accurate, long term corrosion models of nuclear waste.

Radiation Induced Oxidative Dissolution

Previous studies suggest that within a failed nuclear storage container, the corrosion of UO_2 is primarily driven by oxidative dissolution [4]. This is where the surface of UO_2 is oxidised to give the readily soluble U^{6+} ion, resulting in the dissolution of the fuel matrix [4]. While the groundwater present within a failed storage container does not comprise the oxidation products (H_2O_2, $OH^\bullet$) required to drive this reaction, they are instead generated via water radiolysis, initiated by residual radiation fields of the stored fuel [5-6], Fig. 1.

The focus of this research will therefore be to investigate the impact of oxidative dissolution on the surface of uranium oxides. The key aim is to expose uranium dioxide samples to a simulated failed storage environment in order to monitor the changes in surface morphology of UO_2.

Experimental Methodology

A Thin Film Approach

Spent nuclear fuel (SNF) possesses a great deal of complexity, including defects, He bubbles, microscopic cracking, and fission daughter products. When investigating the oxidative dissolution of SNF, the individual effects of these complexities become difficult to isolate, and thus highly complicated to analyse.
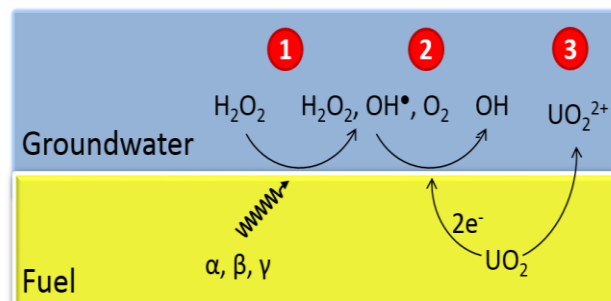

Figure 1: *Oxidative dissolution of UO_2 via radiolysis of groundwater in a failed geological disposal facility. 1) Radiolytic production of oxidants via interaction of groundwater with residual radiation fields. 2) Cathodic reduction of oxidants. 3) Anodic oxidation and dissolution of the UO_2 fuel.*

This project therefore aims to remove much of this complexity in order to first understand the corrosion mechanism for an idealised UO_2 surface, before systematically increasing material complexity. To achieve this, idealised epitaxial UO_2 thin films have been grown via Reactive DC Magnetron Sputtering at the University of Bristol. To investigate the reactions taking place at film/water interface in the presence of strong radiation fields, we have developed an experimental technique that induces dissolution of a UO_2 surface using an intense beam of x-rays, mimicking the radiation fields found at the surface of spent nuclear fuel. Initial experiments were carried out using an [001] oriented, single crystal UO_2 thin film, where synchrotron diffraction was used to measure variations in the film morphology at the Angstrom length-scale. This work has been published in Faraday Discussions [7] and will be summarised in this report.

In March 2016 we conducted a further synchrotron experiment to expand on these first measurements. Here we investigated the effect of two further variables on the dissolution of UO_2: crystal orientation and fission product damage. While the analysis from these experiments is still in progress, here we will present the preliminary findings on the effect of crystal orientation on radiation induced UO_2 dissolution.

Simulating Corrosion with Synchrotron Radiation
To investigate the effect of oxidative dissolution on the surface morphology of uranium dioxide, a series of synchrotron x-ray diffraction experiments have been conducted at both BM28, ESRF and I07, Diamond Light Source beamlines.
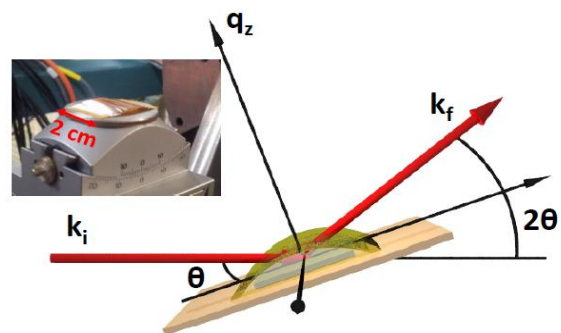

Figure 2: Schematic of the experimental set-up used at the Diamond Light Source, where k_i and k_f are the incident and exit wavevectors, ϑ the angle of incidence with respect to the detector 2ϑ and q_z the wavevector momentum transfer. The thin layer surface tension cell (insert) holds a fixed volume of water over the sample during x-ray irradiation.

To simulate the oxidising environment required for oxidative dissolution to occur within a failed geological disposal facility, a layer of milliQ water was maintained across the surface of the UO_2 film using a thin layer surface tension cell, Fig 3. The film, entirely covered by the water, was then exposed to a 17.116keV x-ray beam in order to radiolyse the water and produce the oxidation products (H_2O_2, $OH^\bullet$) required for the dissolution process to occur. X-ray Reflectivity (XRR) and high angle x-ray diffraction were then used to probe the changes in surface morphology of the UO_2 film after exposure to milliQ water in the presence of a strong radiation field.
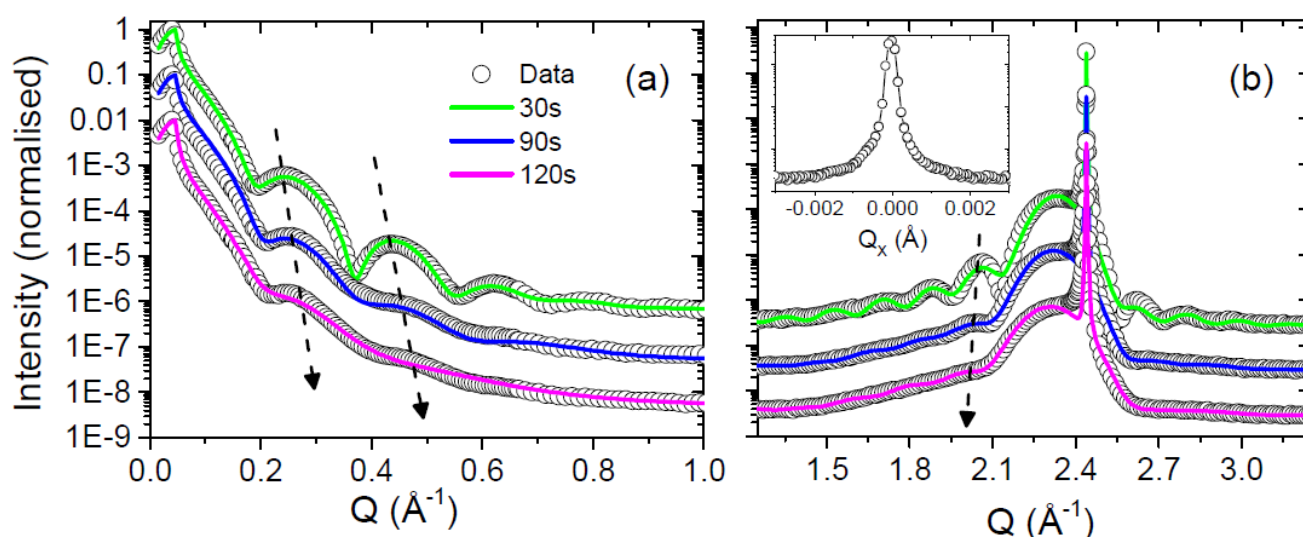

Figure 3: Panel (a) shows x-ray reflectivity and panel (b) shows high angle diffraction data, measured at exposure times of 30 s, 90 s and 120 s, the experimental data are represented by the open black circles and the fitted calculations by the solid green, blue and magenta lines, respectively. The insert of panel (b) shows the rocking curve of the (002) Bragg peak for the 30 s exposure. The dashed black arrows indicate an increase in fringe separation as a function of exposure time, which suggests a concomitant loss of material.

Exposure time (s)	t_{UO_2}	σ_{UO_2}	t_{UO_X}	σ_{UO_X}
0	34	3	10	6
30	27.5	2.5	16	9
90	21	7.6	20	11.5
120	13.5	11	22	13

Table 1: *Parameters used in the fitted calculations to model the experimental reflectivity and high angle diffraction data. All values are in Å, where t_{UO2} is the thickness of the UO2 and σ_{UO2} is the root mean squared roughness, t_{UOX} and σ_{UOX} are the thicknesses and roughnesses of the top layer of complex oxide, respectively.*

Results and Discussion

Published Results

Initial experiments carried out at synchrotron beamlines BM28, ESRF and I07, Diamond Light Source, using single crystal [001] oriented UO2 thin films were used to study the effect of radiolysis at the fuel interface. As shown in Fig. 3, a combination of X-ray Reflectivity (XRR) and high angle x-ray diffraction were used to probe changes in the thickness, roughness, electron density, crystallinity and dissolution of the film on exposure to milliQ water radiolysed by the x-ray beam for a series of exposure times. Data are presented for three exposure times, 30 s (green), 90 s (blue) and 120 s (magenta), where the data are shown as open black circles and fitted calculations are represented by solid lines. The XRR data was fitted using the Parratt recursion method [8], using the GENX computer program. These fitted calculations are based on a structural model of the UO2 film that consists of a layer of crystalline UO2 with the standard bulk density and a surface layer of reduced electron density, labelled UOX.

The fitting parameters, including layer roughnesses are summarised in Table 1. While this experiment was successful in providing a detailed insight into the oxidative dissolution of the ideal UO2 single crystal surface [7], further work is required to investigate the precise mechanism that is responsible for the observed corrosion.

Ongoing Work

The Effect of Crystal Orientation

The effect of crystal orientation on radiolysis induced UO2 dissolution was investigated by applying the previously described experimental technique for [001], [110] and [111] oriented UO2 thin films. XRR and XRD measurements were carried out for following exposure times: 30s, 60s, 90s, 120s, 150s, 210s, 270s and 330s. While a full analysis of these data sets is still in progress

Fig. 4 shows a comparison of the XRR measurements before corrosion and after an exposure time of 330s, for each film orientation. From these scans alone it is clear that there is a crystal orientation effect, with the [111] oriented UO2 being significantly more resilient to radiation induced surface corrosion, with only 7.8 Å of film being corroded over the course of 330s, compared
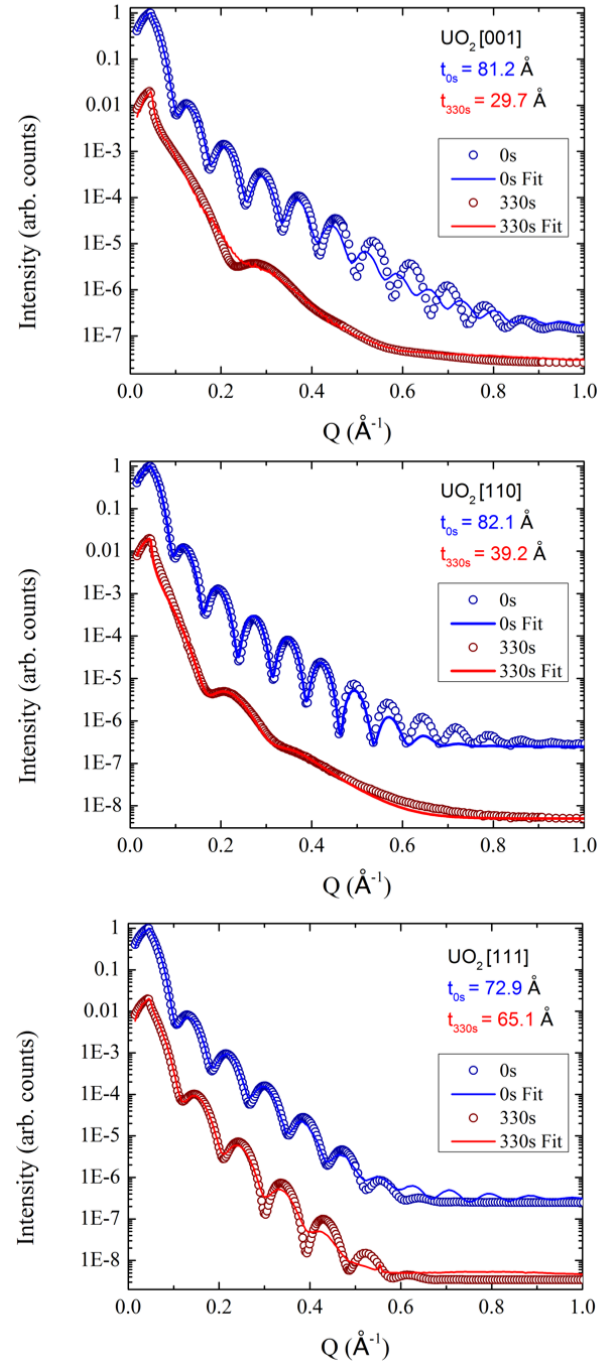

Figure 4: *XRR profile comparison of 0s and 330s corrosion of [001], [110] and [111] oriented UO2 thin films, where t is the film thickness. Corrosion rates differ between each of the orientations, with the [111] oriented film being significantly more resistant to radiolysis induced dissolution than the [001] and [110] orientations.*

with 42.9 Å and 51.5 Å for the [110] and [001] orientations. Further analysis for each of the measured exposure times will enable us to better understand how the dissolution reaction progresses for each orientation, and further elucidate the reasons for the observed differences in rates of dissolution.

The Effect of Fission Products

Further work has also been completed to implant UO_2 thin films with well-known fission products. To achieve this, thin films of UO_2 have been irradiated at the Surrey Ion Beam Centre to achieve a Xe and Cs dopant concentration of 0.5 w.t%. Subsequesnt characterisation of the implanted films has been carried out via XRD and TEM. Figure 5 shows TEM of a Xe irradiated UO_2 thin film taken using a JEOL JEF-ARM200F STEM located within the Materials Department at the University of Oxford. As displayed, damage within the crystal is not observed, suggesting that the Xe is substitutionally implanted within the UO_2 lattice.
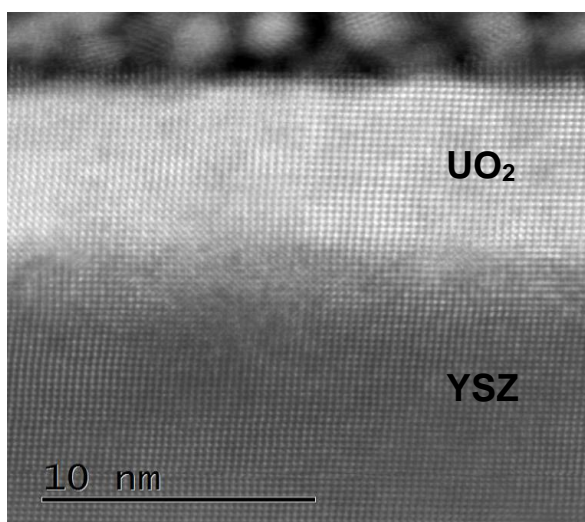
Figure 5: HAADF TEM of an Xe irradiated UO_2 thin film. With no damage being easily observed, the Xe is predicted to be substitutionally implanted within the UO_2 lattice.

Conclusions and Future Work

Building on our previous synchrotron experiments, epitaxial UO_2 thin films have been used to systematically investigate the impact of crystal orientation and fission product damage on the radiation induced dissolution of UO_2 surfaces. This approach enables us to study the complexities found within spent nuclear fuel in isolation, which is particularly advantageous for the validation of long term storage models of nuclear materials.

Initial results from the investigation into crystal orientation demonstrate that the rate of dissolution differs significantly between the principle UO_2 directions. The [111] oriented films appear to be far more resilient to the dissolution process, than both the [110] and [001] orientations. However further experimental analysis is required to understand the progression of the dissolution reaction in further detail, in order to elucidate the reason for the observed differences in dissolution rates.

Measurements were also carried out to investigate the effect of fission product damage on UO_2 dissolution. This was achieved using UO_2 thin films that had been implanted with Xe and Cs ions at the Surrey Ion Beam Centre. Analysis of these results is currently being performed.

Acknowledgements

References

[1] U. Strandberg and M. Andren, Journal of Risk Research 12 (2009) 879-895.

[2] World Nuclear Association, Available at: http://www.worldnuclear.org/info/inf103.html [Acessed: January 2013].

[3] D. W. Shoesmith, Journal of Nuclear Materials 282 (2000) 1-31.

[4] D. W. Shoesmith, Nuclear Waste Management Organization, (2007).

[5] O. Roth, PhD Thesis, University of Stockholm (2008).

[6] M. G. Bailey, L. H. Johnson and D. W. Shoesmith, Corrosion Science 25 (1985) 233-238.

[7] R. S. Springell et al., Faraday Discussions (2015) DOI: 10.1039/C4FD00254G.

[8] L. G. Parratt, Phys. Rev., 1954, 95, 359.

Uranium carbide and zirconium carbide oxidation: an *in situ* high temperature environmental SEM study

C. Gasparrini*[1], R. Podor[2], D. Horlait[1,3], M. J.D. Rushton[1], D. Coppersthwaite[4], O. Fiquet[5] and W.E. Lee[1]

*Correspondence: c.gasparrini14@imperial.ac.uk

[1] *Centre for Nuclear Engineering and Dpt. Materials, Imperial College London, Exhibition Road, SW7 2AZ, London, UK*
[2] *Institut de Chimie Séparative de Marcoule (ICSM), Bagnols-sur-Cèze, Marcoule, France*
[3] *CNRS, Centre d'Etudes Nucléaires de Bordeaux-Gradignan, UMR 5797, Chemin du Solarium, 33175 Gradignan, France*
[4] *National Nuclear Laboratory Preston, Preston, PR4 0XJ, Lancashire, UK*
[5] *Commissariat à l'Energie Atomique, CEA, CADARACHE, France*

Abstract

Oxidation of depleted uranium carbide (UC) was investigated via experiments on sintered fragments oxidised in air in a furnace and *in situ* with a state-of-the-art technique: High temperature Environmental Scanning Electron Microscopy (HT-ESEM). This technique revealed the morphological changes occurring during the transformation between UC to UO_2 and UO_2 to U_3O_8. Experiments performed in an atmosphere of 10 Pa of oxygen and in a furnace in air from $873 - 1173$ K revealed the influence of temperature in the final oxide product characteristics: oxide morphology, conversion and specific surface area (SSA). Samples oxidised at T> 873 K showed partial sintering of the oxide which acts as a diffusion barrier and limits the occurrence of UO_2 to U_3O_8 to cracked surfaces. Experiments performed from $723 - 848$ K in an atmosphere of 10 to 100 Pa O_2 revealed the key role of crack propagation, monitored with an image analysis technique, in the oxidation and the self-ignition process of UC.

Prior to UC active work, zirconium carbide (ZrC) oxidation was investigated. Oxidation performed from $1073 - 1473$ K in air and oxygen atmosphere revealed the interface in between the carbide and the oxide to be comprised of an amorphous carbon matrix with nanocrystals of zirconia embedded in it. *In situ* analysis performed on ZrC with an HT-ESEM was used to examine the influence of crack propagation on the Maltese Cross shape development of the oxide.

Introduction

Uranium carbide (UC) [1],[2] has the potential to be used in the nuclear industry as nuclear fuel for Generation IV reactors thanks to its higher metal atom density and better thermal conductivity when compared to the commonly used uranium oxide fuels [3].While UC offer improved properties during use, at the end of its fuel cycle it cannot be safely disposed of without being conditioned into a suitable oxide form as it is reactive and potentially pyrophoric [4]. UC oxidation has been widely studied in the past, during the 50s and 60s, however many aspects related to its mechanism of oxidation and ignition, for example the formation of a protective or non-protective oxide layer, are still not yet understood [5][6]. The aim of this project is to investigate the oxidation mechanism of depleted uranium carbide fuels that have been stored for several decades at the Dounreay site, Scotland, and to convert them into a suitable oxide form that meets repository specifications (specific surface area (SSA), conversion and carbon content). Experimental work has been performed on depleted UC pellets and fragments in the National Nuclear Laboratory (NNL) facilities in Preston, UK. The main parameters investigated during the oxidation studies performed at NNL are the influence of temperature and time on the oxide product characteristics (oxide morphology, SSA, conversion and carbon content) from $873 - 1173$ K n air atmosphere. Heat of combustion from UC pellets kept and crushed in air or inert atmosphere has also been investigated in order to assess the degradation of this material when handled in air. The influence of partial pressure of oxygen and temperature on the oxidation mechanism from 723 to 1173 K was investigated with *in situ* experiments with a state-of-the-art characterisation technique: high-temperature environmental scanning electron microscopy (HT-ESEM) in collaboration with the Marcoule Institute of Separative Chemistry, France. These *in situ* study were performed on UC fragments kindly provided by Commissariat à l'Energie Atomique, (CEA), Cadarache, France. *Post mortem* analysis on the oxide products were performed at Imperial College, Department of Materials with a high resolution transmission electron microscopy (HRTEM).

Before getting access to the NNL nuclear site preliminary work was performed on a non active carbide material, zirconium carbide (ZrC). This carbide has potential to be used in the nuclear industry as an inert matrix in carbide fuels or as a structural component in tristructural-isotropic (TRISO)[7],[8] fuel particles for Generation IV reactors. Advantageous properties of ZrC include high melting point (around 3700 K[9]), and high thermal conductivity (20 $Wm^{-1}K^{-1}$ at 300 K[10]). Oxidation studies were performed on dense hot pressed specimens of ZrC from 1073-1473 K for kinetics analysis and characterization of the ZrC/ZrO_2 interface on samples cross sections. *In situ* oxidation was performed with the HT-ESEM, ICSM, France, from 1073-1473 K in 200 Pa O_2 atmosphere. This study revealed the main steps involved in the formation of the typical Maltese cross [11] shape of the oxide.

Methodology Details

Uranium Carbide

Oxidation studies on depleted UC were carried out by TGA/DSC-MS on fragments of about 50 mg in weight crushed in air atmosphere or inert atmosphere after XRD (X-ray diffraction) characterization. Oxidation on UC pellets of about 80 g and fragments of about 1 g in weight were performed in a muffle furnace from 873 – 1173 K in air atmosphere. The oxide products were thoroughly characterized using SEM equipped with an energy dispersive x-ray spectrometer (EDX), XRD, carbon analyser and Brunauer-Emmett-Teller (BET) surface area analysis. Fragments with masses from 3.3-17.5 mg were oxidized in the HT-ESEM from 723 – 1173 K in an atmosphere of 10-100 Pa O_2. Image analysis on the secondary electron images was performed by ImageJ. A process called skeletonization was used to identify crack length and network, this was performed using the plugins Skeletonize (2D/3D) and Analyse Skeleton in ImageJ. Oxide products were characterized by SEM and HRTEM.

Zirconium Carbide

ZrC specimens were cut from hot pressed discs of commercial ZrC powder (Grade B, Starck, Germany) by electrical discharge machining method. After density and characterisation performed by SEM and XRD, 1cm cubic specimens were oxidised in a furnace with air atmosphere from 1073-1473 K. Cuboid specimens with size 4×4×0.5 mm^3 were oxidised in a HT-ESEM at 1073 K in a 200 Pa oxygen atmosphere. Characterisation on partly oxidised sample cross sections was performed via SEM and HRTEM. Chemical analysis was done by EDX and a Focused Ion Beam instrument coupled with a Secondary Ions Mass Spectrometer (FIB-SIMS).

Results and Discussion

Uranium Carbide

Figure 1 is a sequence of photos and SEI of UC fragments oxidised in a furnace for 4h at 873-1173 K in air. The influence of temperature on the U_3O_8 (confirmed by XRD) products was first assessed by eye and then with SEI analysis and BET. Samples oxidised at low temperature (873 K) showed a fine powdery morphology (Figure 1a and d) while by increasing the temperature (to 973 K and 1173 K) oxide samples had a compact morphology (Figures 1 b and e, 1c and f). The SEI of this compact oxide resembles the microstructure of a material that underwent a sintering process (Figures 1f). BET analysis confirmed that SSA decreased with increasing temperature: from 0.61 ± 0.03m^2/g at 873 K down to 0.22 ± 0.02 m^2/g for samples oxidised at 1173 K for 4 h. Increasing the oxidation time from 4 h to 17 h at 1173 K the oxide SSA decreased to 0.14 ± 0.003 m^2/g. All samples were oxidised to U_3O_8, however UC was still present as confirmed by XRD.

Pellets oxidised in a furnace in air at 873 and 1173 K showed that similar conversions (76 % and 73% respectively) were achieved in less time (17 h instead of 22h) at lower temperature oxidation, 873 K instead of 1173 K.
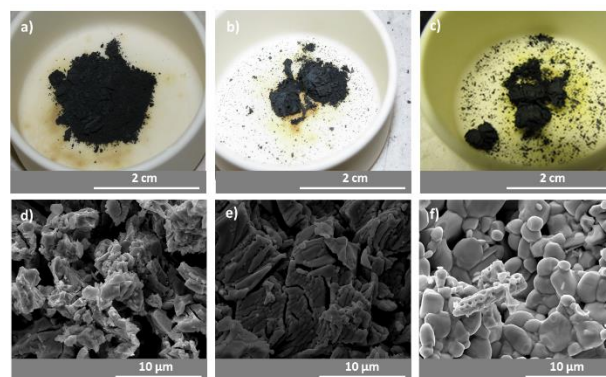

Fig 1. Appearance and morphology of uranium oxide revealed by photos (top) and SEI (bottom) of UC fragments (about 1g) oxidised at: a) d) 873 K for 4 h, b) e) 973 K for 4 h, c) f) 1173 K for 4 h in air

HT-ESEM experiments performed from 873 - 1173 K in an atmosphere of 10 Pa O_2 on UC fragments (mass from 8-10 mg) revealed the compacting process occurring for temperature above 873 K. The popcorn-like[12] morphology typical for transformation of UO_2 to U_3O_8 appeared first at the edges and subsequently on as-cracked surfaces in samples oxidised at T > 873 K. Oxidation on samples at 873 K instead occurred all over the surface as soon as oxygen was inserted in the chamber. The time needed for the fragments to oxidise completely in the HT-ESEM was lower at 873 K showing that the compacting process of the oxide at high temperatures acted as a barrier that slowed the oxidation reaction.

HT-ESEM experiments performed from 723-848 K in an atmosphere from 10-100 Pa O_2 showed the influence of

temperature and oxygen partial pressure on UC ignition. By monitoring the samples with an image analysis technique it was possible to show the influence of crack propagation and crack network on the UC fragmentation and consequent ignition. The explosive nature of the transformation from UO_2 to U_3O_8 shown in Figure 2 occurred after an exponential propagation of cracks area and cracks length.
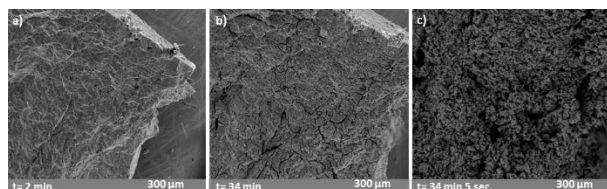

Fig. 2 Sequence of SEI showing in situ oxidation of a UC fragment oxidised at 773 K in 10 Pa O_2 a) 2 minutes after oxygen insertion, b) 34 minutes after oxygen insertion showing sample expansion, c) 34 minutes and 5 seconds showing the pop-corn like transformation

Zirconium Carbide

The oxide layer of ZrC, as well as of UC and of other carbides of the group IV, V and VI of the transition metals, assumes a particular shape, the so called "Maltese cross"[11]. Furnace experiments revealed the development of the oxide with time at different temperatures, from 1073 – 1373 K. Kinetic analysis showed ZrC oxidation to follow a linear trend before drastic oxidation occurs with growth of the oxide in the shape of a Maltese cross. *In situ* investigations performed on hot pressed ZrC samples in a HT-ESEM revealed the role of cracks in the development of the Maltese Cross (see Figure 3). By monitoring the surface and edges of the sample, cracks were seen to form first at the outer corners and then towards the inner unoxidised carbide core. At this stage microcracks parallel to the interface oxide/carbide were cyclically formed when the oxide layer reached a thickness of about 20μm.
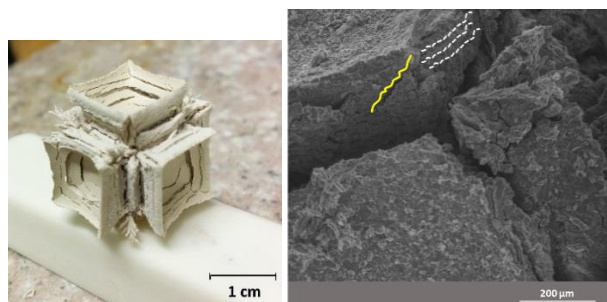

Fig 3. Photograph of a ZrC specimen oxidized at 1273 K for 4h (left) and SEI of ZrC specimen oxidized for 300 min at 1073 K in a 200 Pa oxygen atmosphere in a HT-ESEM (right): details of crack formation at the corners and propagation towards the inner carbide core (yellow continous line) and microcracks parallel to the interface carbide/oxide (dashed line)

Characterisation of the oxide/carbide interface was performed by SEM and HRTEM on sample cross sections. This showed the presence of an interface rich in carbon where nanocrystals of m-ZrO_2 of about 5nm in diameter were embedded[11]. Chemical analysis was performed by EDX and by FIB-SIMS across the interface of a sample oxidised in an atmosphere of O^{16} and subsequently in O^{18}. These isotopes were used as markers in order to monitor the oxygen pathway through the oxide layer during oxidation.

Conclusions and Future Work

This research aims is to give commercially useful information about an optimized UC conditioning process. Experimental results show that oxidation performed on UC at 873 K gives an oxide with higher SSA and with same degree of conversion in less time compared to oxidation at 1173 K. The lower efficiency of the oxidation process at high temperature (T > 873 K) is related to a compacting mechanism of the oxide. Crack propagation and network are shown to be responsible for the explosive oxidation reaction occurring in the range of temperature of 723 – 848 K in an atmosphere of 10-100 Pa O_2 monitored *in situ* with a HT-ESEM.

Parallel work performed on an inactive carbide, ZrC, helps our understanding of UC oxidation. The Maltese Cross shape of the oxide during ZrC oxidation monitored *in situ* develops due to crack formation at corners and microcrack propagation parallel to the interface due to its debonding. ZrC/ZrO_2 interface was seen to be comprised of an enriched carbon layer with nanocrystals of ZrO_2. This helps understanding the presence and role of carbon during oxidation and ignition of UC.

The role of cracks and therefore the increase of reactive surface area is seen to play a major role in oxidation of carbide materials. The approach used for UC and ZrC oxidation used in this work can be applied to other carbides in order to assess the role of parameters such as temperature and pressure on the oxidation mechanism.

Acknowledgements

References

[1]   C. Berthinier, C. Rado, O. Dugne, M. Cabie, C. Chatillon, R. Boichot, E. Blanquet, Experimental

kinetic study of oxidation of uranium monocarbide powders under controlled oxygen partial pressures below 230°C, J. Nucl. Mater. 432 (2013) 505–519. doi:10.1016/j.jnucmat.2012.08.002.

[2]   C. Berthinier, S. Coullomb, C. Rado, E. Blanquet, R. Boichot, C. Chatillon, Experimental study of uranium carbide pyrophoricity, Powder Technol. 208 (2011) 312–317. doi:10.1016/j.powtec.2010.08.022.

[3]   IAEA - International Atomic Energy Agency, Thermophysical Properties of Materials for Nuclear Engineering: A tutorial and Collection of data., IAEA-THPH, Vienna, 2008.

[4]   M. Dell, V.J. Wheeler, The ignition of uranium mononitride and uranium monocarbide in oxygen, J. Nucl. Mater. 21 (1966) 328–336.

[5]   K. Naito, N. Kamegashira, T. Kondo, S. Takeda, Isothermal oxidation of uranium monocarbide powder under controlled oxygen partial pressures, J. Nucl. Sci. Technol. 13 (1976) 260–267. doi:10.1080/18811248.1976.9734020.

[6]   J.S. Shepherd, M. Fairweather, B.C. Hanson, P.J. Heggs, Mathematical model of the oxidation of a uranium carbide fuel pellet including an adherent product layer, Appl. Math. Model. 45 (2017) 784–801. doi:10.1016/j.apm.2017.01.041.

[7]   W.E. Lee, M. Gilbert, S.T. Murphy, R.W. Grimes, Opportunities for advanced ceramics and composites in the nuclear sector, J. Am. Ceram. Soc. 96 (2013) 2005–2030. doi:10.1111/jace.12406.

[8]   K. Minato, T. Ogawa, K. Fukuda, H. Nabielek, H. Sekino, Y. Nozawa, I. Takahashi, Fission product release from Zrc-coated fuel particles during postirradiation heating at 1600 C, J. Nucl. Mater. 224 (1995) 85–92. doi:10.1016/0022-3115(95)00032-1.

[9]   H.F. Jackson, D.D. Jayaseelan, D. Manara, C.P. Casoni, W.E. Lee, Laser melting of zirconium carbide: determination of phase transitions in refractory ceramic systems, J. Am. Ceram. Soc. 94 (2011) 3561–3569. doi:10.1111/j.1551-2916.2011.04560.x.

[10]   H.F. Jackson, W.E. Lee, Properties and characteristics of ZrC, in: Elsevier (Ed.), Compr. Nucl. Mater. - Vol. 2, 2012: pp. 339–372. doi:10.1016/B978-0-08-056033-5.00085-9.

[11]   C. Gasparrini, R. Podor, D. Horlait, R. Chater, W.E. Lee, Zirconium carbide oxidation: maltese cross formation and interface characterization, Oxid. Met. (2016) 1–8. doi:10.1007/s11085-016-9672-6.

[12]   R.J. McEachern, P. Taylor, A review of the oxidation of uranium dioxide at temperatures below 400°C, J. Nucl. Mater. 254 (1998) 87–121. doi:10.1016/S0022-3115(97)00343-7.

The Behaviour of Spent Nuclear Fuel in Wet Storage

Elizabeth Howett*[1], Colin Boxall[1], and David Hambley[2]

*Correspondence: e.howett@lancaster.ac.uk

[1] *Lancaster University, Lancaster LA1 4YW*
[2] *National Nuclear Laboratory, Cumbria CA20 PG*

Abstract

The project aims to investigate the behaviour of Spent Nuclear Fuel (SNF) in interim storage, specifically AGR fuel in storage ponds at Sellafield. Corrosion behaviour will be studied in order to assess the validity of extended storage periods. Studies will be carried out on UO_2, SIMFUEL and AGR cladding samples separately and in binary systems. Once these initial experiments have been completed, analogous experiments will be carried out on real spent AGR fuel. Studies have been carried out on the corrosion behaviour of sensitised and unsensitised stainless steel cladding samples in simulant pond water with varying temperature, chloride concentration, pH and hydrogen peroxide concentration.

Introduction

The Thermal Oxide Reprocessing Plant (THORP) at Sellafield is due to close in 2018. Future un-reprocessed spent nuclear fuel (SNF) will be sent to a GDF (geological disposal facility) although this is currently not expected to be available for receipt of SNF before 2075. Between THORP closing and the GDF opening, AGR SNF will be held in interim wet storage in ponds containing demineralised water dosed with NaOH (to pH≈11.4 at 24°C) which acts as a corrosion inhibitor, at sites such as Sellafield. Current storage periods are typically less than 10 years, although this may extend to as long as 100 years after THORP closes. It therefore necessary to determine if the SNF can be stored safely in the same manner without significant degradation of the SNF over this time scale.

AGR cladding can be breached due to inter-granular Stress Corrosion Cracking (igSCC) or damaged during dismantling. The former may be at least in-part facilitated by the steel cladding becoming sensitised to corrosion processes due to its in-reactor irradiation history. If the cladding is breached, the fuel itself can also become exposed. Evolution of both the steel & UO_2 surfaces upon consequent exposure to pond water can be considered as corrosion processes and so conveniently studied by electrochemical methods.

In order to accommodate all future AGR SNF, a new racking system for the Thorp receipt and Storage pond has been proposed. This new storage arrangement will mean that fuel will be packed closer together, causing a rise in temperature of the fuel and the pond water within the storage racks compared to that which would be expected in the current storage arrangement. Current assessments indicate that rack water temperature could be up to approximately 60°C with an average of around 45°C. For this section of the project the corrosion behaviour of both sensitised and unsensitised samples is studied by linear sweep voltammetry to assess short time corrosion susceptibility of these materials at existing and proposed pond temperatures as well as a pond maloperation temperature of 90°C.

Methodology Details

The surfaces of unsensitised and sensitised 20/25/Nb SS (AGR cladding) were etching of in oxalic acid in order to assess the degree of sensitisation present. An SEM was used to visualise the results of the etching process. A series of linear sweep voltammetry (LSV) experiments were then carried out on several samples of unsensitised and sensitised 20/25/Nb SS in pond water simulant. Figure 1 shows the experimental set-up, where CE is the counter electrode (platinum mesh), WE is the working electrode (the SS sample) and RE is the reference electrode (Ag/AgCl), the circuit here represents the potentiostat. The potential was swept from -0.8V to 1.2V in most cases, some experiments started at the open circuit potential of the sample. The scan rate was 1mV/s.

Figure 1: Experimental set-up for voltammetry

Results and Discussion

In the first instance experiments were carried were carried out on cladding samples to assess the effect of heat treatment on the degree of sensitisation. Metallographic etching with 10wt% oxalic acid was used to identify the presence of sensitistation. Oxalic acid attacks chromium carbide precipitates at grain boundaries indicating the existance of Cr depleted regions adjacent to such carbides [1]. Figure 2 shows the resulting images taken using an SEM, the step like structure seen for the untreated sample in Figure 2(a) implys that the sample is free from sensitisation. Where as the heat treated sample in Figure 2(b) shows a ditch structure which signifys sensitisation.
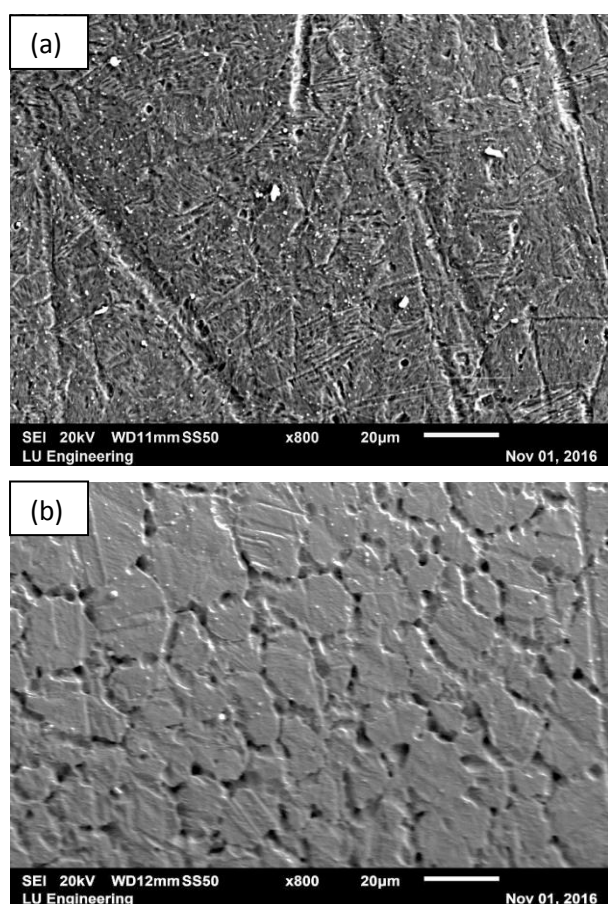
Figure 2: Effect of heat treatment on AGR cladding samples, (a) untreated and (b) solution annealed at 1500°C and aged for 48hours at 600°C.

The general corrosion behaviour of the heated treated and unsensitised samples is seen is Figure 3. Pitting is observed at pH≈7, but there's no pitting evident at 11.4 for either sample, this could be due to a lack of passive nickel protection in neutral solution. The transpassive currents for the heated treated sample are slightly larger than those of the unsensitised sample. However, it appears that chromium depletion has not had a significant effect on the general corrosion behaviour at pH≈11.4.
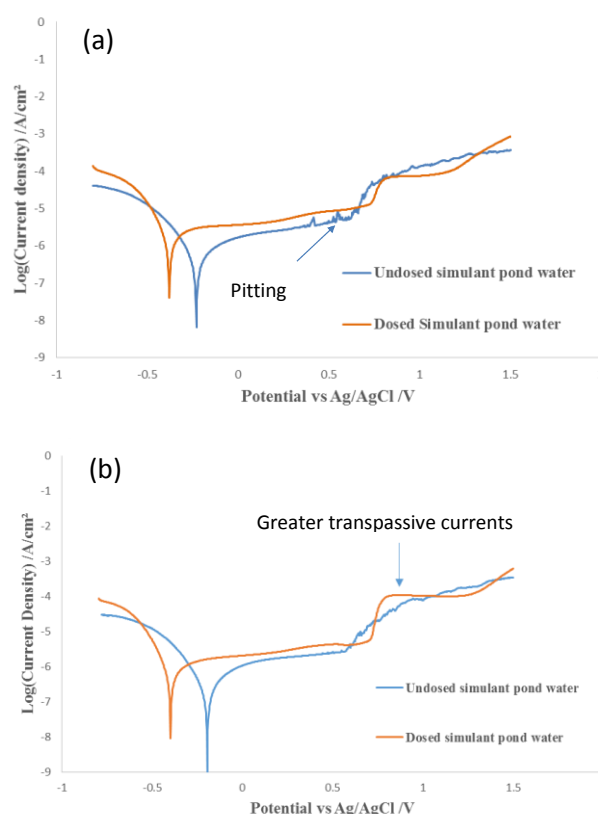
Figure 3: Effect of dosing pond water to a pH≈11.4, unsensitised (a) and heat treated (b) 20/25/Nb SS.

The ion which is the principal corroding threat in the simulant pond water is chloride. Thus an investigation into the effect of its concentration on the corrosion behaviour of AGR cladding was investigated, the results of which are found in Figure 4. For unsensitised steel (Figure 4(a)) concentration ≈56mM as necessary to impact significantly on the behaviour. At this concentration peaks associated with pitting corrosion are evident. It contrast to this for the sensitised sample there is a much larger transpassive current seen at the same chloride concentration (Figure 4(b)), this is possibly due to intergranular attack. A secondary process (proposed to be derived from hexachloroferric electrochemistry) occurring in the post transpassive region, for the heat treated sample, is evident. The onset of this process appears to shift in the cathodic direction with an increase in chloride concentration. This suggests that chloride may be interfering with the formation of the secondary iron oxide passive layer.

(a)

(b)
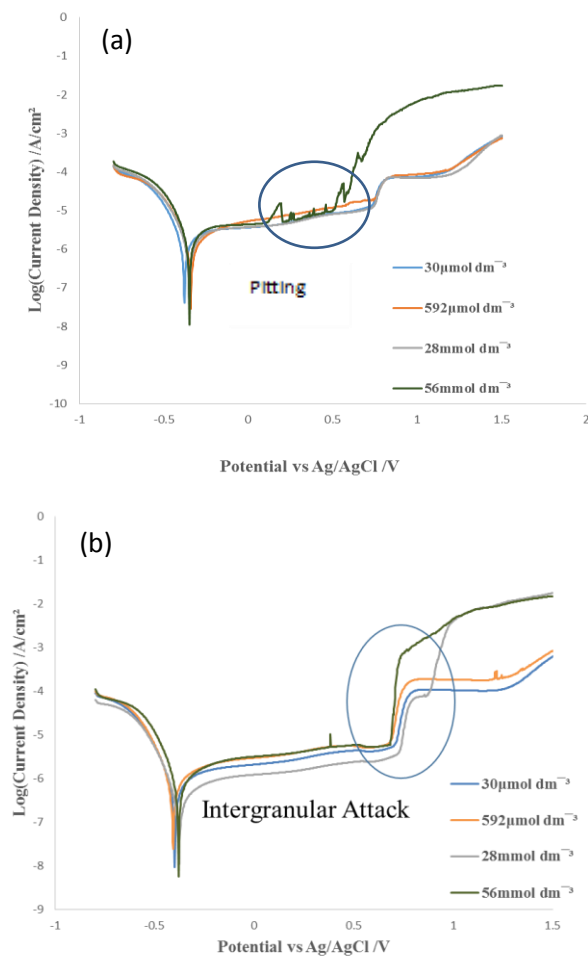
Figure 4: Effect of chloride concentration on unsensitised (a) and heat treated (b) 20/25/Nb SS.

The effect of the temperature on the corrosion behaviour of unsensitised steel is seen in Figure 5. The most significant changes between 24°C, 45°C and 60°C are the shift in the corrosion potential in the anodic direction and the movement of the onset of transpassivity to lower potentials with increasing temperature.
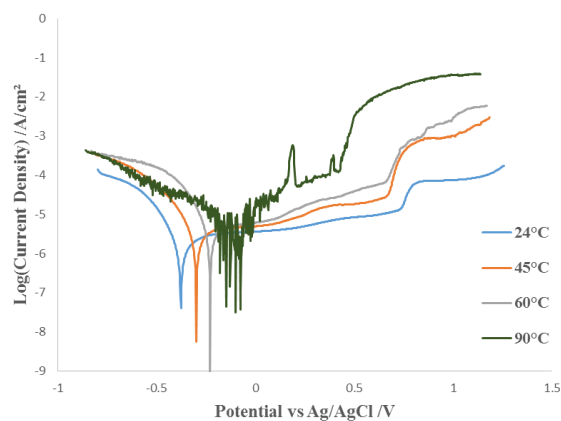
Figure 5: Effect of increasing temperature on corrosion behaviour of unsensitised 20/25/Nb SS.

Therefore the passive region for 20/25/Nb SS in simulant pond water becomes smaller as temperature increases. The open circuit potentials of the sample, which are ~0V, ~ -0.07 and ~ -0.1V at 24, 45 and 60 °C respectively, all of which still lie safely in the passive region for these operating temperatures.

At 90°C the passive range contracted compared to that seen at 24-60°C, additionally the general corrosion current in the passive range has increased; and several transient current peaks associated with pitting corrosion are observed in the this range. It is hypothesized that this change is associated with increased solubility of passivating oxide layers with temperature, resulting in the formation of only a thin porous protective oxide layer at the electrode surface leading to greater corrosion currents. This oxide layer is expected to consist of Fe, Ni and Cr oxides, with Fe being the main contributor in alkaline solutions [2, 3].
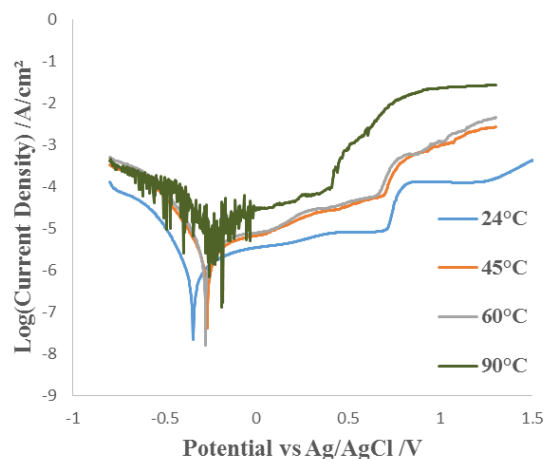
Figure 6: Effect of temperature change on the corrosion behaviour of 20/25/Nb SS with $[H_2O_2]=10\mu$mol dm^{-3}.

The addition of hydrogen peroxide to the solution is used to mimic the effect of radiolysis, it is expected that around 1ppm H_2O_2 will be present in solution during the storage period. Figure 6 shows the effect of increasing the temperature in the presence of H_2O_2 at a concentration of 10μM. No major changes are evident at 24°C, 45°C and 60°C. There is only a minor increase in the general corrosion. However, at 90°C the peaks associated with metastable pitting have shrunk or even entirely disappeared suggesting that H_2O_2 has a protective effect on the steel.

Conclusions and Future Work

The results demonstrate the following, with respect to the initiation of corrosion:

- It is advantageous in terms of minimising corrosion to dose the ponds to pH≈11.4. In most cases, at pH ≈ 7 the initiation of pitting is observed ~ 0.4V vs Ag/AgCl, pits are considered to be initiators of stress corrosion cracking (SCC).

- In the absence of peroxide, higher chloride concentrations than those expected in pond water, ~30 μmol dm^{-3}, are necessary to cause significant cathodic movement in breakdown potential and thus the onset of intergranular attack for all samples discussed.

- There generally appears to be no localised corrosion threat to fuel cladding as the electrolyte temperature is increased in the range 24°C-60°C, in the absence of peroxide, assuming that the fuel has not undergone SSC or intergranular attack before submersion in the ponds.

- In the presence of peroxide, initiation of pitting is evident for a peroxide concentration of 10μmol dm^{-3} for temperatures greater than 60°C for unsensitised samples. The surface does seem to be protected from the larger metastable pits observed at 90°C in the absence of peroxide.

The next steps for this project include:

- Carrying out similar experiments on real irradiated AGR cladding and demonstrating whether or not the heat treated samples are an effective analogue.

- The corrosion behaviour of uranium dioxide and AGR SIMFUELs in simulant pond water under the expected interim storage conditions is currently being investigated.

- Experiments with real spent nuclear fuel will hopefully be carried out in the near future also.

Acknowledgements

References

1. M. Streicher, J. Electrochem. Soc, 1959. **106**(3): p.161-180
2. C. Olsson and D. Landolt, Electrochimica Acta, 2003. **48**: p. 1093-1104.
3. T. Jabs, P. Borthen, and H. Strehblaw, J. Electrochem. Soc, 1997. **144**(4): p. 1231-1243.

Transitioning of Spent AGR Fuel from Wet to Dry Storage.

James Goode*[1], Bruce Hanson and David Harbottle

*Correspondence: pmjbg@Leeds.ac.uk

[1] *School of Chemical and Process Engineering, University of Leeds, Leeds, LS2 9JT*

Abstract

UK strategy relating to the treatment of spent nuclear fuel (SNF) has recently changed from reprocessing as part of a closed fuel cycle to direct disposal into a geological disposal facility (GDF). Since a GDF is not expected to be available until 2075 interim storage of fuel will be required. The use of interim dry storage has been mooted however, little research has been carried out into the effects of drying stainless steel (SS) clad spent nuclear fuel and this PhD is intended to begin work in this area.

Preliminary work has been carried out on simulant aluminium clad fuels as part of an MSc project which has been used to evaluate some initial experimental methods, however going forward work will concentrate on SS clad fuels. The initial phase of this work will be the development of a method for producing and characterising samples representative of SNF that has been stored for 20 years in caustic conditions (Sellafield's current strategy).

Introduction

The UK government has made the strategic decision to stop spent fuel reprocessing and adopt an open fuel cycle. Empirical evidence has shown that caustic dosing allows fuel to be safely wet stored for at least 25 years and the Thorp receipt and storage pond (TR&S) will be used for the this purpose until at least2038. In the long term, fuel will need to be transferred to a geological disposal facility (GDF) however since this is not expected to be available until 2075[1] a decision will need to be made in the future as to how the fuel will be stored during the interim period of approximately 35 years.

Should continued storage in caustic conditions be shown to cause unacceptable levels of cladding degradation, then the fuel will need to be stored dry. Dry storage is being utilised in many countries for the storage of LWR and MTR fuels however little research has been carried out into the dry storage of fuels utilising stainless steel (SS) cladding such as AGR fuel. Consequently, considerable work will be required to ensure that a safety case can be made for such work, and the current PhD project intends to begin working in this area.

Methodology Details

A multi-purpose drying rig has been constructed (see Figure 1) which allows comparison of vacuum and flowed gas drying methods.
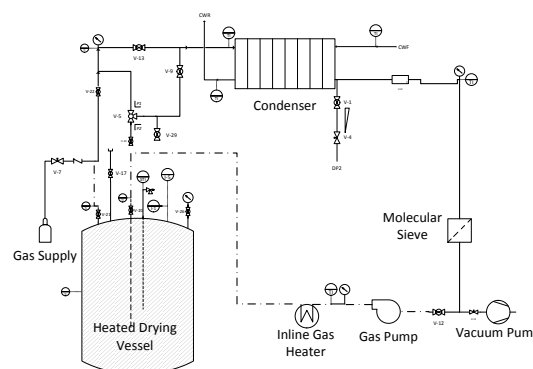
Figure 1. P&ID of the multi -purpose drying rig used.

A number of test pieces (TP) have been produced to represent failed fuels (see Figure 2).

Figure 2. The four test pieces (TP) used. These are pinholed acrylic tube (PinA), pinholed SS (PinSS), crcaked acrylic tube (CA) and cracked SS (CSS).

The TP's were filled with water and then underwent a number of drying operations until all water was removed. The TP was weighed before and after each operation to allow a drying rate to be calculated. During the tests the vessel walls were held at 30°C. The TP was placed inside the vessel and then the vessel was evacuated. The pressure inside the vessel was recorded as was the mass flow rate and several temperatures around the system including the TP surface temperature, the vessel air temperature and the temperature at the inlet to the condenser. To remove all water from a TP typically required around ten drying operations of around one hour although in some cases longer drying tests were required.

Results and Discussion

Results were obtained in the form of data plots for the live data collected and an individual drying rate for each test. The data discussed below is for the cracked acrylic tube.

Three different drying regimes were seen in all operations. The first regime is seen in Figure 3. At the start of the test the vessel is evacuated. This causes the air space in the vessel to expand ejecting water from the TP through the crack. This pools in the base of the vessel. This first regime shows a relatively steady drop in flow rate and pressure (P) as this water is boiled away.

The first regime transitions into the second regime around 2300 seconds (Figure 3). During the second regime there are spikes in P and flow as slugs of water are ejected from the TP however the majority of the time the flow rate is below the level of detection and the P is constant. This behaviour continues for 3 operations.
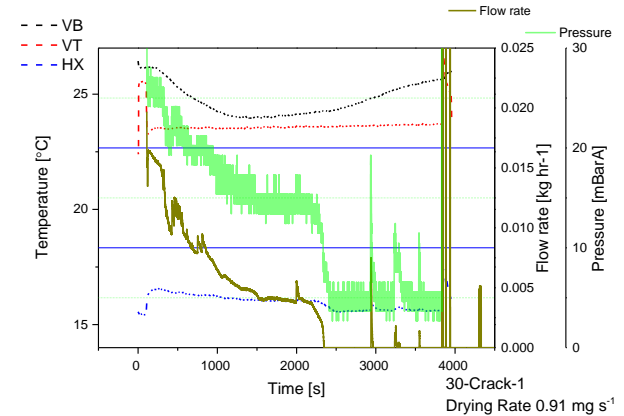
Figure 3. Data Plot for first drying operation.

In test four regime 2 transitions to regime 3 and this is seen in Figure 4. During the final drying regime the water level has dropped below the level of the cap on the TP so slugs of water can no longer be ejected from the tube. This means that drying is by the removal of water vapour only and this is below the level of detection for the flow meter. Pressure remains constant.
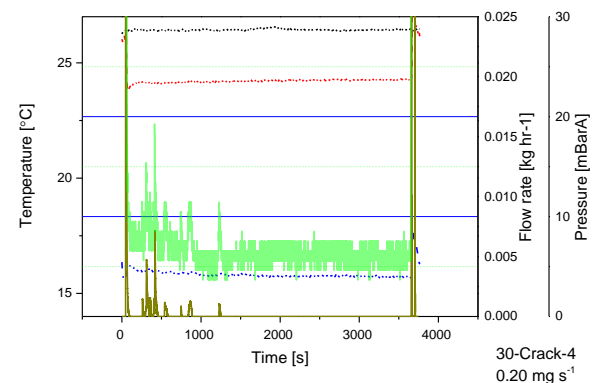
Figure 4. Data plot for fourth drying operation.

This continues until the eighth test when all free water is removed. At this point there is a final drop in P (Figure 5).

Figure 5. Data plot for eighth drying operation.

Figure 6 shows the drying rates for all operations and for all four TP's. For the cracked acrylic described above it can be seen that when a test shows only one drying regime the drying rate is found to be constant. For tests with a transition an intermediate value is found for the drying rate.
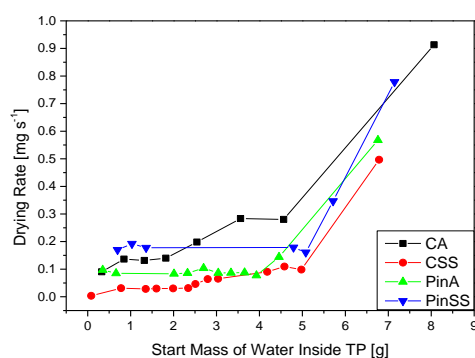
Figure 6. Drying rates for all drying operations for different TP's.

Similar results are seen for all TP's. The key difference is that the pinholed TP's have only two regimes while the cracked the SS TP spears to have four regimes. This is being investigated further.

Acknowledgements

References

1   Kyffin, J. The technical case for interim Storage of AGR fuel and development of a programme of further work, in Manchester, IChemE, 9-11 April.

Grain Boundary Damage Mechanism in AGR Claddings under Irradiation

C. Barcellini[1*], S. Dumbill[2], E. Jimenez-Melero[1]

*Correspondence: chiara.barcellini@postgrad.manchester.ac.uk

[1]*School of Materials, University of Manchester, Oxford Road, Manchester, M13 9PL, UK*
[2]*National Nuclear Laboratories, Central Laboratory, Sellafield, Seascale, Cumbria, CA20 1PG, UK*

Abstract

The safe interim storage of AGR irradiated fuel in water ponds requires a detailed knowledge of the corrosion behaviour of the fuel cladding material. The systematic study of corrosion relies on the availability of sensitised 20Cr25Ni Nb-stabilised stainless steel, ideally with a microstructure close to that produced by neutron irradiation but less radioactive. The aim of this PhD project is the production of sensitised specimens using an intense beam of protons, and to develop thereupon an understanding of the mechanisms driving the radiation-induced segregation of chemical species in the vicinity of grain boundaries. Analytical electron microscopy will be used to investigate the damaged structures resulting from the irradiation experiments, in order to compare them with those of claddings removed from the reactor core. A profound knowledge of the behaviour of 20Cr25Ni Nb-stabilised stainless steel under irradiation, however, starts with the characterisation in the pre-irradiation conditions (cold-rolled and annealed), and to determine the optimum conditions for the ion irradiation experiments.

Introduction

British nuclear fuel strategy has changed in the last years. In 2018, the reprocessing operation in THORP is scheduled to end. Therefore, the AGR fuel will interim be stored in water ponds, pending packaging and disposal. Long wet storage challenges the cladding integrity; therefore, studies on the ageing degradation characteristics are strongly needed. One of the possible challenges is related to the corrosion resistance of 20Cr25Ni Nb-stabilised stainless steel claddings.

The interim storage of irradiated AGR fuel in water ponds requires a very detailed knowledge of the corrosion behaviour of the fuel cladding material. The systematic study of corrosion relies on the availability of sensitised 20Cr25Ni Nb-stabilised stainless steel. Irradiating the material seems to be the best way to achieve the sensitisation, since thermally-sensitised samples do not present a microstructure comparable to that of the claddings removed from the reactor core.

Protons beams have already been used to simulate neutron effects in other austenitic stainless steels with very promising results. For this reason, irradiation of AGR cladding material with an intense beam of protons looks like to be the best approach for the production of sensitised samples, with a microstructure similar to that of neutron-irradiated steel, but reduced or no radioactivity. This will open the door to the systematic study in this project on the effect of irradiation on the structure and chemistry of these materials. The result of this project will provide a valuable input to predict reliably the corrosion resistance of the AGR spent fuel in storage conditions.

The characterisation of the microstructures obtained by proton irradiation is fundamental to assess if the sensitisation obtained can be compared with neutron-damaged structures. However, the profound knowledge of the non-irradiated microstructure is also important as the baseline to assess the effects of irradiation on the material.

In the following an update on the project can be found. The microscopic characterisation of three chemistries of 20Cr25Ni Nb-stabilised stainless is reported, together with the first results obtain with nano-indentation on four irradiated specimens.

Methods

Materials and Sample Preparation

Three different batches of AGR cladding material have been so far received and characterised in the as-received and heat treated condition. They differ in the niobium content and the thermal history. Batch 1 has been received already in the heat treated condition, Batch 2 was in an unknown condition and Batch 3 comes from a non-irradiated AGR tube cut and flattened.

The as-received condition and the heat-treated condition (930°C for 40min in argon atmosphere) have been studied using scanning and transmission electron microscopy (SEM/TEM). Samples have been ground with SiC paper to grit4000, and then electropolished with 5% perchloric acid in methanol in order to reach a final finish suitable for Electron BackScattered Diffraction (EBSD) characterization in the SEM. Samples for ion irradiation were heat treated, and then ground and polished down to 0.25μm OP-S solution.

Irradiation Experiments

Twelve specimens of heat treated 20Cr25Ni Nb-stabilised stainless steel have been irradiated at a constant temperature, either with proton beams or heavy ion beams. The irradiations were performed at the Dalton Cumbrian Facility of the University of Manchester and at the Ion Beam Centre of the University of Surrey. The irradiation experiments have been planned to obtain samples with characteristics comparable to those of neutron irradiated specimens reported in the literature. Therefore, we could directly compare the segregation profiles obtained by proton/iron irradiations with those found in the literature, and also assess potential dose rate effects and temperature shifts during the ion/neutron benchmarking exercise. In **Figure 1** the irradiations so far completed are plotted in a temperature-damage map, together with the neutron-irradiated data from literature.

Figure 1 Location of the irradiated samples in the temperature-damage map. Black triangles are neutron-irradiated data from literature ([1] [2]); red circles are proton irradiated samples; blue squares are iron irradiated samples.

The sample stage for the DCF irradiations is described elsewhere [3]. At the Ion Beam Centre, samples were mounted on a circular plate of tantalum with the aid of clips, and positioned at the end of the beam line. The heating was provided by a heater located at the back of the plate. The current control was provided by four Faraday cups located at the edges of a square in which the circular plate is inscribed. The beam in scanned over the four Faraday cups to checked not only the intensity, but also the uniformity of the beam over the scanned area. The microscopic characterisation of the irradiated samples has recently started. The proton-irradiated samples become active, therefore we needed to prepare protocols and risk assessments for receiving and working with those active materials in Manchester.

Results and Discussion

Non-irradiated samples

The material in the as-received and heat-treated condition have been characterised in detail, in order to have a baseline for assessing the radiation effects on 20Cr25Ni Nb-stabilised stainless steel. A number of small, very disperse round Nb(C,N) particles have been found in as received specimen of Batch 1 and 2. EBSD measurements show a very deformed microstructure. In contrast, bigger and clustered particles of Nb(C,N) have been found in Batch 3. Those samples were also heavily deformed, as expected, since the material had been flattened.

Specimens from Batch 2 and 3 have been heat treated at 930°C for 40min in argon atmosphere and water quenched. The results of the heat treatment are shown in **Figure 2** together with the microstructure of Batch 1.

Figure 2 SEM micrographs showing the typical grain morphology after the heat treatment (930°C for 40min in argon atmosphere) of each batch.

The morphology of the matrix and of second phases results different after the heat treatment, as can be seen in **Figures 2 and 3**. In Batch 2 big Nb(C,N) grown along the grain boundaries are not present; a fine and dense dispersion of nano-particles is instead found. It is expected that this will affect the segregation of elements during the irradiation.
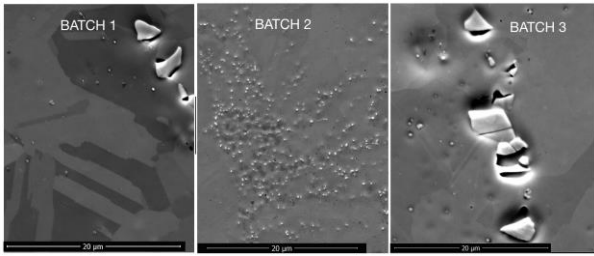
Figure 4 SEM micrographs showing typical Nb(C,N) precipitates in the heat treated samples (930°C for 40min in argon atmosphere) of the three batches.

The precipitate morphologies in the samples look very different. The differences are probably due to the different initial microstructures and to the amount of Nb present, which affect the stabilisation ratio, therefore the precipitation behaviour [2]. The average composition of the three materials has been measured with EDX and is reported in **Table 2**

	Batch 1		Batch 2		Batch 3	
	[wt-%]	σ [wt-%]	[wt-%]	σ [wt-%]	[wt-%]	σ[wt-%]
Si	0.53	0.04	0.64	0.06	0.65	0.04
Cr	20.71	0.11	21.32	0.18	20.23	0.11
Mn	0.89	0.08	0.73	0.12	0.75	0.08
Fe	53.19	0.17	53.19	0.26	54.07	0.17
Ni	24.40	0.16	24.71	0.24	23.73	0.16
Nb	0.27	0.08	0.56	0.15	0.57	0.1

Table 2 Average composition of the materials received measured with EDX.

The heat treatment produced complete recrystallisation. In **Figure 5** the grain dimension distribution function is reported for the three batches, together with the band contrast maps.

The biggest grains are found in Batch 3, whereas the smallest are present in Batch 2. This result is expected since the small precipitate/matrix interface in this material acts as nucleation sites for new grain. Once nucleated their growth is hindered, due to the pinning effect of the precipitates. In order to generate bigger grains, either a longer heat treatment is needed or at higher temperature.
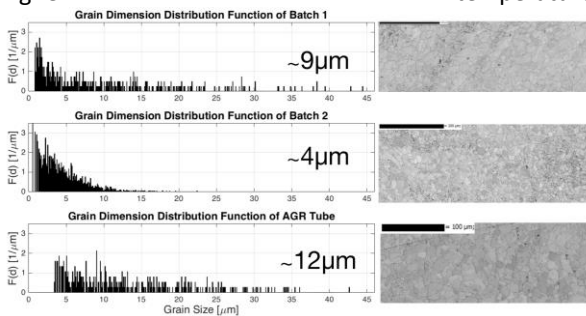
Figure 4 Grain dimension distribution functions and band contrast maps for heat treated specimens of the three sample batches.

The heat treatment produces a certain amount of annealing twin boundaries: more than 40% in all the batches. It can be pointed out that the amount of grain boundaries per unit volume in Batch 2 is larger than in the other two batches. Specific grain boundaries are preferential channels for the diffusion of elements in the polycrystalline material. This will therefore affect the segregation in the irradiated samples.

The microstructure of the un-irradiated materials has been also characterised using TEM and Scanning TEM (STEM). These two techniques will be of fundamental importance in the characterisation of the irradiated materials, therefore significant work has been done in order to master them. In **Figure 5** two STEM micrographs are shown. In the left image a twin boundary is visible on the right corner. The two grains have a different contrast due probably to the different orientation. In **Figure 5b**, a closer look to the precipitates and the dislocations found in the heat-treated sample is reported. One of the objectives in the following months is using STEM to get chemical information about the nanoscale precipitates found in the heat-treated materials.
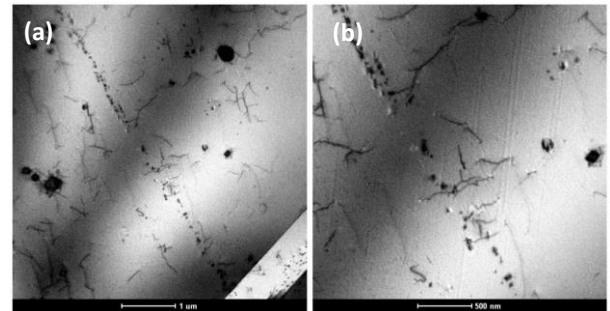
Figure 5 (a) STEM micrograph All TEM specimens have been prepared with electropolishing.

In **Figure 6a** and **b** two SEM bright field micrographs of grain boundaries are shown. In **Figure 6a** a round Nb(C,N) precipitate grown along a grain boundary is shown, whereas in **Figure 6b** a twin boundary decorated with nano-scale precipitates is shown.
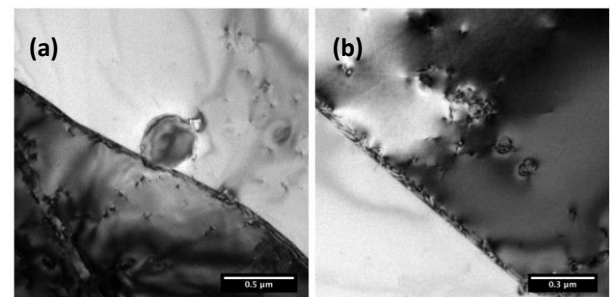
Figure 6 (a) TEM bright field micrograph of a heat-treated sample from Batch 3, where a second phase grown on a grain boundary can be observed. **(b)** TEM bright field micrograph.

Nano-indentation on Irradiated Samples

The preparation and characterisation of irradiated samples has just started. So far four samples have been tested using nano-indentation to assess the change in the hardness and in the elastic modulus induced by proton and iron irradiation. In the following months, some samples for TEM will be lift out using Focus Ion Beam (FIB) in order to check the extension of the plastic zone, as reported for other irradiated steels [5].

Continuous Stiffness Measurements (CSM) have been carried out using a Berkovich tip on the irradiated layer of four samples. This technique is suitable for layered materials, such as an irradiated specimen composed of two layers: the thin irradiated layer of the material and the non-irradiated substrate. A small sinusoidal oscillation in the load signal measures stiffness dynamically during the indentation sequence and the corresponding displacement signal is monitored. The technique is fully explained in [6]. The samples have been mounted on aluminium stubs using a thin layer of Crystalbond resin. In **Figure 7** the results of the nano-indentation measurements are shown. Two samples have been irradiated with protons and two with iron heavy ions, all at the same temperature of 400°C. The data presented are an average of 9 indents for each of the four samples.
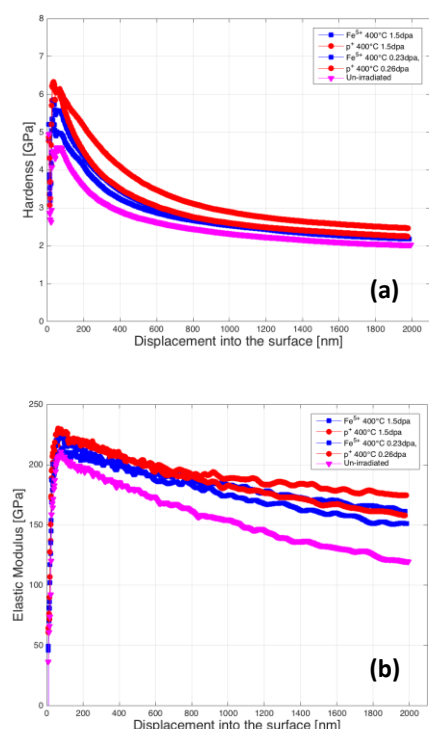
Figure 7 (a) Average hardness as a function of the indentation depth for the irradiated and un-irradiated samples. The average has been calculated on an array of nine tests performed on each sample. (b) Average elastic modulus as a function of the indentation depth for the irradiated and un-irradiated samples. The average has been calculated on an array of nine tests performed on each sample.

The hardness as a function of the penetration depth into the specimen surface is shown **in Figure 7a**. The results for the irradiated samples are plotted together with the curve for a heat treated un-irradiated sample. An irradiation hardening effect can be clearly observed. Both proton and iron irradiated specimens have an average hardness greater than the non-irradiated samples. The highest hardness has been measured for sample irradiated with 2MeV protons up to 1.5dpa. Sample IR 2, irradiated with iron ions at the same temperature and dose, has a lower hardness. The same happens for samples IR 5 and IR 4. Whereas, the higher hardness of IR 4 with respect to IR 2 cannot be easily explained. These two samples have been irradiated with iron at the same temperature, but at different doses, 0.26dpa and 1.5dpa. Due to the higher dose received by IR 2, a higher hardness is expected. It has to be point out that these two specimens have not been irradiated with the same dose rate, 8.53E-6dpa/s for IR 4 and 1.62E-5dpa/s for IR 2.

The elastic modulus as a function of the penetration depth into the specimen surface is shown in **Figure 7(b)**. Also for this parameter the values for IR 4 and IR 2 do not follow the expected trend, but the deviation from it is consistent with that seen for the hardness.

The irradiations for this set of four samples have been designed to compare the effects due to protons and heavy ions at the same temperature and dose in 20Cr25Ni Nb-stabilised stainless steel. The results obtained with the nano-indentation measurements follow the trend expected. At the same dose and temperature, the hardening due to protons is higher than that due to iron ions. This is due to the substantial difference in the damage morphology between proton and heavy ions. Protons produced damage as isolated Frenkel pairs or in small clusters while heavy ions it in larger clusters.

Conclusions and Future Work

Three different batches of 20Cr25Ni Nb-stabilised stainless steel have been so far received and analysed. Work has been done to obtain similar microstructures in order to have a common starting point for assessing the effects of irradiation in the AGR cladding material.

Twelve samples of heat treated AGR cladding materials have been so far irradiated using intense beam of protons and iron heavy ions at different conditions of temperature and damage.

A set of fours samples, two irradiated with proton and two with iron ions, have been tested with nano-indentation in order to access the effects of ions irradiation on the mechanical properties of 20Cr25Ni Nb-stabilised stainless steel. The results show a radiation hardening effect on the material. The

phenomenon is greater for proton irradiated specimen in respect to iron irradiated ones at the same conditions of dose and temperature.

In the next months, the work on un-irradiated and irradiated sample will continue as listed below:

- a new proton irradiation experiment is planned. Four samples are going to be irradiated with proton at the same temperature, 420°C, but at different level of damage, i.e. 0.3dpa, 1dpa, 2dpa and 4dpa.

- nano-indentation experiments will be carried out also on the remaining irradiated samples. Moreover, the plastic behaviour of irradiated 20Cr25Ni Nb-stabilised stainless steel is going to be investigated.

- preparation of some TEM samples using FIB. We plan to prepare first some un-irradiated material in order to check the damage introduce by the beam in 20Cr25Ni Nb-stabilised stainless steel. If the technique is suitable we will proceed with the irradiated samples to get site-specific TEM samples. We are interested in grain boundaries and second phases.

- keep on with TEM work on both un-irradiated and irradiated samples using both electropolishing and FIB as preparation technique.

Acknowledgements

References

[1] D. I. R. Norris, C. Baker, C. Taylor and J.M. Titchmarsh, Effects of Radiation on Materials: 15th International Symposium, ASTM STP 1125, 1996

[2] D. I. R. Norris, C. Baker, J.M. Titchmarsh, Radiation-induced Sensitisation of Stainless Steel, 1987

[3] P. T. Wady, A. Draude, S. M. Shubeita, A. D. Smith, N. Mason, S. M. Pimblott, E. Jimenez-Melero, Nuclear Instruments and Methods in Physics, Research A, 806, 109-116, 2016.

[4] D. J. Powell, R. Pilkington, D. A. Miller, Acta Metal, 36, 1988.

[5] C. D. Hardie, S. G. Robert, A. J. Bushby, Journal of Nuclear Materials, 462, 391-401, 2015.

[6] X. Li and B. Bhushan, Materials Characterization, 48, 11 – 36, 2002

Assessing the impact of radioactive emissions in Life Cycle Assessment

Andrea Paulillo*[1], Roland Clift[2], Jonathan Dodds[3], Andrew Milliken[4], Stephen Palethorpe[3] and Paola Lettieri[1]

*Correspondence: Andrea.Paulillo.14@ucl.ac.uk

[1] *Department of Chemical Engineering, University College London, Torrington Place, London, WC1 E7JE, United Kingdom*
[2] *Centre for Environmental Strategy, The University of Surrey, Guildford, Surrey, GU2 7XH, United Kingdom*
[3] *National Nuclear Laboratory, Workington, Cumbria, CA14 3YQ, United Kingdom*
[4]*Sellafield Limited,* Sellafield, Seascale, Cumbria, CA20 1PG, United Kingdom

Abstract

Life Cycle Assessment (LCA) tool must be able to consider and assess potential impacts of all main types of pollutants, since the holistic environmental perspective represents its key feature. Nevertheless, to date radioactive materials and ionising radiations impacts have been largely disregarded - this practice can be linked to the lack of a standard, internationally agreed framework. Building up on a review of Radiological Impact Assessment methodologies for LCA studies, we developed an overarching framework for integrating impacts of radionuclides in the Impact Assessment phase of LCA. From this framework, two alternative methodologies have been derived: the Critical Group Methodology (CGM) and USErad. The former has been adapted from Risk Assessment practices, whilst the latter represents the first-of-its-kind compartment-type methodology for radionuclides. Those methodologies will enable LCA practitioners to consistently assess the environmental impacts of radioactive emissions. Future work will consist in applying the LCA tool and the newly developed methodologies to assess the environmental impacts of three alternative approaches for the management of spent nuclear fuels in the UK.

Introduction

Life Cycle Assessment (LCA) studies aim at assessing potential impacts of industrial processes onto human beings and the environment. Although there are many reasons for carrying out an LCA (e.g. learning about the life cycle, support product development, strategic planning, etc..), primarily LCA studies can be linked with either of those two purposes: identify the most polluting streams/stages in a product's life cycle or compare alternative methods for obtaining the same specific product [1]. LCA prime feature – and also its main advantage with respect to other environmental tools – lies in its holistic environmental perspective, which has made it a central concept for both environmental management in industry and environmental policy-making in public government. For this reason LCA methodology must be able to consider and assess potential impacts of all main types of pollutants; only in this way its holistic feature is maintained. Nonetheless, to date radioactive materials and ionising radiations impacts have been largely disregarded in LCA studies. This practice can be linked to the lack of an internationally agreed framework for radiological impact assessment. Several industrial processes (e.g. nuclear, coal, oil and gas, fertiliser and building industries) routinely release radionuclides in the form of air and waterborne streams; whilst others (mainly nuclear industry, hospitals and defence departments) generate radioactive solid waste, which are either disposed of in near-surface landfills (after inertisation), or stored awaiting construction of special repositories. Radioactive solid waste will eventually deteriorate releasing the stored radioactivity in the environment. Probabilistic simulations estimate this event to occur between hundreds of thousands and millions years, depending on the type of waste (e.g. [2]). Amongst the many industries, indeed nuclear is one of the main source, both for its scale and the materials it employs and produces. From this reasoning arises the need to develop a framework which allows LCA practitioners to integrate in the impact assessment phase the effects of ionising radiations. A small number of methodologies for radiological impact assessment are currently available for use in the Life Cycle Impact Assessment (LCIA) phase. These have been either developed exclusively for LCA applications or may be adapted from standard assessment procedures in other fields. We have undertaken a detailed review (to be published soon) of radiological impact assessment methodologies for LCA studies. The review concludes that none of the methodologies currently available is enough mature to be included as a standard procedure within the LCIA. Besides analysing characteristic, differences and limitations of several methodologies, the review also identifies the main features that a methodology for radiological impact assessment should have.

In light of the review findings, a general framework for assessing the impact of radioactive emissions on human beings has been conceived. This general framework lays the foundations on which two alternative – and conceptually very different - methodologies have been developed. The Critical Group Methodology (CGM), adapted from typical Human and Environmental Risk Assessment (HERA) practices, makes use of the concept of the Critical Group and Gaussian-type dispersion models. Conversely, USErad is a multimedia compartment-type model; it is based on the approach first proposed by Mackay [3] and widely used for toxicity characterisation in LCA, e.g. USEtox [4]. To date, no compartment-type models has ever been implemented for radionuclides; hence USErad constitutes the first-of-its-kind multimedia model for radionuclides. This summary includes a brief overview of the general framework and the two derived methodologies and provides an example on how those methodologies have been compared to each other. The summary will end with a conclusive section that, besides highlighting the main findings of the study and their practical consequences, introduces the scenarios to which the LCA tool and the developed methodologies will be applied.

Methodology

General framework

The framework for radiological impact assessment has been conceived with two main purposes in mind: establish a standard, widely agreed approach for integrating radiological impacts in LCA, and produce characterisation factors to be included as a new impact category. Like most generic frameworks for human impact assessment, it consists of three main modules: a fate module, an exposure (or intake) module and an effect module (dose and risk calculation).

The fate analysis's aim is to model transport and dispersion of radionuclides from source of release to estimate their concentrations in environmental media. For this purpose, a number of approaches may be used (e.g. numerical, analytical, box–type) depending on the level of accuracy required and the amount of information available. The exposure analysis directly follows the fate analysis and uses the environmental concentrations to estimate the amount of ionising radiation adsorbed by human beings according to specific habits and behaviours. Finally, the effect analysis consists of two steps. Firstly, the amount of radioactive radiations to which individuals are exposed (in terms of Becquerels, Bq) is converted into an effective dose (Sieverts, Sv). This is a SI unit which considers both the type of radiation and the human tissue involved in the process. Then the dose is converted into a risk metric for detrimental effects.

As mentioned above, from the general framework two alternative different methodologies have been derived. They share the same exposure and effect modules, but differentiate in the fate module; specifically, in the type of model used to simulate transport and dispersion mechanisms of radionuclides in the environment. The exposure and effect module, by contrast, constitute standard approaches relying on sets of parameters and assumptions widely accepted in the radiological protection community.

Critical Group methodology

The Critical Group Methodology (CGM) adopts the concept of the 'critical group', developed for risk assessment purposes and defined as 'the individual members of a population who can realistically be expected to receive the highest dose due to their lifestyle, location and habits' [5]. The application of the 'critical group' concept has one considerable consequence: results of the assessment are location-dependent, i.e. they depend on where (how far) the critical group is located with respect to the source of release. With regard to the fate analysis, CGM makes use of analytical models (e.g. Gaussian plume model for air emissions) to simulate the dispersion and transport of radionuclides in the environment. Furthermore, the methodology includes both radioactive direct discharges (i.e. gases to the air or liquids to freshwater bodies or sea), and radioactive solid waste disposed in a final repository. Their impacts, however, occur on very different time scales (days/weeks/months vs hundreds of thousands of years), hence any comparison between them must be drawn with caution.

Two reports constitute the foundations of the CGM's fate module. The IAEA framework for assessing the impact of routine discharges from nuclear plants is used for direct discharges [5]; whilst, the generic Post-Closure Performance Assessment (PCSA) [2] developed by the Radioactive Waste Management Ltd. (RWM) under contract to the UK Nuclear Decommissioning Authority (NDA) is used for assessing potential impacts of nuclear solid wastes stored in a generic-design of a Geological Disposal Facility.

USErad

Compartment-type (also known as MacKay-type) models are multimedia environmental models largely used in environmental chemistry to simulate behaviour and predict the fate of organic chemicals released in the environment. Their principle and assumptions were conceived by Donald MacKay [3] with the aim of laying the groundwork for the development of remedial and proactive strategies, and sustainable approaches to industrial processes. MacKay's approach consists in dividing the environment in a number of interlinked compartments (e.g. air, fresh water, seawater, agricultural soil, etc.) and spatial scales (e.g. regional,

continental and global). Exchange of substances, and pollutants, can occur among compartments within the same spatial scale and among same compartments belonging to different spatial scales. Partitioning and advective/diffusive mechanisms govern exchange processes. Partition coefficients are indeed the key important parameters in MacKay-type models; they represent how substances segregate at equilibrium among different environmental media, and different phases within the same medium. Notably, advective/diffusive mechanisms are compartment-specific, whilst partition coefficients are substance-specific. Several relations have been developed to estimate substance-specific partition coefficient, should they not be available in the literature. The majority of those relations, however, have been specifically conceived for organic chemicals. To date, several multimedia models have been developed and operationalised for assessing the potential impact of toxic substances within LCA. Amongst them, USEtox appears to be the most used in the LCA community. It was born under the United Nations Environment Program (UNEP) – Society for Environmental Toxicology and Chemistry (SETAC) Life Cycle Initiative with the aim of carrying out a comprehensive comparison of life cycle impact assessment toxicity characterisation models. The result of such comparison was the development of a scientific consensus model that provided recommended LCIA characterisation factors for more than 1,000 chemicals. The USEtox model mainly focuses on organic substances; inorganic substances characterisation factors are flagged as interim.

USErad is a compartment-type methodology adapted from the USEtox model to specifically address radionuclides' fate in the environment. Notably USEtox has been modified to account for radionuclides key properties and their main differences with organic chemicals. As USEtox, also USErad is implemented in the Microsoft Excel environment. An outline of USErad fate analysis is shown in Figure 4.
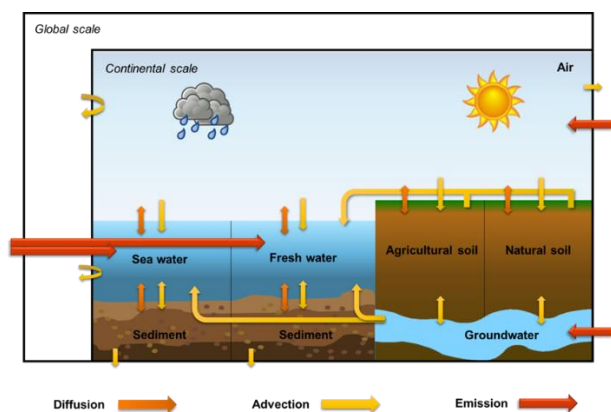
Figure 1 Representation of compartments setup of USErad.

Results and Discussion

A comprehensive analysis of the methodologies is included in a series of articles currently under preparation. For the purpose of this summary, we present an example of how those methodologies have been compared. The comparison refers to the characterisation factors obtained for radioactive atmospheric emissions. Figure 2 reports CGM characterisation factors for 4 distances of the Critical Group (from the release source) compared to a single USErad reference set. The graph shows that by increasing the receptor distance CGM factors - as expected – tend to decrease and approach, or go below USErad reference set (identified by the bisecting line). The Mean Log Deviation (MLD) parameter has been used to quantify the deviation between two sets of characterisation factors. An MLD value of 0 identifies two sets of characterisation factors featuring, on average (i.e. across the whole set), negligible deviation – although single factors may feature high deviation. With this in mind, the best agreement between the two methodologies (i.e. MLD=0) is found (by extrapolation) for a distance equal to 816 km. This means that for distances below 816 km, CGM methodology returns on average higher characterisation factors than USErad, whilst the opposite occurs for distances above 816 km.
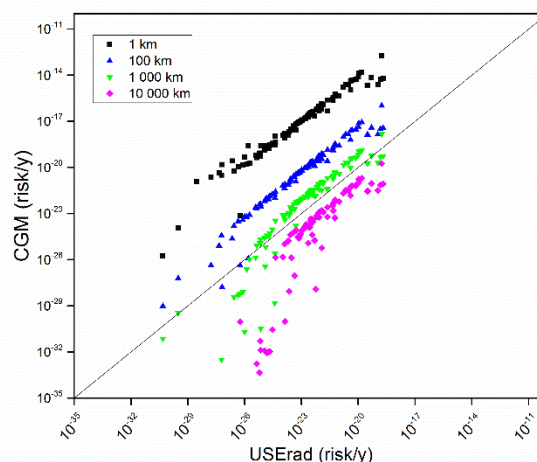
Figure 2 Comparison of CGM and USErad characterisation factors for air emissions.

The graphs also implicitly show that radionuclides' half-life is a crucial parameter for both methodologies. On a general basis, the lower the half-life, the lower the characterisation factor is. CGM characterisation factors, however, appear to be significantly more affected than USErad ones. In the charts, this can be seen in the peculiar 'tail' that CGM sets feature, and it is further proven by Figure 3. This shows logarithmic deviations as a function of radionuclides' half-lives. Logarithmic deviations are evidently dependent on the half-life, but also on the distance of the critical group. The smaller the

half-life, the lower the log deviations become; but at the same time, the bigger the distance, the lower the log deviations are at the same value of half-life. In other words, the graph is showing that CGM is more affected than USErad by the half-life parameter. For low half-lives, CGM will give lower characterisation factors when compared to USErad, and this will be more and more evidently as the distance increases. For this reason, the best agreement between the methodologies is found in the 100 – 1 000 km range, as opposite to what it can be seen from the graph where the bisecting line is actually located between 1 000 and 10 000 km distances.
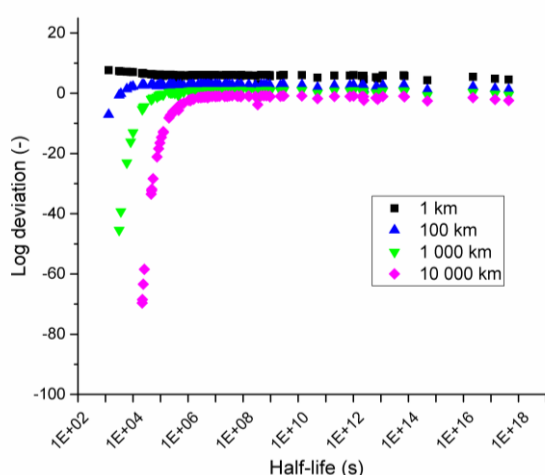
Figure 3 Characterisation factors' log-deviations vs radionuclides' half-lives.

Conclusions and Future Work

This short paper has summarised a work which lasted more than a year and that will culminate in a series of papers which are currently under preparation. This work has developed a novel, overarching framework for assessing the impact of radioactive emissions within the impact assessment phase of LCA. From this framework, two very different methodologies have been derived. Their comparison gives interesting insight regarding their similarities and differences, and identifies radionuclides' half-life as a crucial parameter affecting differently the methodologies. At this stage we do not specifically recommend the use of one methodology over the other; rather the choice is down to the LCA practitioner and depends both on the goal and scope of the study and on what information and data are available.

Future work will envisage the application of LCA and the newly developed methodologies to specific scenarios for nuclear waste management in the UK. Notably, along with the National Nuclear Laboratory and Sellafield Ltd, three relevant scenarios have been identified; these represent three potential options for managing reprocessed Uranium and Plutonium. At present, in fact, a clear policy for their management has not been established yet, and both Uranium and Plutonium are currently stored awaiting a final decision. The first scenario assumes that Uranium and Plutonium are declared as waste, grouted in an inert matrix, encapsulated in a suitable waste container and disposed in the national Geological Disposal Facility (GDF). In the second scenario, it is assumed that Uranium is recycled to produce new fuel assemblies – hence avoiding mining of fresh natural uranium - whilst Plutonium is declared as waste and disposed of in the national GDF. Finally, in the last scenario it is imagined that both Uranium and Plutonium are recycled to produced Mixed Oxide (MOx) fuel which will be then used to produced power in UK nuclear power reactors. The production of MOx fuel would avoid altogether the production of new fuel assemblies from fresh uranium, hence giving an environmental benefit to the system. All scenarios include operations of the Thermal Oxide Reprocessing Plant (THORP) and the management of its waste streams by ancillary plants. The operation – and consequential environmental impacts – of those plants is modelled by means of operational data.

References

[1] Baumann, H., Tillman, A.M., 2004. The Hitch Hiker's Guide to LCA: An orientation in life cycle assessment methodology and application. Studentlitteratur, Lund, Sweden. doi:10.1065/lca2006.02.008

[2] NDA, 2010. Geological Disposal: Generic post-closure safety assessment.

[3] Mackay, D., 2001. Multimedia Environmental Models: The fugacity approach, Second edi. ed. Lewis Publishers.

[4] Rosenbaum, R.K., Bachmann, T.M., Gold, L.S., Huijbregts, M.A.J., Jolliet, O., Juraske, R., Koehler, A., Larsen, H.F., MacLeod, M., Margni, M., McKone, T.E., Payet, J., Schuhmacher, M., Van De Meent, D., Hauschild, M.Z., 2008. USEtox - The UNEP-SETAC toxicity model: Recommended characterisation factors for human toxicity and freshwater ecotoxicity in life cycle impact assessment. Int. J. Life Cycle Assess. 13, 532–546. doi:10.1007/s11367-008-0038-4

[5] ICRP, 1990. 1990 Recommendations of the International Commission on Radiological Protection. ICRP Pubblication 60. Ann. ICRP 21.

[6] IAEA, 2001. Generic Models for Use in Assessing the Impact of Discharges of Radioactive Substances to the Environment - Safety Series. Vienna.

Atomistic simulations of helium incorporation in PuO₂ and surface modelling

N.A. Palmer*[1], M.S.D. Read*[1], and S.C. Parker[2]

*Correspondence: NAP131@student.bham.ac.uk, M.S.D.Read@bham.ac.uk

[1] School of Chemistry, University of Birmingham, Edgbaston, Birmingham, B15 2TT, United Kingdom
[2] Department of Chemistry, University of Bath, Claverton Down, Bath, BA2 7AY, United Kingdom

Abstract

Static lattice simulations have been performed using robust and accurate potentials to gain insight into properties of PuO₂. Using the GULP code [1], the potentials by Read et al. (2014) [2] and Grimes et al. (1990) [3] have been used to model helium atom incorporation in pure and defective PuO₂ lattice. The results show that helium gas incorporation in octahedral sites is endothermic. In addition, they show that plutonium vacancies are the preferred trapping sites, in agreement with other studies for UO₂ [4-6].

In addition, migration energy barriers between oxygen ions are predicted to be appreciably high at around 4 eV. Pure PuO₂ surfaces have been modelled using the METADISE program [7]. The simulations show that the (111) surface is the most energetically stable surface, followed by the (221) and (331) then the (110) surface. The (221) and (331) surfaces are relatively stable surfaces, exhibiting complicated faceted structures, which would be predicted to appear in the morphology of PuO₂.

Introduction

The United Kingdom has the largest stockpile of plutonium in the world, with approximately 126 tonnes of civil separated plutonium stored at the Sellafield site, Cumbria in 2014 [8]. This is in the form of plutonium dioxide, PuO₂, in powdered form in stainless steel cans. There are plans to extend the current storage facility to store plutonium for an extended period of many decades. Consequently, there is a need to understand the behaviour of stored PuO₂ over extended timescales. One of the potential issues is the helium gas accumulation due to the alpha decay of plutonium, with the main isotope Pu-239 having a long radioactive half-life of 24,100 years [9]. This could have a potentially large impact on the behaviour of the material in the long run.

Atomistic simulations provide a useful and powerful tool to understanding such phenomena. Robust interatomic potentials have been used to predict helium atoms behaviour in PuO₂ and to model a range of pure surfaces. The results presented are static lattice simulations using the GULP code for helium and METADISE program for surfaces.

Methodology Details

Surface modelling

Using the robust interatomic PuO₂ potentials, METADISE cleaves surfaces from the bulk and performs a geometry optimisation. The surface is modelled in the two-region approach [7], shown in Figure 1 whereby region 2 represents the bulk and region 1 represents the optimisable surface region.
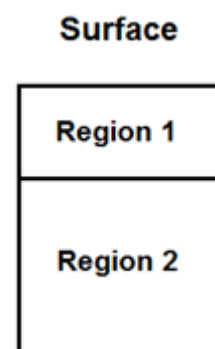
Figure 1. Schematic diagram of the surface.

The specific surface energy is defined as the energy required to create a surface per unit area relative to the bulk, expressed by the following equation

$$E_{Surf} = \frac{U_s - \frac{1}{2}U_b}{A} \qquad (1)$$

U_s is the surface energy of region 1 and U_b is the bulk energy of region 1 and A is the surface area. The factor of ½ is due to the fact there are twice as many ions in region 2 as in region 1, as shown in Figure 1. However, this factor can vary as the relative size of the two regions depends on the level of energy convergence.

Helium modelling

Helium atoms were treated as defects and hence the Mott-Littleton method [10] was used in GULP. In this approach, the crystal is partitioned into two spherical regions centred on the defect, namely region I and II. There is the innermost region I surrounded by a spherical shell region IIa. Region IIb extends out to infinity surrounding region IIa. Region I is explicitly relaxed, whilst in region IIb ions experience the electrostatic potential due to the defect. Ions in region IIa are assumed to relax harmonically. In this modelling, helium is treated as weakly interacting neutral atoms. Grimes et al. (1990) [3] Lennard-Jones potentials are used.

The incorporation energy of a helium atom in a crystal E_{He}^{Incorp} is given by the difference in the defect formation energy, E_d^f of the final and initial state which was either localised or at infinite dilution, given by equation (2) and (3) respectively.

$$E_{He}^{Incorp} = E_d^f\{He_V\} - E_d^f\{He_i^X + V_{O/Pu}\} \qquad (2)$$

$$E_{He}^{Incorp} = E_d^f\{He_V\} - E_d^f(He_i^X + V_{O/Pu}) \qquad (3)$$

The initial state is with the helium atom separated from a vacancy (either localised or at infinite dilution). The final state is with the helium atom trapped in a vacancy. In modelling helium migration, the transition state activation energy (or energy barrier) is given by the difference in the defect formation energy of the transition state to the initial state (localised only), given by

$$E_{act}^{TS} = E_d^f\{He_{TS}\} - E_d^f\{He_i + V_{O/Pu}\} \qquad (4)$$

Results and Discussion

Surface modelling results

In an approach similar to Williams et al. (2015) [11] for UO_2, the {n10}, {n11} and {nn1} for n=1,2,3 sets of surfaces were modelled with surface energies and structures predicted.

Table 1. Surface energies of energetically preferred PuO₂ surfaces.

Surface	$\bar{E}_{Surf}^{Unrel}$ (Jm⁻²)	$E_{Surf}^{Relaxed}$ (Jm⁻²)	ΔE_{Surf} (Jm⁻²)
(111)	1.65, 1.479[a]	1.32, 1.069[a], 1.33[b]	-0.32
(221)	2.41	1.63, 1.65[b]	-0.78
(331)	2.61	1.74, 1.76[b]	-0.87

Refs. a- [12], b- [11].
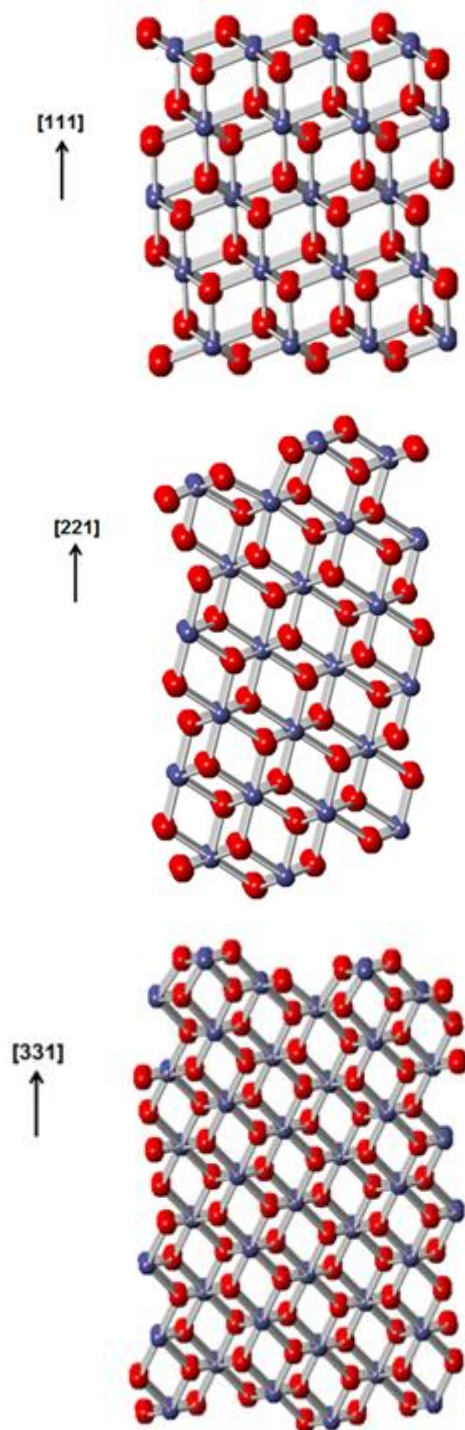
Figure 2. Relaxed surface structures of the (111), (221) and (331) pure surfaces. (Red and purple coloured spheres represent oxygen and plutonium ions respectively).

Table 2. d spacings of energetically preferred PuO₂ surfaces.

Surface	Calc. d spacing (Å)	Exp. d spacing [a] (Å)	% Δ (×10⁻²)
(111)	3.1166	3.5144	4.00
(221)	1.7994	1.7987	3.87
(331)	1.2384	1.2379	4.28

Ref. a- [13].

Surface modelling discussion

The (111) surface is the most energetically stable surface, followed by the (221) and (331) then the (110) surface. The (221) and (331) surfaces are relatively stable surfaces, exhibiting complicated faceted structures. The effect of relaxation on the surface structures is relatively small. The change in energy of the most stable surfaces is in the range of -0.32 eV (111) to -1.24 eV (110), but for the less stable is much larger at -5.09 eV (211) to -15.19 eV (310), showing the relaxation is more important for the inherently less stable surfaces. The validity of the Read et al. [2] potential for surface modelling has been shown due to good agreement with reported surface (relaxed) energies and excellent agreement with the experimental d spacing's with less than 0.05% deviation.

Helium modelling results

Helium atoms were substituted in octahedral sites and lattice vacancies and incorporation energies predicted. Helium incorporation in octahedral sites in pure PuO₂ is predicted to be endothermic with incorporation energy of 0.65 eV per helium atom. Migration of a helium atom from octahedral site to an adjacent one and to lattice vacancies was modelled. There is assumed to be no barrier to a helium atom 'jump' to the nearest oxygen vacancy. There are energy barriers in other cases. This is when the helium atom passes between adjacent oxygen ions to another octahedral site or to a plutonium vacancy, creating lattice distortion. These energy barriers have been predicted.

Table 3. Helium incorporation energies of helium atoms in lattice vacancies.

Initial position of He atom	Final position of He atom	E_{He}^{Incorp} for He trapped compared to ∞ dilution (eV)	E_{He}^{Incorp} for He trapped compared to localised (eV)	Reported E_{He}^{Incorp} (eV) for UO₂
$\left(\frac{1}{2}, \frac{1}{2}, \frac{1}{2}\right)$ He_i^X	$\left(\frac{1}{4}, \frac{1}{4}, \frac{1}{4}\right)$ $V_O^{\bullet\bullet}$	-0.26	-0.40	-0.08 [a], -0.90[b], 0.90[c], 1.60[d], 0.67[e]
$\left(\frac{1}{2}, \frac{1}{2}, \frac{1}{2}\right)$ He_i^X	$(0, 0, 0)$ $V_{Pu}^{////}$	-0.57	-0.79	-0.08 [a], 0.30[b], -8.70[c], -1.20[d], -0.70[e]

Refs. a- [3], b- [14] (for PuO₂), c- [5], d- [6], e- [4].

Table 4. Helium migration energy barriers in PuO₂.

Helium atom pathway	Position of Transition State	E_{act}^{TS} (eV)	Reported E_{act}^{TS} (eV) for UO₂
$He_i^X \rightarrow TS \rightarrow He_i^X$	$\left(\frac{1}{2}, \frac{1}{4}, \frac{1}{4}\right)$	3.59	3.80[a], 2.97[b], 2.0[c]
$He_i^X \rightarrow TS \rightarrow V_{Pu}^{////}$	$\left(\frac{1}{2}, \frac{1}{4}, \frac{1}{4}\right)$	4.14	-

Refs. a- [3], b- [4], c- [15].

Helium modelling discussion

Lattice vacancies are possible helium 'trapping' sites. In particular, plutonium vacancies are preferred, in agreement with a number of theoretical studies for UO_2 [4-6]. Nevertheless, trapping by nearest oxygen vacancies is perhaps more likely given the much lower formation energy and predicted zero energy barrier. Migration of a helium atom from an octahedral site involves passage through adjacent oxygen ions, creating an energy barrier due to lattice distortion. For helium migration to an adjacent octahedral site, the transition state activation energy is predicted to be 3.59 eV comparable with the result from Grimes et al. [3] of 3.80 eV. A similar value of 4.14 eV was obtained for migration to a plutonium vacancy. These are considerable barriers and therefore limit migration. However, at elevated temperatures the barriers will be reduced, as shown by the experimental value of 2.0 eV for UO_2 [15] .

Future Work

- Progress to using molecular dynamics using DL_POLY to model thermal properties of PuO_2 to assess and improve current potentials.
- To model diffusion of defects including helium in the bulk lattice.
- To model self-irradiation damage in PuO_2 due to the alpha decay of plutonium.
- To extend surface simulations to model defects on surfaces, and compare defect energies to the bulk case.

Acknowledgements

References

1. Gale, J.D. and A.L. Rohl, *The General Utility Lattice Program (GULP).* Molecular Simulation, 2003. **29**(5): p. 292-293.
2. Read, M.S.D., S.R. Walker, and R.A. Jackson, *Derivation of enhanced potentials for plutonium dioxide and the calculation of lattice and intrinsic defect properties.* Journal of Nuclear Materials, 2014. **448**(1–3): p. 20-25.
3. Grimes, R.W., R.H. Miller, and C.R.A. Catlow, *The behaviour of helium in UO2: Solution and migration energies.* Journal of Nuclear Materials, 1990. **172**(1): p. 123-125.
4. Yun, Y., O. Eriksson, and P.M. Oppeneer, *Theory of He trapping, diffusion, and clustering in UO2.* Journal of Nuclear Materials, 2009. **385**(3): p. 510-516.
5. Petit, T., et al., *Molecular modelling of transmutation fuels and targets.* Journal of Nuclear Materials, 2003. **320**(1–2): p. 133-137.
6. Crocombette, J.P., *Ab initio energetics of some fission products (Kr, I, Cs, Sr and He) in uranium dioxide.* Journal of Nuclear Materials, 2002. **305**(1): p. 29-36.
7. Watson, G.W., et al., *Atomistic simulation of dislocations, surfaces and interfaces in MgO.* Journal of the Chemical Society, Faraday Transactions, 1996. **92**(3): p. 433-438.
8. *Managing the UK Plutonium Stockpile.* 2016, The Parliamentary Office of Science and Technology.
9. *Pu-239- NuDat 2.6.* Available from: https://www.nndc.bnl.gov/nudat2/chartNuc.jsp.
10. Mott, N.F. and M.J. Littleton, Trans. Faraday Soc., 1938: p. 485.
11. Williams, N.R., et al., *Atomistic investigation of the structure and transport properties of tilt grain boundaries of UO2.* Journal of Nuclear Materials, 2015. **458**: p. 45-55.
12. Tasker, P.W., *The surface properties of uranium dioxide.* Surface Science, 1979. **87**(2): p. 315-324.
13. R. Belin, P.V., M. Reynaud, P. Raison, J. Appl. Crystallogr., 2004. **37**(6): p. 1034–1037.
14. Freyss, M., N. Vergnet, and T. Petit, *Ab initio modeling of the behavior of helium and xenon in actinide dioxide nuclear fuels.* Journal of Nuclear Materials, 2006. **352**(1–3): p. 144-150.
15. Roudil, D., et al., *Helium thermal diffusion in a uranium dioxide matrix.* Journal of Nuclear Materials, 2004. **325**(2–3): p. 148-158.
16. Available from: http://www.birmingham.ac.uk/bear.

Real-time fast-neutron plutonium assay for storage and ageing applications

R. Sarwar*[1], C. H. Zimmerman[2] and M. J. Joyce[1]

*Correspondence: r.sarwar@lancaster.ac.uk
[1] *Engineering Department (Lancaster University, Lancaster, UK LA1 4YR)*
[2] *The Central Laboratory (The UK National Nuclear Laboratory, Sellafield, Cumbria, UK CA20 1PG)*

Abstract

Nuclear safeguards is the discipline that ensures that civilian nuclear installations are not being misused to pursue weapons and that associated materials are not diverted to illegal usage. The well-established techniques for verifying this include passive/active radiation monitors using one of several detection methods including gamma-ray tomography, neutron coincidence counters using He-3 detectors and the Cherenkov viewing device etc. Each method has its benefits but individual limitations too. Additionally, the development of advanced fuel-cycle material, such as mixed-oxide (MOX) fuel has indicated further limitations of existing safeguard techniques due to presence, for example, of multiple actinides acting like neutron sources having signatures comparable to plutonium. A solution to this can be achieved by using liquid scintillation detectors (LSD) for fast neutron multiplicity analysis or coincidence counting. These detectors are sensitive to both fast neutrons and gamma radiation. The primary advantage of using such detectors is that they enable an extremely short gate time (three orders of magnitude lower than He-3 detectors) to be used, allowing reduced accidental coincidences and thus being able to detect higher orders of multiplicity.

This studentship is supported by the National Nuclear Laboratory as part of the EPSRC DISTINCTIVE consortium along with Lancaster University with the aim of (i) identifying the multiplicity distribution of a sample in real-time using liquid scintillation detectors to discriminate between different isotopes and (ii) exploiting (α, n) reactions to distinguish the uncorrelated events from the correlated neutrons. This report primarily focuses on the design and development of a real-time system capable of the rapid data processing needed to this end. This is required due to the very short pulse length (in the order of 50-70 ns) originating from LSD when radiation is detected. Moreover, considering practical geometry of an experimental setup (i.e. several rings of detectors surrounding a source within a radius of 50-100cm) and the high speed at which fast neutrons travel, it is expected that fission neutrons will theoretically arrive at the detector after within 20 to 40 ns of the fission event taking place. Hence it is imperative that the system is capable of sampling the detector response at 200 MHz or higher. This feat was achieved utilizing a platform based on System-on-Chip Field-Programmable Gate Array (SoC–FPGA) which combines a dual-core Cortex-A9 embedded core with a FPGA fabric using a high-bandwidth interconnecting link. The system is capable of constructing neutron coincidence distributions in real-time by sampling up to 16 detectors every 5 ns over a user-defined gate-width or coincidence window. This distribution can then be unfolded to carry out neutron multiplicity analysis.

Introduction

During spontaneous and induced fission a significant number of neutrons are produced that are difficult to distinguish from one another. For neutrons, the number may range from zero to ten while photons often exhibit a wider range in multiplicity. This distribution of number of emitted particles, while being a statistically-random event, is called the neutron multiplicity distribution [1]. Figure 1 shows the multiplicity distributions of a number of fissioning isotopes. It is clear that isotopes of individual elements (i.e. Pu-238, Pu-240 and Pu-242) do not vary a great deal in this respect. However, comparing different elements (i.e. plutonium versus curium versus californium) indicates that these distributions are quite different. Identifying this

difference in experiments using liquid scintillation detectors has the potential to assist in the identification of the elemental composition of a sample of nuclear material.

In theory, neutron multiplicity analysis refers to counting the number of neutrons that are emitted per fission event. However, since it is rarely possible to associate detected neutrons with their particular fission event, the number of neutrons that are detected within a specified interval of time (also called the gate-width or detector window) is determined in order to construct a coincidence distribution. This method is often referred to as *neutron coincidence counting*. Although there are several methods [2] of detecting multiplicity from such neutron coincidence distributions, the primary focus is

usually the Rossi-α Method [3] as per the discussion of this work.
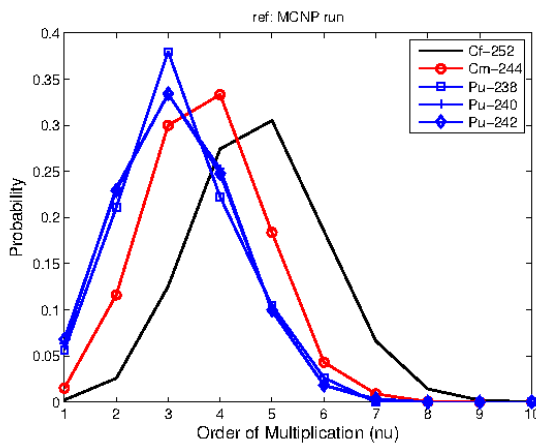
Figure 1 Multiplicity distribution from MCNP6 simulations

The Rossi-α Method allows direct observation of the behaviour of fission neutrons following a fission event by measuring the time distribution of neutron pulses following every triggering pulse [3]. This exploits the fact that the probability of having one fission event followed by multiple neutron detections within a small time interval can be divided into two components: (i) *real* counts or neutrons from a given fission event and (ii) *accidental* counts associated with neutrons from other sources or that have been scattered in the environment. Although this is a well-established method that is used with He-3 detectors [4], the difference in the physics of detection of radiation between He-3 and liquid scintillation detectors, the requisite electronics and the unfolding methodology needed to use it with liquid scintillation detectors must be revisited.

The studentship supported by the National Nuclear Laboratory on this topic is part of the EPSRC DISTINCTIVE consortium along with Lancaster University with the aim of (i) identifying the multiplicity distribution of a sample in real-time using liquid scintillation detectors to discriminated between different isotopes and (ii) exploiting (α, n) reactions to identify the uncorrelated events from the correlated neutrons. This report aims to outline progress in the development of a system capable of determining the multiplicity of fissile materials using LSD in real-time.

Methodology Details

Implementation

The Rossi-α method was implemented in Altera DE1-SoC Development Board. This board was chosen for the high speed and flexibility of Field-Programmable Gate Array (FPGA) needed to implement the digital circuitry and also to take advantage of the dual-core ARM
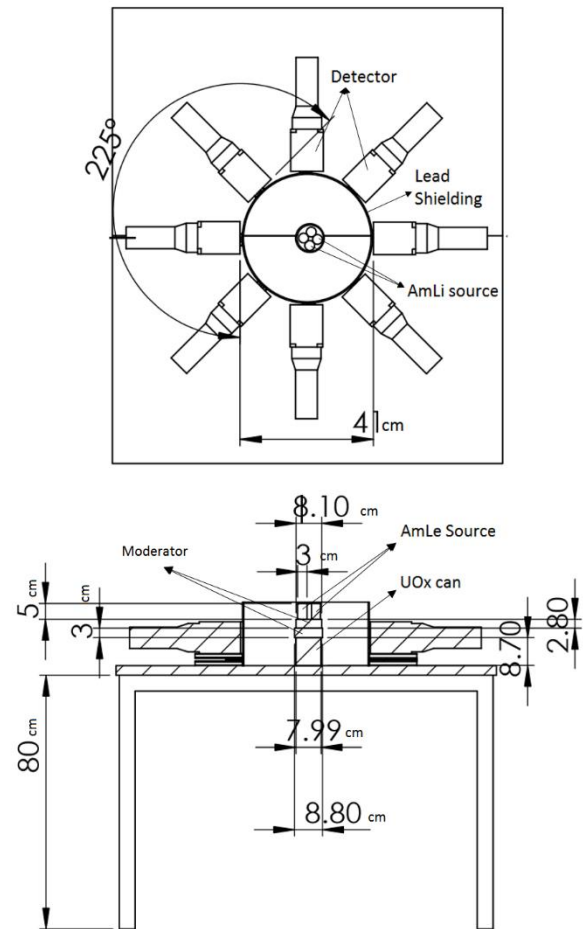
Figure 1 (Top) An arrangement of 8 fast scintillation detectors around UOx sample which is being irradiated using an AmLi source. The detectors are placed at a radius of 20.5 cm from the sample. (Bottom) The cross-sectional view of the arrangement along with the dimensions of different objects.

processor to send data from the device to a host computer avoiding any bottleneck in data acquisition.

The assay utilizes 4-channel real-time mixed-field-analysers (MFA) which are capable of driving two TTL outputs per channel, each indicating if a neutron or gamma ray was detected. The reasons for this choice of device for the project are the following advantages: (i) integration of multichannel processing in one self-contained portable unit driven by the same clock of 250 MHz and (ii) evidence of real-time coincidence assay of plutonium with an assessment of the limiting mass uncertainty achieved with four-channel system. Four of these MFAs were connected in parallel to 15 E-309 liquid scintillators in an assay, providing real-time PSD results. These 16 TTL outputs were compiled together in a "signal hub" and were fed into a field-programmable gate array (FPGA) using 16-bit wide general-purpose

input-outputs. To minimize development time, Altera DE1-SoC Development Kit was used. The device integrates both a FPGA and a dual-core ARM processor in the same fabric using high-speed interlink for fast data transfer. The FPGA samples the input at 200 MHz (once every 5 ns) and implements noise dampening techniques to filter out any undesirable fluctuation from the cabling and the signal hub. The neutron coincidence distribution is then constructed using a one-shot circuit [1] based on a gate-width which is defined by the user via 8-bit sliding-switch that gives an effective range of 5 ns to 1270 ns. Additionally, raw signal data along with timestamp information is transferred to the ARM core which uses the information to construct a Type I Rossi-α distribution. These distributions are then transferred to a host computer or laptop using a 1 Gbps Ethernet connection. The host computer runs a program which receives the data, displays the results and saves the data.

Experimental Setup & Results

In order to test the system, experiments were conducted at Oak Ridge National Laboratory with access to standardized uranium oxide samples of different enrichment (0% to 93% enrichment) stored inside steel canisters. Figure 2 shows the experimental setup using eight EJ-309 fast organic scintillators. When four AmLi sources are placed on top of the cans with 6.8 cm of moderator, the (α, n) neutrons are thermalized and induce fission in the UOx sample which emits time correlated neutrons. The emitted neutrons from the fission are then captured in the detector array and the recorded doubles per second and singles per second are plotted against the corresponding mass in Figure 3.
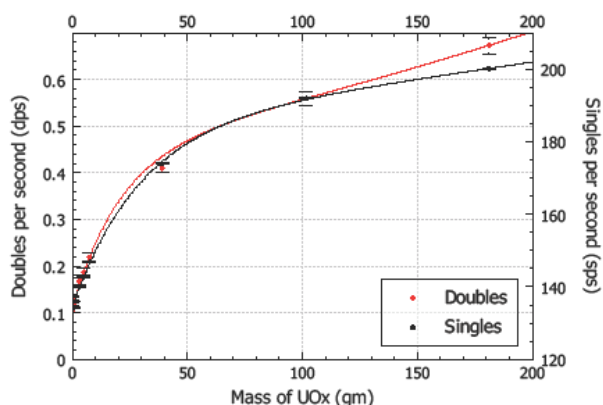
Figure 3 Singles and doubles rates as a function of mass clearly showing the increase in activity with mass with an exponential fit.

The results show a clear trend in doubles and singles rates as mass increases. This trend can be exploited to determine the mass of an unknown sample, either via calibration or via analytical means. It can be noted that with increased mass, the trend in count rates becomes non-linear due to self-absorption.

Conclusion and Future Work

The project is progressing well. The major research undertaken during the period has been the development of the multiplicity register. Listed below are some of the plans for the upcoming six months:

1. Carry out further experiments using PuOx.

2. Analyse the data already obtained from ORNL.

3. Unfolding of the distribution.

References

[1] N. Ensslin, Chapter 11: The origin of neutron radiation, in: D. Reilly, N. Ensslin, H. S. Jr. (Eds.), Passive Non-destructive Assay of Nuclear Material, Los Alamos National Laboratory Report,Report LA-UR-90-732, Washington, DC 20555, 1991.

[2] N. Ensslin, Chapter 16: Principles of Neutron Coincidence Counting, in: D. Reilly, N. Ensslin, H. S. Jr. (Eds.), Passive Non-destructive Assay of Nuclear Material, Los Alamos National Laboratory Report,Report LA-UR-90-732, Washington, DC 20555, 1991.

[3] ORNDOFF J. D. (1957) Nucl. Sci. Engng 2,450.

[4] Joyce, M.J.; Gamage, K.A.A.; Aspinall, M.D.; Cave, F.D.; Lavietes, A., "Real-Time, Fast Neutron Coincidence Assay of Plutonium With a 4-Channel Multiplexed Analyzer and Organic Scintillators," in Nuclear Science, IEEE Transactions on , vol.61, no.3, pp.1340 -1348, June 2014

The Behaviour of Used Nuclear Fuel in Wet Storage

D. M. Laventine*[1], C. Boxall[1] and R. Orr[2]

*Correspondence: d.laventine@lancaster.ac.uk

[1] University of Lancaster, Lancaster, LA1 4YR, UK
[2] Central laboratory, B170, National Nuclear Laboratory, Sellafield, CA20 1PG, UK

Abstract

Plutonium oxide (PuO_2) is one of the most highly radioactive components of nuclear fuel waste streams and its storage poses particular challenges due to the high temperatures produced by its decay and the production of gases (particularly H_2 and steam). Its high radiotoxicity necessitates the use of analogues, such as ceria and urania, to allow the comprehensive study of its interaction with water under storage conditions. We have developed a method which enables direct gravimetric measurement of water adsorption onto CeO_2 thin films with masses in the microgram region. Porous CeO_2 films were fabricated from a surfactant based precursor solution. The absorption of water onto the CeO_2 coating at different relative humidities was studied in a closed reactor. Quartz Crystal Microbalance (QCM) gravimetry was used as a signal transducer, as changes in crystal resonant frequency due to absorbed mass are directly and linearly related to mass changes occurring at the crystal surface. Using this method, we have determined the enthalpy of absorption of water onto CeO_2 to be 49.7 kJmol^{-1} at 75°C, and onto U_3O_8 to be 54.1 kJmol^{-1} at 75°C, 11 and 15 kJmol^{-1} greater than the enthalpy of evaporation, respectively. These enthalpy is within the range predicted for the absorption of water onto PuO_2, indicating this method allows for investigation of water absorption using microgram samples.

Introduction

Plutonium oxide (PuO_2) is one of the most highly radioactive components of nuclear fuel waste streams. This poses particular challenges in storing large amounts for reuse as mixed oxide fuel for the next generation of fast reactors or for eventual deposition into long-term geological storage, which has been proposed at a number of sites worldwide. Interim storage is typically within a series of nested steel canisters under a partially inert atmosphere. These canisters develop high internal temperatures due to the PuO_2 decay heat and have been observed to become pressurised due to the evolution of hydrogen gas and steam. A greater understanding of PuO_2 interaction with water is therefore imperative to allow the design of safe long-term storage facilities.

Ceria (CeO_2) is widely employed as a model substrate for radioactive metal oxides such as plutonium oxide, due to the metals similar ionic radii and the oxides similar fluorite structure. Ceria polycrystals exhibit a significant absorption of water vapour at temperatures up to 600°C, and previous studies have indicated this to be true of plutonium oxide. The absorption of water results in numerous physio- and chemi-absorbed layers, but the subsequent fate of this water under elevated temperatures and pressures and in the presence of highly radioactive material is unknown. Water adsorption on PuO_2 has previously been investigated by measuring headspace pressure, as a function of temperature within a closed system containing a fixed quantity of PuO_2 in the presence of varying amounts of deliberately added water. This involves making a number of assumptions relating to the PVT behaviour of the headspace of

the closed system, usually based on the behaviour of an ideal gas, in order to estimate the mass of water adsorbed at the PuO_2 surface.

We have developed a method which enables direct gravimetric measurement of water adsorption onto CeO_2 and U_3O_8 thin films. We have previously reported the use of Quartz Crystal Microbalance (QCM) gravimetry as a signal transducer, as changes in crystal resonant frequency are directly related to mass changes occurring at the crystal surface at ambient temperatures. In this work, *ortho*-gallium phosphate (*o*-$GaPO_4$) crystals were used instead of quartz due to the linear temperature-dependence of their resonant frequency as well as their higher piezoelectric limiting temperature, allowing the absorption of water to be analysed under the temperature conditions that develop in typical PuO_2 storage conditions of up to 600°C. Herein, we describe preliminary experiments in the coating of *o*-$GaPO_4$ crystal electrodes with nano-scale crystalline CeO_2 films and measurements of their absorption of water.

Methodology

A CeO_2 film was deposited on *o*-$GaPO_4$ crystals using an adapted version of the Lundberg method for generating thin films of crystalline CeO_2. A stock solution of 0.01 moles of $CeNO_3$ and 5% of triton-X (a non-ionic polxamer surfactant) dissolved in 10 mL of 1:1 water-methanol was created. A second solution was produced by 10-fold dilution of the stock solution. 10 µl of the diluted solutions were drop-coated onto one electrode surface of *o*-$GaPO_4$ crystals and allowed to evaporate in air, then calcined in air at 650°C for 5 h, resulting in formation of iridescent layers adhered to the platinum piezoelectrode surface.

The formation of crystalline CeO_2 was confirmed by Raman spectroscopy and by XRD analysis of the layers. The morphology of the layers was investigated using a Phenom™ scanning electron microscope (Lambda Photometrics, Herfordshire).

CeO_2-coated crystal electrodes were mounted into commercially available crystal holders (Colnatec, US) constructed of steel and ceramic leaving only the coated crystal face accessible. The crystal mount was suspended within a steel reaction vessel (vol = 1L) such that it was not in contact with any internal surface. A stream of dry nitrogen was passed into an inlet port on the reaction vessel and allowed to escape from an exhaust port while the vessel was heated in a furnace to ~400°C. This procedure continued for 6+ hours, or until the observed frequency of the crystal remained steady. The system was then sealed and allowed to return to RT and the baseline frequency recorded. A defined amount of water was added by microsyringe and the system was then re-sealed and the frequency and temperature recorded every second. As the water added to the system evaporated and redeposited onto the crystal surface, the frequency (inversely proportional to mass) was observed to drop. Once a steady frequency was reached, the system was temperature cycled from RT to ~350°C with continuous recording of the temperature and corresponding frequency. Once at RT again, the gas inlet was re-attached and a slow stream of nitrogen passed through the system until the frequency stabilises. The above procedure was then repeated (from the initial heat cycling) with a different amount of water added.

Results and Discussion

The layers formed by drop-coating and calcination were found to be strongly adhered to the platinum electrode surface, being resistant to manual abrasion. Raman spectroscopy (785 nm excitation) showed a characteristic CeO_2 peak at 464 nm. XRD measurements of a powder CeO_2 sample produced under the same conditions as the crystal coatings indicated the samples were crystalline CeO_2.

Deposition of the CeO_2 layers resulted in a resonant frequency drop of 7450 Hz, equating to a 42 µg increase in mass. This is below the 2% threshold at which the Sauerbrey equation

becomes unreliable to describe mass changes occurring at the composite resonator surface. Using the area of the crystal electrode coated and the density of bulk ceria (7.65 g.cm^{-3}), the layers were estimated to be 125 nm thick, assuming a homogenous non-porous coating with ideal geometry.
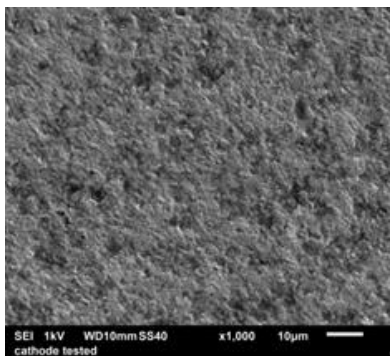
Figure 1. SEM image of a CeO2 film on a platinum / o-GaPO4 piezoelectrode.
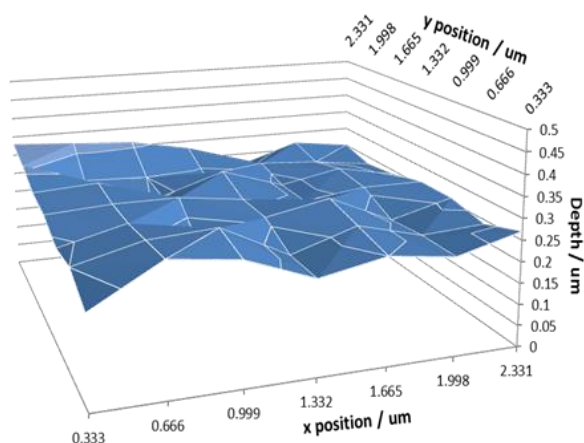
Figure 2. XRF map of CeO2 film thickness at 36 points. Mean thickness = 261 nm.

SEM imaging showed the layer to be comprised of a densely packed CeO$_2$ network with voids and pores present (fig. 1). The thickness of the films was also measured by X-ray Fluorescence (XRF) in a 36 point grid, giving an average thickness of 261 nm, ± 29 nm (fig. 2). This gave a piezoactive volume of 8.9 x 10^{-6} cm^3 and therefore a porosity of 54%.

Initial microbalance experiments with the coated crystals were conducted at 75°C. It was found that the resonant frequency of the coated crystals reduced in response to the addition of water to the system, corresponding to a 2.4 µg mass increase per coated crystal (approximately 90 mg of water absorbed per gram CeO$_2$ layer) at 100% relative humidity. The relative humidity was varied by changing the amount of water added to the system and maintaining the temperature at a constant 75°C. It was found the amount of water absorbed onto the ceria coating increased with increasing partial pressure of water. A plot of this change in frequency or mass against the partial pressure resulted in a graph typical of a type II absorption isotherm (fig. 3). Addition of further water to the already saturated system resulted in a linear increase in the mass of water detected on the crystal due to simple physical deposition. The BET equation can be used to calculate the enthalpy of absorption (ΔH_{ads}) and the volume of a monolayer of molecular water adsorbed onto a surface:

$$ 1/\left[Va\left(\frac{P0}{P} - 1\right) \right] = \left(\frac{C-1}{V_M C}\right)\left(\frac{P}{P_0}\right) + \frac{1}{VmC} $$

where V_m is the volume of an adsorbed monolayer and $C = \exp(\Delta H_{ads} - \Delta H_{liq} / RT)$. A plot of $P/V_a(P_0-P)$ versus P/P_0 yields a straight line, the slope of which is $(C-1)/(V_M C)$ and intercept is $1/V_m C$. The BET plot for H$_2$O adsorption produces a straight line, with R^2 values of 0.995 .

The volume of an adsorbed monolayer of water on the CeO$_2$ films was calculated to be 2.38 x 10^{-13} m^3 (1.34 x 10^{-8} m^3.g^{-1} CeO$_2$). Using a literature estimate for the footprint of a molecule of water of 1.60 x 10^{-19} m^2, this corresponds to an accessible surface area of 1.27 x 10^{-3} m^2 (71 m^{2}g^{-1} CeO$_2$). The mass of water absorbed at saturated humidity at 75°C corresponds to 7 monolayers of water. The ΔH_{ads} for water adsorption can also be calculated: Taking the ΔH_{liq} of water at 75°C to be 38.5 kJmol^{-1}, ΔH_{ads} for H$_2$O on CeO$_2$ was calculated to be 49.7 kJmol^{-1} ± 0.31 kJmol^{-1}. This value is within the range proposed by Paffett *et al.* for H$_2$O adsorption on PuO$_2$ of between 44 and 51 kJmol^{-1}, which suggests that molecular water adsorbed on CeO$_2$ is bound by a similar mechanism as on PuO$_2$.
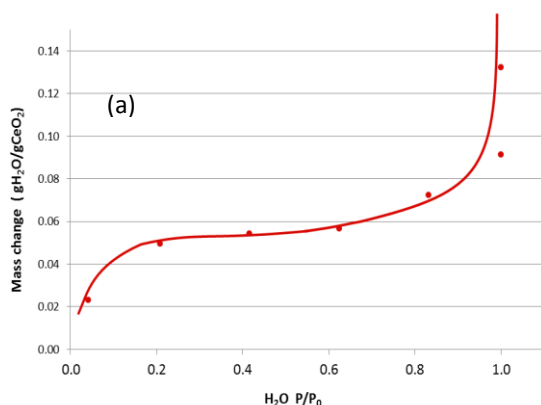
Figure 3 Graph showing the absorption of water onto a CeO_2 coated (160 nm thick) quartz crystal at different humidities.

Urania (U_3O_8) thin films have been synthesised using the same method described above, using a uranium nitrate precursor solution. QCM measurements indicate about 18 ug of urania is deposited, which would be equivalent to a 28 nm thick layer. XRF measurements of the layer thickness give an average thickness of approximately 42nm (fig. 5), indicting a porosity of 35%. ΔH_{ads} for H_2O on U_3O_8 was calculated to be 54.1 kJmol^{-1}
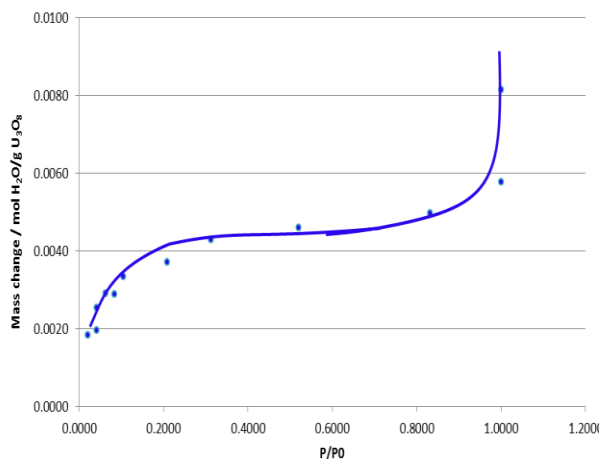
Figure 4. Graph showing the absorption of water onto a U_3O_8 coated (42 nm thick) quartz crystal at different humidities.

Conclusions and Future Work

We have developed a QCM based method for measuring water adsorption on CeO_2, in closed conditions. In our system, an *o*-$GaPO_4$ crystal is coated on one face with void CeO_2 and U_3O_8 film. Water adsorption onto these films was measured by introducing various amounts of water into the vessel at 75°C, resulting in a range of humidities up to the saturation vapour pressure. It was found that up to 2.4 mg of H_2O adsorbs on the films at 75°C and 100% relative humidity, equivalent to 7 monolayers of water adsorbed over the top surface of the metal oxide layer. This is within the range of monolayers of water reported to adsorb on PuO_2 powders, suggesting a similar mechanism for CeO_2 binding of water. We have determined the enthalpy of absorption of water to be 49.7 kJmol^{-1} and 54.1 kJmol^{-1} onto CeO_2 and U_3O_8, 11 and 15 kJmol^{-1} greater than the enthalpy of evaporation, respectively. These enthalpies are within the range predicted for the absorption of water onto PuO_2, indicating this method allows for investigation of water absorption using microgram samples. Plans are also currently underway to apply this method directly to PuO_2 waste samples at the National Nuclear Laboratories at Sellafield.

Acknowledgements

References

[1] H. S. Kim, C. Y. Joung, B. H. Lee, J. Y. Oh, Y. H. Koo, and P. Heimgartner, J. Nucl. Mater., 98-104, 2008.
[2] J. L. Stakebake, J. Physical Chemistry, vol. 77, pp. 581-586, 1973.
[3] J. L. Stakebake and L. M. Steward, Journal of Colloid and Interface Science, vol. 42, pp. 328-333, 1973.
[4] M. T. Paffett, D. Kelly, S. A. Joyce, J. Morris, and K. Veirs, J. Nuclear Materials, vol. 322, pp. 45-56, 2003.
[5] J. M. Haschke and T. E. Ricketts, Plutonium Dioxide Storage: Conditions for Preparation and Handling, 1995
[6] J. M. Haschke, T. H. Allen, and J. L. Stakebake, J. Alloys and Compounds, vol. 243, pp. 23-35, 1996.
[7] P. Murphy, C. Boxall, R. Taylor, and D. Woodhead, ECS Trans., vol. 53, pp. 81-94, 14 pp., 2013.

Water Adsorption on Reduced Actinide Oxide Surfaces

B. E. Tegner*[1], A. Kerridge[2], and N. Kaltsoyannis*[1]

*Correspondence: bengt.tegner@manchester.ac.uk, nikolas.kaltsoyannis@manchester.ac.uk

[1] School of Chemistry (The University of Manchester, Oxford Road, Manchester, M13 9PL, UK)
[2] Department of Chemistry (Lancaster University, Bailrigg, Lancaster, LA1 4YW, UK)

Abstract

The interactions between water and the actinide oxides UO$_2$ and PuO$_2$ are important when considering the long-term storage of spent nuclear fuel. However, experimental studies in this area are severely limited by plutonium's intense radioactivity, and hence we have recently begun to investigate these interactions computationally. In this summary we report the results of first principles calculations of the interaction of water with UO$_2$ surfaces. Strongly-correlated effects are taken into account using a Hubbard corrected potential, which enables us to perform efficacious plane-wave density functional calculations of extended systems. In particular, we compare results of water adsorption on reduced UO$_2$ {111}, {110} and {100} with the corresponding results on CeO$_2$, focusing on the energetics and structural properties of molecular versus dissociative adsorption, on or near an oxygen vacancy.

Introduction

One of the problems with nuclear energy is the long term storage of nuclear waste, spent nuclear fuel and the products of fuel reprocessing. Our particular project concerns the civilian stores of highly radioactive plutonium dioxide. Presently, the UK's PuO$_2$ is stored as a powder in stainless steel storage containers, while the government decides its long term fate. However, some of these steel containers have started to buckle, leading to the hypothesis that gas build up, possibly from water vapour due to desorption or the production of hydrogen gas due to the radiolysis of water, causes some of the containers to pressurise. We are exploring these suggestions computationally.

Previously, we have studied and published water on the stochiometric AnO$_2$ surfaces [1] and we are now moving on to defect surfaces, as we expect defects to be present on the surfaces of the powders in the cans.

Methodology Details

The calculations were performed using VASP 5.4.1 [2-5], a plane-wave DFT code using Projector-Augmented Wave (PAW)-pseudopotentials [6, 7] to describe the ions and employing Monkhorst-Pack (MP) [8] grids for the *k*-space integration. All calculations used a plane wave cut-off of 650 eV and a MP-grid of 5×5×1 k-points for the Brillouin zone sampling. The generalized gradient approximation of Perdew, Burke, and Ernzerhof (PBE) [9, 10], with a Hubbard correction [11, 12], was used for the exchange-correlation. The surface is constructed using a repeating slab of 24 AnO$_2$ units arranged in six layers with 18 Å of vacuum between each slab. Adsorbates and defects are introduced on both sides of the slab.

Results and Discussion

Surface oxygen vacancies

We started by calculating the oxygen vacancy formation energy for each surface, that is, the energy cost of removing one oxygen from the surface. The results are shown in table 1 below.

Surface	UO$_2$ {111}	UO$_2$ {110}	UO$_2$ {100}
This work	6.45	5.69	5.93
Bo *et al.* [13]	5.95	5.38	N/A

Table 1 Oxygen vacancy formation energies on uranium dioxide surfaces in eV, compared to corresponding data from Bo *et al*. [13].

Unsurprisingly, the most stable surface, (111), has the highest vacancy formation energy whereas the less stable surfaces have lower vacancy formation energies. Moreover, our results compare well with results from Bo and co-workers [13], though we note that our results are consistently higher by about 0.4 eV.

Water on the reduced UO$_2$ {111} surface

We then moved on to calculating water adsorption on the reduced {111} surface. A ball-and-stick figure of water adsorbed on the {111} surface can be seen in figure 1. The oxygen vacancy is right below the water molecule in the top panel and on the corresponding place in the bottom panel. Comparing the two panels, we see that the OH-molecule fills the vacancy, whereas the molecular water does not.
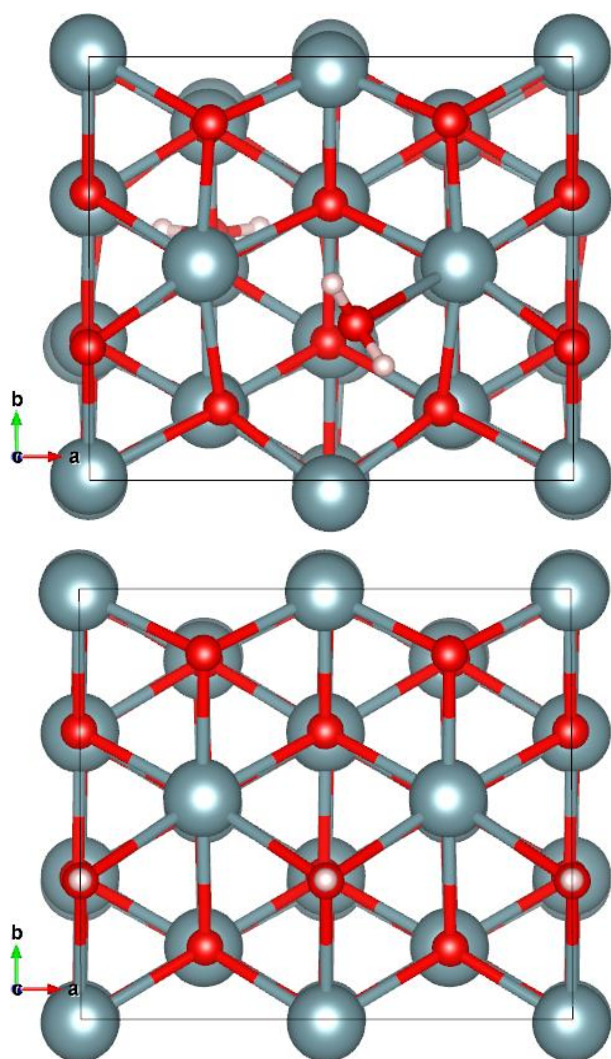
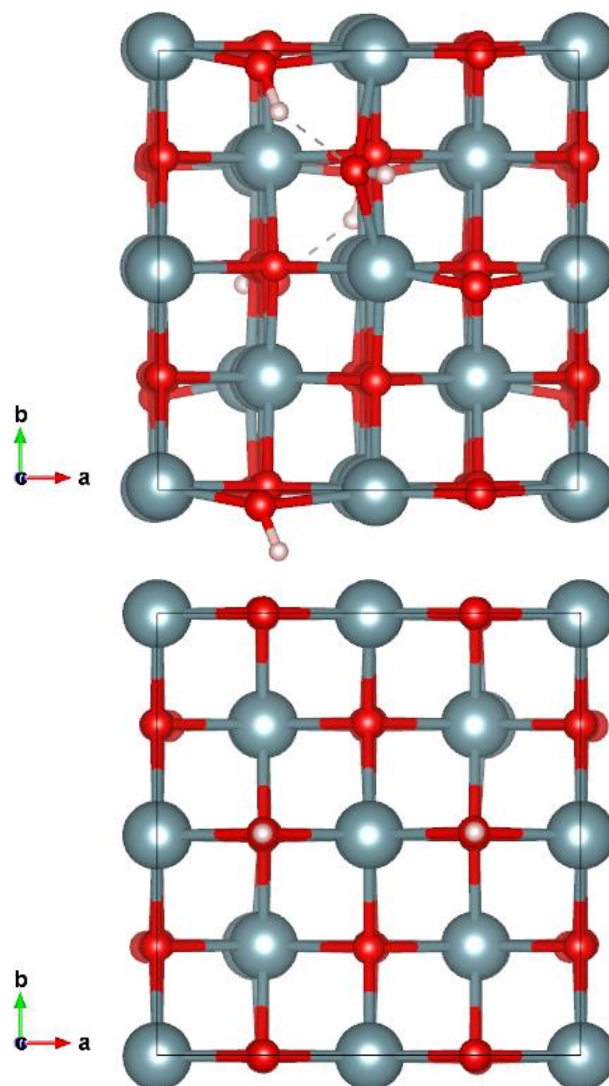**Figure 1** Water adsorbed molecularly (top) and dissociatively (bottom) on the reduced UO₂ {111} surface.

The calculated adsorption energies can be found in table 2 below. Throughout, we compare with the stochiometric case, as well as with the corresponding data on CeO₂ from Molinari *et al*. [14], as ceria is often used as a non-radioactive analogue to the actinide oxides for water adsorption studies.

System	Stoch. UO$_2$ {111}	Reduced UO$_2$ {111}	Stoch. CeO$_2$ {111} [14]	Reduced CeO$_2$ {111} [14]
H$_2$O adsorption	-0.53	-0.90	-0.56	-0.58
OH + H adsorption	-0.50	-2.23	-0.59	-2.12

Table 2 Adsorption energies in eV for a single water molecule on the stochiometric and the reduced UO₂ {111} surface, compared to the corresponding data on ceria from Molinari *et al.* [14].

Comparing the data in table 2, we note that dissociative adsorption is energetically favoured on the reduced {111} surface, compared to the stochiometric case both

for UO₂ and CeO₂, probably because the OH-molecule fits the vacancy better.

Water on the reduced UO₂ {110} surface

We then moved on to the {110} surface. A ball-and-stick figure of water adsorbed on the {110} surface can be seen in figure 2. In this case, the oxygen vacancy is located on the lower left, near the water molecule on the top panel and on the corresponding place in the bottom panel, occupied by the right OH-molecule. Comparing the two panels, we again see that the OH-molecule fills the vacancy, whereas the molecular water does not.
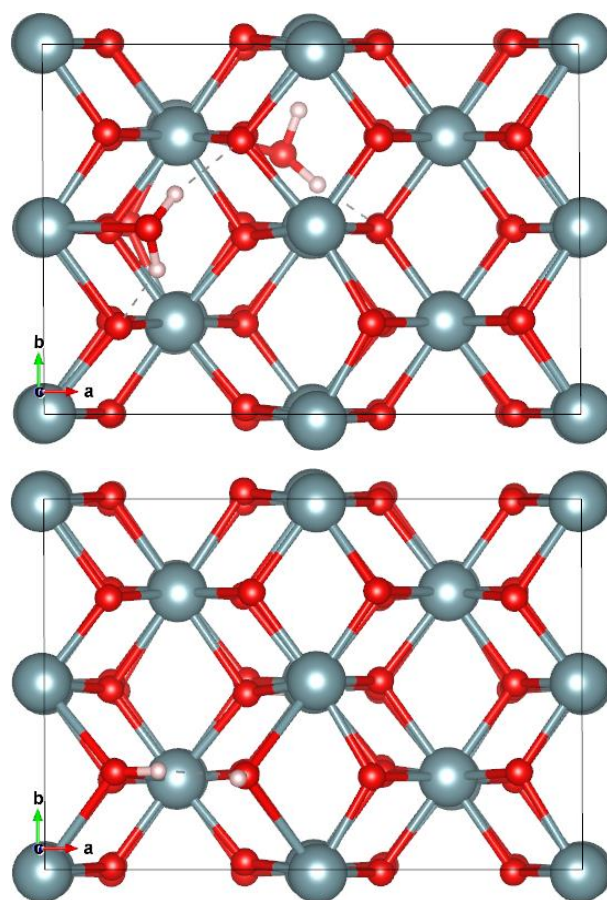
Figure 2 Water adsorbed molecularly (top) and dissociatively (bottom) on the reduced UO₂ {110} surface.

The calculated adsorption energies can be found in table 3 below.

System	Stoch. UO$_2$ {110}	Reduced UO$_2$ {110}	Stoch. CeO$_2$ {110} [14]	Reduced CeO$_2$ {110} [14]

H_2O adsorption	-0.93	-0.82	-0.85	N/A
OH + H adsorption	-1.39	-1.50	-1.12	-1.44

Table 3 Adsorption energies in eV for a single water molecule on the stochiometric and the reduced UO_2 {110} surface, compared to the corresponding data on ceria from Molinari *et al.* [14].

Comparing the data in table 3, we again note that dissociative adsorption is energetically favoured on the reduced {110} surface compared to the stochiometric one, both for UO_2 and CeO_2, but the energy difference is less pronounced in this case, probably due to the lower coordination of the {110} surface.

Water on the reduced UO_2 {100} surface

Finally, we considered the {100} surface. A ball-and-stick figure of water adsorbed on the {100} surface can be seen in figure 3. In this case, the oxygen vacancy is located just left of centre, below the stretched OH-molecule on the top panel and on the corresponding place in the bottom panel, occupied by the left OH-molecule. Comparing the two panels, we again see that the OH-molecule fills the vacancy, whereas the molecular water does not. Interestingly, in this case the molecular water dissociated, leaving two OH-groups.

Figure 3 Water adsorbed molecularly* (top) and dissociatively (bottom) on the reduced UO2 {111} surface. *The water molecule dissociated.

The calculated adsorption energies can be found in table 4 below.

System	Stoch. UO_2 {100}	Reduced UO_2 {100}	Stoch. CeO_2 {110} [14]	Reduced CeO_2 {100} [14]
H_2O adsorption	-0.97	-1.62*	-1.00	-0.87
OH + H adsorption	-1.55	-2.43	-1.57	-2.54

Table 4 Adsorption energies in eV for a single water molecule on the stochiometric and the reduced UO_2 {100} surface, compared to the corresponding data on ceria from Molinari *et al.* [14]. *The water molecule dissociated.

Comparing the data in table 4, we again note that dissociative adsorption is energetically favoured on the reduced {100} surface compared to the stochiometric

one, both for UO_2 and CeO_2, but the energy difference is even more pronounced. In fact, we were unable to calculate an adsorption energy for molecular adsorption in this case, as the water molecule dissociated when placed near the vacancy.

Conclusions and Future Work

Oxygen vacancy formation energies on the different UO_2 surfaces look similar to previous work by Bo and co-workers [13], further increasing our confidence in the validity of our computational approach. Furthermore, our calculated adsorption energies suggest that dissociative adsorption is preferred on all three reduced surfaces, unlike our previous results for the stochiometric ones. Moreover, the resulting adsorption energies and geometries on the reduced UO_2 {111}, {110}, and {100} surfaces also compare well with corresponding values on CeO_2, further strengthening the notion that CeO_2 can be used as an actinide oxide analogue for water adsorption studies.

Moving forwards, we will continue to study water adsorption on all three surfaces of both actinide oxides, this time focusing on multiple layers of water.

Acknowledgements

References

[1] B. E. Tegner, M. Molinari, A. Kerridge, S. C. Parker and N. Kaltsoyannis, J. Phys Chem. C, 121, 1675, (2017).

[2] G. Kresse and J. Hafner, Phys. Rev. B, 47, 558, (1993).

[3] G. Kresse and J. Hafner, Phys. Rev. B, 49, 14251, (1994).

[4] G. Kresse and J. Furthmüller, Comput. Mat. Sci., 6, 15, (1996).

[5] G. Kresse and J. Furthmüller, Phys. Rev. B, 54, 11169, (1996).

[6] P. E. Blöchl, Phys. Rev. B, 50, 17953, (1994).

[7] G. Kresse and D. Joubert, Phys. Rev. B, 59, 1758, (1999).

[8] H. J. Monkhorst and J. D. Pack, Phys. Rev. B, 13, 5188, (1976).

[9] J. P. Perdew, K. Burke and M. Ernzerhof, Phys. Rev. Lett., 77, 3865, (1996).

[10] J. P. Perdew, K. Burke and M. Ernzerhof, Phys. Rev. Lett., 78, 1396, (1997).

[11] S. L. Dudarev, D. Nguyen Manh and A. P. Sutton, Philosophical Magazine Part B, 75, 613 (1997).

[12] A. I. Liechtenstein, V. I. Anisimov and J. Zaanen, Phys. Rev. B, 52, R5467, (1995).

[13] T. Bo, J. Lan, Y. Zhao, Y. Zhang, C. He, Z. Chai and W. Shi, J. Phys. Chem. C, 118, 21935, (2014).

[14] M. Molinari, S. C. Parker, D. C. Sayle and M. S. Islam, J. Phys. Chem. C, 116, 7073, (2012).

Importance of Secondary Electrons in Water Irradiation

M. E. Smith*[1,2] and S. M. Pimblott[1,2]

*Correspondence: marisa.smith@manchester.ac.uk

[1] *Dalton Cumbrian Facility (Westlakes Science and Technology Park, Moor Row, CA24 3HA)*
[2] *Department of Chemistry (University of Manchester, Oxford Rd., Manchester, M13 9PL)*

Abstract

Monte Carlo simulation of the track structure of low energy electrons in water has been performed using experimental cross-sections for the collision processes in amorphous solid water and gaseous water scaled to liquid density. There are significant differences between the predictions of the two calculations for the number of interactions and the thermalization distance. These differences between the two sets of simulations clearly demonstrate that collective effects due to condensation, i.e. interaction between molecules, are important. The use of gas phase cross sections to simulate energy loss processes of low energy electrons in condensed water, where in bulk or adsorbed onto surfaces, is inappropriate and an erroneous point to start modeling radiation chemical kinetics.

Introduction

Water radiolysis with energetic electrons has been studied for the last half century, however the effects of sub-excitation electrons was largely ignored.[1,2,3] Recent studies have suggested their affect on the radiolysis products of water is significant.[2,4-6] Track structure chemistry simulations of radiolysis has been focused almost entirely on fast (low LET) particles due to the relative ease at which they can be accurately described, leaving a gap in the understanding in the ultra low energy regime.

A cascade of low energy sub-excitation electrons are generated from high energy radiation tracks.[7-9] For every 100 eV deposited the yield of secondary electrons is 5, therefore for a particle with 1 MeV energy, this gives approximately 50,000 secondary electrons. Therefore, high-energy incident particles have the capability to generate 10^4-10^5 low energy electrons. It has been well documented by Pimblott *et al.* that heavy fast particles deposit 65% of its energy via spurs of ionized low energy electrons of 100 eV or less.

The nuclear industry currently has a number of areas where it is crucial to understand the fast reaction dynamics of the physical and physiochemical stages of radiolysis in liquid water. The safe storage of intermediate and high level waste is of great importance, both for the safety of the workers and surrounding environment. It is speculated that some hydrogen gas is produced in fast processes following the deposit of primary energy.[1,2]

Methodology Details

Low energy electron track structures were simulated using a collision by collision approach of gaseous water and amorphous ice employing a compilation of experimental cross sections from Hayashi (gas) and Michaud (ice).[12,13] These cross sections describe the likelihood of an electron to have particular interactions. Cross sections are energy dependent and can vary greatly.

The penetration of the electron into the medium, more commonly known as the thermalization distance, $\langle r_{th} \rangle$, is defined as the length of the vector difference of the initial position ($\vec{\rho}_i$) from the total distance ($\vec{\rho}_f$), that the electron has travelled before track termination.

$$\langle r_{th} \rangle = \left\| \vec{\rho}_f - \vec{\rho}_i \right\|$$

Continuum Method

This method assumes the electron is travelling through a continuous water sample and at any point in space the electron has the possibility to interact with a water molecule. To achieve this, the Mean Free Path ($MFP \overset{\text{def}}{=} \Lambda_{\{tot\}}$) of the electron is treated like a continuous maximum by generating a pusedo-random number between (0,1] and multiplying that by the specific MFP at that energy. This limits the next electron 'jump' distance ($\rho_{\{i+1\}}$), up to the maximum; where $0 < \alpha \leq 1$ determines the fraction of the total MFP that the electron travels. This simulation method is widely accepted in the scientific community as it treats water as a continuous bulk structure.

$$\rho_{\{i+1\}} = \alpha \, \Lambda_{\{tot\}}$$

Radial Distribution Method

This method uses the full radial distribution function for water to determine the 'jump' to the next interaction.[14] Specifically, the integral of the distribution is used as the electron approaches

distances large enough for the bulk density of water to be assumed.

Molecular Dynamics (MD) Method

Using the water structure laid out in configuration files, the electron is simulated to move within an infinite box. The position of the electron is related to its position within the configuration file and the relative positions of the water molecules. When the electron makes a 'jump', an algorithm in the simulation determines whether it is within the proximity of an oxygen atom to have an interaction. The volume of the electron cloud around the oxygen atom is taken into account. If the incoming electron is within this volume, then the radiation electron is sufficiently close to have an interaction with one of the oxygen's electrons. There are six different configuration files, and a random number is generated at the beginning of each iteration to determine which of the six is used.

Results and Discussion

1- Gas Phase

Presented in Figure 1.1 is a log graph of the effect of initial electron energy on the frequency of interaction type. The gas phase is dominated by elastic collisions (blue). The inferior inelastic processes (green) describes the process of intra-molecular excitation of the water medium. This includes the vibrational bending, stretching and rotation of the water molecule. Unsurprisingly, this becomes the most frequent way for the low energy electron to dissipate energy in this region. At the bottom right of the graph, the electronic excitation and ionization threshold energy is reached (red and cyan respectively).

The electronic excitation and ionization interaction types are infrequent, occurring only 1-2 times per electron. However, due to the nature of these interactions the majority of the total energy loss occurs during these events. The most kinetic energy the electron can transfer in these events is half of its current kinetic energy a phenomenon known as indistinguishability. The energy required to excite the first electronic energy level is 5.5 eV, which results in a rate of 1 excitation per electron at 11 eV.

The excitation curve plateaus after this energy, as below 20 eV the likelihood of multiple excitations to occur in this energy regime is not energetically favorable. The same logic applies to the ionization

curve. Ionization does not increase past 0.3 interactions at 20 eV. This can be interpreted in the following manner: out of 10 electrons with an initial energy of 20 eV only 3 of those would have an ionizing event. It is these infrequent but high threshold energy events that affect the other interaction types, causing the plateau seen in the inferior inelastic (green) and elastic (blue) collisions.

Figure 1.1 Average Number of Interactions for Gas Phase
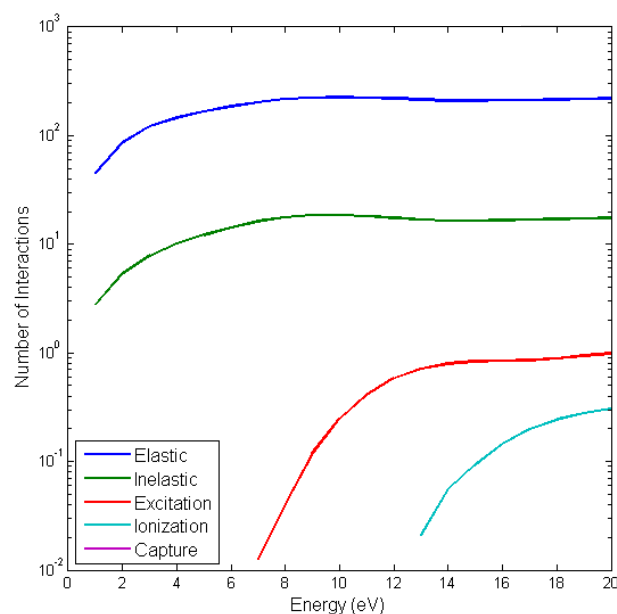
Figure 1.2 describes the dependence of the log of the penetration depth to the initial electron energy. This graph has a vertical axis that ranges from 1-11. The green curve is the radial distribution function method. The two other methods include the well-known standard continuum method (blue) and a molecular dynamics method (red). The difference in these calculated values are explained by the differences in the calculation of the electron jump distance. The radial distribution function is a symmetric distribution of solvation shells about each collision interaction. This imposes a minimum distance that the electron travels to encounter another water molecule to have an interaction. Resulting in a significant affect on the average distance between each collision interaction-increasing the overall penetration.

Figure 1.2 The penetration of an electron in a gaseous medium

Penetration

Figure 2.1 Average number of interactions in a condensed medium

Average Number of Interactions
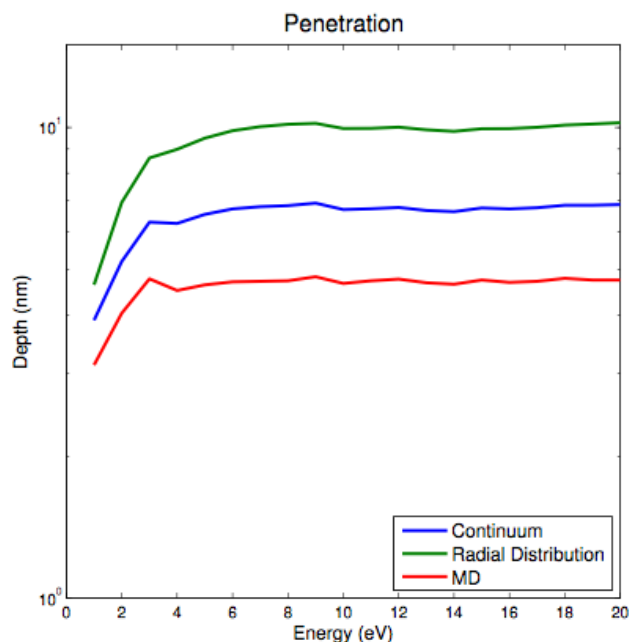
The radial distribution and the continuum both only account for the position of the centre of the oxygen atom. This slightly increases the distance the electron must travel between each interaction for an event to occur. Giving values slightly larger than the MD method, which factors the electron cloud into the inter-ion distance that the radiation electron travels. Obviously, if the jump distance between each interaction is reduced for each event by the length of the vector from the centre of the nucleus to the electron shell- the penetration of the electron will be reduced.

2- Amorphous Ice Phase

The average frequency with which events occur is ascertained in Figure 2.1, where the log of average interaction versus initial electron energy proves more complicated in the condensed phase. This energy regime is dominated by inelastic collisions, particularly those inferior inelastic collisions (green). In this phase, the mode of energy loss for sub-excitation electrons becomes the inter- and intra-molecular excitations, which include molecular excitations described previously and lattice phonons of the larger structure. However, due to the limitations in the intra-molecular excitations, the majority of this energy loss is due to the phonon phenomenon due to the strong hydrogen bonding in this phase.

Elastic collisions previously thought to be dominant in this energy regime are shown to play a insignificant role. Elastic collisions randomize the trajectory of the electrons and the implication being that the secondary electrons generated in radiation tracks are unlikely to be randomized.
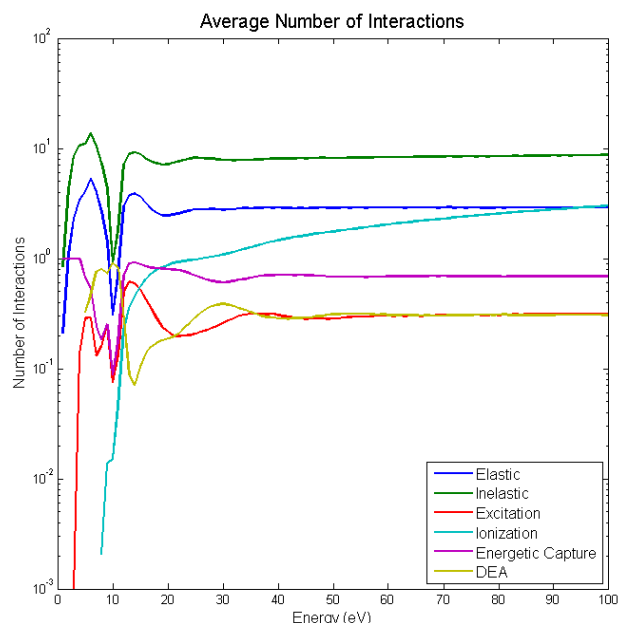
The excitation curve (red) peaks at 14 eV, which is double the energy required to excite the state- again due to the nature of indistinguishability. This peak dissipates due to the increasing likelihood of an ionization (cyan) to occur. Only one out of the two processes are energetically possible at this energy. It should be noted that the smaller peaks in the excitation below 10 eV are artifacts from the experimental data.

Electronic ionization is a rare but substantial source of energy loss for the electron due to the fraction of energy lost to overcome the binding energy. Coupled with the electronic excitations, together they represent the average method of energy loss for an electron above 10 eV. Once ionization processes have become available to the electron, it quickly increases in frequency at higher electron energies creating a similar plateau as seen in the gas phase.

In the process of electron track structure simulations there are a number of ways that the electron can terminate its track. Thermalization of the electron to an energy below 0.1 eV is essentially non-existent. The processes of track termination favoured in the ice phase is the energetic capture of the electron into an aqueous state and capture into the Dissociative Electron Attachment (DEA) cross section. The sum of the energetic capture and the DEA is one. DEA is a capture of the electron without dissipating any energy- this creates an unstable negative ion that has a high probability of disassociation by one of three pathways described by Melton.[15] The DEA creates a resonance in which the electron cannot escape, the affinity for

water to capture an electron at 10 eV is so strong that it occurs immediately upon encounter with a molecule. This has serious implications in the local distribution of reactive species that are generated in the `spurs' of the track structure of high-energy particles. The full range of the DEA cross sections lines up well with the lower and upper limit Melton discovered for the DEA pathways.

Figure 2.2 Average penetration in a condensed medium
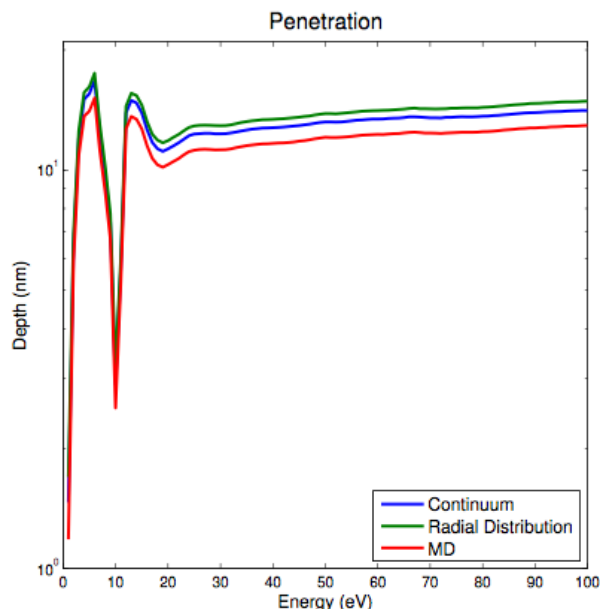
In comparison with the previous findings with density normalized water vapour the penetration of an electron in the ice phase is drastically different. It is evident that for few interactions the values obtained from the different methods gradually approach the same value. Only with large numbers of interactions does the method have significant effect. The differences in the range for the various methods follow a logical trend at energies where a difference is seen. This is a similar trend as to what is seen in the gas phase. Again, this is due to the mathematics of the calculation of the mean free path (MFP) of the electron.

Conclusions and Future Work

Based on the current evidence the thermalization distance of the electron in the ice phase at these low energies will be highly directional. The electron will thermalize at lengths much larger than originally anticipated. This has implications, as electrons with energies under 10 eV will penetrate farther into an ice medium than an electron of 100 eV.

The penetrative power of the low energy electron is essentially constant in this energy regime in the gas phase. Therefore, using the gas phase as analogous to the ice phase for electrons in this energy domain is unjustified.

The low energy electron is the main way many radiation particles dissipate energy to the medium. To fully comprehend the radiation track of any species, the intimate study and comprehension the medium dependent electron interactions is needed. It is the secondary electrons in most radiation tracks that will create the products and secondary chemistry that is under investigation.

References

[1] Garrett, B. C. et. al. Chemical Reviews 2005, 105, 355–390.

[2] Jonah, C. D. Radiation Research 1995, 144, 141–147

[3] Angell, C. A. Annual Review of Physical Chemistry 2004, 55, 559–583

[4] Totemeier, T. C. A Review of the Corrosion and Pyrophoricity Behavior of Uranium and Plutonium; 1995.

[5] Huels, M. A.; Boudäffa, B.; Cloutier, P.; Hunting, D.; Sanche, L. Journal of the American Chemical Society 2003, 125, 4467–4477.

[6] Boyer, M. C.; Rivas, N.; Tran, A. A.; Verish, C. A.; Arumainayagam, C. R. Surface Science 2016, 652, 26–32.

[7] Pimblott, S. M.; LaVerne, J. A.; Mozumder, A. Journal of Physical Chemistry 1996, 100, 8595–8606.

[8] Pimblott, S. M.; LaVerne, J. A. The Journal of Physical Chemistry A 1997, 101, 5828–5838.

[9] Pimblott, S. M.; LaVerne, J. A. The Journal of Physical Chemistry A 2002, 106, 9420– 9427.

[10] Rigny, P., Spotheim-Maurizot, M., Mostafavi, M., Douki, T., Belloni, J., Eds. Radiation Chemistry: From Basics to Applications in Material and Life Sciences; l'actualité chimique livres; EDP Sciences, Les Ulis Cedex A, France, 2008

[11] Barrios, R.; Skurski, P.; Simons, J. The Journal of Physical Chemistry B 2002, 106, 7991–7994

[12] Hayashi, M. Atomic and Molecular Data for Radiotherapy. Proceedings of IAEA Advi- sory Group Meeting. Vienna. 1989

[13] Michaud, M.; Wen, A.; Sanche, L. Radiation Research 2003, 159, 3–22

[14] Soper, A. K.; Bruni, F.; Ricci, M. A. The Journal of Chemical Physics 1997, 106, 247–254.

[15] Melton, C. E. The Journal of Chemical Physics 1972, 57, 4218–4225

Methodology for the Heat Treatments of Chloride- and Water-contaminated PuO$_2$ at NNL

Sophie Sutherland-Harper[1]*, Simon Pimblott[1], Robin Taylor[2], Jeff Hobbs[3], Francis Livens[1], Carolyn Pearce[4] and Nik Kaltsoyannis[1]

*Correspondence: sophie.sutherland-harper@postgrad.manchester.ac.uk

[1]University of Manchester, UK

[2]National Nuclear Laboratory, Sellafield, Cumbria, UK

[3]Sellafield Ltd., Cumbria, UK

[4]Pacific Northwest National Laboratory, Washington, USA

Abstract

Heat treatment of chloride-contaminated PuO$_2$ powders has been carried out at the National Nuclear Laboratory, Cumbria using a furnace in an air glove box to volatilise the chloride species. Untreated PuO$_2$ and PuO$_2$ heat treated to a range of temperatures have been analysed by X-Ray Diffraction. Water-adsorption experiments on PuO$_2$ powders have also been undertaken in a sealed vessel by heating the powders and measuring the pressure as they cool in the presence of water. The following paper is a review of the technical methodology used to perform these experiments and analyses.

Introduction

An inventory of Magnox PuO$_2$, produced in the early 1970s on a now decommissioned finishing line, has become contaminated with: (i) chloride from storage in PVC bags and (ii) water from exposure to the atmosphere. Heat treatment has been proposed as a method of decontaminating PuO$_2$ for either reuse in Mixed Oxide (MOX) fuel or safe disposal in a Geological Disposal Facility (GDF), as it would not produce additional aqueous waste.[1] Furnace heat treatment experiments at various temperatures in air have been carried out in order to verify the extent to which chloride and water are removed from PuO$_2$ by this method and to establish the most effective and efficient temperature at which to heat treat the PuO$_2$. X-Ray Diffraction (XRD) was used to detect any changes in crystal structure. Specific experiments investigating gas production and water adsorption onto the PuO$_2$ surface were carried out in a sealed (`Baskerville´) vessel. This paper explains the methodology used to perform these experiments with PuO$_2$.

Methodology

Furnace heat treatments

These heat treatments were carried out in an air atmosphere radiochemical (negative pressure) glove box. The powders were poured into a boiling tube and placed inside a glass tube within a vertical tube furnace (Instron). The glass tube was connected to an anti-suck back trap and caustic solution in order to trap any volatile chlorine-containing species and determine the effectiveness of the heat treatment (Fig. 1). Air was pumped through the system with a flow rate of 250 mL min^{-1}. The furnace was heated to the desired temperature (400, 600, 800 or 950 °C) at 10 °C min^{-1} for 2 h. The powders were left to cool with the air still flowing for 1 h. Ion chromatography was carried out on the PuO$_2$ solid and caustic solution both before and after heat treatment using a Dionex ion chromatography unit.
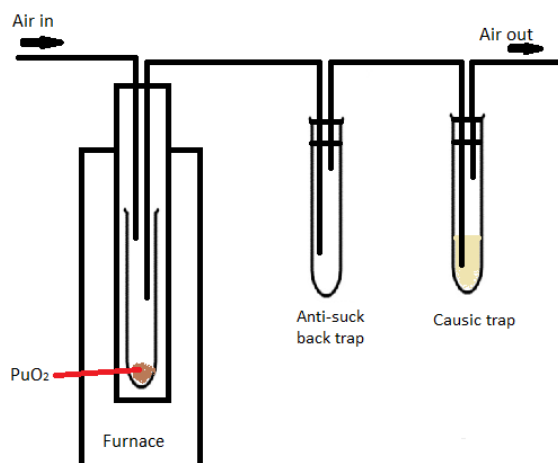
Figure 1 Apparatus used to heat treat chloride-contaminated PuO₂ in an Instron furnace.

Baskerville heat treatments

Magnox PuO₂ heat treated at 700 °C: PuO₂ powder (previously heat treated at 700 °C) was put into a vessel, which was sealed, pressurised and leak checked (Fig. 2). The vessel was then vented through a valve and sealed again. It was placed in a furnace and insulated before being heated to 225 °C at 5 °C min^{-1} for 4 h and left to cool, while the pressure was recorded throughout. The heat cycle was repeated before the vessel was opened. The process was carried out a second time with 0.05 mL water in a side chamber within the vessel.
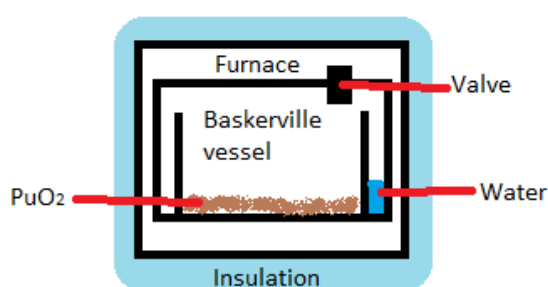
Figure 2 Apparatus used to measure the pressure increase of PuO₂ at 225 °C with/without water.

Sequential heating of Magnox PuO₂: The preparation process is the same as above. The PuO₂ powder was heated to 100 °C at 5 °C min^{-1} for 4 h and allowed to cool. Keeping the vessel sealed, this was repeated up to temperatures of 150, 200 and 230 °C, recording the pressure throughout. The gas was then sampled and sent for gas chromatography analysis. As before, the process was repeated for this material in the presence of 0.05 mL water at 150 and 230 °C.

Background results of pressure increase in an open vessel with temperature were subtracted from the measured results.

X-Ray Diffraction

Epofix resin and epofix hardener were mixed together and pipetted into a mould. These were chosen because epoxy resin is transparent to X-Rays. PuO₂ powder was spread across the resin in a glove box and more resin was added before being left to set overnight (Fig. 3). The puck was taken out of the mould and the surfaces were cleaned with deionised water and a Kimtex wipe. More resin/hardener mix was put on a base and the set powder was placed face down, spread around so that the resin was evenly distributed and left to set again overnight. Excess resin around the sides was scraped off. The brim of the mould was painted with resin and placed over the puck (exposed face down). The unexposed puck face was also painted with resin and left to set overnight. More resin was added to the unexposed face before a stopper and plate were put on top. The puck was swabbed to check for contamination before being taken out of the glove box and placed into a fume cupboard. If contamination had been found, more resin was added to the puck. The decontamination process was repeated in the fume cupboard before the puck was placed in a sample holder ready for XRD analysis. XRD patterns were recorded on a Brücker D8 diffractometer with step size = 0.02 ° and time per step = 9 s (between 2ϑ = 25 and 58 °) and 18 s (between 2ϑ = 58 and 145 °). An example of a reference PuO₂ XRD pattern is shown (Fig. 4).
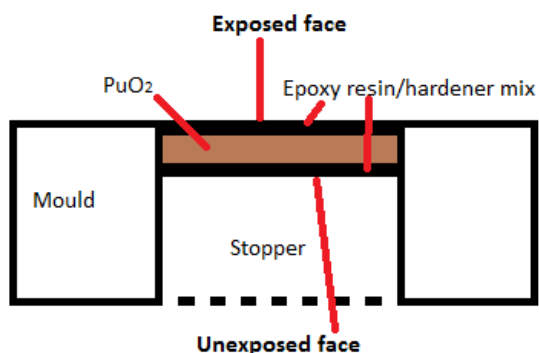
Figure 3 XRD puck for PuO₂ set in a mould.
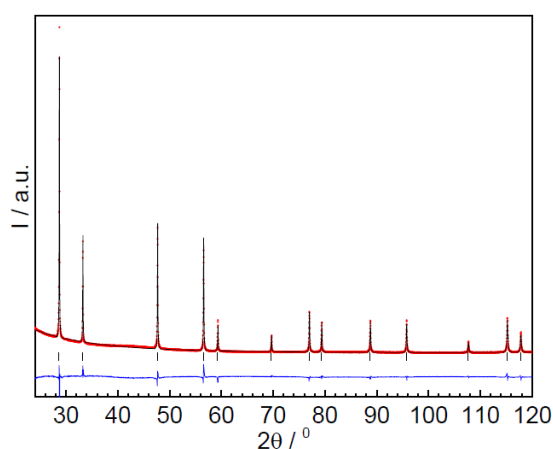
Figure 4 Example XRD pattern of PuO₂ microcrystals annealed for 8 hours at 1800 K in air.[2]

Conclusions and Future Work

The experiments described above have produced XRD, ion chromatography and sealed (Baskerville) vessel data to aid understanding of the desorption processes of chloride and water from PuO₂ powders over a range of temperatures. These data are currently undergoing analysis and will be written up for publication in the near future.

Acknowledgements

References

1. C. Campbell, C. Gregson, R. Orr, H. Sims, R. Taylor and K. Webb, *NNL, National Nuclear Laboratory, Sellafield*, 2014, **12869**, 1–68.

2. D. Hudry, C. Apostolidis, O. Walter, A. Janßen, D. Manara, C. Griveau, E. Colineau, T. Vitova, T. Prüßmann, D. Wang, C. Kübel and D. Meyer, *Chemistry-A European Journal*, 2014, **20**, 10431–10438.

Gas Generation from Water on the Surface of Plutonium Dioxide

L. Jones*[1], H.S. Sims[2], R.M. Orr[3], J. Hobbs[4], H. Steele[4] and S.M. Pimblott[1]

*Correspondence: Luke.jones-2@manchester.ac.uk

[1] School of Chemistry (University of Manchester, Dalton Cumbrian Facility, Westlakes Science Park, Moor Row, Cumbria, CA24 3HA, UK)
[2] National Nuclear Laboratory (NNL, Culham Science Centre, Abingdon, Oxfordshire, OX14 3DB, UK)
[3] National Nuclear Laboratory (NNL, Sellafield Central Laboratory, Sellafield, Seascale, Cumbria, CA20 1PG, UK)
[4] Sellafield Sites Ltd, Sellafield, Seascale, Cumbria CA20 1PG

Abstract

The long term storage of separated plutonium dioxide (PuO$_2$) in sealed canisters requires an understanding of the processes occurring within them. There are several processes with the potential to pressurise these canisters. One of these processes is the radiolysis of adsorbed water leading to the formation of hydrogen (H$_2$) and oxygen (O$_2$). A review of previous work investigating H$_2$ production from the interaction of water and PuO$_2$ and discussion of the results is undertaken. An outline of experiments currently ongoing at the National Nuclear Laboratory is also discussed.

Introduction

There is a large quantity of plutonium dioxide (PuO$_2$) in storage at the Sellafield site. The vast majority of UK PuO$_2$ is derived from reprocessing of spent nuclear fuel. There are two PuO$_2$ product streams at the Sellafield site, one from reprocessing spent uranium metal from UK Magnox reactors and one from reprocessing spent oxide fuels in the Thorp reprocessing plant. Current Magnox PuO$_2$ product is contained in an aluminium screw top container, inside a polyethylene bag and contained inside a welded steel canister. The fill gas is a 50:50 mixture of air and argon. Thorp PuO$_2$ is contained in a stainless steel screw top inner can held within a vented intermediate can inside a welded outer container, and stored under an argon atmosphere [1]. During packaging of PuO$_2$, the conditions are closely controlled to limit water uptake by the PuO$_2$ product and to ensure the product meets acceptance criteria for long term storage. A similar arrangement has been adopted by the United States Department of Energy for storage of US PuO$_2$ [2].

PuO$_2$ is known to be a very hygroscopic material, therefore several monolayers of water would be expected to be adsorbed to the material prior to going into storage if there are no controls over the water vapour conditions. It would be expected that this water is radiolysed to H$_2$ and oxygen containing species and lead to pressurisation, however, of the several thousand canisters of PuO$_2$ in storage in the UK, only a few cans containing out of specification, very wet material are known to have pressurised. From this it is assumed that a reverse reaction, such as

recombination of radiolysis products must occur. Little information is known about either process.

Better understanding of the fundamental chemical processes occurring inside the storage canisters can benefit the current safety case underpinning the safe long term storage of PuO$_2$.

The work reviewed in this paper has been undertaken by the radiochemistry team based at NNL's Central laboratory.

Samples of Magnox and Thorp PuO$_2$ were used, as received from plant, to provide material with different specific activities and specific surface areas (SSA). For low SSA samples, Magnox derived PuO$_2$ was re-calcined at 800-950 ^oC under a dry nitrogen flow to reduce the specific area due to partial sintering of the product.

A range of relative humidities were studied from 0-95 %. All experimental work was carried out at room temperature in either an air or nitrogen glovebox.

Methodology Details

Material Preparation

Approximately 0.5-1 g of PuO$_2$ was used in each experiment. The powders were dried for 30 days by placing inside a desiccator prior to the start of experiments. The mass of each sample was recorded at intervals to track progress. At the end of the drying process, the samples were transferred to a vessel with a controlled atmosphere to equilibrate with a humid atmosphere. The appropriate molarity of sulphuric acid

was used to generate the required relative humidity. Whilst inside the humidity chamber, samples were weighed at regular intervals to determine the mass and therefore number of monolayers of water adsorbed to the material.

Experimental

Figure 1 shows a schematic of the glass vessel used for radiolysis experiments
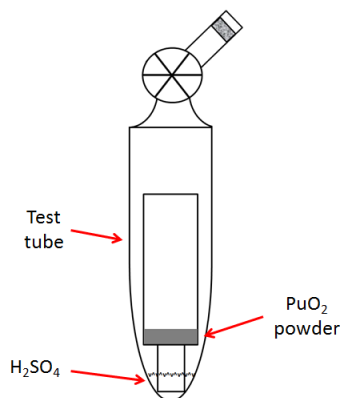
Figure 1: Schematic of Radiolysis Experiment Vessel

The sample vessel consists of a small glass tube which holds the PuO_2 powder and an outer test tube which holds the sulphuric acid. The test tube is fitted with a quickfit valve which allows for periodic sampling of the headspace during the course of the experiments. The sulphuric acid ensures the humidity remains constant during the experimental run.

The headspace is periodically sampled by using a gas tight syringe connected to the vessel and analysed for hydrogen using a gas chromatograph [3].

Approximately 6-8 samples are taken during each experimental run, after which the vessel is opened to the glovebox atmosphere and any remaining hydrogen is removed by a hand vacuum pump. Once the samples have been purged with the relevant atmosphere, the vessels are re-sealed for further experimental runs.

Results and Discussion

The following results have been selected to highlight trends and anomalous behaviour observed throughout the course of the experiments. All graphs indicate hydrogen produced (in nmol) as a function of time [4].

In nearly all of the experiments undertaken at NNL a linear production rate of hydrogen with time has been observed. This is highlighted in Figure 2 which is a graph of Magnox PuO_2 calcined at 950 °C in contact with 50 %RH.
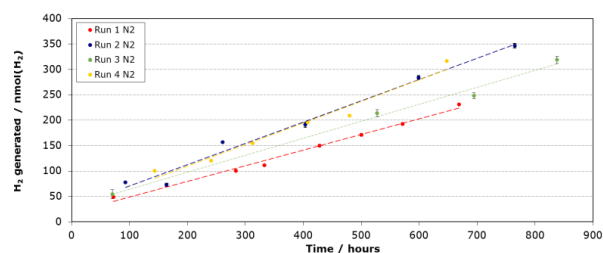
Figure 2: H_2 generated as a function of time for Magnox PuO_2 calcined at 950 °C in 50 %RH

From this behaviour, it would be expected that all PuO_2 storage canisters would pressurise over time as no steady state appears to be forthcoming. However, as this is not the case it can be assumed in these experimental conditions, the forward reaction is favoured over recombination.

Samples that contained Magnox derived PuO_2 held in 25 and 50 %RH exhibited increasing H_2 production rates with subsequent experimental runs. This anomalous behaviour is highlighted in Figure 3.
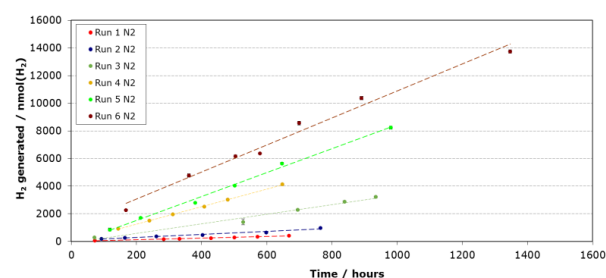
Figure 3: H_2 generated as a function of time for Magnox PuO_2 calcined at 800 °C in 50 %RH

The increase in H_2 production is correlated with additional signals in the gas chromatogram demonstrating new gas species and alteration of the chemistry occurring in the system. This behaviour is yet to be explained.

Switching samples between air and N_2 gloveboxes also had an effect on the H_2 production rates. Figure 4 shows 9 subsequent experimental runs with Magnox PuO_2 calcined at 900 °C in 50 %RH. The experiment started in an N_2 glovebox with the final 2 runs undertaken in an air glovebox.
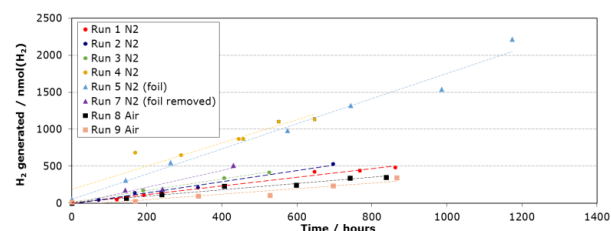
Figure 4: H_2 generated as a function of time for Magnox PuO_2 calcined at 900 °C in 50 %RH

From this figure it is shown that the H_2 production rate decreases when switched to an air atmosphere. This phenomenon has been observed for nearly all Magnox

PuO$_2$ experiments where both atmospheres were tested, regardless of humidity and SSA.

Thorp PuO$_2$ displayed the opposite trend, with H$_2$ production rates increasing when experiments were swapped to an air atmosphere.

There are several hypotheses for this contrasting behaviour of different PuO$_2$ products. These include sample history and the role oxygen plays in the mechanism of H$_2$ generation.

Conclusions and Future Work

It is clear from these selected graphs that the mechanisms involved in the radiolysis of adsorbed water in contact with PuO$_2$ are not well understood and further experimental work is needed to confirm the reproducibility of the observations.

Current experimental work is focussed on Magnox and Thorp PuO$_2$ received fresh from plant without further heat treatment. A range of relative humidities (25-95 %) is also being investigated.

Experiments are being undertaken simultaneously in an inert argon glovebox and an air or N$_2$ glovebox. This will help to determine the role oxygen may play in the production of hydrogen from adsorbed water radiolysis.

Characterisation of the oxide product is also planned, giving a better understanding of the differences in the two oxide product streams.

Acknowledgements

References

[1] Cook, P., H.E. Sims, and D. Woodhead, *Safe and Secure Storage of Plutonium Dioxide in the United Kingdom.* Actinide Research Quarterly, 2013(2): p. 20-25.

[2] *Stabilization, Packaging, and Storage of Plutonium-Bearing Materials*, D. o. Energy, Editor 2012.

[3] Sims, H.E., et al., *Hydrogen yields from water on the surface of plutonium dioxide.* Journal of Nuclear Materials, 2013. **437**(1-3): p. 359-364.

[4] Orr R. M., H. E. Sims, K. Webb, and C. Gregson, *Radiolytic hydrogen production from PuO$_2$: 2015-16 update*, NNL (16) 13820

A Catalytic Approach to H$_2$ and O$_2$ Recombination on PuO$_2$ and PuO$_2$ Surrogates

T. A. Donoclift*[1], R. M. Orr[2], H. E. Sims[3], and S. M. Pimblott[1]

*Correspondence: Thomas.Donoclift@Manchester.ac.uk

[1] Dalton Cumbrian Facility, University of Manchester, Whitehaven, Moor Row, CA24 3HA
[2] National Nuclear Laboratory, Central Laboratory, Seascale, CA20 1PG
[3] National Nuclear Laboratory, Culham Science Centre, Abingdon, Oxfordshire, OX14 3DB

Abstract

A typical plutonium dioxide storage package contains very little water, and as a result, package pressurisation due to alpha radiolysis of water is an anomalous phenomenon, observed in only a few "out-of-specification" packages. Previous measurements of hydrogen production from the surface of dry PuO$_2$ suggest that package pressurisation should be more common. As this is contrary to what is observed at Sellafield, it must be concluded that some removal mechanism is taking place. This work aims to measure the rate of recombination of H$_2$ and O$_2$ over plutonium dioxide. By taking a catalytic approach it is hoped that experimental measurements can provide data to reduce some of the pessimisms built into the Compliance Index model and give insight to the chemical mechanism of recombination taking place on the surface of plutonium dioxide.

Introduction

The accumulation of plutonium dioxide at the Sellafield site is a result of spent fuel reprocessing operations carried out over the last ~50 years. The plutonium dioxide products being stored at Sellafield can be described as being either Magnox PuO$_2$, which has been accrued through the reprocessing of spent uranium metal fuels from UK Magnox reactors, or Thorp PuO$_2$, which is extracted from reprocessing spent oxide fuels from various reactors that held a contract with the Thorp reprocessing plant.

A typical storage package contains very little water, and as a result, package pressurisation is an anomalous phenomenon, observed in only a few out-of-specification packages. Although each of the aforementioned plutonium products is packaged in a slightly different manner, significant efforts are made, in both cases, to limit water adsorption and ensure the strict criteria for storage is met. The pressurisation of the anomalous plutonium storage cans at the Sellafield Site has predominantly been attributed to the alpha radiolysis of water adsorbed to the surface of PuO$_2$.

Previous measurements of hydrogen production from the surface of dry plutonium dioxide (i.e. samples that would normally meet storage criteria) are shown in Table 1. These production rates suggest that, even at very low water content, the hydrogen production rate equates to a can pressurisation of approximately 0.15 bar per year.

As this is contrary to the observations of plutonium packages kept at Sellafield, it must be concluded that some removal mechanism is taking place within the plutonium storage cans.[1]

Sample	SSA ($m^2\ g^{-1}$)	Activity (Bq-α g^{-1} Pu)	H$_2$ production rate ($cm^3\ day^{-1}\ g\ PuO_2^{-1}$)
Magnox	8.9 ± 1.1	5.5×10^9	6.52×10^{-6}
Thorp	6.1 ± 1.0	1.8×10^{10}	1.02×10^{-5}

Table 1 Specific surface area, specific activity, and average hydrogen production rates from dry Magnox and Thorp PuO$_2$ samples.[1]

Work conducted at the Los Alamos National Laboratory (LANL) was carried out in order to investigate the recombination of H$_2$ and O$_2$ over plutonium dioxide. Pressure-volume-temperature (PVT) apparatus was used to measure a pressure drop of a known gas mixture, at a known initial pressure and volume, over plutonium dioxide to obtain a preliminary hydrogen removal rate.[2] The results obtained indicate that surface recombination of H$_2$ and O$_2$ is predominantly a chemical process and is not strongly driven by radiolysis

processes. However, no conclusion whether the surface mechanism fits a Langmuir-Hinshelwood or an Eley-Rideal mechanism could be made.

This work aims to expand the understanding of H_2 and O_2 recombination over plutonium dioxide by deployment of a fixed bed reactor (FBR) catalyst testing technique. Given the hazardous nature of the material in question, and the practical constraints in its use for conducting experiments, significant preparation is required to ensure a safe, yet viable experiment. For this reason, this project is split into two phases, in which a non-active pilot reactor is used as a proof of concept (Phase I) before deployment in an active glovebox for use with plutonium dioxide (Phase II).

Methodology Details

Fixed Bed Reactor

A fixed bed reactor is a type of continuous tubular flow reactor, sometimes called a *plug flow reactor*; named for the close to ideal plug flow pattern they operate under. Unlike batch reactor techniques that can only infer a reaction rate, such as the PVT method, FBRs can directly measure a reaction rate. Moreover, an FBR operating under steady-state conditions means the reaction time scale is decoupled from that of the analytical technique. This allows for numerous measurements under a single condition to be made, which greatly improves the accuracy of the data collected over that obtained from a batch technique.[3] FBRs generally consist of a heated isothermal reactor tube containing a known quantity of catalyst material. Reactant gas is fed through the catalyst in a controlled manner, generally requiring the use of high accuracy mass flow controllers (MFCs). The conversion of reactant gas to products is then quantified by gas chromatography techniques. Figure 1 shows a schematic for the fixed bed reactor.
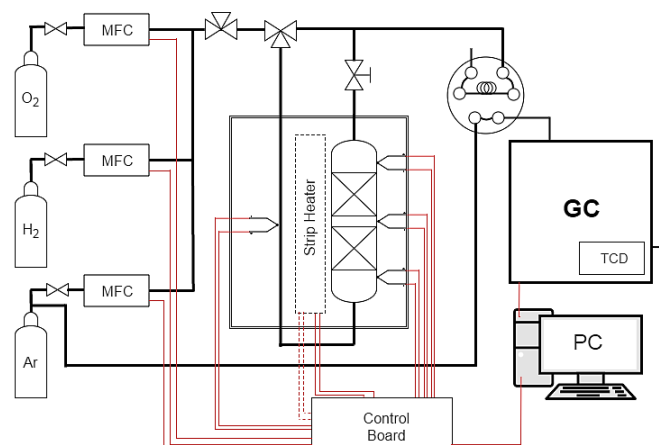
Figure 1 Schematic of the pilot FBR

Phase I is currently being carried out at the University of Manchester, Dalton Cumbrian Facility and involves the construction of a non-active pilot reactor that will use cerium dioxide as a surrogate for PuO_2. Cerium dioxide is used as a surrogate for plutonium dioxide as it is thought that the similar ionic radius, oxidation states, and the FCC crystal structure of cerium dioxide will provide a chemically similar surface for thermal recombination to occur. The pilot FBR will provide a necessary benchmark from which an active version can be designed and built into a glovebox at the National Nuclear Laboratory (NNL).

Conclusions and Future Work

As previously mentioned, it is unknown if the mechanism for H_2 and O_2 recombination is a Langmuir-Hinshelwood or an Eley-Rideal mechanism, shown in Figure 2. The use of a fixed bed reactor allows for experiments to independently vary the concentrations of hydrogen and oxygen, which, when plotted as a function of conversion rate, can reveal which of the two possible mechanisms the process fits.
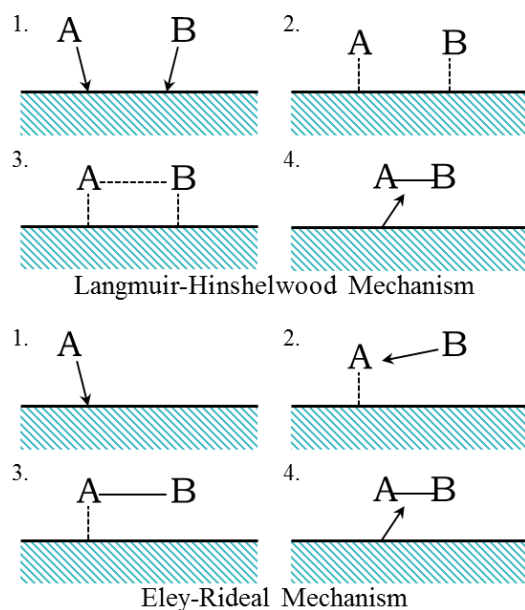
Figure 2 Examples of the Langmuir-Hinshelwood and Eley-Rideal mechanisms.

In addition to providing information on the mechanism involved, this approach will also be able to provide data useful to the Compliance Index model. This is a model used to predict the behaviour of plutonium storage canisters over a given period of time; however, given the lack of data available, this model incorporates a large number of estimations that give the calculations a rather pessimistic bias. More accurate data can help to reduce the pessimisms within the compliance index model.

Acknowledgements

References

[1] Sims, H.E., et al., *Hydrogen yields from water on the surface of plutonium dioxide.* Journal of Nuclear Materials, 2013. 437(1–3): p. 359-364.

[2] Morales, L., *Preliminary Report on the Recombination Rates of Hydrogen and Oxygen Over Pure and Impure Plutonium Oxides.* US Department of Energy, Los Alamos National Laboratory LA-UR-98-5200, 1998.

[3] Davis M.E., Davis R.J. *Fundamentals of Chemical Reaction Engineering.* ISBN: 0-07-119260-3 2003

Ceramic and glass-ceramic wasteforms for actinide disposition

Shikuan Sun, Martin Stennett, Claire Corkhill and Neil Hyatt

*Correspondence: shikuan.sun@sheffield.ac.uk

[1] 1 Immobilisation Science Laboratory, Department of Materials Science and Engineering, The University of Sheffield,
(Mappin Street, Sheffield S1 3JD, United Kingdom)

Abstract

Pyrochlore ceramic and zirconolite glass-ceramic wasteforms are the potential host phases for actinide disposition. Composition – processing – structure relations in a series of wasteforms (uranium betafite, cerium pyrochlore and zirconolite glass ceramic) was investigated in this work. Fully dense uranium betafite ceramic was prepared by sintering of the oxide precursors ($CaTiO_3$, TiO_2, ZrO_2 and U_3O_8) at 1320°C in flowing N_2. The betafite phase in high yield (> 85%) with uranium oxidation state of 4.2±0.1 was found in the resulted ceramics and all U_3O_8 was incorporated into the ceramic. As a Pu surrogate, cerium pyrochlore with nearly single phase was obtained and the crystal structure (Space group *Fd-3m*, *a* = 10.1469 Å) was determined from neutron diffraction data. After heavy ion irradiation on zirconolite glass-ceramic, the crystallinity of zirconolite phase decreased in the damaged surface layer, and the swelling feature of glass phase was observed along the zirconolite grain boundary. The morphology evolution during the dissolution at 90°C in water showed the glass dissolved first and the depth difference between zirconolite and glass phase after 28 days was around 2.0 μm.

Introduction

Ceramic materials were considered as one of potential wasteform for the stabilization of high level waste (HLW), specially the actinides.[1,2] The naturally occurring forms of pyrochlore were found to be highly durable under environment condition and actinides were effectively retained for geological time period.[3] Therefore, pyrochlore-group synthetic ceramic were proposed for the immobilisation of HLW. In this work, two subgroups of pyrochlore minerals, Ce-pyrochlore and U-betafite were prepared. The phase assemblage, the chemical composition, the crystal structure and the oxidation state (Ce/U) of the ceramic wasteforms were investigated.

Glass-ceramic is designed with double barrier system, where actinides can be retained in the ceramic phase and the miscellaneous material in the glass phase.[4] In this work, zirconolite glass ceramic was prepared and the heavy ion implantation was employed to simulate the damage arising from α-decay of the actinides (4.5-5.8 MeV), focusing on the variation of crystallinity and morphology. Furthermore, the morphology and phase evolution during dissolution was also studied in the present work.

The aims of the present work are to develop an understanding of the composition – processing – structure relations in pyrochlore ceramic and zirconolite glass-ceramic wasteform.

Methodology Details

Preparation

Uranium pyrochlore were prepared by adding U_3O_8 to the oxide precursor material ($CaTiO_3$, TiO_2 and ZrO_2 provided by National Nuclear Laboratory, UK) at two different U_3O_8 waste loading – 35 wt% and 45 wt%, labelled as U35 and U45. Metallic fractions (Fe and Ni, 10 wt%) were added to access the effect of redox active species on final wasteform assemblage. The raw materials were mixed using rotary ball milling for 16 hours. The mixture was pressed in a stainless steel die using 1.5 tonnes loads. The resulting powder compact were then placed in alumina crucibles and sintered in flowing N_2 at 1320°C for 2 hours.

Cerium pyrochlore samples were prepared by solid state reaction between $CaCO_3$, CeO_2 and TiO_2. Instead of stoichiometric ratios, the raw materials with various molar ratios of Ca:Ce:Ti were mixed, targeting pure pyrochlore product. Reagents were mixed using planetary milling containing Si_3N_4 milling media and isopropanol as a carried fluid. The mixed precursors were reacted in alumina crucibles at 1250°C for 10 h in air with a ramp rate of 5°C/min.

Zirconolite glass ceramic was prepared by mixing of fluorspar, CeO_2 and glass ceramic precursors, and afterward Hot Isostatic Pressing (HIP) at National Nuclear Laboratory (NNL). Specimens were cut from the HIPed canister using a diamond saw and polished to an optical finish with SiC paper and diamond paste (to 0.1 μm grade). Ion beam irradiations (2 MeV Au ion) with uniform and Gaussian profile were performed, respectively. The dissolution behaviour was also studied under the environment of water at 90°C.

Characterisation

The phase analysis of the samples were performed by X-ray diffraction (XRD, D2 Phaser, Bruker). The quantification phase analysis by Rietveld refinement was performed using the GSAS suite of programs [5]. X-ray photoelectron spectroscopy (XPS) data of U35 and U45 were recorded (SPECS Phoibos 150 hemispherical analyser). For the irradiated sample, the amorphous (or crystal) structure on the near surface region was evaluated using GIXRD (X'pert 3, Panalytical) at 0.5° incidence angle. Neutron diffraction data of Ce-pyrochlore were acquired at room temperature on the High Resolution Powder Diffractometer at NIST Centre for Neutron Research (USA). Ce and U L_3 edge X-ray absorption spectroscopy data were acquired on beamline B18 at Diamond Light Source and Beamline X23A2 at the National Synchrotron Light Source (USA), respectively. For the bulk specimens, the microstructure was observed using a scanning electron microscope (SEM, TM3030, Hitachi) with EDX (Quantax 70, Bruker). Characterization of morphology on glass-ceramic samples was also studied using vertical scanning interferometry (ContourGT, Bruker).

Results and Discussion

Uranium betafite
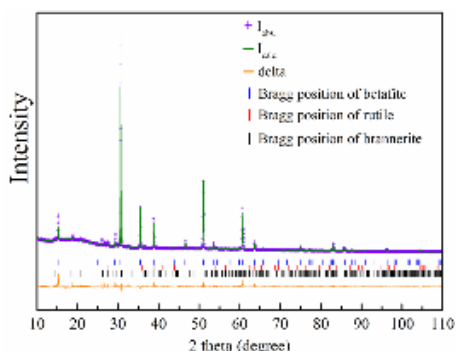
Figure 1 Rietveld refinement of the XRD pattern for U45 sample. The quality of the fit: R_p(%) = 6.41, R_{wp}(%) = 9.39 and χ^2 = 4.45.

This section will emphasize U35 and U45 for a better comparison of the obtained results. In both U35 and U45 samples, the major phase was betafite phase ($CaUTi_2O_7$). No free uranium oxides (UO_3, UO_2 or U_3O_8) were detected in any of the samples, indicating that U_3O_8 in the starting materials had been completely incorporated. Rietveld refinement of XRD patterns was performed for the quantitative phase analysis (QPA) of the product. QPA on U45 is shown in the Fig. 1 as an example, with the secondary phases of TiO2 (tetragonal, $P4_2/mnm$) and UTi_2O_6 (monoclinic, $C2/m$) adding for calculation of the weight fraction. The mass fraction of betafite was determined to be 84.80 wt% and 94.38 wt% in U35 and U45, respectively. On basis of the QPA results and calculation of theoretical density of each phase, it was possible to allow an accurate calculation

of the relative density of these multiphase samples. Full densification was nearly achieved for the U35 (99.51% theoretical) and U45 (98.76%).

Figure 2 shows SEM images of U35 and U45. The U35 and U45 sample both showed very little porosity and the presence of three distinct phases (Fig. 2a). The major phase (labelled B) was betafite, as confirmed by the presence of U, Ca and Ti in the EDS spectra. The minor phase labelled R in Fig. 2a was confirmed to be TiO2, and the minor phase labelled P was confirmed to be CaTiO3. These results are consistent with the XRD results. Fig. 2b shows that the U45 sample consists of majority betafite with minor inclusions of TiO2 (labelled R) and UTi_2O_6 (labelled Br). Based on the chemical composition measured by EDX, the content of U_3O_8 was calculated to be 32.48 wt% in U35 and 42.66 wt% in U45, which are both close to the nominal waste loadings of 35 wt% and 45 wt%.
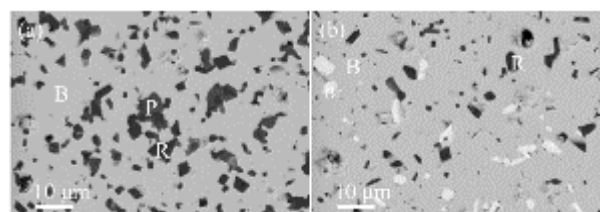
Figure 2 SEM observation of the polishing surface of sample U35 (a), U45 (b)

The oxidation state of uranium in the U35 and U45 was investigated using XPS. The location of the satellite peak was used to identify the existence of uranium with different oxidation state. As shown in Fig.3, a strong satellite peak was found 6.7 eV apart from the major band in the U $4f_{5/2}$ peak, indicating that U^{4+} was the dominant species in samples of U35 and U45.[6] As seen in Figs. 3B, the U $4f_{5/2}$ peak was fitted into U^{4+}, U^{5+} and U^{6+} components. The fitting peaks of U35 and U45 located at 380.1, 381.2 and 382.5 eV (with error of ± 0.1 eV) were attributed to U^{4+}, U^{5+} and U^{6+}, respectively. The fitting in U45 contained a prominent U^{4+} component and a small U^{5+} component. The occurrence of U^{6+} could not be found, consistent with our previous results from XANS. The locations of two major components were with separations of 0.9 eV (U^{4+} - U^{5+}), in accordance with literature for mixed valence of uraninite [7].
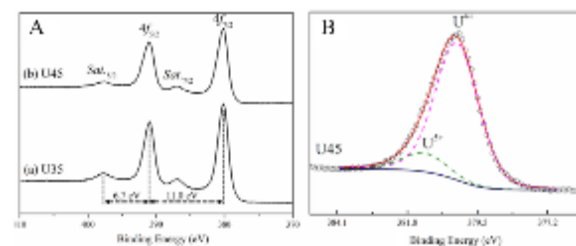
Figure 3 (A) The U $4f_{7/2}$ and U $4f_{5/2}$ regions of the XPS spectra for U35 and U45. (B) Deconvolution of the U $4f_{7/2}$ photoelectron peaks for U45.

The ratio of U^{4+} and U^{5+} for U45 wss 88.0 wt% and 12.0 wt%, respectively. Results of the curve fitting give the average uranium oxidation state of 4.1 (v.u.) for both U35 and U45, which agreed well with those from linear combination fitting of XANS data (4.2 and 4.1 v.u. for U35 and U45).

Cerium pyrochlore

Rather than the stoichiometry ($CaCeTi_2O_7$), the nearly pure phase was obtained by introducing Ca vacancies and Ti excess (for charge balance) in the starting materials of $CaCO_3$, CeO_2 and TiO_2. As shown in Fig. 4, refinement of the neutron pattern. Refinements shows a satisfactory fit with χ^2=2.428, R_{wp}=5.48%, R_p=4.41%. A small quantity of TiO_2 impurity was observed in the product. The final refined results in ND were space group of *Fd-3m* with lattice parameter of a = 10.1462(4) Å, which were slightly smaller than the previous reported lattice parameter 10.1477 Å [8]. Together with Ca atoms, Ce (Pu surrogate) occupy the *16d* site with coordination number of 8. A small portion of Ti substitution on to Ca/Ce site was also observed. It is noteworthy that this is the first reliable structure determination on ND data of Ce-pyrochlore.
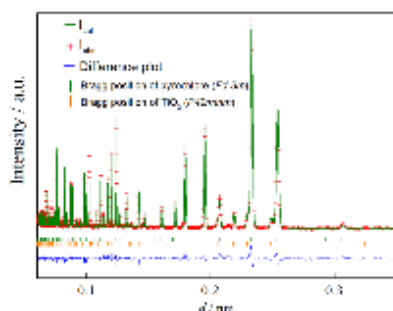
Figure 4 Fitted powder neutron diffraction pattern of Ce-pyrochlore.
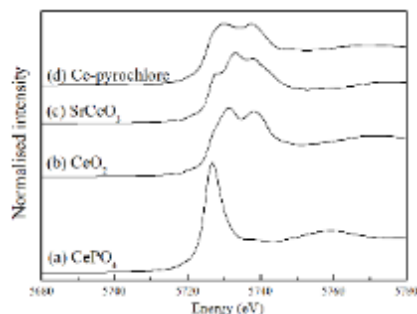
Figure 5 X-ray absorption near edge spectra (XANES) of Ce-pyrochlore.

The XANES spectra can be seen in Fig. 5 and from comparison of the spectra it is apparent that the XANES of Ce-pyrochlore closely resemble those of CeO_2, and to a lesser extent those of $SrCeO_3$, demonstrating that Ce^{4+} with CN = 8 was the dominant species in Ce-pyrochlore phase. The amount of Ce^{3+} was calculated to be 10 wt% by linear combination fitting and the average oxidation state of Ce was estimated to be 3.9 v.u (with the experimental error ±0.1).

Zirconolite glass-ceramic

Figure 6 shows grazing incident X-ray diffraction (GIXRD, glancing angle=0.5°) results for the zirconolite glass-ceramic: pristine, irradiated to a fluence of 3×10^{15} and 5×10^{15} Au ions per cm^2 (labelled as Sample A and B, respectively). The pristine diffraction patterns confirmed the existence of two phases in the as-synthesized state: $CaZrTi_2O_7$ and CaF_2. The glass phase contributed an amorphous hump to the pattern. The penetration depth at glancing incident angles of 0.5° on $CaZrTi_2O_7$ and CaF_2 phases are 375 and 640 nm, respectively. Based on the SRIM calculation, the damage level of zirconolite after irradiated at the fluences of 3×10^{15} and 5×10^{15} Au ions per cm^2 is estimated to be 10 and 15 d.p.a. on the region of roughly 250 nm, suggesting the undamaged and/or partially damaged layer was likely to contribute to the peak intensity in Fig. 6.
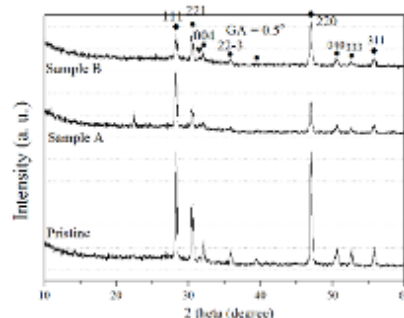
Figure 6 Grazing incidence X-ray diffraction patterns obtained from zirconolite glass-ceramic before and after 2MeV Au ion irradiated to a fluence of 3×10^{15} (Sample A) and 5×10^{15} (Sample B) ions per cm^2
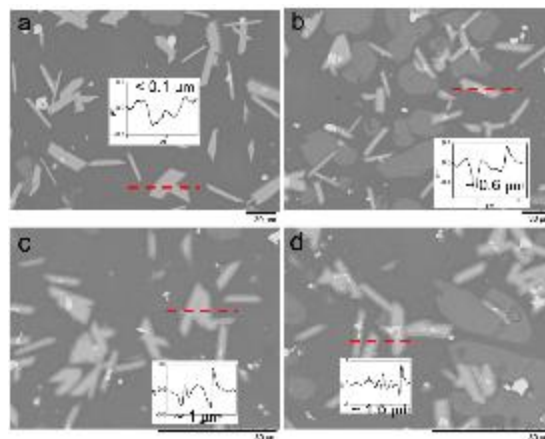
Figure 7 SEM images comparing irradiation damage along the Gaussian profile beam radius. a → d: Observation area from edge to centre with equal distance.

Gaussian profile irradiation was performed as well. Similar to the above-mentioned works, 2 MeV Au ion was employed and the overall fluence of the irradiated area was equal to 5×10^{15} ions/cm^2. The microstructure variation was investigated along the beam radius, as shown in Figs. 7a-d. The edge of the Gaussian profile shows a relatively flat surface, with the depth difference

of lower than 0.1 μm (Fig. 7a). Whereas, the depth difference in zirconolite grain boundary increased (insets of b and c) with closer distance to the centre and zirconolite grain was below the glass level, indicating that irradiation induced damage might lead to the swelling of the glass matrix. Finally the depth difference in the centre area was about 1.5 μm.
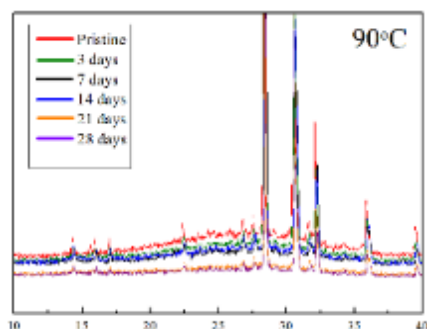
Figure 8 XRD patterns of the glass-ceramic during the dissolution from 1 day to 28 days, compared to the pristine.

The evolution during the dissolution condition of 90°C in water of the as-obtained bulk was studied. No obvious change in regards to the position and intensity of the crystallized peaks could be observed with increasing leaching dates. However, the diffuse scattering, which was caused by the glass phase, decreased gradually, as shown in the Fig. 8. It indicated the glass firstly dissolved in the environment, which was consistent with the PCT test results of the powdered samples.

The surface morphology observation of the same area was performed using the combined SEM-VSI technology. It can be seen from Fig. 9 that the level of the glass matrix continentally decreased as the leaching test performed at 90°C in water, compared to the sample before dissolution. The depth difference in the grain boundary of zirconolite was estimated to be approximately 2.0 μm after dissolution at 28 days.
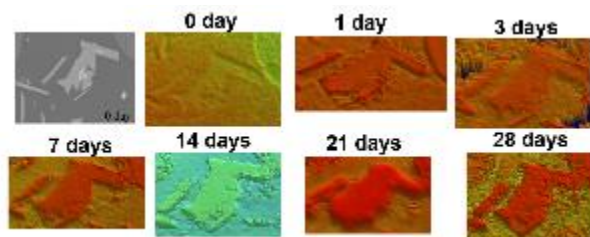
Figure 9 VSI-SEM combined observation of zirconolite glass ceramic during the dissolution

Conclusions and Future Work

A series of pyrochlore ceramic and zirconolite glass ceramic were fabricated to understand composition – processing – structure relations. Results shown that

(1) Nearly dense U-betafite ceramics were obtained starting from two different U_3O_8 loading. No residual U_3O_8 was detected in the ceramics and a high yield of betafite phase was found;

(2) Ce-pyrochlore with a nearly single phase crystallized in *Fd-3m* space group (a = 10.1469 Å) and oxidation state of Ce was determined to be 3.9 v.u.;

(3) Glass swelling feature was observed after Au-ion irradiation on zirconolite glass-ceramic. The evolution during the dissolution showed the glass dissolved first and the depth difference after 28 days was around 2.0 μm.

Future experiments will seek to understand 1). Leaching rate of zirconolite glass ceramic; 2) Radiation tolerance comparing to zirconolite glass ceramic with the high ceramic fraction. .

References

[1] W. E. Lee, M. I. Ojovan, M. C. Stennett and N. C. Hyatt, *Advances in Applied Ceramics*, 105[1] 3-12 (2006).

[2] B. E. Burakov, M. I. Ojovan and W. E. Lee, *Crystalline materials for actinide immobilisation*, Imperial College Press, London, 2010.

[3] G. R. Lumpkin and R. C. Ewing, *American Mineralogist*, 81[9-10] 1237-1248 (1996).

[4] E. Maddrell, S. Thornber, N. Hyatt, *Journal of Nuclear Materials*, 456 461-466 (2015).

[5] B. H. Toby, EXPGUI, *Journal of Applied Crystallography*, 34 210-213 (2001).

[6] M. Schindler, F.C. Hawthorne, M.S. Freund and P.C. Burns, *Geochimica et Cosmochimica Acta*, 73[9] 2471-2487 (2009).

[7] M. Colella, G. R. Lumpkin, Z. Zhang, E. C. Buck and K. L. Smith, *Physics and Chemistry of Minerals*, 32[1] 52-64 (2005).

[8] B. Ebbinghaus, O. Krikorian, J. Lian, L. M. Wang, J. G. Catalano, *Journal of Nuclear Materials.*, 303 226-239 (2002).

Ce Incorporation in Zirconolite Glass-Ceramics.

S. M. Thornber[*1], M. C. Stennett[1] & N. C. Hyatt[1]

*Correspondence: sthornber1@sheffield.ac.uk

[1] *The University of Sheffield, Hadfield Building, Mapping Street, Sheffield, S1 3JD, UK*

Abstract

The UK has 140 tonnes of separated civil PuO_2 stored at the Sellafield site. The strategy for dealing with this stockpile is to fabricate MOx fuel, however a significant fraction has been identified as higher activity waste requiring immobilisation into stable wasteforms. In addition, Pu-residues are a classification of Pu-bearing higher activity wastes that range in Pu concentration, composition and physical form, thus requiring flexible wasteforms for immobilisation. This project investigates zirconolite glass-ceramics as future wasteforms for impure streams of these Pu wastes. Consolidated by hot isostatic pressing, Ce was targeted for incorporation on either the Ca^{2+} and / or Zr^{4+} sites as either Ce^{3+} or Ce^{4+}. The formation of a Ce-bearing perovskite phase was the result of Ce reduction when targeting Zr substitution, and has been discussed on the account of ionic radii arguments.

Introduction

The UK's current policy for dealing with the plutonium stockpile stored at the Sellafield site involves reuse as nuclear fuel where possible[1, 2], however, a significant fraction of the stockpile is unsuitable for retrieval of the Pu and has been classified as higher activity waste.[3] In addition, Pu-residues are a classification of Pu-bearing higher activity wastes that range in Pu concentration, composition and physical form, thus requiring flexible wasteforms for immobilisation [4, 5]. In this project we develop zirconolite based glass-ceramic wasteforms, consolidated by hot isostatic pressing for immobilising impure streams of these Pu-bearing wastes.

The glass-ceramic matrix provides a dual barrier system to Pu disposition by partitioning the actinides into the durable ceramic phase and accommodating impurities within the amorphous glass. The flexibility of the glass phase to accommodate impurities makes glass-ceramics a promising matrix for immobilising low purity Pu-residues that contain glass formers. As well as the flexibility and ease of processing the glass, glass-ceramics also couple the high actinide loading capacity and durability properties of full ceramic wasteforms [6]. Zirconolite readily accepts Pu into its structure as seen through its use in Synroc-C, and natural analogues show excellent radionuclide retention even when completely metamict [7, 8].

The zirconolite structure is a derivative of the pyrochlore structure ($A_2B_2O_7$) and consists of parallel planes of Ca and Zr ions alternated with planes of Ti octahedra. Whilst actinides substitute on the A-site lattice sites, the partially filled B-sites allow for charge compensation to take place. All elemental substitutions are limited by the size of the ion and the lattice site, which governs what substitutions can take place on specific sites. The multiphase Synroc system combines ceramic phases with different lattice sizes in order to accommodate a wide range of problematic elements associated with nuclear waste [9].

In this study CeO_2 was utilised as a surrogate for PuO_2 and we investigated its incorporation into the Sheffield glass-ceramic formulation when targeting Ca and / or Zr substitution within the zirconolite structure.

Method

All samples were batched with the same starting formulation that comprised 30 wt% glass forming oxides targeting composition $Na_2Al_2Si_6O_{16}$, and 70 wt% ceramic forming oxides. The stoichiometry of the ceramic was varied to target Ce^{3+} or Ce^{4+} incorporation on the Ca^{2+} and / or Zr^{4+} lattice sites, summarised in Table 1. When targeting Ce^{4+} incorporation on the Ca site (sample A) Al_2O_3 was added for charge compensation. All samples were hot isostatically pressed at 1250 °C for 4 h under 100 MPa of pressure. Characterisation of the samples was performed by SEM-EDX, XRD and Ce L_3 XANES to study the microstructure, phase assemblage, Ce partitioning and Ce valence state with respect to each targeted formulation.

Table 1: All samples consisted of 30 wt% glass of composition $Na_2Al_2Si_6O_{16}$ and 70 wt% of the target ceramic formulations listed. The targeted Ce valence state is also given.

Sample	Target ceramic composition	Target Ce oxidation state
A	$Ca_{0.8}Ce_{0.2}ZrTi_{1.6}Al_{0.4}O_7$	4+
B	$Ca_{0.9}Ce_{0.1}Zr_{0.9}Ce_{0.1}Ti_2O_7$	3+
C	$CaZr_{0.8}Ce_{0.2}Ti_2O_7$	4+

Results

Zirconolite was obtained as the major crystalline phase in all samples present with minor phases; rutile (TiO_2), zircon ($ZrSiO_4$), sphene ($CaTiSiO_5$), baddeleyite (ZrO_2) and ceria (CeO_2). Albite ($NaAlSi_3O_8$) was present in sample A due to the excess of Al_2O_3 added for charge compensation. SEM-EDX showed Ce incorporation had occurred preferentially into the ceramic phase, demonstrated by the signal rich areas on the elemental map in Figure 1. Figure 1 also shows a secondary Ce-rich phase present in sample C. Coupling the SEM-EDX data with the XRD data in Figure 2, the secondary phase was identified as a perovskite. The relative intensities of the perovskite reflections in the XRD data increase from sample A to B and again to C, as the zirconolite stoichiometries target Ce incorporation on the Zr site.
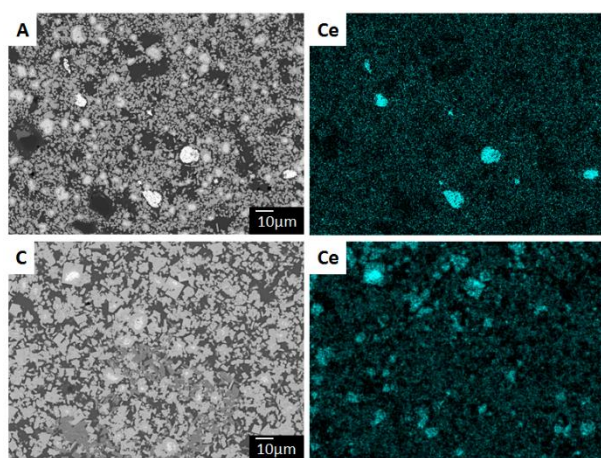
Figure 2. SEM-EDX for samples A and C showing the Ce distribution. The Ce signal is deficient in the glass phase and shows the formation of the secondary Ce-bearing perovskite phase when targeting Zr^{4+} substitution (Figure taken from [10]).

Ce L_3 XANES data (data not shown) was collected to study the distribution of Ce oxidation states in the samples. Sample A retained the highest fraction of Ce^{4+} signal. The XANES data consisted of signals indicative of both Ce^{3+} and Ce^{4+} for all samples. The lack of perovskite in sample A and presence of unincorporated CeO_2 confirms the stronger Ce^{4+} signal in the XANES compared to samples B and C. Samples B and C have less CeO_2 present and a clear reduction of Ce to Ce^{3+} shown

by its incorporation in the perovskite phase, thus increasing the Ce^{3+} signal in the XANES data.
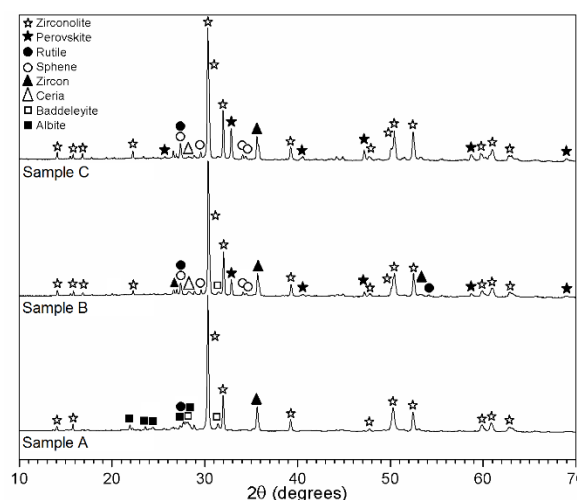
Figure 1. XRD plot showing zirconolite as the major crystalline phase for all samples and an increase in relative intensity of the perovskite phase when targeting Zr substitution (Figure taken from [10]).

Discussion

As a non-active analogue, Ce has similar ionic radii to Pu and can be incorporated onto similar lattice sites. The zirconolite-2M structure is monoclinic with Ca^{2+} ions in 8-fold coordination and Zr^{4+} ions in 7-fold coordination. Their effective ionic radii are 1.12 Å and 0.78 Å, respectively [11]. The ionic radii of Ce, Pu, Zr and Ca in different coordination environments are summarised in Table 2.

The incorporation of Ce into sample A did not result in perovskite formation. When we consider ionic radii (Table 2), Ce^{4+} in 8-fold coordination is smaller than the Ca site therefore is a favourable substitution. Although sample A had the strongest Ce^{4+} XANES signal, Ce^{3+} signal was also observed. The ionic radii for Ce^{3+} is very closely matched to the Ca site and can be assumed to have also substituted onto the Ca site.

In comparison, samples B and C each have significant perovskite formation. Ce^{4+} has an ionic radii ca. 18% bigger than the Zr lattice site. This means Ce^{4+} substitution for Zr is less favourable than for Ca on the grounds of ionic radii. The substitution of Ce^{3+} for Zr however, is very unfavourable due to a size mismatch of ca. 35%. Concurrently, Ce^{3+} is known to facilitate perovskite formation, which is in agreement with the equal ionic size of Ce^{3+} and Ca^{2+} in 12-fold coordination, as in the perovskite structure. As such it is highly favourable for perovskite to incorporate Ce^{3+}, as oppsed to its substitution for Zr in zirconolite. The formation of a Ce-bearing perovskite phase when targeting Ce^{4+} substitution for Zr has previously been reported by Begg *et al.* whom also concluded the limited solubility of Ce

for Zr compared to the Ca site within the zirconolite-2M structure [12].

Ce is known to have limitations as a Pu analogue due to its redox potential. Pu does not reduce as readily as Ce thus is expected to be incorporated into zirconolite as Pu^{4+}. Begg *et al.* reported successful Pu substitution for Zr within zirconolite that resulted in a structural change to pyrochlore with increasing levels of substitution [13]. At higher Pu concentrations the formation of perovskite as a minor phase was seen. When annealed under reducing conditions the Pu was reduced to Pu^{3+} and the zirconolite was destabilised, thus increasing perovskite formation. So far our results are in agreement with those reported by Begg *et al.* and prove promising for Pu incorporation under controlled conditions.

Table 2: Ionic radii of different ions with respect to coordination number and oxidation state. Data highlighted with an asterisk are estimated based on linear interpolation.

Ion	Ionic Radii (Å)			
	12-fold	8-fold	7-fold	6-fold
Ce^{4+}	1.14	0.97	0.92*	0.87
Ce^{3+}	1.34	1.14	1.07	1.01
Pu^{4+}	-	0.96	0.91*	0.86
Ca^{2+}	1.34	1.12	1.06	1.00
Zr^{4+}	-	0.84	0.78	0.72

Conclusions

Although complete waste digestion was not achieved, Ce incorporation into the ceramic phase(s) was shown to be preferential over incorporation into the glass. The formation of a Ce-bearing perovskite phase has been justified through ionic radii arguments. Further investigations looking at the effect of redox control and oxygen fugacity on the oxidation state of Ce and incorporation into zirconolite is underway.

Acknowledgements

References

[1] Nuclear Decommissioning Authority (NDA), *Progress on approaches to the management of separated plutonium - Position paper - v1.0*. Nuclear Decommissioning Authority, 2014.

[2] N. C. Hyatt, "Plutonium management policy in the United Kingdom: The need for a dual track strategy," *Energy Policy*, **101** 303–309 (2017).

[3] Nuclear Decommissioning Authority, *Conditioning of Plutonium Residues by Hot Isostatic Pressing and Options for packaging and Disposal (pre-conceptual stage) Summary of Assessment Report*. 2009.

[4] C.R. Scales, E.R. Maddrell, N. Gawthorpe, B.D. Begg, S. Moricca, R.A. Day, and M.A. Stewart, "Demonstrating a Glass Ceramic route for the Immobilisation of Plutonium containing Wastes and Residues on the Sellafield Site," *Proc. WM*, **6** (2006).

[5] J. W. Hobbs, *A programme to immobilise plutonium residues at Sellafield*, (2012).

[6] R.A. Day, S. Moricca, M.W.A. Stewart, B.D. Begg, E.R. Maddrell, C.R. Scales, and N. Gawthorpe, "Technical Demonstration of Zirconolite Glass-Ceramics Processed in a Hot Isostatic Press: An Option for Immobilisation of Actinide Containing Residues at Sellafield;" in ICEM, Scotland, UK, 2005.

[7] S. Moricca, C. Orcutt, M.W.A. Stewart, W. Bermudez, E.R. Vance, T. Eddowes, R. Persaud, and D. Taylor, "Hot isostatic pressing of synroc for nuclear waste disposal.;" in *Adv. Powder Metall. Part. Mater. - Part 4*. Nashville, Tennessee, 2012.

[8] F. Bellatreccia, G. Della Ventura, E. Caprilli, C.T. Williams, and G.C. Parodi, "Crystal-chemistry of zirconolite and calzirtite from Jacupiranga, Sao Paulo (Brazil)," *Mineral. Mag.*, **63** [5] 649–660 (1999).

[9] A. E. Ringwood, S. E. Kesson, N. G. Ware, W. Hibberson, and A. Major, "Immobilisation of high level nuclear reactor wastes in SYNROC," *Nature*, **278** 219–223 (1979).

[10] S.M. Thornber, M.C. Stennett, and N.C. Hyatt, "Investigation of Ce incorporation in zirconolite glass-ceramics for UK plutonium disposition," *MRS Adv.*, 1–6 (2017).

[11] R. D. Shannon, "Revised effective ionic radii and systematic studies of interatomic distances in halides and chalcogenides," *Acta Crystallogr.*, **A32** 751–767 (1976).

[12] B. D. Begg and E. R. Vance, "The incorporation of cerium in zirconolite," *Mater. Res. Soc.*, **465** 333–340 (1997).

[13] B.D. Begg, R.A. Day, and A. Brownscombe, "Structural Effect of Pu Substitutions on the Zr-Site in Zirconolite," *MRS Proc.*, **663** (2000).

Understanding radionuclide interactions with cementitious materials for radioactive waste management

Antonia S. Yorkshire*[1], John L. Provis[1], Sarah A. Kearney[1], Neil C. Hyatt[1], Mike Angus[2], Robin Orr[2] and Claire L. Corkhill[1]

*Correspondence: asyorkshire1@sheffield.ac.uk

[1]*University of Sheffield, NucleUS Immobilisation Science Laboratory, Department of Materials Science & Engineering, Sheffield, UK*
[2]*The National Nuclear Laboratory, Workington, Cumbria, UK*

Abstract

In the UK, the current method for immobilisation of intermediate level waste (ILW) streams is encapsulation in Portland cement grouts. Cement hydrate phases, which form during the hydration of cement clinker and pozzolanic additives, are capable of binding radionuclides. One of the key issues associated with cement encapsulation of ILW is the uncertainty of radionuclide fate within the cementitious matrix over the long timescales and varying local conditions of extended interim storage and geological disposal. Discussed here are the syntheses of singular cement hydrate minerals including Calcium-Silicate-Hydrate (CSH), hydrotalcite ($Mg_6Al_2CO_3(OH)_{16}.4H_2O$) and ettringite ($Ca_6(Al_2O_6)(SO_4)_3.32H_2O$). These minerals have been exposed to solutions of U, Tc, Ce and Pu to develop an understanding of the mechanisms of uptake and incorporation into simplified systems for those Portland cement systems used for ILW. These experiments form the focus of longer term sorption / de-sorption studies to observe long-term radionuclide incorporation cements. The results of uranium incorporation in CSH are discussed in detail, as are the results from experiments performed at the National Nuclear Laboratory, where particles of PuO$_2$ were encapsulated in Portland cement blends that are used in the encapsulation of ILW, including Plutonium Containing Material (PCM).

Introduction

Intermediate level waste (ILW) in the UK is encapsulated and immobilised using cement grouts comprised of Portland cement clinker and pozzolanic additives such as blast-furnace slag (BFS) and fly ash (FA). On addition of water, these materials undergo hydration reactions that form hardened cement minerals over time.

Radionuclides in ILW, such as U, Tc, and Pu, are bound by cementitious encapsulation during interim storage, with longer term geological disposal planned for tens of thousands of years. Plutonium contaminated material (PCM) waste is a sub-category of ILW that includes materials contaminated with plutonium, in addition to other actinides associated with plutonium decay.[1] The current method for PCM storage is super-compaction and encapsulation in steel drums that are infilled with a FA / Portland cement grout,[2,3] whereas a range of other ILW wastes are treated using a BFS / Portland cement grout.

Calcium-Silicate-Hydrate (CSH) is the main component of Portland cements; making up ~50 wt% of a hardened cement paste. The structure of CSH is based on a disordered form of the mineral tobermorite ($Ca_5Si_6O_{16}(OH)_2\cdot4H_2O$).[4,5] Calcium oxide components also hydrate in water to precipitate portlandite (the mineral form of $Ca(OH)_2$), additionally making up a significant percentage of a Portland cement. Minor hydrate phases such as the sulfur-containing minerals ettringite ($Ca_6(Al_2O_6)(SO_4)_3.32H_2O$) and monosulfate ($Ca_4(Al_2O_6)(SO_4).12H_2O$) form on a less extensive scale. However, the potential for such minerals to retain radionuclides cannot be overlooked.[6] The formation of some hydrate phases is dependent on the composition of the unhydrated pozzolanic additive; for example, hydrotalcite ($Mg_6Al_2CO_3(OH)_{16}.4H_2O$) is a magnesium rich mineral that forms in BFS / Portland cement grouts.

The retention of radionuclides by such cement hydrate minerals is not yet fully understood, especially on longer timescales and with varying conditions. Discussed here is the work aiming to underpin the mechanisms of radionuclide uptake and incorporation by cements, which includes:

1. Synthesis and characterisation of individual cement minerals including CSH, hydrotalcite and ettringite for use in sorption studies.

2. Observing the structural changes in mineral phases that have been contacted with aqueous solutions of radionuclides, such as CSH with $UO_2(NO_3)_2(H_2O)_2$.

3. Characterisation of Portland cement grouts blended with PuO_2 particles at the National Nuclear Laboratory (NNL) cured for ~1 year to investigate Pu-cement hydrate mineral interactions during hydration.

Methodology Details

Mineral syntheses

All procedures described here were conducted under an inert N_2 atmosphere unless otherwise stated.

For the synthesis of the CSH phase, CaO and SiO_2 at 1:1 wt were mixed in deionised water at w/s = 15 to achieve a theoretical Ca/Si molar ratio of 1.06. The resulting slurry was agitated on a rotary shaker at 40 rpm for 120 hrs to prevent solidification / gel-formation. The solid was filtered gravitationally through a Whatman-542-ashless filter paper and left to dry for 24 hrs. After grinding into a fine powder, a sample of the solid was mounted onto a low background Si X-ray diffraction (XRD) sample holder and covered with Kapton tape to minimise CO_2 exposure outside of the N_2 chamber. Powder XRD was measured from 5-70 ° 2θ with a step size of 0.02 ° and counting time of 2 s.

Use of Kapton tape to minimise CO_2 exposure resulted in a large background interference reading on the XRD diffraction pattern from 5-28 ° 2θ. A scan of the Kapton tape alone was produced, and the signal subtracted from the original CSH measurement.

Additionally, a co-precipitation method was adopted to observe uranium uptake into the CSH structure. The 1:1 $CaO:SiO_2$ slurry was reproduced using a 0.1 M solution of $UO_2(NO_3)_2(H_2O)_2$ in replacement of deionised water. After a 10 day agitation at 40 rpm under N_2, the slurry was filtered gravitationally through a Whatman-542-ashless filter paper and left to dry for 24 hrs. The resulting powder was yellow in colour and the solution colourless. The procedure for XRD analysis of the CSH sample was also followed in this case.

The yellow powder was retained for thermal treatment to induce crystallisation of the material prior to further analysis.

A pH controlled solution mixing method was adopted to precipitate a layered double hydroxide for the synthesis of hydrotalcite, similar to that used by *Aimoz et. al. (2012)*.[6] A 0.5 M $Mg(NO_3)_3$ / 0.5 M $Al(NO_3)_3$ solution was added dropwise to a 1 M Na_2CO_3 solution. The pH was maintained at ≥10.0 with additions of 1 M NaOH, where necessary, to avoid precipitation of aluminium hydroxides (pH ~4-5). The precipitated solid was filtered gravitationally using a Whatman-542-ashless filter paper, washed with ≤10 mL deionised water and left to dry for 24 hrs. For XRD analysis the

use of Kapton tape was not considered a necessary practice and the solid was removed from the N_2 atmosphere after synthesis. The solid was ground into a fine powder and an XRD pattern was measured from 5-90 ° 2θ with a step size of 0.02 ° and counting time of 1 s.

Ettringite synthesis was first attempted under ambient conditions to determine if the mineral synthesis was achievable using the current method. $Al_2(SO_4)_3.16H_2O$ was dissolved in deionised water at 90 °C. CaO was added to achieve w/s = 15 and a $Al_2(SO_4)_3:CaO$ molar ratio of ~1:1. CaO **did not** appear to dissolve. The mixture was magnetically stirred at 90 °C for 1 h. After this time, two solid phases appeared to be present; an agglomerated solid and a solid dispersed within the solution. The mixture was left to cool to ambient temperature and the solids were collected by vacuum filtration through a Whatman-542-ashless filter paper, washed with ≤10 mL deionised water and dried at 35 °C for 1 hr. For powder XRD, the solid(s) were ground to a fine powder and measurements taken from 5-60 ° 2θ with a step size of 0.02 ° and counting time of 0.5 s.

Portland cement PuO_2 blends

Portland cement blends containing Magnox PuO_2 particles were prepared at the NNL Central Lab facility at the Sellafield Ltd. site and cured for ~1 year. The OPC and BFS used was of UK nuclear specification sourced from Hanson cement as Ketton coarse ground OPC^a and Scunthorpe $GGBS^b$ blended with calumite (70:30), respectively. PFA^c was also of UK nuclear specification supplied by the CEMEX Drax plant. PuO_2 particles were typically 20-40 μm in diameter with a measured specific surface area of 11.8 $m^2 g^{-1}$.

The characterisation of 3.44:1 BFS/OPC and 3:1 PFA/OPC cement blends containing 0.5 wt % PuO_2 at w/s ratios of 0.35 and 0.43 respectively are discussed in the next section, including a comparison to non-active control samples.

[a]OPC = Ordinary Portland cement; [b]GGBS = Ground granulated blast-furnace slag; [c]PFA = Pulverised fuel ash.

Results and Discussion

Mineral characterisation

The following is a discussion of the analytical results obtained for the characterisation of synthetic mineral samples.

XRD: CSH

Figure 1 shows the XRD pattern (with background subtraction) for the CSH phase. The peaks identified correspond well with the diffraction pattern for CSH observed by *Rodriguez et. al. (2017)*. However due to the poor signal at earlier 2θ measurements, peaks at ~7.1° (the basal reflection) and ~16.2° coinciding with

the remainder of the diffraction pattern are not readily identifiable. The most intense peak for CSH however is observed at ~29°, which is seen here.[7]
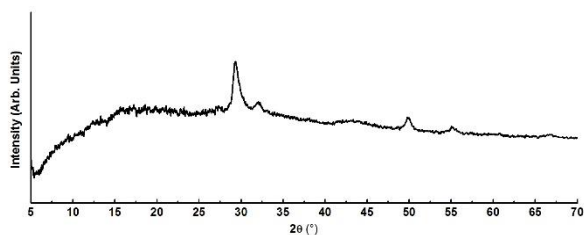

Figure 1 XRD pattern for the synthetic CSH phase with Kapton background trace subtracted from the original measurement.

CSH synthesised in contact with a $UO_2(NO_3)_2(H_2O)_2$ solution did not yield a significantly different XRD pattern (**Figure 2**) to that shown for CSH. The same peaks were present with lower relative intensity; however, these were still identifiable as CSH only. As the solid precipitated was yellow in colour, and the solution remaining after filtration turned from yellow to colourless, this suggests the formation of a precipitated phase containing uranium that is yet to be identified.
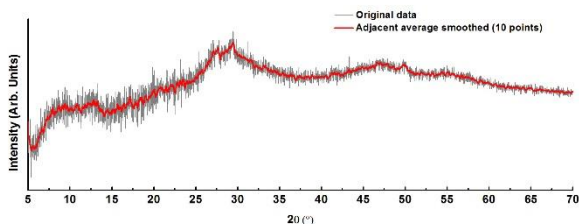
Figure 2 XRD pattern for the CSH phase synthesised with a 0.1 M $UO_2(NO_3)_2(H_2O)_2$ solution with Kapton background trace subtracted from the original measurement (grey). The data was smoothed using an adjacent average of 10 points (red).

The CSH-uranium mixture could potentially form a uranophane-type $(Ca(UO_2)_2(SiO_3OH)_2 \cdot 5H_2O)$ mineral phase (among other possible uranium, calcium and silicon bearing phases).[8] Uranophane has a U/Si ratio of 1, however the material synthesised in this study has a theoretical U/Si ratio of 0.18 (based on 100% precipitation of uranium from solution). This suggests that if crystallites of uranophane-type phases are forming (for example), the resolution limitations of the XRD instrument used in this study means identification of this phase is not possible. Verification of the phase(s) will eventually be carried out using high resolution XRD on a synchrotron beamline.

XRD: Hydrotalcite

Hydrotalcite powder previously obtained from Sigma Aldrich was used as a standard comparison for the XRD data of the synthetic hydrotalcite in this study. **Figure 3** shows both XRD patterns, showing good agreement between the two materials. The peaks for the synthetic material are notably broader, suggesting a nano-crystalline material.
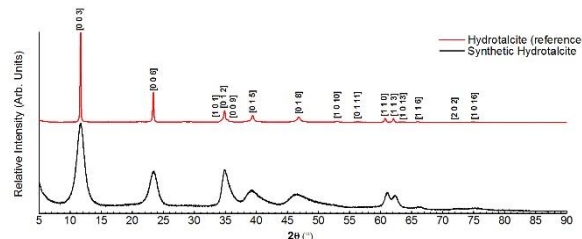
Figure 3 XRD pattern for the synthetic hydrotalcite phase (bottom, black) with the known hydrotalcite reference pattern (top, red). Miller indices are shown.

XRD: Ettringite

From the XRD pattern for the attempted synthesis of ettringite (**Figure 4**), two separate phases have been identified as ettringite and gypsum $(CaSO_4.2H_2O)$. This is likely the reason for the observation of two separate solid phases forming during synthesis. There are also peaks present that suggest the formation of a small amount of the mineral kuzelite; a monosulfate phase.
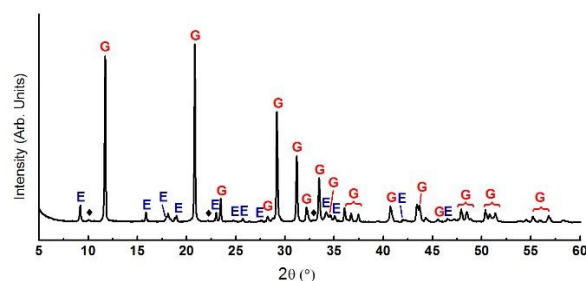
Figure 4 XRD pattern for synthetic ettringite phase with gypsum present. E = ettringite (blue); G = gypsum (red); ♦ = monosulfate phase.

Gypsum exhibits retrograde solubility, i.e. the solubility decreases with increased temperature. Despite the acidic pH generated by the $Al_2(SO_4)_3$ solution, Ca ions present from the CaO source precipitate as gypsum at the higher synthesis temperature of 90 °C. This makes the synthesis of a pure ettringite phase particularly difficult using a wet chemistry method. An alternative method for preparing this material is currently under investigation.

Particle size distribution: CSH and hydrotalcite

The synthetic CSH and hydrotalcite phases were analysed by particle size distribution (PSD) analysis. Due to agglomeration of the powders, a wet dispersion technique was used. The dispersants used were isopropanol and deionised water for CSH and hydrotalcite, respectively. The powders were sonicated in their respective dispersants for 5 mins prior to analysis, to minimise agglomerates. PSD measurements were taken for 5 s and averaged over 10 measurements. The results are shown in **Figure 5**.
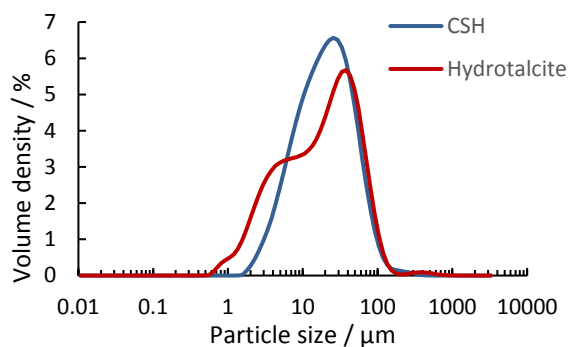
Figure 5 PSD results for the CSH (blue) and hydrotalcite (red) synthetic phases.

For both phases the majority of particles lie within the 1-100 μm range. CSH shows a near Gaussian particle distribution, whereas hydrotalcite particle distribution is more varied.

Portland cement PuO_2 blends

PuO_2 cement data will not be discussed here as analysis is ongoing. To date, active samples have been finely ground and thermogravimetric - mass spectrometry (TG-MS) analysis is ongoing. XRD and preparation of scanning electron microscopy / energy dispersive X-ray (SEM/EDX) analysis samples is due to commence within the coming weeks.

At the MIDAS facility at the University of Sheffield, we are currently undergoing analysis of non-active control samples; XRD and TG-MS have been performed on the non-active analogue cement samples for comparison with PuO_2 samples at a later date.

Conclusions and Future Work

Conclusions

The data presented in this study suggests the successful synthesis of the CSH and hydrotalcite phases, relevant to Portland cement grouts. Ettringite was also synthesised, however the solubility behaviour of gypsum provides difficulty in isolating this particular sulfate phase using wet chemistry methods.

Future work

In order to synthesise a pure sulfate phase, sintering methods used previously in the literature will be adopted to attempt thermal synthesis of ettringite.[9]

The uranium-CSH phase will also be thermally treated to induce potential crystallisation of unidentified uranium phases present. Further to this, we aim to carry out high resolution powder XRD using a synchrotron facility. Further sorption and incorporation studies will soon commence, using Tc, Ce (as a Pu surrogate) and Pu.

Acknowledgements

References

1. *Introduction to plutonium contaminated material (PCM) issues*, NDA Waste & Nuclear Materials Department, Position Paper W&NM/PP/008, (2008).

2. Egan, M., Paulley, A. & Towler, G. *Treatment of Plutonium Contaminated Material at Sellafield*, Report QRS-1372A-1, Sellafield Ltd., (2008).

3. Aggarwal, S., Angus, M. J. & Ketchen, J. *Sorption of radionuclides onto specific mineral phases present in repository cements* AEA Report NSS/R312, Windscale, Cumbria, (2000).

4. Yu, P., Kirkpatrick, R. J., Poe, B., McMillan, P. F. & Cong, X. "Structure of Calcium Silicate Hydrate (C-S-H): Near-, Mid-, and Far-Infrared Spectroscopy." *J. Am. Ceram. Soc.* **82,** 742–748 (1999).

5. Myers, R.J., Bernal, S.A., San Nicolas, R., & Provis, J.L. "Generalized Structural Description of Calcium–Sodium Aluminosilicate Hydrate Gels: The Cross-Linked Substituted Tobermorite Model." *Langmuir* **29,** 5294–5306 (2013).

6. Aimoz, L., Wieland, E., Vespa, M. & Churakov, S. V. "Structural Insight into Iodide Uptake by AFm Phases." *Environ. Sci. Technol.* **46,** 3874–3881 (2012).

7. Rodriguez, E. T., Garbev, K., Merz, D., Black, L. & Richardson, I. G. Cement and Concrete Research Thermal stability of C-S-H phases and applicability of Richardson and Groves ' and Richardson C-(A)-S-H (I) models to synthetic C-S-H. *Cem. Concr. Res.* **93,** 45–56 (2017).

8. Harfouche, M., Wieland, E., Dähn, R., Fujita, T., Tits, J., Kunz, D., & Tsukamoto, M. "EXAFS study of U(VI) uptake by calcium silicate hydrates." *J.Colloid Interface Sci.* **303,** 195–204 (2006).

9. Matschei, T., Lothenbach, B. & Glasser, F. P. "The AFm phase in Portland cement." *Cem. Concr. Res.* **37,** 118–130 (2007).

Switching on Ion Exchange in Metal Germanates

R.George*[1] and Dr J.A.Hriljac[1]

*Correspondence: RXG034@bham.ac.uk

[1] School of Chemistry, University of Birmingham, Edgbaston, Birmingham, UK B15 2TT.

Abstract

The synthesis of materials for ion exchange and subsequent disposal of radionuclides will be explored in this work. The successful synthesis of the germanium form of the natural mineral umbite ($K_2ZrSi_3O_9.H_2O$) and subsequent ion exchange results shows both caesium and strontium uptake by Ge-Zr-umbite ($K_2ZrGe_3O_9.H_2O$) but at low levels. This is substantially improved by chemical modification of the umbite structure with the incorporation of up to 30% Nb for Zr at the octahedral site. Further doping results in mixed phases with the formation of umbite and another interesting pharmacosiderite phase ($HK_3Ge_7O_{16}.4H_2O$), this phase also shows potentially interesting ion exchange properties.

Introduction

The synthesis of novel ion exchange materials for uses in nuclear waste management and environmental remediation is a key area of research. Much effort is being placed in designing materials with high selectivity and ion exchange capacity, especially in relation to caesium and strontium. The established methodology for the removal of these radionuclides in the UK involves the use of a natural zeolite material clinoptilolite[1], but future waste streams and POCO activities may be better tackled with other systems.

One family of materials which have been widely investigated are mixed octahedral and tetrahedral framework metal silicates, due to potentially interesting ion exchange properties and better chemical and radiation stability than aluminosilicate zeolites. Altering the composition of these metal silicates by substituting in different metal ions affects the properties, making it a great tool for modification of the product [2]. Materials have been synthesised with a range of metals such as Zr [3], Sn [4] and Ti [5] in the silicate framework. This allows for fine tuning of the materials properties by either total substitution or partial doping into the structure. It has been of great interest to introduce a wide range of different metal atoms into the framework in order to develop materials that can be of use industrially as cation-exchangers.

One of these types of materials, a natural zirconosilicate mineral umbite ($K_2ZrSi_3O_9.H_2O$) has been synthesised with both Sn and Ti as the octahedral component, for which the ion exchange properties have been explored in the literature [6]. Very little work has been done focusing on the variation of the tetrahedral component of these mixed OT materials. A germanate derivative, $K_2ZrGe_3O_9.H_2O$, has been reported in the literature [7]. The resulting unit cell expansion from the replacement of silicon for germanium could make it a good candidate for the uptake of large cations. However the potential caesium and strontium uptake capabilities were never investigated by the original authors.

The focus of this work will be looking at the ion exchange properties of the parent zirconogermanate material and subsequent chemical modifications to alter exchange properties.

Methodology Details

Synthesis of $K_2ZrGe_3O_9.H_2O$

The zirconogermanate umbite was prepared by mixing 1.52g of germanium dioxide (Gerald wise and co) and1.66g of potassium hydroxide (85%, Sigma) in 20ml of deionised water. To the stirring mixture 1.50g of zirconyl chloride octahydrate (98%, Sigma) was added until dissolved. The mixture is then stirred for a further hour to allow it to homogenise.

The resulting mixture was then transferred to a 45ml Teflon liner and placed in a Parr autoclave at 200°C for 24 hours. The resulting product was then filtered and washed in deionised water before being dried overnight at 60°C.

Synthesis of $K_{2-x}Zr_{1-x}Nb_xGe_3O_9.H_2O$
Typical synthesis for x = 0.3

The zirconogermanate umbite was prepared by mixing 0.76g of germanium dioxide (Gerald wise and co) and 0.85g of potassium hydroxide (85%, Sigma) in 10ml of deionised water. To the stirring mixture 0.19g of

niobium chloride (99%, Sigma) was added with 0.52g of zirconyl chloride octahydrate (98%, Sigma). The mixture is then stirred for a further hour to allow it to homogenise. The resulting mixture was then transferred to a 45ml Teflon liner and placed in a Parr autoclave at 200°C for 24 hours. The resulting product was then filtered and washed in deionised water before being dried overnight at 60°C.

Any compounds synthesised were analysed using Powder X-ray diffraction (XRD) on a Bruker D8 Advance using a Cu Kα source at room temperature. Phase matching was performed using the EVA software from known databases.

<u>Ion exchange studies</u>
0.1M solutions of strontium nitrate (98%, Sigma) or caesium nitrate (99.8%, Sigma) were added to 0.2-0.5g of sample with an overall w/v ratio of 1:100. This was then shaken for 24 hours before being filtered, washed and dried overnight at 60°C. Elemental analysis was undertaken using X-ray fluorescence (XRF) on a Bruker S8 Tiger with the samples prepared as either a loose powder or pressed pellet.

Results and Discussion

The synthesis of the zirconogermanate umbite, $K_2ZrGe_3O_9.H_2O$, first reported by Plevert et al [7], would yield around 0.3g of isolated product. Synthesis optimisation allowed for the production of much larger batches of material (ca. 2.0g sample at ca. 80% yield) in 24 hours. Subsequent ion exchange tests for caesium and strontium show very limited uptake of both cations, as seen in table 1.

Table 1: Ion exchange data for the parent zirconogermanate umbite phase.

Element	Molar ratio	Molar ratio	Molar ratio
Ge	1	1	1
Zr	0.44	0.37	0.48
K	0.62	0.44	0.54
Sr	-	-	0.01
Cs	-	0.02	-

Varying the tetrahedral component of the umbite structure in this case reduced the ion exchange properties of the material relative to the zirconosilicate[8]. The material shows a high selectivity towards potassium with mixed caesium/potassium ion exchange tests reducing the Cs uptake by half; this may explain the low cation uptake. However the material

shows no sodium uptake despite using forcing reflux conditions and concentrated sodium chloride solutions.

The low caesium uptake provided an opportunity to chemically modify the zirconogermanate umbite to improve ion exchange properties. It was hoped that by doping into the octahedral site by replacing Nb^{5+} for Zr^{4+}, it would possible to lose some framework potassium whilst maintaining the umbite structure. The incorporation of Nb into the umbite structure was explored with potential doping of up to 30% Nb for Zr as seen in figure 1.
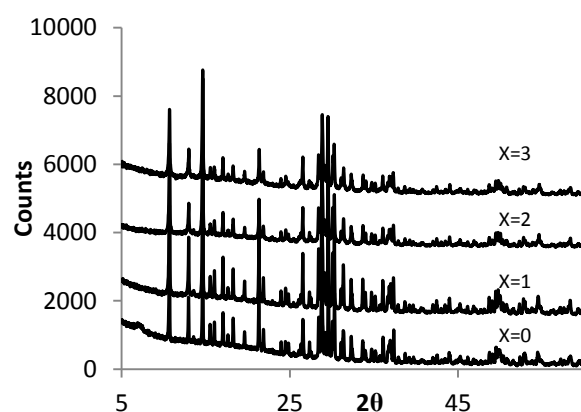
Figure 1: Powder X-ray diffraction patterns for $K_{2-x}Zr_{1-x}Nb_xGe3O9.H_2O$.

XRD showed very little difference in the patterns between the doping levels. It is of note that despite some small loss of crystallinity when comparing x=0.3 and x=0, the umbite structure would appear to readily accommodate this amount of niobium doping. Further niobium doping beyond this point perturbs the formation of phase pure umbite. At levels above 30% niobium doping another germanate phase is formed as well as umbite, a pharmacosiderite phase of composition $HK_3Ge_7O_{16}.4H_2O$. XRF analysis complimented the XRD results as it showed niobium present, as seen in table 2.

Table 2: Nb doped XRF data.

	10% Nb	20% Nb	30%Nb
Elements	Molar ratio	Molar ratio	Molar ratio
Ge	1	1	1
Zr	0.39	0.35	0.33
K	0.62	0.65	0.68
Nb	0.04	0.08	0.12

However despite reasonable ratio's between Zr:Nb:Ge, a decrease in potassium content was not observed with increasing niobium content. As the XRD patterns

were phase pure and no crystalline niobium containing phases were observed, it was possible that niobium may be in an amorphous phase. However subsequent ion exchange tests for caesium showed a much increased exchange capacity as seen in table 3.

Table 3: Cs exchange data for Nb doped umbites.

	10% Nb	20% Nb	30% Nb
Elements	Molar ratio	Molar ratio	Molar ratio
Ge	1	1	1
Cs	0.29	0.37	0.63
Zr	0.37	0.33	0.30
K	0.38	0.33	0.25
Nb	0.04	0.08	0.11

A major increase in caesium uptake is observed in all doped samples relative to the parent material, with 30% Nb showing the highest uptake. With the loss of some of the interpore potassium, a potential reason for the improvement of exchange properties is the presence of defects in the pore system. This may facilitate better mobility of the entering cations and hence improve ion exchange properties. The niobium doped umbites, like the parent material, show no sodium uptake which is a benefit when considering selectivity.

Other variations of the octahedral site attempted included total substitution of zirconium for tin and titanium, which have been observed in the silicate umbite. In the case of the germanate umbite, tin and titanium substitution have proven to be unsuccessful, with the formation of the $HK_3Ge_7O_{16}.4H_2O$ phase.

Conclusions and Future Work

Successful synthesis optimisation of a zirconogermate umbite, $K_2ZrGe_3O_9.H_2O$, allowed for the investigation into the material ion exchange properties. The parent materials low caesium uptake can be improved by doping niobium into the structure up to 30% Nb for Zr, with little impact on the sample quality. Further attempts to vary the octahedral component prevent the formation of the umbite phase and instead promote the formation of a pharmacosiderite phase.

Further work will focus on the synthesis and optimisation of the pharmacosiderite phase; it has been reported in the literature [9] to show interesting ion exchange properties and this will be further explored. Exploring the sodium exchange properties of the umbite phase will also be focused on, with the hope of gaining an understanding as to why the germanate shows no sodium uptake.

References

[1] A.Dyer, A.Chimedtsogzol, L.Campbell and C.Williams, *Micropor.Mesopo. Mat*, 2006, **95**, 172-175.

[2] S.D.Sharma, K.G.Varshney and S.C.Mojumdar, *J Therm Anal Calorim,*2012,**108**, 843-850.

[3] S.Ferdov,U.Kolitsch,O.Petrov,V.Kostov-Kytin,C.Lengauer and E.Tillmanns, *Micropor.Mesopor.Mat*, 2005, **81,** 79–86.

[4] F.Pan, X.Lu, Y.Wang, S.Chen, T.Wang and Y.Yan, *Micropor.Mesopor.Mat,*2014, **184** 134–140.

[5] Y.Zou, R.Wang, Z.Zhang, G.Li and S.Qiu, *Micropor.Mesopor.Mat, 2013*, **182,** 178–184.

[6] C.S.Fewox,A.Clearfield and A.J.Celestian, *Inorg. Chem*,2011, **50**, 3596–3604

[7] J.Plevert, R.Sanchez-Smith, T.M.Gentz, H.Li, T.L.Groy, O.M.Yaghi and M.O'Keeffe, *Inorg.Chem*, 2003,**42,** 5954-5959.

[8] D.M.Poojary, A.I.Bortun, L.N.Burton and A.Clearfield, *Inorg. Chem.* 1997,**36,** 3072-3079.

[9] E.A.Behrens, D.M.Poojary and A.Clearfield, *Chem. Mater .* 1998, **10,** 959-967.

Thermal conversion of Sr-loaded IONSIV

G.Day*[1], T.Chen[1], J.A. Hriljac[1] and Y. Guo[2]

*Email: gxd988@bham.ac.uk

[1] University of Birmingham, Birmingham, UK
[2] Materials and Surface Science Institute, University of Limerick, Sreelane, Limerick, Ireland

Abstract

The separation of radioactive Cs and Sr from waste streams has been an important process for the last 40/50 years. Many exchangers have been used or 'spent' and now await final conditioning and storage. In this study we focus on the consolidation of spent Sr-IONSIV R9120-B (formally IE-911), a commercial exchanger developed and engineered by Honeywell UOP, via hot isostatic pressing (HIPing).

Introduction

^{137}Cs and ^{90}Sr are two of the more problematic radionuclides produced from the fission process. They are both primary heat generators with half-life's of around 30 years. Cs is a strong beta-gamma emitter and Sr a beta emitter.[1] Thus, Cs and Sr are usually removed from waste streams using inorganic ion exchangers such as Cs-Treat (hexacyanoferrate), Sr-Treat (titanium oxide exchanger), clinoptilolite (natural zeolites) and IONSIV (Crystalline Silicotitanates). [2–6] Inorganic exchangers are usually employed on account of their high selectivity, effectiveness in a wide pH range, radiation and thermal resistance and usually compatibility to be converted into a final waste form. [3,7,8,1,9]
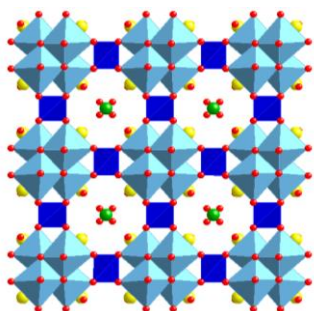
Figure 1. Crystal Structure of CST [10]

Crystalline Silicotitanate (CST) with a formula $Na_2Ti_2O_3(SiO_4)\cdot 2H_2O$, is an ion exchanger developed by the Sandia National Laboratory and Texas A&M University.[4,5,7] CST crystallises in a tetragonal system with space group $P4_2/mcm$. It consists of Ti_4O_{16} cubane units that are linked by corner sharing SiO_4 tetrahedra, creating a zeolite-like open framework. This framework contains pores which are occupied with exchangeable cations **(figure 1)**. Universal Oil Products (UOP) and Sandia in a joint collaboration commercialised an optimised version of CST, labelled as IONSIV R9120-B, an engineered form of Niobium doped CST. Despite IONSIV being used primarily for Cs clean up, it is also selective for Sr, particularly in highly alkaline media.

As discussed, inorganic exchangers require certain properties in order to be used for radioisotope removal. However the nuclear industry has not previously been concerned with what do with the exchanger once it has been used. IONSIV has been used (or 'spent') all around the globe and currently the plan in the UK is to place spent IONSIV in steel drums and fill with cement. Here we suggest a different final immobilisation technique, hot isostatic pressing (HIPing).

HIPing was first used in the 1950s for diffusion bonding of nuclear fuels but it has since found applications for nuclear waste consolidation. [11] The basic process involves loading the waste (spent IONSIV) into a can (mild steel in this study) and then applying heat and pressure (via inert gas) on the can after it is hermetically sealed **(figure 2).** HIPing is carried out in a closed system, therefore making it ideal for immobilising volatile wastes such as Cs. Furthermore there is a large volume reduction associated with HIPing which could be hugely advantageous if intended for final storage in geological disposal facility (GDF).

Figure 2. HIP unit(left). HIP cans (right)

A recent study demonstrated that Cs-loaded R9120-B could be immobilised into a robust waste form through HIPing.[12,13] The major Cs waste form produced was identified as $Cs_2TiNb_6O_{18}$. This phase demonstrated exceptional leach rates which compared well to other ceramic Cs waste forms such as hollandite.[12] In this

study a series of Sr and mixed Cs/Sr loaded IONSIV samples have been HIPed and the wasteforms subsequently analysed and tested.

Methodology Details

Characterisation of materials

HIPing was carried using a EPSI Lab HIP unit at 1100°C, 150 MPa for 2 hours in an argon atmosphere. X-ray diffraction (XRD) experiments were carried out on a Bruker D8 Diffractometer in transmission mode using a Cu kα1 1.5406 X-ray source. Wavelength dispersive X-ray fluorescence spectroscopy was carried out using a Bruker S8 Tiger (WDXRF). Scanning electron microscopy (SEM) studies were performed using a Philips XL30 ESEM-FEG with an Oxford Inca 300 EDX system operating at 10 kV. Transmission electron microscopy (TEM) experiments were carried out using JEOL JEM-2100F equipped with a EDAX Genesis XM 4 system 60, a double tilt holder and SEI/BSE detector operating at 200 kV in STEM mode. MCC-1 (Matrix – B, 28 days, 90°C) were carried out on monoliths cut from the mild steel HIP cans.

Results and Discussion

Initial IONSIV samples were exchanged to levels of 1.5 and 3 wt % Sr which was confirmed via XRF **(table 1)**. Following HIPing, the cans were cut and the steel dissolved (in~20 % HNO_3) leaving a dense ceramic monolith. Subsequent analysis revealed that the 1.5 and 3 wt % samples produced similar phase assemblies and many of the phases identified in these samples were also observed in the previous study.[12] Rietveld refinements of the powder XRD data were performed in order to quantify the phases present **(figure 3, table 2).** For both samples, the major Sr phase is a $(Na,Sr)NbO_3$ perovskite, a potentially encouraging result considering this is the major Sr containing phase in the multi-phase ceramic SYNROC.[14]

Table 1. XRF analysis Sr-IONSIV 1.5 and 3 wt %

Element	3 wt%	1.5 wt%
Ti	20.9(1)	20.32(1)
Nb	15.03(2)	14.820(1)
Zr	14.95(2)	15.184(2)
Si	8.5(15)	8.18(1)
Sr	1.78(5)	1.190(4)
Na	1.7(1)	1.851(1)
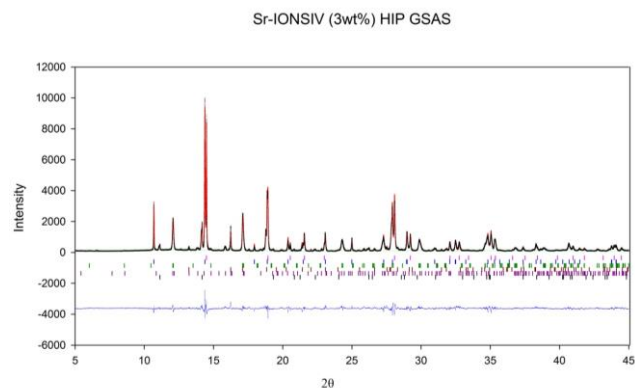
Figure 3. Rietveld refinement 3 wt % Sr-IONSIV, wRp: 13.61, Rp: 10.32 and $χ^2$: 9.023

Table 2. Weight fractions for Sr-IONSIV (3 wt %)

Phase	wt%
$(Ti,Nb)O_2$	48.0880(8)
$ZrSiO_4$	20.8670(4)
$(Na,Sr)NbO_3$	10.8510(4)
$ZrTiO_4$	5.6150(5)
$(Sr,Na)_3Nb_5O_{15}$	4.256(1)
SiO_2	10.3236(8)

SEM
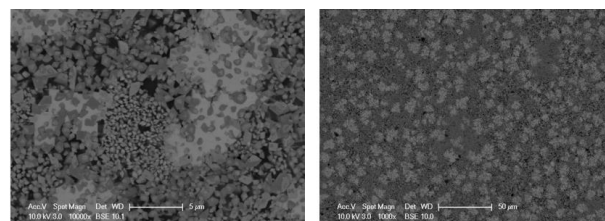
Figure 4. Back scattered electron (BSE) image 3 wt % IONSIV. Left: 5 μm scale, right: 50 μm scale.

Despite XRD being able to identify the major Sr phases, it proved difficult to fully characterise the material on account of overlapping peaks in the XRD pattern. Therefore a series of microscopy studies were carried out to better characterise them. SEM/BSE images **(figure 4)** did give an indication of morphology but it proved difficult to analyse individual Sr containing phases because of the small particles. As a result of this, TEM studies have been carried out.

TEM
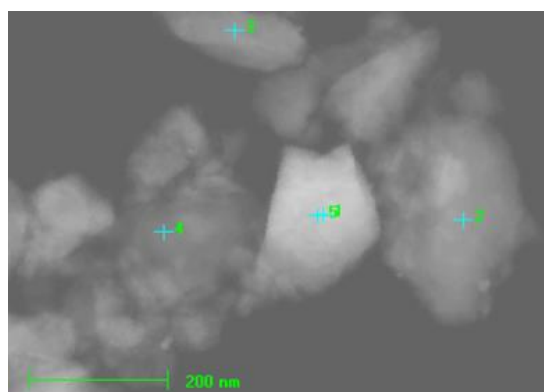
Figure 5. Multipoint analysis

Table 3. EDS (Energy Dispersive X-ray Spectroscopy) of multi-point analysis (from **figure 6**)

Wt%	OK	NaK	SiK	TiK	SrK	ZrK	NbK
1	9.09	3.24	1.4	1.17	**7.27**	1.16	25.74
2	9.3	0	0.39	12.18	**0.19**	1.41	8.59
3	8.74	0.04	0.31	12.91	**0.33**	1.75	9.12
4	16.72	0.03	18.94	0.16	**0.16**	0.25	0.28
5	6.88	2.46	1.09	0.96	**5.63**	0.8	20.02

Multi-point analysis **(figure 6, table 2)** also indicated the Sr phase suggested from XRD. EDS of points 1 and 5 identified a particle likely to be the $(Na,Sr)NbO_3$. Line analysis of the particle in **figure 6** also indicated a Na, Sr, Nb containing phase at the start of the line **figure 7.**
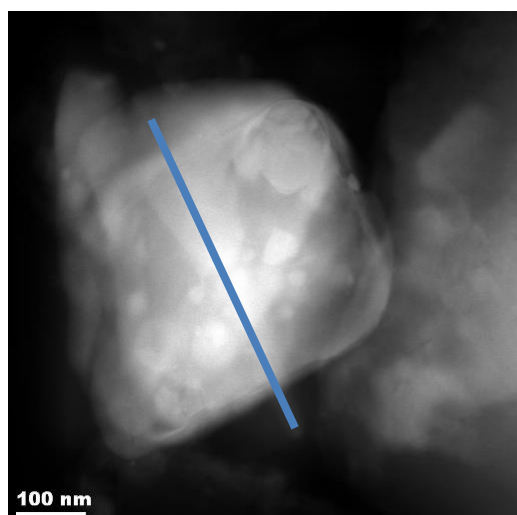
Figure 6. Line analysis TEM
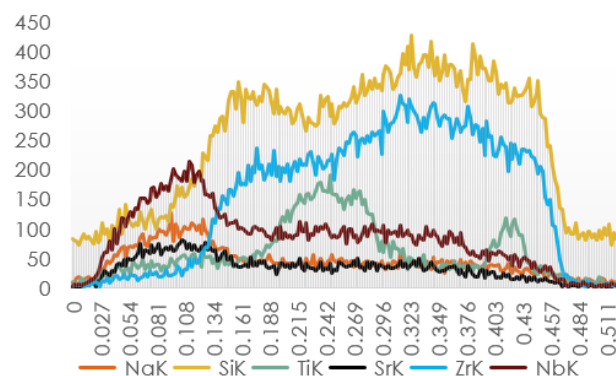
Figure 7. Line analysis, (figure 6). Concentration versus distance

Sr-IONSIV samples of higher loading and Cs/Sr-IONSIV have also been HIPed. XRD at higher level loadings of Sr (4 wt%) **(figure 8)** revealed different Sr phases as did HIPing mixed Cs/Sr-IONSIV **(figure 9)**. In the mixed sample, the Cs resides in the familiar $Cs_2TiNb_6O_{18}$ phase. This phase has already been previously studied and demonstrated to be an excellent wasteform. [12]
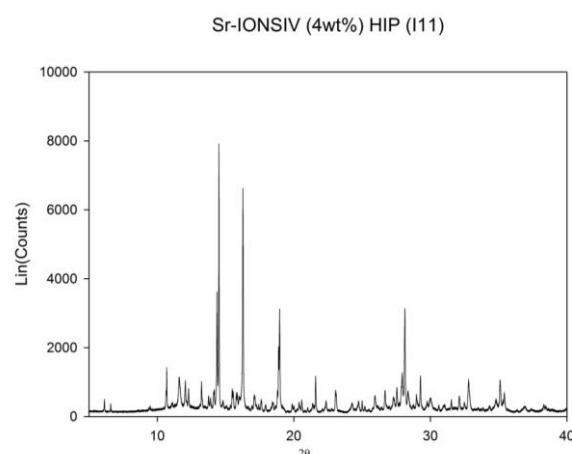
Figure 8. XRD pattern Sr-IONSIV 4 wt %
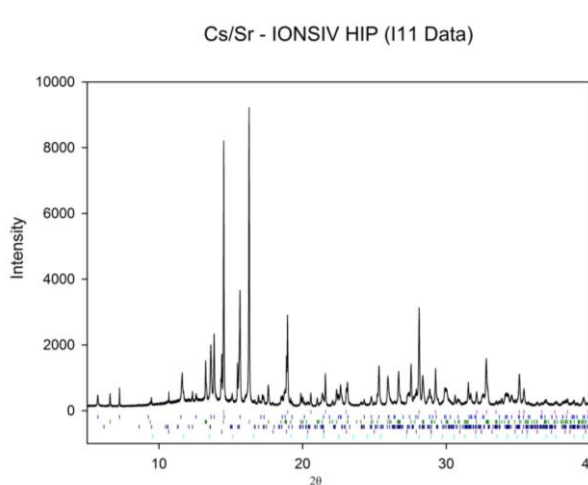
Figure 9. XRD pattern Cs/Sr – IONSIV

Table 4. Phases from HIPing higher loading Sr-IONSIV and mixed Cs/Sr-IONSIV

Sr-IONSIV (4 wt%)	Cs/Sr-IONSIV
$(Ti,Nb)O_2$	$(Ti,Nb)O_2$
$ZrSiO_4$	$Cs_2TiNb_6O_{18}$
$(Sr,Na)_3Nb_5O_{15}$	$ZrTiO_4$
$SrNb_2O_6$	$SrNb_2O_6$
$Sr_4Nb_2O_9$	$ZrSiO_4$
SiO_2	SiO_2
$ZrTiO_4$	

Leach Tests
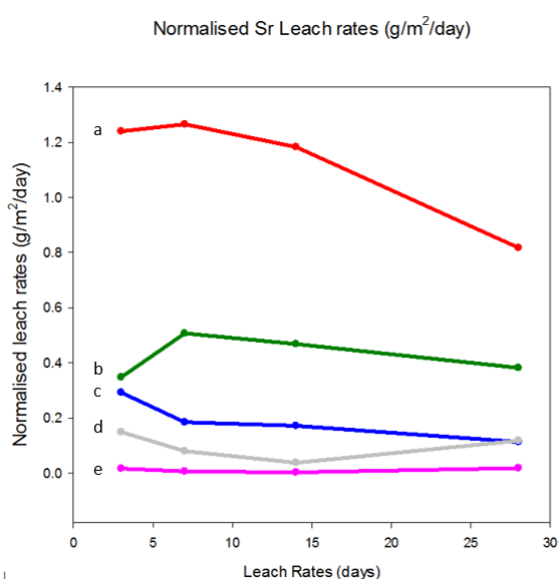
Figure 10. Sr and Cs Normalised leach rates (g/m^2/day). a: Sr leach rates Sr/Cs – IONSIV, b: Cs leach rates Sr/Cs – IONSIV, c: Sr leach rates Sr-IONSIV (4.0 wt%), d: Sr leach rates Sr IONSIV (1.5 wt%) and e: Sr leach rates Sr – IONSIV (3.0 wt%).

In general, for all samples, leach rates are at the highest in the early stages and reduce as a function of time. Sr-IONSIV 3.0 wt% display the lowest Sr leach rates, ~10^{-2} g/m^2/day. Possibly due to the Sr residing in a robust perovskite phase similar to that found in SYNROC. Sr leach rates in Cs/Sr-IONSIV are comparatively high. This is likely the result of Sr residing in the less durable phase $SrNb_2O_6$. The Cs leach rates in the mixed sample compare well to the previous study. [12] The leach rates of Sr from Sr-IONSIV (3wt%) compare well to what is reported for the multi-phase ceramic SYNROC and significantly better than borosilicate glass.[14]

Conclusions and Future Work

HIPing Sr-loaded IONSIV at 3 wt % loading has produced a robust wasteform which compare well to similar waste forms reported in the literature. Further work will involve more detailed analysis of the Sr-IONSIV and mixed Cs/Sr-IONSIV in order to better characterise the Sr containing phases.

Acknowledgements

References

1 A. Clearfield, L. Bortun and A. Bortun, *React. Funct. Polym.*, 2000, **43**, 85–95.

2 A. Dyer, A. Chimedtsogzol, L. Campbell and C. Williams, *Microporous Mesoporous Mater.*, 2006, **95**, 172–175.

3 R. Harjula, J. Lehto, A. Paajanen, E. Tusa and P. Yarnell, *React. Funct. Polym.*, 2004, **60**, 85–95.

4 National-Research-Council, in *Alternatives for High-Level Waste Salt Processing at the Savannah River Site*, National Academies Press, Washington DC, 2000, pp. 55–65.

5 R. G. Anthony, R. G. Dosch, D. Gu and C. V. Philip, *Ind. Eng. Chem. Res.*, 1994, **33**, 2702–2705.

6 J. Lehto, L. Brodkin and R. Harjula, *fortum.com*.

7 B. Yu, J. Chen and C. Song, *J. Mater. Sci. Technol.*, 2002, **18**, 206–210.

8 T. . Tranter, R. . Herbst, T. . Todd, A. . Olson and H. . Eldredge, *Adv. Environ. Res.*, 2002, **6**, 107–121.

9 A. Clearfield, *Ind. Eng. Chem. Res.*, 1995, **34**, 2865–2872.

10 G. J. Thorogood, B. J. Kennedy, C. S. Griffith, M. M. Elcombe, M. Avdeev, J. V. Hanna, S. K. Thorogood and V. Luca, *Chem. Mater.*, 2010, **22**, 4222–4231.

11 M. H. Bocanegra-Bernal, *J. Mater. Sci.*, 2004, **39**, 6399–6420.

12 T.-Y. Chen, J. . Hriljac, A. . Gandy, M. . Stennett, N. C. Hyatt and E. . Maddrell, in *Scientific Basis for Nuclear Waste Management XXXVI, MRS Symp*, 2013, pp. 67–72.

13 E. Maddrell, *Chem. Eng. Res. Des.*, 2013, **91**, 735–741.

14 A. Ringwood, *Miner. Mag.*, 1985, **49**, 159–176.

Metal substitution and Cs/Sr Ion Exchange in Sn-silicate Umbites and Thermal Conversion by Hot Isostatic Pressing

T. Chen*[1] and J.A. Hriljac[1]

*Correspondence: t.chen.3@bham.ac.uk

[1] University of Birmingham

(School of Chemistry, the University of Birmingham, Edgbaston, Birmingham, UK. B15 2TT)

Abstract

Sn-silicate umbite ($K_2SnSi_3O_9 \cdot H_2O$) crystallises in an orthorhombic system with the space group $P2_12_12_1$ (a = 10.101, b = 13.136, c = 7.157 Å) and is reported to ion exchange both Cs and Sr. Various metal doped microporous stannosilicates with an umbite structure of composition $K_{2-x}Sn_{1-x}M_xSi_3O_9 \cdot H_2O$ (where x = 0.125 - 0.25, and M=Nb^{5+}, Sb^{5+}, Y^{3+} and Sc^{3+}) have been prepared successfully via hydrothermal synthesis. It was found that the Cs and Sr uptake can be significantly improved by modifying the framework. Current work has focused on the structural studies on the Rietveld analyses of the synchrotron and neutron data. The systems with pentavalent metal substitution, e.g. Nb^{5+} and Sb^{5+} doping, structural analyses are consistent with no obvious change in the unit cell parameters or K^+ bonding prior to the exchange, it is proposed that the improved property is due to the creation of cation defect sites within the pores of the material that facilies greater cation mobility and leads to exchange. After ion exchange, a preliminary study of HIPing umbite materials is also presented aiming to obtain a dense wasteform.

Introduction

Sn-umbite possesses a framework structure built of [SnO_6] octahedra and long-chain [SiO_4] tetrahedra by corner-sharing, as shown as Figure 1a. There are two unique ion exchange sites in the tunnels. The first exchange site (*Site 1* in Figure 1b) is in an 8-membered ring (8MR) tunnel consisting of six SiO_4 tetrahedra and two SnO_6 octahedra; the second site (*Site 2*) is in another 8MR tunnel consisted of four SiO_4 tetrahedra and four SnO_6 octahedra. Water molecules only locate in channels along with Site 2 cations.[1] Pure umbites have shown the ability for Cs and Sr uptake over a wide pH range, however typically much poorer in low pH condition.[1-3] Furthermore, one of the advantages of umbite is that the phase can be thermally transformed to a ceramic phase wadeite[4, 5], which is considered as a potential ceramic wasteform.

Previous work has demonstrated that significantly better Cs^+ selectivity can be achieved in some materials by framework substitution, for example, partial Nb^{5+} substitution for Ti^{4+} in the crystalline silicotitanate (CST) structure[6-8] or complete/partial substitution of Ge or Nb in the pharmacosiderite framework[9-11]. The crystallographic and electrostatic environment in which the Cs^+/Sr^{2+} ions are accommodated can be tailored by varying the ratio or species of substitution.

A range of substituted Sn-umbites [($K_{2-x}(Sn_{0.75}M_{0.25})Si_3O_9 \cdot H_2O$, M= Nb^{5+}, Sb^{5+}, and (Y^{3+}+Nb^{5+}), (Sc^{3+}+Nb^{5+})]] were prepared via direct hydrothermal synthesis, and synchrotron and neutron data collected for structural studies.

After ion exchange, an easy conversion pathway is being sought to transform the spent ion exchanger into dense ceramics that retain the Sr and Cs for long term storage. As one of the advanced ceramic processing methods, hot isostatic pressing (HIPing) has been extensively studied due to many obvious advantages over the conventional methods (such as sintering or melting) for processing of high-level radioactive wastes. The waste is enclosed in a metal can, which can be left in place when the repository is closed, and processed at relatively low temperature, thus high temperature volatility losses and costs of off-gas emission processing system are greatly reduced. In this summary, a preliminary study of HIPing umbite materials is also presented.
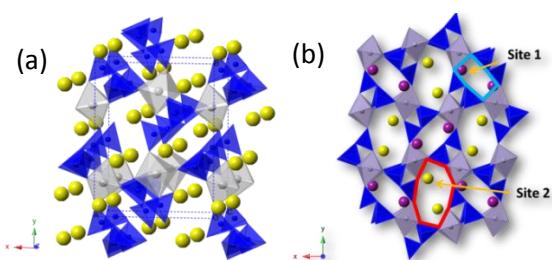
Figure 1 (a) Projections of the structure *Sn-Umbite* (b) structural overview of Sn-umbite showing two unique ion exchange sites (sites 1 & 2) in the 8MR tunnels

Methodology Details

1. Ion exchange test

The Cs and Sr uptake was tested by shaking the materials in 0.1 M $Sr(NO_3)_2$ or $CsNO_3$ solution under batch conditions at V:m = 100:1 (mL:g) for 24 hr at room temperature. The white powders were washed first with water and dried at 50 °C. The Cs and Sr content in the material were evaluated using XRF.

2. Thermal conversion by hot isostatic pressing

Cs, Sr-exchanged umbites were prepared by ion exchange and pre-calcined in air at 800 °C for 12 hours before filling into 2 mm thick mild steel HIP cans. The tubes were welded shut and then hot isostatically pressed at 1100 °C and 150 MPa for 2 hours under an argon atmosphere. HIPed samples were sectioned and polished for SEM and ground for XRD and XRF analyses.

Results and Discussion

1. Ion exchange tests

Metal substituted umbites were evaluated for the removal of Cs and Sr using static batch experiments. The recovered ion exchangers were then analysed by XRF, the molar ratios of Cs or Sr normalised to the sum of octahedral site elements such as Sn, Nb, Y, and Sc. These are compared to unsubstituted Sn-umbite in Figure 2, but as samples were not prepared as fused beads the numbers should not be over interpreted.

It is of interests that most of the umbites containing pentavalent elements have a significant improvement in Sr or Cs uptake. The effect of Nb substitution on the ion exchange properties of the Sn-umbite framework has been evaluated. As shown as in Figure 3, a strong correlation between the Cs/Sr uptake and Nb doping is observed. Structural analyses are consistent with no obvious change in the unit cell parameters due to the similar size of Sn^{4+} (0.69 Å) and Nb^{5+} (0.64 Å), or K^+ bonding prior to the exchange. It is proposed that it is because of the less crowded tunnels formed with fewer charge neutralising K cations, as observed as in Nb substituted CST.
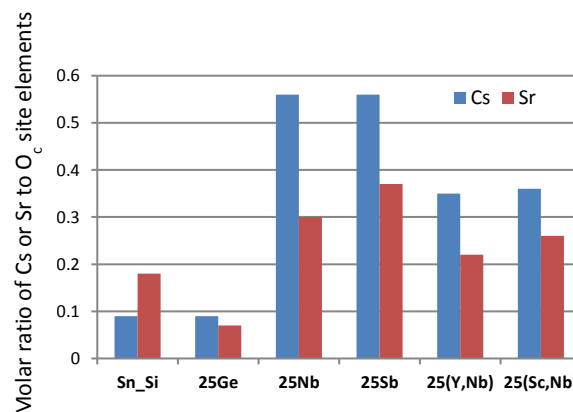
Figure 2 Cs and Sr uptake in batch tests. The materials (left to right) are the parent $K_2[SnSi_3O_9]\cdot H_2O$, 25% Ge for Si, 25% Nb for Sn, 25% Sb for Sn, 12.5% each Y and Nb for Sn and 12.5% each Sc and Nb for Sn
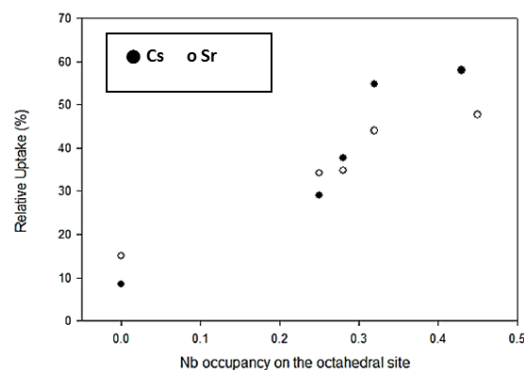
Figure 3 Uptake of Cs or Sr for K in $K_{2-x}(Sn_{1-x}Nb_x)Si_3O_9\cdot H_2O$

2. Thermal conversion by hot isostatic pressing

Cs, Sr-exchanged umbites were HIPed in order to transform umbite to a high temperature phase – wadeite, which is a potential ceramic wasteform. However, the HIPing process for all the Cs and Sr-exchanged metal-doped umbites produced a uniform glass material, shown in Figure 4(b). XRD pattern, Figure 4(c), revealed the sample to contain only amorphous content. The pressure induced and reducing condition of the HIP process has caused an interaction between the iron from the mild steel and the material making this sample mechanically fragile compared to the ceramic.

Although an amorphous glass material was formed after HIPing, SEM-BSE image shown in Figure 4(a) demonstrated that Cs, the bright dots in the image, is encapsulated inside the material. The chemical compositions analysed using XRF in the Table 1 also showed that no Cs loss was observed during the HIPing process. To obtain a ceramic wasteform by HIPing, a less reactive can material, such as stainless steel, will be used for the next HIP run.
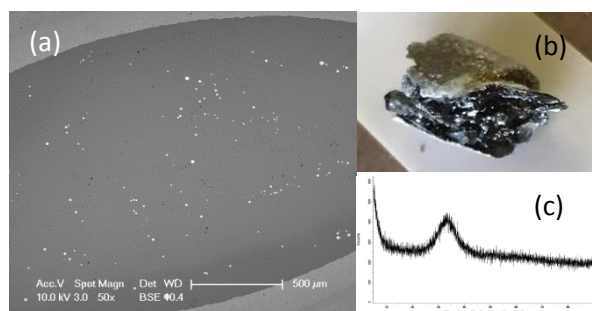
Figure 4 (a) SEM-BSE image of HIPed Cs-exchanged 25% Nb Sn-umbite (b) image showing a dense glass formed after HIPing (c) XRD pattern of the HIPed Cs-exchanged 25% Nb Sn-umbite showing that no crystalline phases were formed after HIPing

Table 1 XRF result of HIPed Cs-exchanged 25% Nb Sn-umbite

Formula	Concentration (wt%)
Cs	**17.94%**
Fe	**17.83%**
Si	14.79%
K	13.74%
Sn	8.95%
Nb	7.37%

Conclusions and Future Work

Conclusions

It is observed that ion exchange properties are strongly related to the level of doping. The different tunnel/pore size due to the partial substitution in the framework has not affected much on ion exchange capacity.

Current work is focused on solving the crystal structures of the undoped and doped umbite materials on synchrotron X-ray and neutron diffraction data in order to investigate the structural effect of the substitution on Cs and Sr exchange behaviour.

Computational simulation is also ongoing to firstly reconstruct the crystal structure based on the neutron diffraction data, and fit the potential if required, then predict the K^+-Cs^+/Sr^{2+} ion exchange process in the umbite system. The theoretical predictions will be compared to the experimental results.

Future Work

1. Various ion exchange conditions such as pH control, kinetic, or competitive ions present to monitor the change of K^+, Cs^+, and Sr^{2+} using ICP are required.

2. Potassium mobility measurements to support the proposed mechanism that the improved Cs/Sr exchange in the doped system is attributed to the ease of Cs/Sr cations moving in the less crowded tunnels.

References

1. Fewox, C.S. and A. Clearfield, *Synthesis and characterization of protonated zirconium trisilicate and its exchange phases with strontium.* Journal of Physical Chemistry A, 2008. **112**(12): p. 2589-2597.

2. Pertierra, P., et al., *Thermal behavior of K2MSi3O9 center dot H2O with the structure of umbite (M = Sn) and kostylevite (M = Pb) minerals.* Thermochimica Acta, 2004. **423**(1-2): p. 113-119.

3. Doebelin, N. and T. Armbruster, *Microporous titanosilicate AM-2: Ion-exchange and thermal stability.* Microporous and Mesoporous Materials, 2007. **99**(3): p. 279-287.

4. Xu, H., et al., *Crystal-chemical and energetic systematics of wadeite-type phases A 2 BSi 3 O 9 (A = K, Cs; B = Si, Ti, Zr).* Physics and Chemistry of Minerals, 2005. **32**(5): p. 426-435.

5. Poojary, D.M., et al., *Syntheses and X-ray Powder Structures of K2(ZrSi3O9)·H2O and Its Ion-Exchanged Phases with Na and Cs.* Inorganic Chemistry, 1997. **36**(14): p. 3072-3079.

6. Chitra, S., et al., *Optimization of Nb-substitution and Cs+/Sr+2 ion exchange in crystalline silicotitanates (CST).* Journal of Radioanalytical and Nuclear Chemistry, 2012: p. 1-7.

7. Luca, V., et al., *Nb-substitution and Cs+ ion-exchange in the titanosilicate sitinakite.* Microporous and Mesoporous Materials, 2002. **55**(1): p. 1-13.

8. Kerlegon, S.M., et al., *Synthetic optimization of crystalline silicotitanate and Nb-substituted crystalline silicotitanate for nuclear waste remediation.* Abstracts of Papers of the American Chemical Society, 2006. **231**: p. 987.

9.   Tripathi, A., et al., *Optimizing Cs-exchange in titanosilicate with the mineral pharmacosiderite topology: framework substitution of Nb and Ge.* Journal of Solid State Chemistry, 2004. **177**(8): p. 2903-2915.

10.   Behrens, E.A., D.M. Poojary, and A. Clearfield, *Syntheses, crystal structures, and ion-exchange properties of porous titanosilicates, HM(3)Ti(4)O(4)(SiO4)(3)center dot 4H(2)O (M=H+, K+, Cs+), structural analogues of the mineral pharmacosiderite.* Chemistry of Materials, 1996. **8**(6): p. 1236-1244.

11.   Behrens, E.A., D.M. Poojary, and A. Clearfield, *Syntheses, X-ray Powder Structures, and Preliminary Ion-Exchange Properties of Germanium-Substituted Titanosilicate Pharmacosiderites: HM3(AO)4(BO4)3·4H2O (M = K, Rb, Cs; A = Ti, Ge; B = Si, Ge).* Chemistry of Materials, 1998. **10**(4): p. 959-967.

Raman Probe Development: Sample preparation for active material.

K.Wyness*[1], J.Day[1], and B.Rogerson[2]

*Correspondence: kw14747@bristol.ac.uk

[1] *Interface Analysis Centre (University of Bristol, H H wills physics laboratory, Bristol, UK)*
[2] *Sellafield Ltd. (Sellafield, Seascale, UK)*

Abstract

Sellafield Ltd. is situated in the north east of England and is the UK's nuclear decommissioning site. Within the site, it houses some of the UK's oldest wet storage ponds [1]. This project seeks to analyse the bottom of the pond environment using Raman Spectroscopy with an in-situ Stand-off probe. The ponds house a layer of mobile sludge and is a mixture of nuclear waste, pond infrastructure and organic matter such as algae and windblown debris. This has formed due to decades of corrosion from the aqueous environment. An analysis will dictate the long term strategy for the retrieval and removal of this sludge, so characterising it is essential. The probe geometry and design are imperative for successful data sampling, with samplings ranging a wide variety of material. In particular interest to us is uranium fuel left exposed from the outer claddings deterioration. This has given rise to forming many different compounds of uranium. This work is the fabrication of some of these oxide samples.

Introduction

With Sellafield needing a long term storage strategy, a full diagnosis must be completed on all their unknown waste contents. The legacy ponds (pile fuel and FGMSP) are amongst the containers which have unidentified waste products in. The majority of the sludge components is known, however in what quantities and locality is not. Sellafield are currently processing the sludge as homogenous, whereas they need it to be considered a heterogeneous mixture. With an in-situ analysis technique, this could chemically map the ponds floor and be able to decipher between high actinide concentration and lower concentration.

The sludge matrix found in these ponds needs to be fully understood, the following work will examine the processes used when synthesising different uranium oxides. Although the ponds will not have pure forms of each compound, it provides a good understanding of what bonds are associated with uranium oxides and how this differs between compounds.

Techniques

Raman spectroscopy is a powerful analytical tool to characterise chemical compounds, which can determine the different chemical speciation found in this environment. Using the measurement of inelastic scattering of light from interactions with the vibrational modes on the materials surface. Raman spectroscopy can produce an individual spectrum or "fingerprint". From this fingerprint, it is possible to distinguish between two materials with the same elemental components, but in different phase.

X-ray Diffraction is technique primarily used for determining the crystal structure of a material. It uses incident X-rays to diffract into specific directions, indicative of a materials atomic structure. Typically, it gives us information of crystalline material. When dealing with synthesised material, a single phase conversion has been occurred, meaning the final product should be crystalline.

Methodology Details

Synthesis processes. Under controlled and isolated conditions, such as high temperatures and under a vacuum, provide the necessary environment for the synthesis of different uranium oxides. These are normally exact recipes that involve a range of heating and exposure to gas with a set time duration to achieve different compositions. Oxidation increases the uranium to a higher stoichiometry state, whereas hydration can interaction with the material and reduces the amount of oxygen bonds. The oxides formed heavily depend on temperature, as intermediate U phases can be formed when performing the same experiment at lower temperatures [4]. Some of these oxides involve simply one process being performed, however some others can include multiple phases being changed before the correct stoichiometry is created
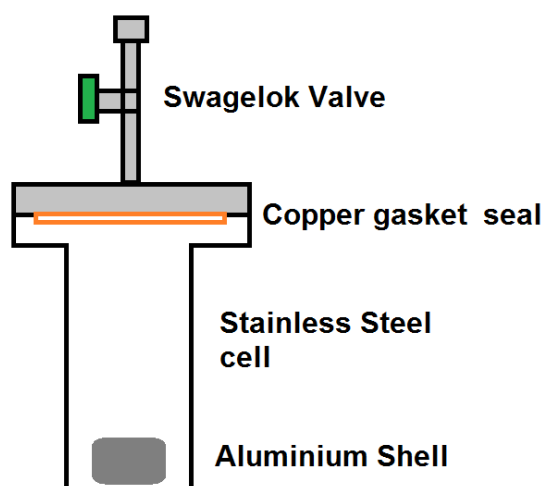
Figure 1. Schematic of experimental cell

Experimental method

Sample Preparation

NB : All samples are prepared in the same way

The cell was prepared in an inert argon environment for minimal oxidisation. Using a pestle and mortar the material was ground into a fine powder, and placed into a small aluminium shell to keep the powder intact when inside of the cell. The cell was sealed with a copper gasket and tightened shut [see figure 1]. The seal was checked by placing the cell under vacuum to check for any leaks. If the cell kept its pressure, it could be placed inside the clam shell furnace and wrapped in an insulation layer of silica wool. During the heating process of the powder, unwanted gas will be released and subsequently removed with outgassing technique. Once the furnace is up to temperature the cell has been out-gassed, the appropriate gas can be leaked into the cell (experiments performed in air missed out this stage and the opening valve was opened briefly and then closed again).

Before synthesis began, the original uranium oxide was verified with XRD. This showed that the material was in fact being formed from uranyl nitrate (hydrated to its hexahydrate form). The $UO_2(NO_3)_2\ (H_2O)_6$ was prepared suitable for the desired oxides, which were UO_3, UO_2, U_3O_8 & U_4O_9.
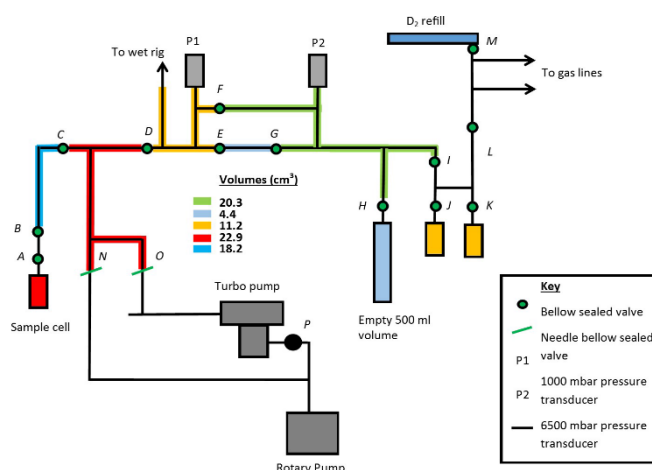
Figure 2. Schematic of gas rig. [5]

Table of Processes

Here we have the list of each sample and its process to fabricate a new material. The variables involved changing temperature, gas input and pressure. The timings used were exaggerated to ensure a full conversion had occurred during the synthesis process. All methods were found through literature in the relevant journals. [2] [3] [4]

Sample name	Material	Process	Weight (grams)	Time (hours)	Temperature (°C)	Gas	Pressure (mbar)	End product
367DA	$UO_2(NO_3)_x$	Oxidation	1	4	600	oxygen	500	Am. UO_3
367DB	$UO_2(NO_3)_x$	Oxidation	1	6	400	air	N/A	Am. UO_3
367DC	UO_3	Hydride reduction	0.9	4	550	hydrogen	500	UO2
367E	$UO_2(NO_3)_x$	Oxidation	5	4	400	air	N/A	Am. UO_3
367EA	UO_3	Hydride reduction	5	4	550	hydrogen	500	UO_2
367EB	UO_2	Oxidation	3	2	370	oxygen	200	U_3O_8
367ED	UO_2	Oxidation	1	2	220	oxygen	200	U_4O_9
367FA	$UO_2(NO_3)_x$	Oxidation	2	4	1000	air	N/A	UO_3

Results and Discussion
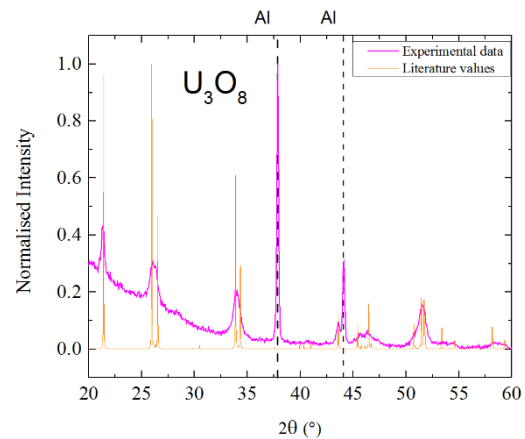
Figure 3. XRD analysis of U_3O_8
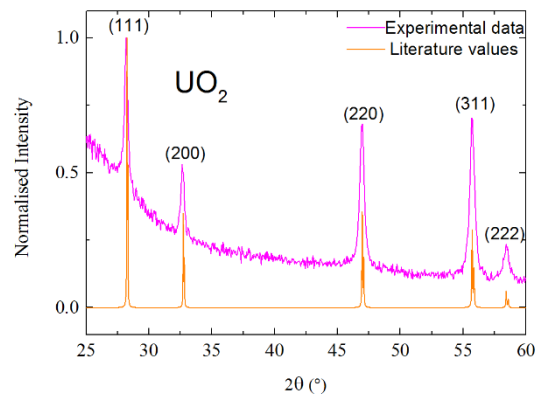
Figure 4. XRD analysis of UO_2
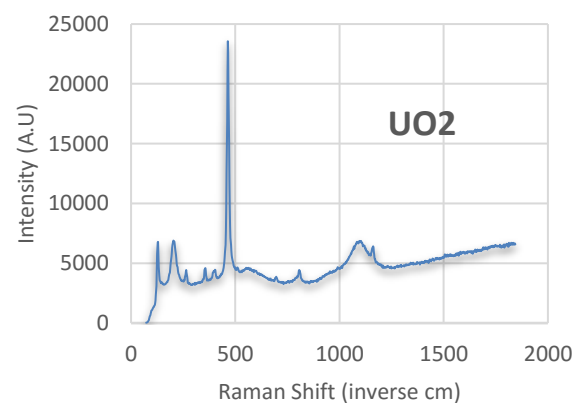
Figure 5. Raman Spectrum of UO_2

For the initial XRD preparation, the powders were pressed into pellets to keep contamination to a minimum and encased in Kapton tape (Kapton has a high transmittance to X-rays and radiation has little effect on its integrity making it ideal for this purpose). After all samples were verified by XRD analysis, a full Raman analysis is to be completed. When taking a Raman measurement, a focused laser beam remains on the samples for some time, so suitable preparation is needed to prevent oxidation to the samples. Samples were prepared for Raman in a similar way to XRD prep, but contained between two glass slides and sealed with epoxy in a glovebox environment, keeping oxidation to a minimum. Some of the uranium pellets have not proved successful when sampling under the Raman spectrometer. The glass slides used to encase the pellet were too thick to focus through and caused the optical focus to be distorted. This will need addressing by replicating the sample preparation process but change to very thin glass cover slips. From figure 5. You can see the UO_2 pellet has given a Raman signal. Small artefacts have appeared in the spectrum, which could be small defects in the powder and could be an indication of impurities.

Conclusions and Future Work

Firstly a completion of all Raman spectra of uranium – oxides is necessary. As mentioned in the discussion, this will be facilitated by altering the method of preparation before sampling. From this fabrication of active samples, the research will now venture into comparing samples through a number of different wavelengths. The current set up is at 633nm (Visible red laser). To minimise the fluorescence laser wavelengths into the NIR would be most suitable. This body of work will continue into looking at non active samples as well.

Acknowledgements

References

[1]http://www.sellafieldsites.com/solution/risk-hazard-reduction/first-generation-magnox-storage-pond/

[2] Neutron powder profile studies of the gamma uranium trioxide phases, Loopstra B Taylor J Waugh A, Journal of Solid State Chemistry, 1977 vol: 20 (1) pp: 9-19

[3]Synthesis of Lanthanide and Actinide Compounds, edited by G. Meyer, Lester R. Morss pp:245

[4] Oxidation behaviour of unirradiated sintered UO2 pellets and powder at different oxygen partial pressures, above 350C, Valdivies et al, Journal of Nuclear Materials, 2006 vol: 354 (3) pp: 85-93

[5] In-situ and Time Resolved Observation of Uranium Corrosion applied to Nuclear Waste Storage and Disposal 2015, Camilla Stitt 2015

Assessment of empirical potentials for simulations of glass/crystal interfaces

P.C.M. Fossati*[1], and W.E. Lee[1]

*Correspondence: p.fossati@imperial.ac.uk

[1] Department of Materials/Centre for Nuclear Engineering (Imperial College London, South Kensington Campus, London SW7 2AZ, United Kingdom)

Abstract

Empirical potentials have been tested in order to assess their usability in the study of glass/crystal interfaces of the type commonly found in nuclear glass wasteforms. Compositions considered in this work are $(Na_2O)_x(SiO_2)_{(1-x)}$ silicate glasses and TiO_2 crystals with the rutile structure ($P4_2/mnm$). Properties of both crystal and glass have been calculated to verify that the potential describes a realistic material. Finally, preliminary results of glass/crystal interface are shown.

Introduction

Vitrification is a technique commonly used to encapsulate nuclear waste. In the UK in particular, High-Level Waste (HLW) left after fuel reprocessing is immobilised in a borosilicate matrix[1]. Some HLW components have limited solubility in the glass melt and thus precipitate into crystalline phases during fabrication of glass wasteforms. These crystallites grow whilst the glass cools, and the resulting material is a Glass/Crystal Composite (GCC) which contains crystal secondary phases embedded in the glass matrix. These phases are diverse in term of structure and composition, common occurrences being oxides with rutile ($P4_2/mnm$) or spinel structures (e.g. $(Ru,Rd)O_2$ or $(Cr,Fe,Ni)_3O_4$ compounds respectively), molybdates or the so-called yellow phase[2].

Some of these heterogeneities have well-known effects on the material's performance as a wasteform. For example, the yellow phase is more soluble in water than the glass matrix. This offers a way for radionuclides to escape the wasteform when water enters in contact with the yellow phase. Other phases are problematic during fabrication. For example, RuO_2 crystals increase viscosity of the glass melt, which complicates melt pouring into canisters by obstructing nozzles[3]. From safety and industrial points of view, it is therefore important to understand the behaviour and properties of these secondary phases and the changes they cause in the wasteform's characteristics.

The purpose of this study is to contribute to the understanding of the issues associated with GCC wasteforms at the atomic length-scale. To this intent, Molecular Dynamics (MD) techniques are employed, based on the empirical potentials described below. The

Nuclear glasses tend to have complex compositions, to immobilise a broad range of radionuclides with different chemical properties. This is a challenge to reproduce using empirical potentials as they need to be accurate for all the present chemical species. In this work, we use potentials derived by Pedone et al.[4], which cover a large number of oxides. This ability to simulate more realistic glasses will be used in the future, however the compositions considered in a first instance and presented here are sodium silicate $(Na_2O)_x(SiO_2)_{(1-x)}$. Available potentials also limit the choice in terms of composition for the crystalline phases. In particular, no empirical potential is available to simulate RuO_2 that would be compatible with Pedone's potentials. For this reason, rutile (TiO_2) was chosen as a surrogate for RuO_2.

Methodology Details

Model

The Pedone potentials are based on a rigid ion, pair interactions model. Pair interactions contain an electrostatic term, non-bonded, short-range contributions represented by a Morse term, as well as a short-range repulsion term. The Wolf method was used to calculate electrostatic interactions [5].

Empirical Potentials simulations

Thermal expansion of TiO_2 was calculated from the average dimensions of a 10x10x10 supercell during NPT simulations at room pressure. Phonon spectra were obtained from the velocity autocorrelation function accumulated during NVT simulations. The LAMMPS code was used in both cases [6].

Bulk glass configurations were created using a standard quench process. Melts were relaxed at 5 000 K for 200 ps to generate random initial positions. The

volume of each configuration was fixed so that each simulation box has the correct room-temperature experimental density (see Table 1). The melts were then quenched using a variable-temperature Nosé-Hoover thermostat with the target temperature decreasing linearly as a function of simulated time, at a rate of 2.5 K/ps. The simulation boxes were finally equilibrated at room temperature for 300 ps.

The method used to create interfaces is based on the same process. However, the high temperature used during the melt randomisation phase is higher than the melting point of the crystal. To prevent the crystal from melting or creating excessive concentrations of point detects, its atoms were kept frozen during the high-temperature phase of glass creation and the subsequent quench. This constraint was lifted for the final relaxation at room temperature to allow the crystal interface to relax.

Results and Discussion

Potential assessment for $P4_2/mnm$ TiO$_2$

Lattice parameters measured at 300 K were 4.587 Å and 3.018 Å for a and c respectively. This is within 0.15% and 2.0% of the experimental values of 4.5941 Å and 2.9589 [7]. Thermal expansion is qualitatively good, with the linear expansion coefficient along c being larger than along a, as is the case experimentally (see Fig. 1).
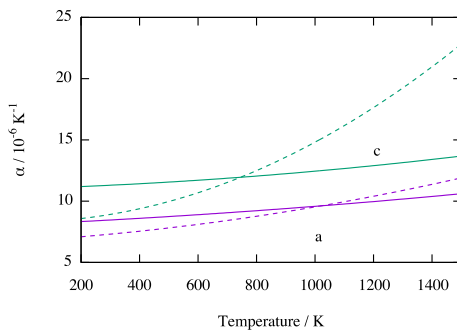
Figure 1 Linear thermal expansion of $P4_2/mnm$ TiO$_2$ predicted by the empirical potential (solid lines) compared to experimental reference (dashed lines show result from [7]).

The phonon density of states predicted from the empirical potential has some features matching experimental spectra (see Fig. 2), but it has significant differences as well. High-frequency features are very well reproduced, as well as the peaks between 5 and 8 THz. The highest peak, however, which is located at 15 THz experimentally, is seen at a significantly lower frequency. The lowest-energy peak, at 2.5 THz seems to be completely missing in the simulated curve.
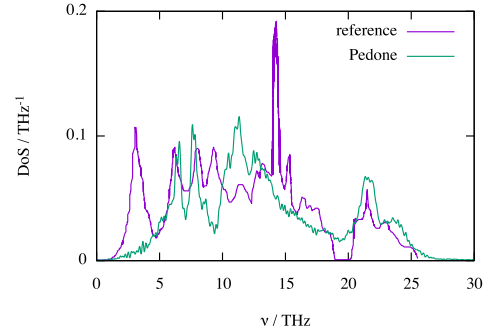
Figure 2 Phonon densities of states of $P4_2/mnm$ TiO$_2$ compared to an experimental reference [8].

Potential assessment for sodium silicate glass

Simulation results of various glass compositions based on the Pedone potentials are available in the literature. The properties they predict for $(Na_2O)_x(SiO_2)_{(1-x)}$, in particular, are well known. Of particular interest are structural parameters linked to the degree of connectivity of the Si-O structure, such as the concentration of Non-Bridging Oxygens (NBOs) or the distributions of Q_n silicate tetrahedra.

Agreement with experimental results is particularly good for NBO concentrations (see Fig. 3).
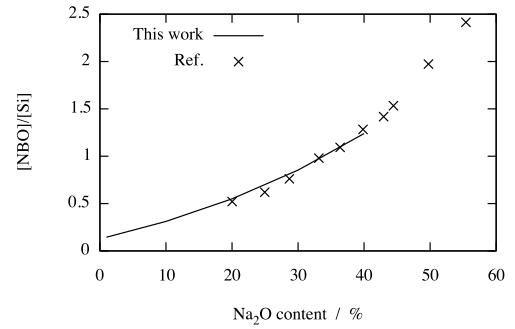
Figure 3 Non-Bridging Oxygens (NBO) concentration in $(Na_2O)_x(SiO_2)_{(1-x)}$ glass as a function of Na$_2$O concentration predicted by the empirical potential (solid lines) compared to experimental reference [9].

Q_n distributions show qualitative agreement with experimental values (see Fig. 4). Although minor quantitative differences can be noted, major features such as the monotonous decrease of Q_4 and increase of Q_2 as Na$_2$O concentration increases. The maximum of Q_3 population is also reproduced, although more data points would be needed to ensure that it is observed as the same concentration as in experiments.

These results show that the quench process used to generate room-temperature glass configurations reproduces well structural features of the material.
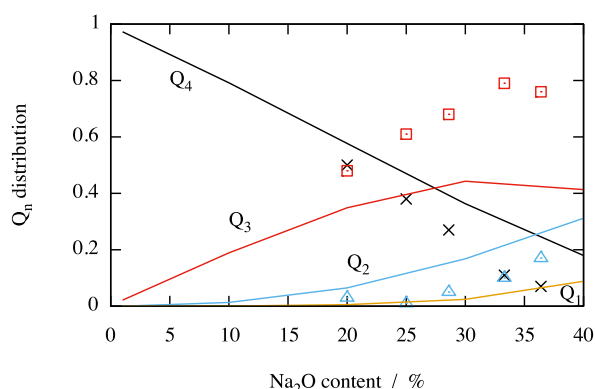
Figure 4 Q_n distribution in $(Na_2O)_x(SiO_2)_{(1-x)}$ glass as a function of Na_2O concentration predicted by the empirical potential (solid lines) compared to experimental results (symbols, [9]).

Simple glass/crystal interfaces

Interfaces were generated, with the crystal surfaces (001), (100), (101) and (110), with a glass containing 10% of Na_2O (see an example in Fig. 5). In all these configurations, the contact layer between the glass and the crystal contains mostly O ions, which have both Ti and Si neighbours (Interface Bridging Oxygens, IBO). Although some disorder is visible in the IBO layer, O ions tend to occupy positions close to where they would have been in the crystal, thus preserving the coordination environment of the Ti layer closest to the interface.
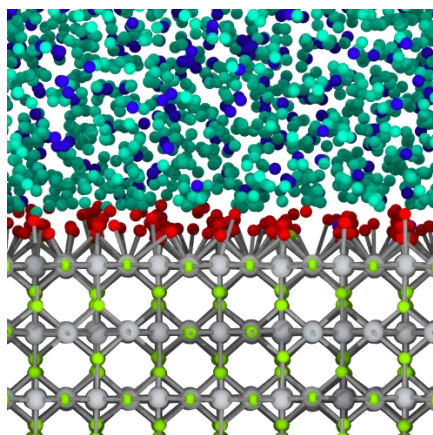
Figure 5 Glass/crystal interface. Si and Na ions have been removed for clarity; larger grey balls indicate Ti ions positions; smaller balls correspond to O ions. Oxygens are coloured according to their structural role: NBO (dark blue), BO (turquoise), IBO (red) and part of the crystal structure (yellow).

Conclusions and Future Work

In this work, we have determined to which extent bulk TiO2 and $(Na_2O)_x(SiO_2)_{(1-x)}$ glasses simulated using the Pedone potential are realistic. This has shown that it reproduces accurately the glass' structure, as well as basic properties of TiO_2. However, the fact that the low-frequency part of the phonon density of states differs significantly from experimental spectra implies that further verifications need to be done in order to determine the accuracy of the potential's prediction of thermodynamic properties such as thermal conductivity and heat capacity. Nevertheless, this study is the foundation of an on-going effort to describe the property of interfaces in simplified GCC wasteforms. Future aims include determining the resistance of different interfaces during phenomena such as fracture, as well as effects of radiation damage on the interface structures.

References

[1] M.I. Ojovan, and W.E. Lee, An introduction to nuclear waste immobilisation, second edition, Elsevier **2014**

[2] P.B. Rose, D.I. Woodward, M.I. Ojovan, N.C. Hyatt, and W.E. Lee, Crystallisation of a simulated borosilicate high-level waste glass produced on a full-scale vitrification line, *J. Non-Cryst. Solids* **357** (2011), 2989-3001

[3] J. Puig, B. Penelon, P. Marchal, and M. Neyret, Rheological properties of nuclear glass melt containing platinum group metals, *Proc. Mater. Sci*. **7** (2014), 156-162

[4] A. Pedone, G. Malavasi, M. C. Menziani, A.N. Cormack, and U. Segre, A new self-consistent empirical interatomic potential model for oxides, silicates, and silica-based glasses, *J. Phys. Chem. B* **110** (2006), 11780-11795

[5] D. Wolf, P. Keblinski, S.R. Philpot, and J. Eggebrecht, Exact method for the simulation of Coulombic systems by spherically truncated pairwise r^{-1} summation, *J. Chem. Phys*. **110** (1999), 8254

[6] S.J. Plimpton, Fast parallel algorithms for short-range Molecular Dynamics, *J. Comp. Phys*. **117** (1995), 1-19

[7] K.V.K. Rao, S.V.N. Naidu, and L. Iyengar, Thermal expansion of rutile and anatase, *J. Amer. Ceram. Soc*. **53** (1970), 124-126

[8] R. Sikora, Ab initio study of phonons in the rutile structure of TiO_2, *J. Phys. Chem. Solids* **66** (2005), 1069-1073

[9] H. Maekawa, T. Maekawa, K. Kawamura, and T. Yokokawa, The structural groups of alkali silicate glasses

determined by ^{29}Si MAS-NMR, *J. Non-Cryst. Solids* **127** (1991), 53-64

Temperature dependence of Cs volatilisation from Fukushima adsorbents

D. Pletser*[1], Y. Yoshii[2] and, W.E. Lee[1]

* Correspondence: D.Pletser@imperial.ac.uk

[1] Centre for Nuclear Engineering (Imperial College London, SW7 2AZ London, United Kingdom)
[2] Center for Technology Innovation (Energy, Research & Development Group, Hitachi, 7-2-1 Omika-cho, Hitachi-shi, Japan)

Abstract

For the remediation of the Fukushima site the volatilization behaviour of Cs from adsorbents is possible concern. Reliable data concerning Cs volatilization behaviour is required. For this work a novel experimental rig was set up and an effective and safe operating procedure was devised. A commercial zeolitic adsorbent was loaded in 1000 ppm Cs solutions to an effective wasteloading of 7-8 wt.% of Cs, and tested in temperature ranges from 600°C to 1000°C. The recovered Cs was analysed using Atomic Absorption Spectroscopy to determine the amount of volatilized Cs. It showed increasing volatilization at higher temperatures, with behaviour following similar reported values in literature. The zeolitic adsorbent showed very little volatilisation with a relative volatilization of 0.097% at 1000°C.

Introduction

Several water treatment systems are currently in place at Fukushima to remove radionuclides from the contaminated water used to cool the reactor cores, such as the HP-ALPS (High Performance Advanced Liquid Processing System), the high performance multi-nuclide removal equipment.
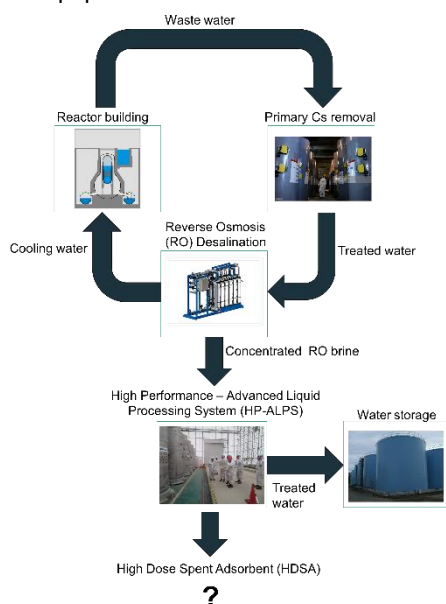
Figure 1 Water treatment cycle in Fukushima

However, the treatment of approximately 500 m^3/day of contaminated water continues to generate large volumes of spent adsorbents, which can be highly radioactive (approximate level of activity concentration of the order of 1E^{11} Bq/kg to 1E^{12} Bq/kg). These spent adsorbents are currently stored on-site, but will require immobilisation in a suitable wasteform before being disposed of permanently. The most common radionuclide species present in the effluent cooling water are Cs and Sr species with short half-lives, the longest is Cs-137 with a 30.08 year half-life. The final ILW wasteform will have an estimated repository lifetime of 300 years and will likely be disposed of at a surface storage facility.

An aspect to consider in any process used to immobilise the adsorbents is Cs and Sr volatilisation. Due to the use of seawater as an emergency coolant and the ingress of groundwater the system has a high chloride content. The high level of chloride could lead to CsCl and SrCl species. Both the chloride species of Sr and Cs are volatile at higher temperatures [1], so to ensure minimal volatilisation a low temperature immobilisation process was designed with a maximum temperature of 600ºC [2]. A fully homogeneous glass wasteform at this temperature is not achievable, as a fully vitreous wasteform incorporating these adsorbents is only achievable above 1100ºC [3].

Radionuclide volatilisation is a problem that has been faced by the nuclear industry in many different clean-up scenarios, including volatilisation from Cs adsorbed onto zeolites. Gray[4] noted that the volatility is significant above 700ºC, and this is echoed by Kamizano

et al.[4] who notes that volatilisation can be significant above 1000ºC. Furthermore, the presence of chloride species can greatly increase volatilisation, the presence of NaCl in a system can push the volatilisation of Cs to >99% above 1000ºC[5]. Due to the situation at Fukushima Daiichi, the waste has a significant chloride presence that would greatly increase both Cs and Sr volatilisation. This may prove problematic during the final immobilization efforts, as many techniques, such as vitrification, are high temperature processes. To this end accurate thermal data of radionuclide volatilization from adsorbents is sought.

Methodology Details
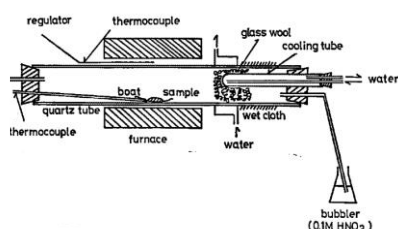
Figure 2 Schematic of volatilisation rig, adapted from Mimura and Kanno[6]

To produce this data an experimental rig was designed and constructed by Nakayama Co Ltd., based on work done by Mimura and Kanno[6]. Thermal data was collected in the range of 600°C - 1000°C in 100°C increments. All experiments were conducted for 3h at the designated temperature. All samples were loaded with an effective Cs loading of 7-8 wt.% and all AAS samples were prepared using a detailed Cs recovery protocol.

The adsorbent is added in 1.00g amounts to 100 ml of a prepared 1000 ppm CsCl stock solution in glass bottles, after 24h the adsorbent is removed from the solution and dried for 3h at 80°C in a drying oven. The remaining solution is retained, with a sample prepared for Atomic Absorption Spectroscopy (AAS) with a dilution factor (DF) of 20.000.

Wet traps are loaded with 150.00 g of 0.1M HNO3. 1.00g of Cs loaded adsorbent is weighed out into a quartz sample boat. Cooling water, kept at 15.1°C, is flowed through the internal cool loop and through the external tubing. Argon gas is flowed through the set-up at ϕ_g=10.2 cm^3/min, controlled by a Mass Flow Controller. The furnace is then heated to its final temperature, as determined by the thermocouple, where it is kept for 3h, after which it is cooled to room temperature.

The wet traps are then sampled for Atomic Absorption Spectroscopy. The spent adsorbent is retrieved and kept. The whole rig is then meticulously disassembled and cleaned. The protective quartz cover, the quartz boat and the quartz wool are retained. The quartz tube, with the connected flanges and caps are then washed with 200.00 g of 0.5M u-HNO3, followed by three washes with 100.0g of u-H2O. Each fraction of the wash is retained and added to the quartz wool, boat and cover. These are then contacted and shaken for 12h to ensure all Cs present on the quartz components is in solution, after which AAS samples are prepared from the wash solution.

Results and Discussion
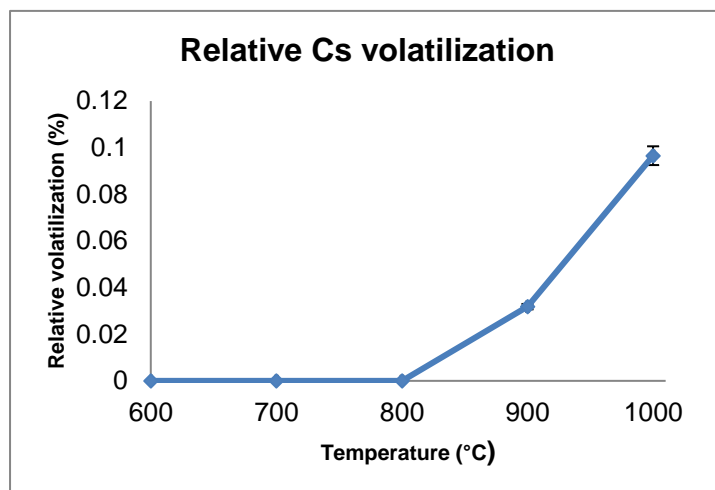
Figure 3 Relative Cs volatilisation from commercial zeolitic adsorbent

The adsorbent exhibited no volatilization below 800°C, as seen in Figure 4. At 900°C the adsorbent had a low
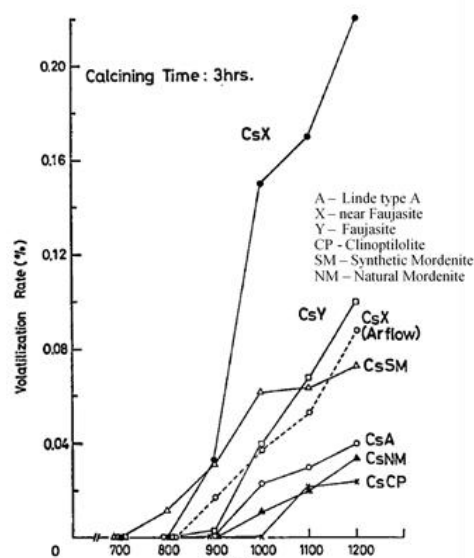

Figure 4 Volatilisation data of Cs adsorbents, adapted from Mimura and Kanno[6]

relative volatilization of 0.032%, with a three-fold increase seen between 900°C and 1000°C.

The commercial behaves in a similar fashion to the data from Mimura and Kanno with their relative volatilization behaviour remaining below 0.1% in all experiments.

The reported data from Mimura and Kanno concerns the behaviour of Linde Type A, faujasite, mordenite, clinoptilolite, all of which have high reported Cs selectivities[7]. If we compare our Cs selective adsorbent, to the adsorbents from the Mimura and Kanno study, we should see similar behaviour. The Cs selectivity of the adsorbent tested, with a high Cs selectivity corresponding to lower volatilization rates, determines the volatilization behaviour of Cs from the adsorbents.

Conclusions and Future Work

The clean-up of the Fukushima Daiichi site continues to generate large volumes of spent adsorbents which need to be disposed of permanently. One of the candidates is a low temperature immobilisation process to avoid volatilising radioactive Cs and Sr species. Detailed radionuclide volatilisation experiments were performed at Hitachi Research Laboratories in Japan, to investigate possible Cs volatilisation behaviour from a commercial zeolitic adsorbent. Cs volatilisation was shown to be negligible, in most cases below detection limits, at temperatures below 800ºC, with volatilisation starting at 800 ºC and strongly increasing above 800ºC.

Acknowledgements

References

1.   M.H. Langowski, J.G. Darab, and P.A. Smith, Volatility Literature of Chlorine, Iodine, Cesium, Strontium, Technetium and Rhenium; Technetium and Rhenium Volatility Testing, Pacific Northwest National Laboratory, Editor. 1996, US Department of Energy,: Oak Ridge, USA.

2.   D. Pletser, R.K. Chinnam, M. Kamoshida and W.E. Lee. Immobilisation process for contaminated zeolitic ion exchangers from Fukushima MRS Advances, 2017, 1-6. DOI: 10.1557/adv.2017.194

3.   D.M. McPherson, B.W. Bowan, and L.D. Pye. The Dissolution of Zeolitic Compounds in Borosilicate Glass Melts. International Congress on Glass. 1986. New Delhi, India.

4.   W.J. Gray, Volatility of some potential high-level radioactive waste forms. Radioactive Waste Management, 1980. 1(2): p. 147-169.

5.   H. Kamizono, S. Kikkawa, S. Tashiro, and H. Nakamura, Volatilization of Cesium from Nuclear Waste Glass in a Canister. Nuclear Technology, 1986. 72(1): p. 84-88.

6.   H. Mimura and T. Kanno, Procesing of Radioactive Waste Solution with Zeolites, (IV). Journal of the Atomic Energy Society of Japan / Atomic Energy Society of Japan, 1978. 20(4): p. 282-287.

7.   M.W. Munthali, E. Johan, H. Aono and N. Matsue, Cs^+ and Sr^{2+} adsorption selectivity of zeolites in relation to radioactive decontamination, Journal of Asian Ceramic Societies, 2015, 3, 245–250.

Ab initio Molecular Dynamics Simulations of Magnesium, Calcium and Strontium Hydrated Hydroxides

O. Lynes*[1], A.Kerridge*[1] , J. Austin[2]

*Correspondence: o.lynes@lancaster.ac.uk, a.kerridge@lancaster.ac.uk

[1] Department of Chemistry (Lancaster University, Bailrigg, Lancaster, LA1 4YB. UK))
[2]   NNL, 5th Floor, Chadwick House , Warrington Road, Birchwood Park, Warrington, WA3 6AE

Abstract

In order to ensure the safe reprocessing of the legacy waste storage ponds at Sellafield in Cumbria the sludge which has formed at the bottom of the ponds must be characterised. This project uses *ab initio* molecular dynamics to study the interactions of Mg^{2+}, Ca^{2+} and Sr^{2+} ions with water as well as in the presence of hydroxide ions. The average coordination number and first solvation shell properties have been investigated at 400 K and are presented here. A complete solvation model of these ions both with water and hydroxide is key to the understanding the behaviour exhibited in the legacy storage ponds.

Introduction

High and intermediate level nuclear waste, such as spent uranium fuel roads and their magnesium-aluminium alloy cladding (Magnox), are held in storage ponds at the Sellafield site in North West England.[1] Over time the corrosion of the Magnox cladding into the mineral brucite, as well as variation in external conditions, have led to a fine particulate sludge forming in the legacy ponds.

This sludge is mainly comprised of brucite and the organic matter which has blown into the ponds; in particular, there is thought to be carbonate and hydroxide complexes of the radionuclide [238]U and two of its fission products, ^{90}Sr and [137]Cs. These radionuclides will be incorporated into the mineral sludge to varying degrees. Characterisation of this sludge can aid effective reprocessing and as such is a key area of research.

Due to the high radioactivity within the ponds a computational approach offers significant advantages when investigating the behaviour of the various radionuclides which are present and how they adsorb onto the minerals present in the sludge, without the risks associated with working with radioactive materials.

By computationally studying the composition of the radionuclides found in the water of the legacy waste ponds we can gain an understanding of their solvation behaviour, before investigating interactions with the minerals present in the sludge itself.

This problem has been previously approached using gas phase Density Functional Theory (DFT) which is used to find the lowest energy conformation of a given system. *Ab initio* molecular dynamics (AIMD) can instead be used to calculate the electronic structure of a given system at regular intervals within a set timescale. AIMD generates a trajectory for each atom in a system, meaning in this case that the coordination of the dications in bulk solution environments can be examined in a dynamic context.

The use of *ab initio* molecular dynamics in this project is of great relevance to the development of strategies for the continued storage and disposal of nuclear waste. It represents be the first time this methodology has been used to address this issue, and builds on work previously performed by Kerridge and Kaltsoyannis into the coordination of aquo and hydroxide complexes of strontium.[2–4]

Methodology Details

All AIMD calculations were carried out with CP2K (version 3.0).[5] The PBE Generalised Gradient Approximation (GGA) exchange-correlation functional was used with Double Zeta Valence Polarised (DZVP) basis sets.[6] A van der Waals dispersion correction was applied to all the systems. The Gaussian Augmented Planewave method (GAPW) was used with Goedecker-Teter-Hutter (GTH) pseudopotentials.

Periodic boundary conditions were used with an initial cell length of 11.99 Å which was treated as an isotropic cell keeping pressure and temperature constant. A

Nosè-Hoover thermostat was used to maintain the temperature of the systems at 400 K.

5 unique trajectories were each run for 20 picoseconds (ps) with an equilibration period of 5 ps, for a total simulation time of 100 ps.

Water Systems

Each system is comprised of 64 water molecules, with a central dication of either magnesium, calcium or strontium.
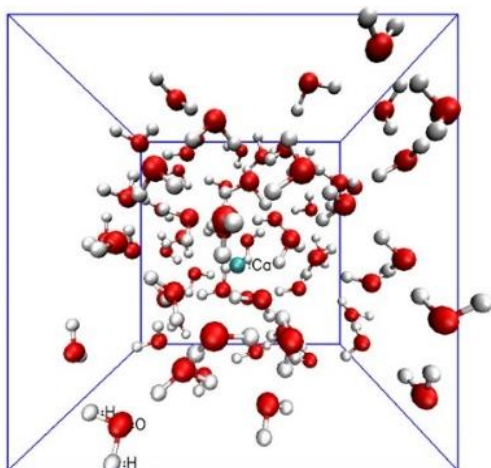

Figure 1: Visual representation of a 64-water molecule cell with a Ca²⁺ ion at its centre

Hydrated Hydroxide Systems

62 water molecules and two hydroxide anions surround the central di-cation of either magnesium, calcium or strontium. The initial first shell coordination (<3 Å) of the hydroxide ion was varied. The system was either a di-hydroxide (both OH- at a distance < 3Å from the ion), mono- hydroxide (both OH- at a distance < 3Å from the ion), or aquo complex in which neither hydroxide was in the first solvation shell.
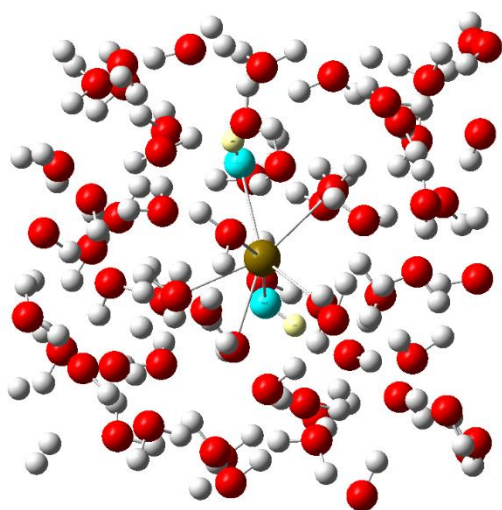
Figure 2: Visual representation of a Strontium dihydroxide. Two OH-ions (O- blue, H- Yellow) with a Sr²⁺ ion (brown) in the centre.

Results and Discussion

For analysis purposes, every 10th time step is used in the characterisation of the dynamics of these systems, this reduces the amount of data which is to be analysed while still giving a full picture of how the various species in the systems are behaving.

Water Systems

First Shell Characterisation

The average metal oxygen (M-O) bond length for the first solvation shell was measured at each step of the simulation. The coordination number has been analysed per the direct method protocol detailed by Hofer. *et al* where variation in coordination number is only considered to be a true transition if its duration is longer than 0.5 ps.[7] All instances where a coordination number change occurs for less than 0.5 ps have therefore been ignored in the analysis. The cutoff for the first solvation shell was set at 2.6, 3 and 3.2 Å for Mg, Ca, Sr respectively.

The standard deviation in these averages was also calculated to show the variance in the 100 ps of data collected. These results are shown in Table 1.

	M-O/ Å	CN
Mg	2.16 (0.02)	6(0.00)
Ca	2.54 (0.07)	7.39(0.29)
Sr	2.66 (0.02)	7.99(0.03)

Table 1: Average M-O bond length (std deviation) for the first solvation shell Å. Average first shell coordination number (std deviation).

For Mg the average bond length is slightly larger than is seen in both computational and experimental literature (2.08 - 2.12 Å)[8–10], however the coordination number of 6 is in line with all current literature which all suggests an hexahydrated structure for magnesium.

For Ca both the computational and experimental literature gives a range of both bond length and first shell coordination number, average first shell bond lengths range between 2.39 - 2.68 Å with coordination numbers from 6-8 seen in the literature. [11–13] Our results fall well within this range, with a Ca-O bond length of 2.52 Å with a CN of 7.3, and we see Ca coordination numbers of 6,7 and 8 are seen in various instances.

For Sr, our average Sr-O bond length of 2.66 Å is in excellent agreement with experimental (2.60-2.67 Å)[10,14–16] and good agreement with computational data

(2.57-2.63 Å). [2,7,14,17] . The coordination number of strontium has been reported to be 6-9 in computational and experimental literature;[18–21] our data is in good agreement. We have calculated an average coordination number of 7.99 and structures with coordination numbers of 7, 8 and 9 are seen in various simulations.

For all systems, we can be confident that the solvation model developed is sufficiently accurate that it shows a clear picture of the behaviour of these radionuclides.

Hydrated Hydroxide Systems

First Shell Characterisation

In the same way as the water systems the average metal-oxygen (M-O) bond length for the first shell of each system was calculated with the standard deviation based on the multiple trajectory runs. A total coordination number for the first shell was calculated as well as a hydroxide coordination number. The hydroxide coordination number indicates the average number of hydroxides in the first solvation shell over the timescale of the reaction. The results are presented in Table 2.

	M-O/Å	Total CN	OH CN
Mg	2.16 (0.03)	5.95 (0.13)	1.03 (0.12)
Ca	2.52 (0.06)	6.61 (0.25)	0.74 (0.08)
Sr	2.68 (0.04)	7.56 (0.26)	0.30 (0.05)

Table 2: Average first shell coordination number (CN) and first shell oxygen- hydroxide CN.

While the average M-O bond length for all systems remains unchanged for all but strontium, there has been a more obvious impact on the coordination structure with the inclusion of hydroxides into the system.

In all cases the total average coordination number of the first solvation shell reduced with the inclusion of the hydroxides, while this was only slight in the case of magnesium it was a reduction of 0.69 for calcium, and 0.43 for strontium.

Magnesium showed the most signs of having a stable structure with a least one hydroxide in the first solvation shell and an average OH CN of 1.03, this reduced with Ca having a OH CN of 0.74 and Sr a OH CN of just 0.30 suggesting that the most favourable solvation structures were when both hydroxide ions were outside of the first solvation shell.

Although di-hydroxide structures were seen in the case of magnesium and calcium, there is only one instance of a dihydroxide strontium complex across all the simulations.

Proton Transfer Events

As well as characterising the solvation structure of the first shell of the hydrated hydroxides, the movement of the hydroxides through the system is also of interest.

Hydroxides move through a body of water either via a proton transfer event (PTE), whereby a proton moves from a nearby water to the current hydroxide, or via hydroxide migration where an OH⁻ moves as a unit through a system. We have calculated the average number of PTEs which are shown in Table 3.

A PTE is defined as having occurred if it lasts for a timescale of longer than 200 fs which is the assumed timescale of a completed proton transfer.[22,23] Any PTE which occurs on a timescale less than 200 fs is not included in the analysis.

	Average PTE	Std. Dev
Mg	20.07	3.75
Ca	22.67	5.09
Sr	27.00	4.79

Table 3: Positions of average proton transfer events (PTE) and Standard deviation (Std. Dev) for each metal.

The average number of PTEs increases down the group, from 20.07 to 27.00. Sr has the largest average number of PTEs combined with the low OH CN in the first shell perhaps suggesting that by a reduced coordination of the OH⁻ with the metal ion, the hydroxide more readily undergoes proton transfer in the wider bulk system. However, to be sure of this, further analysis of when PTEs occur and the coordination of the OH⁻ to the metal ion at that time needs to be performed

Conclusions and Future Work

The clear agreement of our water model with both experimental and computational data demonstrates that we have developed an accurate solvation model for use in future simulations. For the hydroxide systems, further investigation into the proton transfer behaviour and the coordination of the hydroxide ion to the metal centre is required to provide a better understanding of the system.

The next phase of the research is to introduce an oxide surface into both the water and the hydrated hydroxide systems. UO_2 is one of the main minerals of interest in the nuclear fuel storage ponds and we are interested in the absorption of radionuclides onto the mineral surface. Due to the computational complexities of modelling UO_2 a solid oxide surface of cerium dioxide will be developed. CeO_2 is a well-known analogue for uranium dioxide, as it closely resembles the mineral structure of fuel grade UO_2. It is already used both computationally and experimentally with good results.

Bulk oxide calculations of CeO_2 optimising the structure of a 2x2x2 supercell have already been completed, and testing has begun adding water molecules into this system. The aim is to have a CeO_2 surface in contact with 64 water molecules, and then introduce the radionuclide species and hydroxides into the simulations.

Acknowledgements

References

1 S. a. Parry, L. O'Brien, A. S. Fellerman, C. J. Eaves, N. B. Milestone, N. D. Bryan and F. R. Livens, *Energy Environ. Sci.*, 2011, **4**, 1457.

2 A. Kerridge and N. Kaltsoyannis, *Chem. A Eur. J.*, 2011, **17**, 5060–7.

3 E. Makkos, A. Kerridge and N. Kaltsoyannis, *Dalt. Trans.*, 2015, 11572–11581.

4 A. Kerridge and N. Kaltsoyannis, *Dalton Trans.*, 2011, **40**, 11066–9.

5 J. Hutter, M. Iannuzzi, F. Schiffmann and J. VandeVondele, *Wiley Interdiscip. Rev. Comput. Mol. Sci.*, 2014, **4**, 15–25.

6 M. Ernzerhof and G. E. Scuseria, *J. Chem. Phys.*, 1999, **110**, 5029.

7 T. S. Hofer, H. T. Tran, C. F. Schwenk and B. M. Rode, *J. Comput. Chem.*, 2004, **25**, 211–7.

8 T. Tofteberg, A. Öhrn and G. Karlström, *Chem. Phys. Lett.*, 2006, **429**, 436–439.

9 C. W. Bock, A. Kaufman and J. P. Glusker, *Inorg. Chem.*, 1994, **33**, 419–427.

10 S. Ramos, G. W. Neilson, a. C. Barnes and M. J. Capitán, *J. Chem. Phys.*, 2003, **118**, 5542.

11 I. Bakó, J. Hutter and G. Pálinkás, *J. Chem. Phys.*, 2002, **117**, 9838–9843.

12 F. Jalilehvand, D. Spångberg, P. Lindqvist-Reis, K. Hermansson, I. Persson and M. Sandström, *J. Am. Chem. Soc.*, 2001, **123**, 431–441.

13 M. M. Naor, K. Van Nostrand and C. Dellago, *Chem. Phys. Lett.*, 2003, **369**, 159–164.

14 G. Moreau, L. Helm, J. Purans and E. Merbach, *Transition*, 2002, 3034–3043.

15 L. Axe, G. B. Bunker, P. R. Anderson and T. a Tyson, *J. Colloid Interface Sci.*, 1998, **199**, 44–52.

16 T. M. Seward, C. M. B. Henderson, J. M. Charnock and T. Driesner, *Geochim. Cosmochim. Acta*, 1999, **63**, 2409–2418.

17 D. Di Tommaso and N. H. de Leeuw, *Cryst. Growth Des.*, 2010, **10**, 4292–4302.

18 D. Harris, *J.Phys.Chem.B*, 2003, **107**, 9056–9058.

19 R. Caminiti, R. Caminiti, A. Musinu, A. Musinu, G. Paschina, G. Paschina, G. Pinna and G. Pinna, *J. Appl. Crystallogr.*, 1982, **15**, 482–487.

20 S. Ramos, G. W. Neilson, a. C. Barnes and M. J. Capitán, *J. Chem. Phys.*, 2003, **118**, 5542.

21 D. M. Pfund, J. G. Darab, J. L. Fulton and Y. Ma, *J. Phys. Chem.*, 1994, **98**, 13102–13107.

22 G. Tocci and A. Michaelides, *J. Phys. Chem. C*, 2014, **5**, 474.

23 A. Hassanali, F. Giberti, J. Cuny, T. D. Kühne and M. Parrinello, *Proc. Natl. Acad. Sci. U. S. A.*, 2013, **110**, 13723–8.

Developing the use of an Acoustic Backscatter system (ABS) to measure the concentration of nuclear simulants under varying degrees of flocculation

A.S.Tonge[1], S. Freear[2], J. Peakall[3], T.N. Hunter[1]

*Correspondence: pm11a2t@leeds.ac.uk

[1] School of Chemical and Process Engineering (University of Leeds, LS2 9JT, UK)
[2] School of Electronic and Electrical Engineering (University of Leeds, LS2 9JT, UK)
[3] School of Earth and Environment (University of Leeds, LS2 9JT, UK)

Abstract

It is proposed here that further research efforts should be made in order to develop the use of acoustic backscatter to measure concentration in flocculated systems. The use of acoustics is generally widespread in marine, food and water treatment industries and has great potential in applications where access to process fluid presents a chemical or radiological hazard. Despite the fact that there have been many developments made recently by various authors to better understand how acoustic models can be developed to further to broaden their applications to measuring particle size and concentration in flocculated or otherwise cohesive systems there is not a robust model relating flocculated particle structure to its acoustic backscatter properties.

Introduction

Acoustical equipment is used routinely to study sediment transport in coastal and estuarine environments as well as for measuring the flow of currents and their profiles. Sediment transport is calculated from the suspended sediment concentration which can be estimated from the intensity of the backscattered signal [1] [2]. This method of concentration measurement, however, relies on taking a large number of samples in order to determine an empirical relationship between concentration and the backscattered signal intensity which could prove to be both difficult and costly in applications where chemical or Radiological hazards make access to process fluid dangerous or completely impossible. This method also fails to describe the level of flocculation present within the system which can be very important information for both sedimentological and for industrial applications such mineral settling and water treatment operations where settling rates are critical in the design and operation of process equipment [3] [4].

Recent Developments

When attempting to fit experimental values of the particle species backscatter coefficient (k_s) (one of two parameters that define the acoustic properties of a particulate system) to those predicted by the Elastic Sphere and Fluid Sphere models it was found that, although the ES and FS models bounded their data it was not in the way that was first hypothesized as they expected that the experimental data would move from fitting the ES better at smaller sizes and the FS as the flocs grew larger, less dense and incorporated more water [4]. This was not the case however and even applying a distributed mass model to account for floc density change gave results that suggested an alternative model is required [5].

Further to this, Vincent and MacDonald [5] proposed their "flocculi model" when they found that data from a forward-scattering light device (LISST-100) gave particle sizes three times smaller

than that of a camera for flocculated particles and inversion of the ABS data gave particle sizes similar to that seen by the LISST it was proposed, as this phenomenon had been seen previously by Graham [6] with an incredibly high resolution holocamera and other authors [7] [8] , that both the light and ultrasound were interacting, not with the whole structure of the floc, but with flocculi [5]. The small, tightly-bound structures that comprise it. Although the correlation coefficient was typically only 0.44-0.49 when correlating the ABS size data with the LISST-100 If this model can be confirmed, in particular within equipment that does not suffer from the bias toward measuring smaller particles more often and is more in-situ, then samples from flocculated systems would not need to have the structure of the macro flocs preserved during transport making samples more reliable in terms of their acoustic properties even if they have undergone some small amount of shear. [5].

The dual frequency method is a concentration inversion method whereby, if k_s, k_t (the transducer constant), ζ (particle attenuation coefficient) and α (the attenuation coefficient) are known for two different frequencies the concentration at any point in the system can be calculated so long as the backscatter and attenuation coefficients have been found by taking measurements at the desired two frequencies in a homogeneous vessel [9]. The following equation is used to calculate concentration profiles from backscattered signals.

$$M_l = \left(J_{i,l}\right)^{\frac{1}{\left(1-\frac{\xi_i}{\xi_k}\right)}} \left(J_{k,l}\right)^{\frac{1}{\left(1-\frac{\xi_i}{\xi_k}\right)}}$$

Where $J_{i,l}$ and $J_{k,l}$ corresponds to the normalised intensities at frequencies I and k and M is concentration. The advantages of this method are that no assumption needs to be made for the sediment attenuation at any gate in the profile and by eliminating the attenuation integrals the propagation of errors along the profile is avoided.

For the direct inversion the following equation is used from [10]

$$M_i = \left\{\frac{V_{rmsi}}{k_{si}k_{ti}}\right\}^2 \psi_i^2 r^2 e^{4r\alpha_i}$$

Where V_{rmsi} is the root mean square received backscatter voltage, ψ is the near field correction factor and r is the distance from the transducer. This paper details acoustic measurements taken using an Ultrasonic Array Research Platform (UARP) and the concentration profiles produced using both the single frequency and dual inversion method and comparing the two results to expected values.

Methodology Details

Materials
Glass beads (Honite-16, Guyson) were used for

Table 1 Details of Material used in new calibration tank

Material	Supplier	Particle Size (µm)
Honite-16	Guyson	53 - 106

Experimental Setup
Measurements were taken in a water column of height 50 cm and diameter 30cm with a conical base leading to peristaltic pump used to recirculate fluid to the top of the column and a stirrer set at 500 RPM in order to ensure a homogeneous distribution of solids throughout the column as shown in **Error! Reference source not found.Error! Reference source not found.**. The UARP was developed in house at Leeds University by David Cowell and allows for measurements of 16 channels at a range of frequencies. Samples were taken simultaneously at three depths; 10cm, 20cm and 30cm below the waterline. The first 10cm of the tank are assumed not to be homogenous as the recirculating fluid would not have had time to mix in to the bulk. Honite-16 concentration in the tank was varied at a number of concentrations between 2 and 133.7 g l^{-1}. Three Sonatest brand transducers were used with central frequencies of 1, 2 and 5 MHz respectively. Each operated at its central

frequency and two frequencies slightly above and below the central frequency.
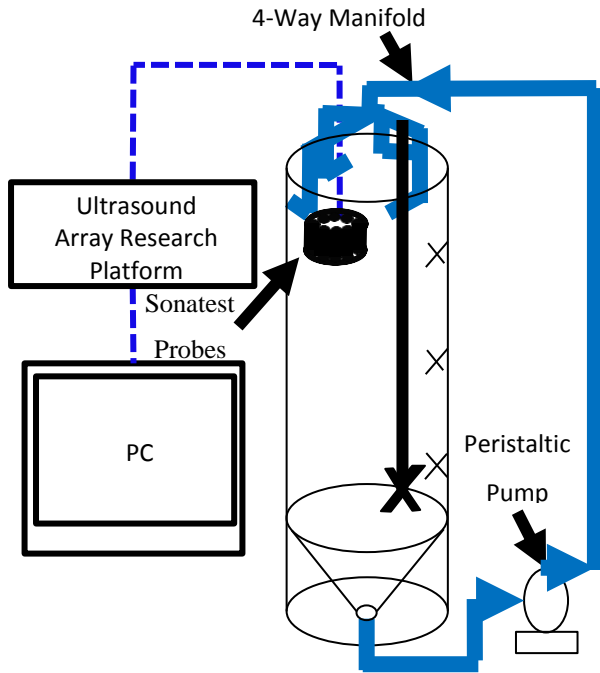

Figure 1 Experimental setup for acoustic measurements

Results and Discussion

Firstly, it was seen that when attempting to use a single probe for a dual-frequency inversion method (figure 2) the scatter on the dual frequency plots was much greater than that of the single-frequency method. This is likely caused by the ratio of the two attenuation coefficients at each frequency being too close to unity to correctly solve for the concentration profile from the backscattered signal. Data from the 1 MHz probe was therefore used with data from the 2 MHz in order to obtain attenuation ratio values that were not as close to unity and concentration profiles produced as shown in figure 3. It can be seen that the scatter was then greatly reduced although direct inversion of the 2 MHz voltage profiles gave highly erroneous results (not shown here).

Furthermore, the resultant dual frequency profile is observed to increasingly underestimate concentration in the column with increased solids content above 12.8 g l^{-1}. The cause of this is most likely due to the assumption that there is no inter-particle scattering being invalid at high particle concentrations where attenuation due to this effect will be greater. Although this assumption is also applied in the standard inversion the dual frequency method multiplies the result from two

profiles (J_1 and J_2) together and so the error will therefore be greater. This has been seen previously by Hurther et al. [10] as they found a limit of 60 kg m^{-3} up to which the dual frequency inversion gave good agreement with optical backscatter measurements.
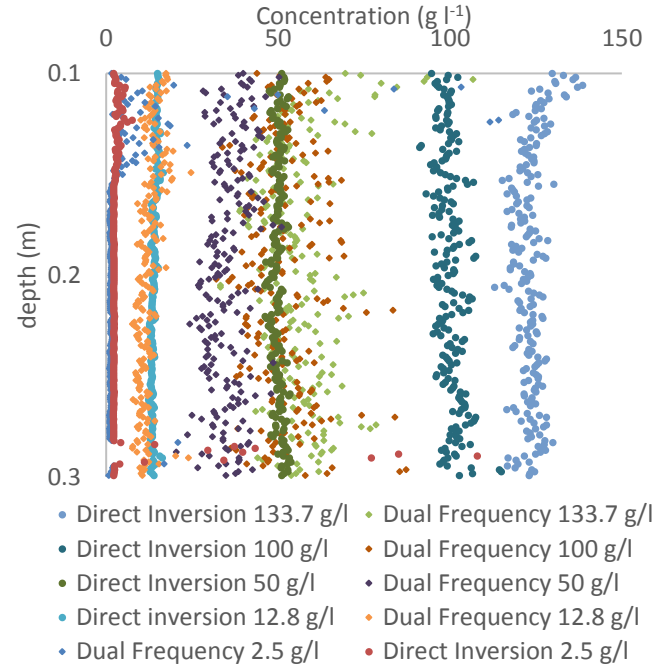
Figure 2 Showing concentration profiles obtained using the UARP with 0.85 MHz used for Direct Inversion and 0.85 & 1.15 MHz used for dual frequency inversion
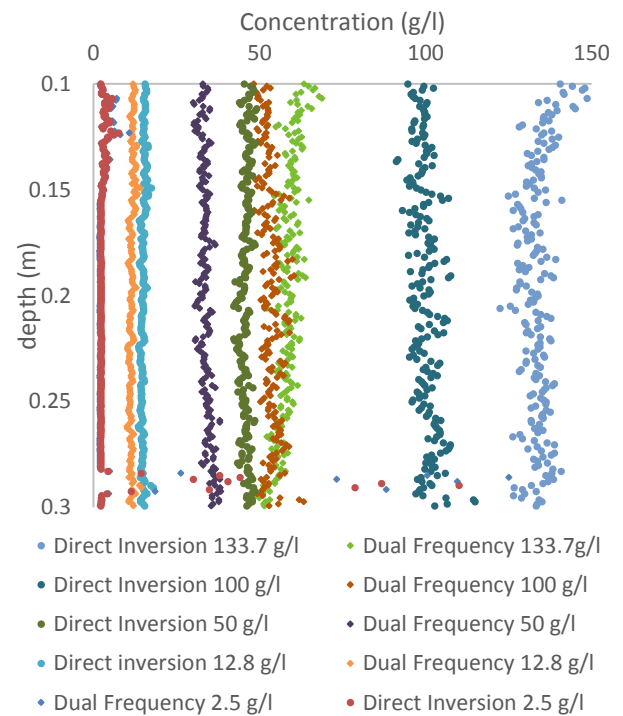
Figure 3 Showing concentration profiles obtained using the UARP with 2 MHz used for Direct Inversion and 0.85 & 2 MHz used for dual frequency inversion

Conclusions and Future Work

It can be seen, therefore, that an accurate model for the interaction of flocculated particles with acoustic devices is somewhat lacking but that recent results support the novel concept of the flocculi model which would seem to explain previously anomalous results as well as suggest that sampling need not be done so carefully as the structure of the macro-flocs will not need to be preserved [5]. More laboratory work must be done to confirm this new model utilising more reliable, in-situ techniques to measure size/degree of flocculation accurately and thereby try and find a relationship between the degree of flocculation and the backscatter and attenuation coefficients so that accurate concentration profiles can be produced for the simulant systems and any real-world systems that have similar acoustic properties if taking samples for calibration would prove too costly [11] [3] [12] [5].

A Saturn Digisizer is to be used to determine the size of flocs at different concentrations of simulant and flocculent as it utilises a peristaltic pump to recirculate the flocs rather than the impeller used by the mastersizer. This will ensure that flocs are not broken during measurement and therefore their size can be accurately determined without breaking up their structure. The Saturn is also capable of determining the fractal dimension; A parameter that allows for prediction of the change in floc density with floc size which determines the fractal structure of the floc.

References

[1] K. Deines, "Backscatter estimation using broadband acoustic Doppler current profilers," in *Proc. Sixth Working Conf. on Current Measurement*, San Diego, CA, 1999.

[2] D. C. Fugate and C. T. Friedrichs, "Determining concentrations and fall velocity of estuarine particle populations using ADV, OBS and LISST," *Continental Shelf Research, 22,* pp. 1867-1886, 2002.

[3] T. N. Hunter, L. Darlison, J. Peakall and S. Biggs, "Using a multi-frequency acoustic backscatter system as an in situ high concentration dispersion monitor," *Chemical Engineering Science 80,* pp. 409-418, 2012.

[4] I. Macdonald, C. Vincent, P. Thorne and B. Moate, "Acoustic scattering from a suspension of flocculated sediments," *Journal of Geophysical Research,* pp. 2581-2594, 2013.

[5] C. Vincent and I. MacDonald, "A flocculi model for the acoustic scattering from flocs," *Continental Shelf Research 104,* pp. 15-24, 2015.

[6] G. Graham, E. Davies, W. Nimmo-Smith, D. Bowers and K. Braithwaite, "Interpreting LISST-100X measurements of particles with complex shape using digital in-line holography," *Journal of Geophysical Research: Oceans 117,* p. C05034, 2012.

[7] O. Mikkelsen, P. Hill, T. Milligan and R. Chant, "In situ particle size distributions and volume concentrations from a LISST-100 laser particle sizer and a digital floc camera," *Continental Shelf Research 25,* pp. 1959-1978, 2005.

[8] P. Hill, J. Newgard, B. Law and T. Milligan, "Flocculation on a muddy intertidal flat in Willapa Bay, Washington, Part II: Observations of suspended particle size in a secondary channel and adjacent flat," *Continental Shelf Research 60 (Suppl.),* pp. S145-S156, 2013.

[9] H. Rice, M. H. T. Fairweather, B. Mahmoud, S. Biggs and J. Peakall, "Measuring particle concentration in multiphase pipe flow using acoustic backscatter: Generalization of the dual-frequency inversion method," *Journal of the Acoustical Society of America 136 (1),* pp. 156-169, 2014.

[10] A. Hay and J. Sheng, "Vertical profiles of suspended sand concentration and size from multifrequency acoustic backscatter," *Journal of Geophysical Research, 97 (C10),* p. pp. 15661–15677, 1992.

[11] D. Hurther, P. D. Thorne, M. Bricault, U. Lemmin and J.-M. Barnoud, "A multi-frequency Acoustic Concentration and Velocity Profiler (ACVP) for boundary layer measurements of fine-scale flow and sediment transport processes," *Coastal Engineering 58,* pp. 594-605, 2011.

[12] P. Thorne and R. Meral, ""Formulations for the scattering properties of suspended sandy sediments for use in the application of acoustics to sediment transport processes," *Continental Shelf Research 28,* pp. 309-317, 2008.

Gas release from weakly consolidated nuclear legacy waste

M. Johnson*[1], J. Peakall[2], M.Fairweather[1], S. Biggs[3], D. Harbottle[1] and T.N. Hunter[1]

*Correspondence: pm12mcj@leeds.ac.uk

[1] *School of Chemical and Process Engineering, University of Leeds, Leeds, LS2 9JT, UK*
[2] *School of Earth and Environment, University of Leeds, Leeds, LS2 9JT, UK*
[3] *Faculty of Engineering, Architecture and Information Technology, University of Queensland, Brisbane, Qld 4072, Australia*

Abstract

Retention of hydrogen bubbles within consolidated soft sediments represents an important safety consideration for the management of legacy nuclear wastes due to the potential for acute gas release. X-ray computed tomography analysis of oxygen bubbles within low-intermediate strength (7-234 Pa yield stress) magnesium hydroxide soft sediments revealed that the largest *mature* bubbles exhibit surprisingly long residence times in the bed, which implies that continuous gas release is governed by a novel mechanism involving sub-millimetre bubbles rather than by the most buoyant population. A new x-ray tomography configuration at reduced scale and increased resolution has enabled the visualisation of a vast population of pore to millimetre scale bubble features which account for over 90 % of the bulk voidage. Three-dimensional image analysis has shown that these sub-millimetre bubbles grow with increased aspect ratios within more consolidated sediments, while these sub-millimetre bubbles are able to form extensive three dimensional networks, even within weakly consolidated sediments, thus enabling transport of retained gas over length-scales of many centimetres. The propagation of permeable bubble networks by capillary invasion is greatly influenced by the microstructure of the bed; a methodology is outlined for characterising pore size distributions of consolidated nuclear legacy waste test materials using a combination of nuclear magnetic resonance and mercury intrusion porosimetry, revealing pore throat radii in the range of 0.08-0.2 μm within a 42.3 % w/w sample of corroded magnesium sludge.

Introduction

In situ gas generation and retention represents a major consideration for the management of consolidated intermediate level waste (ILW) found at Sellafield, UK and Hanford, USA [1, 2]. Hydrogen bubbles are generated by corrosion of first generation cladding materials, such as aluminium and the Magnox alloy [3], and by radioactive decay of water soluble fission products such as caesium and strontium [2]. Previous work [4] has shown that realistic void fractions of 0.16-0.28 would reduce the bulk density of intermediate strength wastes ($\tau < 500$) towards that of an aqueous supernatant, thereby requiring measures to mitigate against acute releases from buoyant *rollover events*.

A bubble within a consolidated soft sediment quickly grows to the scale of pores within the bed [5], at which point growth will be governed by the mechanical, interfacial and microstructural properties of the sediment [6]. It is predicted that low strength, fine grained sediments exhibit minimal resistance to elastic expansion of the bubbles' host cavity [5], whereas high strength, coarse grained sediments are more likely to promote growth into adjacent pore space by capillary invasion [7]. Very highly consolidated sediments may fracture under the pressure exerted during bubble growth, thus enabling gas transport through the bed along these fracture sites [5, 7].

Large scale clinical x-ray computed tomography (CT) has been effective in characterising the mature bubble populations retained in magnesium hydroxide soft sediments and how they evolve over time [5, 8]. Large bubbles of up to 9 mm equivalent spherical diameter have been shown to exhibit long residence times within 7-234 Pa yield stress sediments, implying that the primary mechanism for gas release is not governed by fluidisation of the bed by discrete bubbles with the greatest buoyant force but rather by the bubble population which is only visible below 250-500 μm resolution [8]. X-ray CT has been undertaken at the University of Queensland achieving resolutions an order of magnitude smaller than the previous study [8], enabling analysis of bubble networks closer to pore-scale to investigate discrete avenues for gas transport. Growth of these sub-millimetre bubble populations is greatly influenced by the microstructure of the sediment [5, 6] and so a technique combining mercury intrusion porosimetry (MIP) and nuclear magnetic resonance (NMR) is outlined for characterising pore size distributions of nuclear legacy waste and other consolidated soft sediments.

Methodology

Materials

Two test materials used in this work include a commercial magnesium hydroxide powder, Versamag (Martin Marietta Specialities, USA), and corroded magnesium sludge (CMgS, Sellafield ltd., UK). The former is mixed with water and agitated with an overhead stirrer, enabling the simple formulation of varied solids concentration and yield stress conditions. The latter test material has been synthesised by Sellafield ltd. to better approximate of the particle size distribution and mechanical properties of corroded Magnox sludge (CMS) [9]. For each test material, *in situ* bubble generation is imitated at accelerated time-scales by the decomposition of hydrogen peroxide (Merck Chemicals, Germany) to form oxygen bubbles[4, 8].

X-ray computed tomography

Gas retention tests were performed by decomposing 1.5 ml H_2O_2 in 360 ml $MgOH_2$ or CMgS soft sediment within a 70 mm diameter 150 mm long sideways mounted cylinder. Following 6 hr *in situ* gas generation the retained bubble population was visualised by x-ray CT performed with an Inveon dual PET/CT scanner (Siemens, Germany) using the scanning parameters summarised in Table 1. Post processing and statistical analysis of the tomographs were undertaken using FIJI Image J [10] and DigiUtility [11, 12].

Table 1 X-ray CT scanning parameters

X-ray voltage (kV$_p$)	80
X-ray tube current (mA)	0.5
FOV diameter (mm)	81.8
Voxel resolution (μm)	53.25
Number of axial slices	1024
Total FOV volume	2.86×10^5

Combined mercury intrusion porosimetry (MIP) and nuclear magnetic resonance (NMR) for pore size characterisation

MIP uses an applied pressure to force a non-wetting fluid, mercury, to intrude into a porous sample. The technique is based on the Washburn equation [13], eq (1), which states that the applied pressure, P, required to invade a pore is inversely proportional to the pore's throat radius, r_{th}:

$$r_{th} = \frac{2\sigma \cos(\theta)}{P} \qquad (1)$$

where σ is the mercury-air surface tension and θ is the mercury-air-$Mg(OH)_2$ three phase contact angle. A pore size distribution can be obtained by observing the mercury intrusion volume across a range of applied pressures. MIP was performed on a sample of CMgS, dried at 100°C, using a 413 MPa porosimeter (Micromeretics, USA).
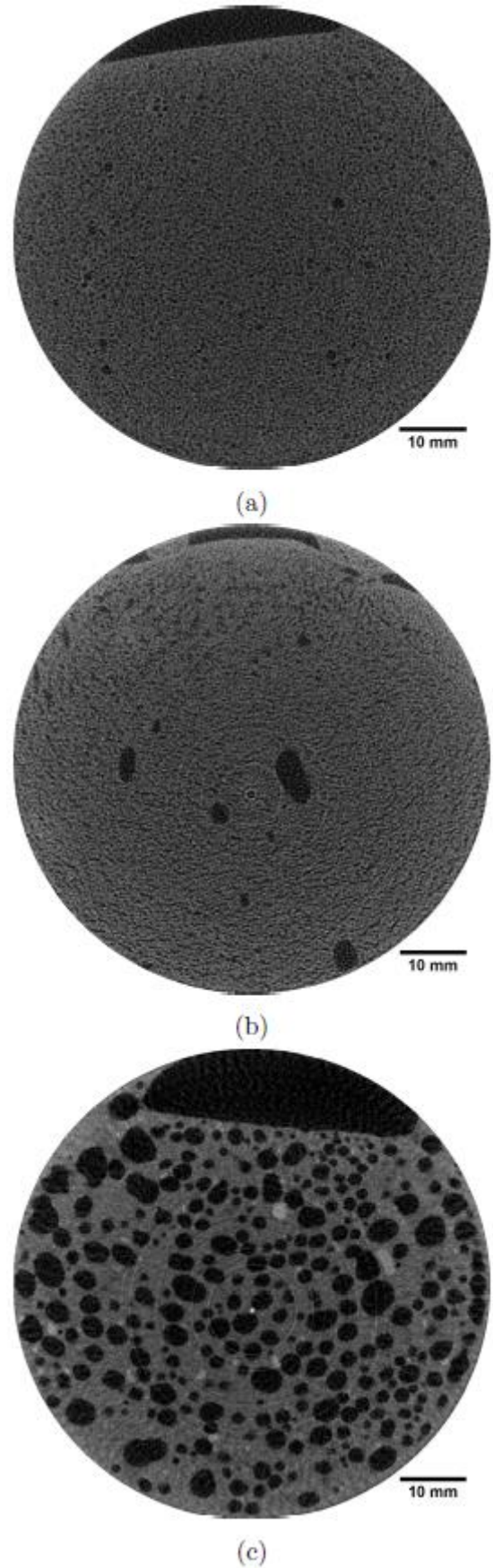
Figure 1 X-ray tomographs of oxygen bubbles retained within (a) 27 Pa and (b) 1112 Pa yield stress magnesium hydroxide soft sediment and (c) 30 Pa corroded magnesium sludge

MIP was employed in conjunction with a low-field NMR MARAN Ultra spectrometer (Oxford Instruments, UK). NMR uses an external magnetic field to manipulate the spin of protons within the free water of a porous material, causing them to align in the direction of the magnetic field. After suspending the magnetic field the protons *relax* away from their uniform orientation. Low field NMR spectroscopy is based on the proportionality between this *transverse relaxation time*, T_2, and the volume to surface area ratio of the pores, with larger pores corresponding to longer relaxation times [13]. The r_{th}/T_2 proportionality is calibrated from a comparison of MIP, performed on dried CMgS, and NMR on a sample of dried CMgS which has been re-saturated with fresh water [13, 14]. This material dependent constant can be used to subsequently calibrate transverse relaxation times for wet sludge samples into pore size distributions, however the technique relies on the assumption of a constant ratio between the pore body and throat radii. It is also possible to interpret further useful characteristics of soft sediments from NMR T_2 spectra including their porosity and permeability [13].

Results and Discussion

X-ray CT of bubbles retained by 27 and 1112 Pa yield stress $Mg(OH)_2$ soft sediments and 30 Pa CMgS are presented in Figure 1. Figure 1a demonstrates an apparently bi-modal population consisting of a honeycomb of fine ($d_b<0.5$ mm) bubbles interspersed with the millimetre scale bubbles previously observed using the lower resolution CT [4,8]. Within the higher strength magnesium hydroxide soft sediment, the large bubbles are observed as distorted ellipsoids with greater aspect ratios, while the sub-millimetre features appear to be fine lateral fractures or dendrites. Both magnesium hydroxide samples contrast with the low strength CMgS sample which retains a substantially narrower size distribution of very coarse bubbles, with little evidence of the sub-millimetre features which constitute the bulk of the voidage within Figure 1a and b. While the CMgS test material is (a) more physically heterogeneous, with a fraction of coarser particles visible as light grey-scales in Figure 1c, (b) contains a small amount of silicon based *sandy* impurities and (c) exhibits a marginally greater increase in shear yield stress with added solids concentration, the justification for this extreme bubble coarsening behaviour remains uncertain.

FIJI Image J and DigiUtility were subsequently used to eliminate ring artefacts, particularly apparent in Figures 1b and c, *despeckle* the larger voids and threshold the images to isolate bubbles and bubble networks from the bulk sediment. After evacuating the bubble voxels, a 600x600x600 pixel (3.26×10^4 mm^3) sub-volume was extracted for analysis. The paths of 250 *random walks* through interconnected void networks within the 27 Pa

$Mg(OH)_2$ sample, starting from the y-z-plane at x=0 (see top right inset of Figure 2) of the sub-volume, are presented in Figure 2. The *walkers* can move orthogonally or diagonally, corresponding to step lengths of 1, √2 or √3 pixels, for up to 10^6 steps with a 0.01 probability of doubling backwards.
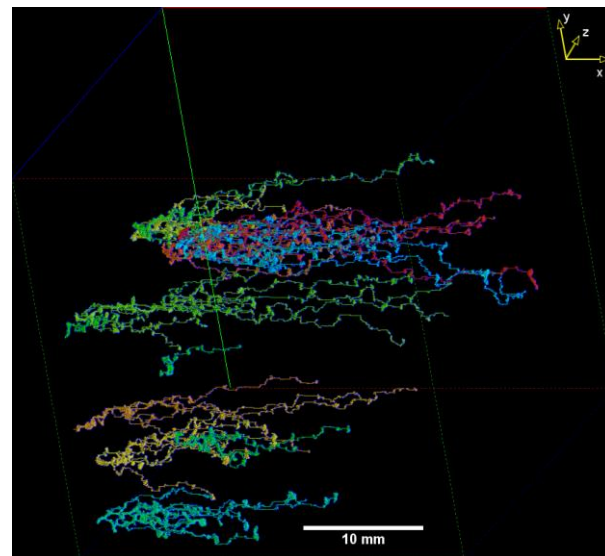
Figure 2 Paths of 250 random walks through retained bubble networks within 35 % w/w ($\tau = 29\ Pa$) magnesium hydroxide soft sediment

The 250 paths shown in Figure 2 traverse an average distance of 63.1 mm, corresponding to almost double the domain length, while some paths demonstrate a continuous interconnected route through the void network of the 31.95 mm wide sub-volume. Conversely, the average chord lengths within this 'free space' is only 0.59 mm indicating that gas is able to diffuse along pathways at least two orders of magnitude larger than the individual bubbles retained by the sediment. Hence, it is realistic that networks of sub-millimetre bubbles can provide extensive pathways for gas transport.
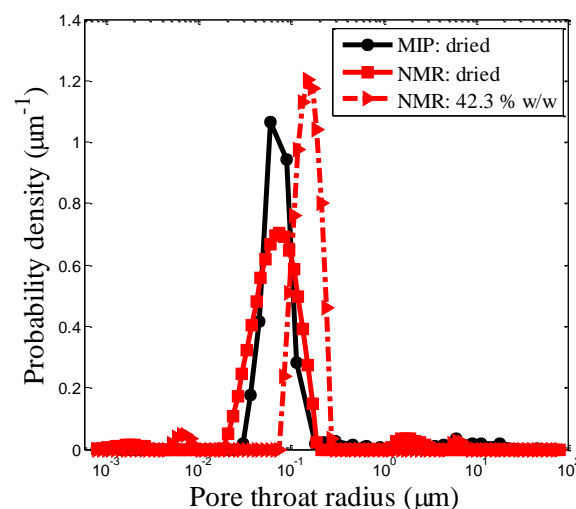

Figure 3 Pore size distribution for corroded magnesium sludge before and after drying obtained using mercury intrusion porosimetry (MIP) and low-field nuclear magnetic resonance (NMR) spectroscopy

Understanding the propagation of permeable *free gas* networks requires appreciation of the original two-phase microstructure. Figure 3 presents MIP and NMR analysis of wet and dried samples of CMgS. MIP and NMR of the two dried samples produced similarly narrow mono-modal distributions, with an MIP modal pore throat radius of 0.08 μm. Comparison of the two modes of the dried samples generated a r_{th}/T_2 calibration coefficient of 8.1×10^{-6} m s^{-1}. The adjusted NMR pore size distribution for 42.3 % w/w CMgS revealed a distinct mode in the range of $0.08<r_{th}<0.2$ μm. Work is currently being undertaken using this combined MIP-NMR technique to reveal the extent to which the two-phase pore network is constricted as a function of increased solids concentration and thus increasing the resistance to bubble growth by capillary invasion.

Conclusions and Future Work

High resolution clinical x-ray computed tomography has been used to observe the population of sub-millimetre bubbles which constitute the bulk of the voidage within magnesium hydroxide soft sediments subject to *in situ* gas generation. The sub-millimetre population greatly increases in aspect ratio with increased sediment yield stress, however, even within a weakly consolidated 27 Pa yield stress sample, the small spherical voids are able to form extensive three-dimensional networks, providing pathways for gas transport over 100 times longer than the individual bubble features apparent within a two-dimensional tomographic slice. Curiously, no such network of sub-millimetre bubbles is observed within a low strength sample of corroded magnesium sludge, which supports a narrow size distribution of very coarse bubbles. Further work is being undertaken to estimate the permeability of bubble networks through consolidated soft sediments using the Lattice Boltzmann method (LBM) to simulate low-pressure flow through the voids within the tomographic volumes.

A methodology is outlined for characterising the two-phase pore size distributions of nuclear legacy wastes, using mercury intrusion porosimetry, performed on a dried nuclear waste test material, to recalibrate nuclear magnetic resonance transverse relaxation times into pore throat radii. This analysis indicated pore throat radii predominantly in the 0.08-0.2 μm range for a 42.3 % w/w corroded magnesium sludge sample. Further work is scheduled to extent this technique to other Magnox waste test materials and to observe pore size distributions across a range of solids concentrations.

Acknowledgements

References

[1] Kam SI, Gauglitz PA, Rossen WR. Effective compressibility of a bubbly slurry. I. Theory of the behavior of bubbles trapped in porous media. *J Colloid Interface Sci*. 2001;241(1):248-259.

[2] Terrones G, Gauglitz PA. Deformation of a spherical bubble in soft solid media under external pressure. *Q J Mech Appl Math*. 2003;56(4):513-525.

[3] Gregson CR, Goddard DT, Sarsfield MJ, Taylor RJ. Combined electron microscopy and vibrational spectroscopy study of corroded Magnox sludge from a legacy spent nuclear fuel storage pond. *J Nucl Mater*. 2011;412:145-156.

[4] Johnson M, Peakall J, Fairweather M, Biggs S, Harbottle D, Hunter T. Gas retention and release from nuclear legacy waste. In: *Waste Management*. Phoenix, USA; 2016.

[5] Boudreau BP. The physics of bubbles in surficial, soft, cohesive sediments. *Mar Pet Geol*. 2012;38(1):1-18.

[6] Wheeler SJ. A conceptual model for soils containing large gas bubbles. *Geotechnique*. 1988;38(3):389-397.

[7] van Kessel T, van Kesteren WGM. Gas production and transport in artificial sludge depots. *Waste Manag*. 2002;22(1):19-28.

[8] Johnson M, Peakall J, Fairweather M, Biggs S, Harbottle D, Hunter TN. An x-ray tomography study of gas retention in nuclear legacy waste. In: *Chemeca*. Adelaide, Australia; 2016.

[9] Blackburn DR, Thompson EJ. The manufacture and use of sludge test materials for R&D purposes in the treatment and processing of Magnox based sludge. In: *ASME 2013 15th International Conference on Environmental Remediation and Radioactive Waste Management*. Vol 1. Brussels, Belgium

[10] Schindelin J, Arganda-Carreras I, Frise E, et al. Fiji: an open-source platform for biological-image analysis. *Nat Methods*. 2012;9(7):676-682.

[11] Menon M, Jia X, Lair GJ, Faraj PH, Blaud A. Analysing the impact of compaction of soil aggregates using X-ray microtomography and water flow simulations. *Soil Tillage Res*. 2015;150:147-157.

[12] Moreno-Atanasio R, Williams RA, Jia X. Combining X-ray microtomography with computer simulation for analysis of granular and porous materials. *Particuology*. 2010;8(2):81-99.

[13] Yao Y, Liu D. Comparison of low-field NMR and mercury intrusion porosimetry in characterizing pore size distributions of coals. *Fuel*. 2012;95:152-158.

[14] Xiao D, Lu Z, Jiang S, Lu S. Comparison and integration of experimental methods to characterize the full-range pore features of tight gas sandstone—A case study in Songliao Basin of China. *J Nat Gas Sci Eng*. 2016;34:1412-1421.

Simulation of dense suspension in pipe flows with homogeneous stationary sediment bed

D.O. Njobuenwu* and M. Fairweather

*Correspondence: d.o.njobuenwu@leeds.ac.uk

School of Chemical and Process Engineering, University of Leeds, Leeds, LS2 9JT, UK

Abstract

Dense suspensions in turbulent pipe flows with stationary variable flat-bed height are studied using large eddy simulation and discrete particle simulation, and compared to a reference full pipe flow. The flat boundary induced to some degree secondary flows and modifications to the fluid turbulence statistics and particle dynamics in the near-wall region. This work is motivated to simulate various degrees of bed formation during nuclear waste mobilisation and transport. Particle-particle interactions (collision and agglomeration) and particle-turbulence interactions (breakup of agglomerates) which can occur during some stages of the decommissioning process (retrieval and transport) of UK legacy nuclear waste, resulting in unwanted effects such as the formation of deposits and plugging of transfer and process pipes are considered in terms of this complex system.

Introduction

In nuclear waste sludge processes, where high mass loadings are desirable to minimise waste volumes, agglomeration processes are undesirable. Although the agglomerate density, which includes the interstitial liquid, is less than the primary particle density, agglomerates usually settle faster than primary particles [1]. Agglomeration, therefore, enhances particle deposition leading to bed formation, pipe blockage, surface erosion and alteration in the designed fluid dynamics of any process. During decommissioning of UK legacy nuclear waste, and those of any nuclear waste in general, in temporary storage, the waste will be retrieved and transported to a supplemental treatment facility for pre-treatment and immobilization before eventually ending up in permanent storage.

The need to understand agglomeration and break-up processes and design effective waste treatment processes drives this research to determine the probability of fouling, bed formation and pipe blockage due to agglomerated particles.

Methodology Details

In this section, the deterministic approach adopted for the two-phase simulations in the large eddy simulation (LES) context is presented. An Eulerian description of the continuous phase is employed and coupled with a Lagrangian approach for the dispersed phase. The two phases are coupled through the inclusion of the forces exerted on the particles by the continuous phase and vice-versa.

The BOFFIN-LES code was used to solve the LES equations. The flow was characterised by its shear Reynolds number, $Re_\tau = u_\tau h/v$, based on the shear velocity, u_τ, the channel half height, h, and the kinematic viscosity, $v = 10^{-6}$ m^2 s^{-1}, with the density $\rho = 10^3$ kg m^{-3} and discretised using grid nodes of 129×129×128 in the wall normal, spanwise and streamwise directions, respectively.

The characteristic dimensions of the dispersed phase are presumed small compared to the length scales of the smallest resolved turbulent motions, enabling the particles to be viewed as point sources with respect to the continuous phase. Since the LES solution provides only the resolved values of the carrier phase properties at the particle position, the influences of unresolved sub-grid scale (SGS) velocity fluctuations of the carrier phase on the particle accelerations are introduced through a stochastic Markov model, [2].

A 4th-order Runge-Kutta scheme is used for the particle equation of motion (Eq.1) integration in a discrete particle simulation (DPS) code, with a trilinear interpolation scheme employed for the fluid dynamic properties at the particle position:

$$\frac{d\mathbf{v}}{dt} = \frac{(\bar{\mathbf{u}} - \mathbf{v})}{\tau_p} f(Re_p) + C_{SL} \frac{3}{4} \frac{\rho}{\rho_p} [(\bar{\mathbf{u}} - \mathbf{v}) \times \boldsymbol{\omega}]$$
$$+ \frac{\rho}{\rho_p} \frac{D\bar{\mathbf{u}}}{Dt} + \frac{1}{2} \frac{\rho}{\rho_p} \left(\frac{d\bar{\mathbf{u}}}{dt} - \frac{d\mathbf{v}}{dt} \right) + \mathbf{X}_{sgs} \tag{1}$$

where a boldfaced letter denotes a matrix-vector and the terms in the RHS of Eq. (1) are respectively contributions from the drag, shear lift, pressure-gradient, added mass and SGS velocity fluctuations terms. The particle properties are denoted by the subscript p, and fluid properties are either given without subscript (for readability) or by the subscript f (where it enhances clarity). $\bar{\mathbf{u}}$ and $\boldsymbol{\omega} = 0.5(\nabla \times \bar{\mathbf{u}})$ are the known resolved fluid velocity and vorticity interpolated at the particle position. The term $f(Re_p)$ is the non-linear Schiller and Newman's correction due to the particle finite Reynolds number, Re_p, expressed as $f(Re_p) = 1.0 + 0.15 Re_p^{0.687}$. The instantaneous particle Reynolds number is defined as $Re_p = |\bar{\mathbf{u}} - \mathbf{v}| d_p / v$, where d_p is the particle diameter. $\tau_p = \Phi_p d_p^2 / (18v)$ is the particle relaxation time and when normalised by the viscous time-scale, $\tau_f = v / u_\tau^2$, gives the particle Stokes number, $\tau_p^+ = \tau_p / \tau_f$, which is then used to characterise the particle response time, with $\Phi_p = \rho_p / \rho$ being the particle to fluid density ratio.

The dispersed phase is dense so that particle-particle collisions, agglomeration and break-up of agglomerates are all accounted for, leading to a four-way coupled simulation. For particle-particle interactions, the deterministic hard sphere frictionless collision model [3, 4] is used subject to the following assumptions: particles and agglomerates are modelled as spheres; interaction between particles is due to binary collisions; only van der Waals' forces are responsible for post-collision adhesion; only small deformations of particles are allowed post-collision; agglomeration is based on the pre-collision energy momentum balance and van der Waals' interactions [4-6]; and agglomerate break-up is due to hydrodynamic shear stresses caused by fluid deformations [7].

Results and Discussion

Figure 1 shows cross-sections of the instantaneous axial velocity for the four shear Reynolds number pipe flows (a) $Re_\tau = 180$, (b) $Re_\tau = 360$, (c) $Re_\tau = 550$, and $Re_\tau = 1000$. It is evident from the two-dimensional visualisation that flow structures become smaller as the fluid Reynolds number increases. In addition, the sizes of the "mushroom" shape structures in the pipe near-wall region reduce significantly with increases in Reynolds number. This observation is consistent with that obtained with direct numerical simulation (DNS).
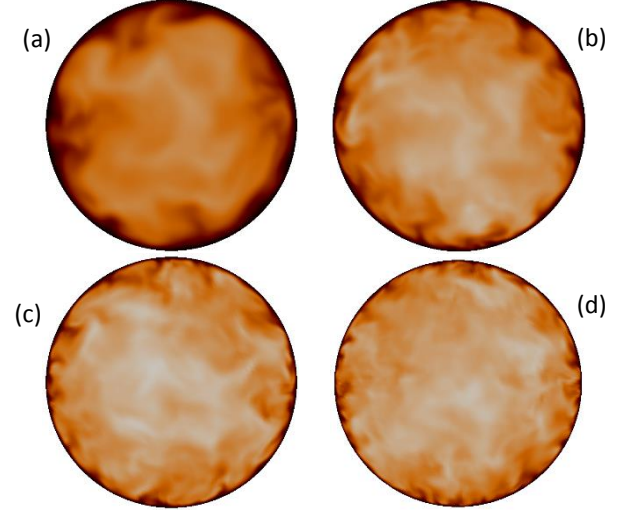
Figure 1: Pseudo-colour visualisation of the instantaneous streamwise velocity $u_z^+ = u_z / u_\tau$: (a) $Re_\tau = 180$, (b) $Re_\tau = 360$, (c) $Re_\tau = 550$, and $Re_\tau = 1000$. Note, the colours vary from 0 (black) to 24 (white).
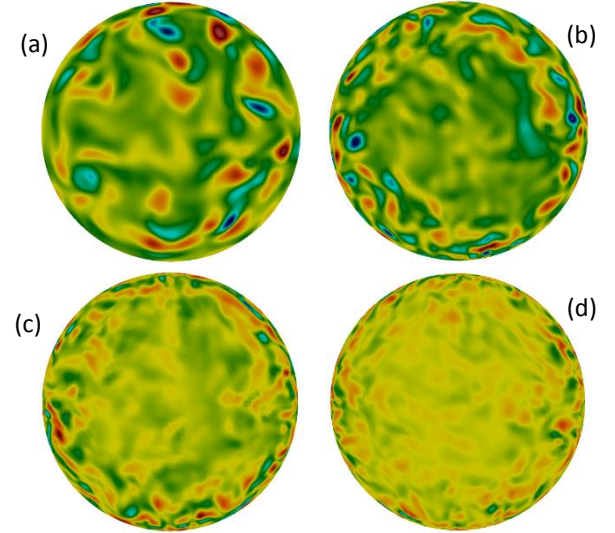
Figure 2: Pseudo-colours of the instantaneous streamwise vorticity ω_z^+ for (a) $Re_\tau = 180$, (b) $Re_\tau = 360$, (c) $Re_\tau = 550$, and $Re_\tau = 1000$. Note, red colour represents positive values and blue colour represents negative values.

Figure 2 shows instantaneous streamwise vorticity of the four shear Reynolds number flows. Similar to the observations in Figure 1, the vortical structures counter-rotating near the pipe wall are clearly seen and their size becomes smaller with increases in the shear Reynolds number from $Re_\tau = 180$ to $Re_\tau = 1000$. Also from Figures 1 and 2, we can observe the small-scale near-wall structures corresponding to the streamwise low-

and high-speed streaks, as well as the large-scale turbulent structures in the outer regions.
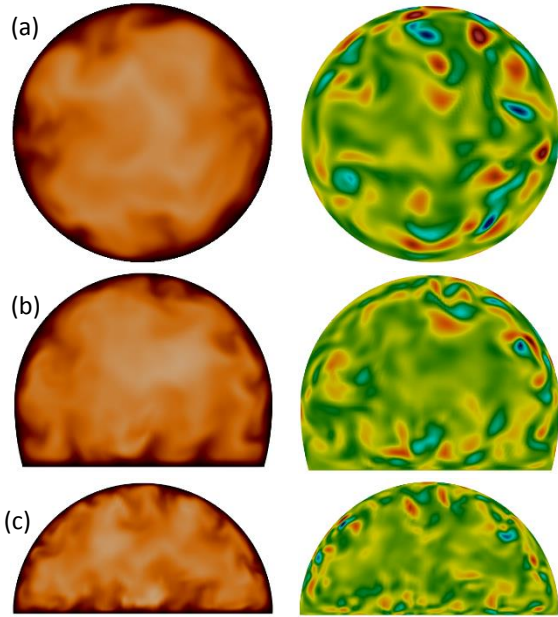

Figure 3: (left) Pseudo-colour visualisation of the instantaneous streamwise velocity for $Re_\tau = 180$ for (a) full pipe, (b) three quarter-pipe, and (c) semi-pipe. Note, the colours vary from 0 (black) to 24 (white). (Right) Pseudo-colours of the instantaneous streamwise vorticity ω_z^+. Note, red colour represents positive values and blue colour represents negative values.
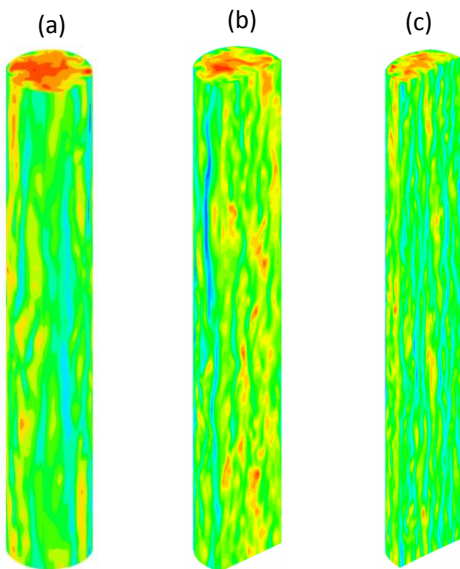

Figure 4: Low-speed-streaks at $x^+ \sim 10$ for shear Reynolds number $Re_\tau = 180$ for (a) full pipe flow (b) three quarter-pipe flow, (c) semi-pipe flow.

Figure 3 shows similar results for full, three quarter-pipe and semi-pipe flows, whilst Figure 4 shows the low-speed-streaks at $x^+ \sim 10$ for shear Reynolds number, $Re_\tau = 180$, and for the (a) full, (b) three quarter-pipe and (c) semi-pipe flows. The non-dimensional velocity vector plots at a cross-section along the streamwise direction for the full-pipe, three quarter-pipe and semi-pipe flow for shear Reynolds number $Re_\tau = 180$ are shown in Figure 5 with instantaneous velocities (left) and mean velocities (right).

There is indication of the presence of secondary flows in Figure 5(c) right, which consists of two pairs of counter rotating corner vortices with the flow convected into the corners from the central region and away from the corners along the walls. The vorticity distribution that results from the rotational flow is symmetrical and decays towards the symmetry line at the centre
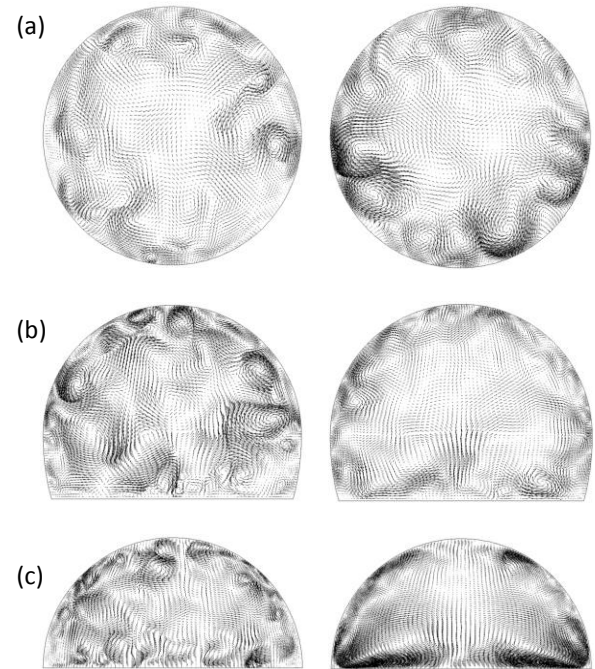
Figure 5: Velocity vector plot for shear Reynolds number $Re_\tau = 180$ for (a) full pipe flow (b) three-quarter pipe flow, (c) semi-pipe flow based on instantaneous velocities (left) and mean velocities (right).

Conclusions and Future Work

Large eddy simulation of turbulent pipe flow with variable bed heights are performed to simulate various degrees of bed formation during nuclear waste mobilisation and transport. The LES results presented in this study indicate that LES, with the dynamic calibration

of the Smagorinsky constant for evaluating the SGS stresses, using a fine grid, reproduced most of the features of the turbulent fluid flows and are consistence with those obtained from direct numerical simulation. We have gained a comprehensive understanding of the space and time dynamics of such flows, at a reduced computational cost (without resorting to any tuning of the SGS turbulence model).

Available results from discrete particle simulation of the particle dispersion and the deterministic modelling of particle-particle interactions will also be presented at the annual meeting.

Acknowledgements

References

[1]. MacLean, G.T. *The settling and compaction of nuclear waste slurries.* Fluor Daniel Northwest, Richland, Washington. , 1999.

[2]. Bini, M. and Jones, W.P. Large-eddy simulation of particle-laden turbulent flows. *J Fluid Mech.* 2008, **614**, 207-252.

[3]. Njobuenwu, D.O. and Fairweather, M. Simulation of turbulent particulate flows for nuclear waste management: Agglomeration in vertical flows. In: Zdravko, K. and Miloš, B. eds. *Computer aided chemical engineering*. Elsevier, 2016, pp.67-72.

[4]. Njobuenwu, D.O. and Fairweather, M. Simulation of deterministic energy-balance particle agglomeration in turbulent liquid-solid flows. *arXiv preprint arXiv:170102346.* 2017.

[5]. Breuer, M. and Almohammed, N. Modeling and simulation of particle agglomeration in turbulent flows using a hard-sphere model with deterministic collision detection and enhanced structure models. *Int J Multiph Flow.* 2015, **73**(0), 171-206.

[6]. Njobuenwu, D.O. and Fairweather, M. Deterministic modelling of particle agglomeration in turbulent flow. In: *Eighth International Symposium on Turbulence, Heat and Mass Transfer*, *Sarajevo*. New York: Begell House Inc., 2015, pp.587-590.

[7]. Babler, M.U. ,Biferale, L. ,Brandt, L. ,Feudel, U. ,Guseva, K. ,Lanotte, A.S. ,Marchioli, C. ,Picano, F. ,Sardina, G. ,Soldati, A. and Toschi, F. Numerical simulations of aggregate breakup in bounded and unbounded turbulent flows. *J Fluid Mech.* 2015, **766**, 104-128.

In-line rheometry and flow characterisation of dense slurries in pipe flow using acoustic methods

H.P. Rice*[1], D. Harbottle[1], T.N. Hunter[1], J. Peakall[2] and M. Fairweather[1]

*Correspondence: h.p.rice@leeds.ac.uk

[1] School of Chemical and Process Engineering (University of Leeds, Leeds LS2 9JT, UK)
[2] School of Earth and Environment (University of Leeds, Leeds LS2 9JT, UK)

Abstract

The UK's civil nuclear waste inventory is large, diverse and requires processing and disposal but characterisation of nuclear waste slurries during storage, resuspension and hydraulic transport is made difficult by poor accessibility, radioactivity and chemical hazards. The aim of this study is to develop a suite of safe, accurate, versatile and cost-effective acoustic methods for rapid monitoring and characterisation of high-concentration nuclear waste-analogue slurries, based on existing expertise at the University of Leeds. Results from several acoustic methods are described – in-line pipe rheometry, bed depth measurement and critical deposition velocity determination, for several nuclear-analogue solid-liquid slurries (calcium carbonate, barium sulphate, magnesium hydroxide, several plastics and glasses). A new flow loop laboratory has been commissioned in which these methods have been combined with sampling to investigate horizontal and vertical flow of suspensions of relevance to nuclear waste decommissioning and disposal.

Introduction

The sludges, slurries and suspensions that comprise a proportion of the UK's nuclear waste inventory have a wide range of properties – in terms of particle size, density, concentration, chemistry and radioactivity – and so the methods that are used to characterise them must be versatile and simple to deploy. Following on from expertise developed at the University of Leeds, a number of acoustic methods have been used for nuclear waste characterisation and flow measurement in flow laboratories (Figure 1, Figure 2); in-line rheometry [1], bed depth measurement and critical deposition velocity measurement [2]) are described in detail below, while several others that are established or under development (particle concentration measurement [3], time-domain velocimetry [4] and pumped sampling) are excluded for brevity.

Methodology details

In-line rheometry

When access to a hazardous flow is difficult, in-line rheometry means physical samples do not need to be taken for off-line analysis. Results from the in-line velocimetry-pressure drop rheometry method described below were compared against off-line rheometer data.

Figure 1: Pipe flow loop in Sorby Laboratory, with acoustic and pressure transducers attached.

Figure 2: Pipe flow loop at University of Leeds, temporary placement.

The viscosity, η, of a fluid can be measured in tube or pipe flow as a function of radial distance from the centreline, r, as follows:

$$\eta(r) = \frac{\tau(r)}{\dot{\gamma}(r)},$$

where $\tau(r)$ and $\dot{\gamma}(r)$ are the local shear stress and shear rate, respectively, and are defined below:

$$\tau(r) = \frac{\Delta P r}{2L},$$

$$\dot{\gamma}(r) = \frac{dU(r)}{dr},$$

where ΔP is the pressure drop over a measurement distance L, measured using standard pressure transducers, and U is the local mean axial flow velocity, measured *via* ultrasonic Doppler velocimetry. This method has been shown to give accurate results when compared with conventional off-line viscometry, as shown in Figure 3 [1].

This method can be used in situ and non-intrusively, and avoids the need for potentially costly and dangerous off-line measurement of viscosity.
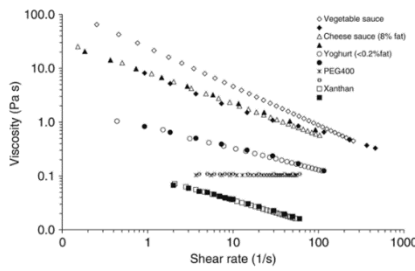
Figure 3: In-line pipe rheometry for various substances compared to conventional off-line results [1].

The method was first tested with water (Newtonian), glycerol-water and xanthan-water (shear-thinning) then the nuclear analogues over a range of solids fractions. The velocity profile corresponding to a rheological model shown in Figure 4 (in that case, Bingham pseudo-plastic, *i.e.* shear-thinning with a yield stress) will be extracted from the data by fitting.
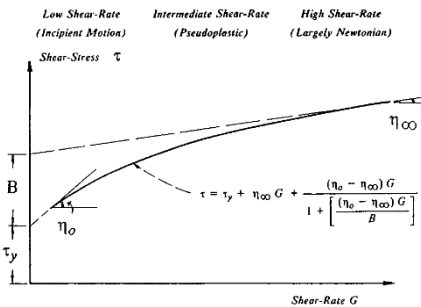
Figure 4: Schematic rheological behaviour of Bingham pseudo-plastic substance; η_0 and η_∞ are viscosities at zero and infinite shear, B depends on particle size and volume fraction [5].

Bed depth and critical deposition velocity (CDV) determination

The CDV is the flow velocity below which a bed of particles forms on the bottom of the pipe. A method for bed depth and critical deposition velocity measurement developed at the University of Leeds [2] has been applied to nuclear-analogue suspensions, with a view to providing predictive capabilities to the nuclear industry and to expand the database of materials and volume fractions for which data exist. At solids volume fractions up to a few per cent:

$$Re_{pc} = 12.4\ Ar^{0.493}\ (1 + 8.91\ \phi^{0.5}),$$

where Re_{pc} an Ar are the particle Reynolds number and Archimedes number that account for the flow and particle material properties, respectively. This correlation in the case of very low concentrations is shown in Figure 5 [2]. If Re_{pc} is written as $Re_{pc} = f(Ar)g(\text{other variables})$, then the data available suggest a form of g at intermediate volume fractions similar to that shown in Figure 6, at which the CDV behaviour is not well understood. A form for g will be sought that includes the influence of *e.g.* flow diameter, particle size distribution (PSD) and settling velocity.
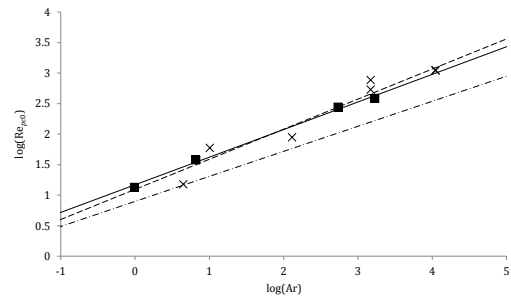

Figure 5: Variation of critical particle Reynolds number in the limit of zero concentration, Re_{pc0}, versus Archimedes number, Ar. Squares: [2]; crosses: literature. Solid line: fit to [2] data; dashed line: fit to all data. Dashed-dotted (lower) line: prediction of [6].
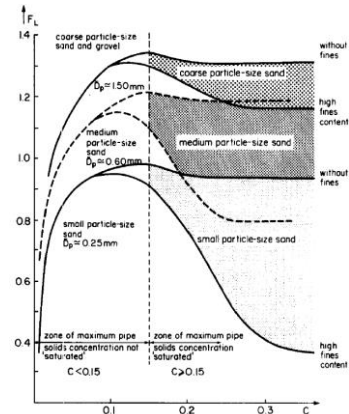

Figure 6: Variation of CDV (F_L is Froude number, depends linearly on CDV) with solids concentration and particle size for slurries of sand and gravel in water [7].

Effect of particle size distribution, settling velocity and aggregation properties

In-line rheometry data will be modelled using Herschel-Bulkley, Bingham and power-law models. At higher solids fractions, it is thought that (a) such rheological parameters will be required to account for inter-particle effects, along with (b) the effect of particle size distribution on the maximum packing fraction, settling velocity, resulting viscosity of the suspensions and the yield stress – examples for the simple case of a mono-sized spherical particle species are given in Figure 7 – and (c) the effect of aggregation through the modification of settling velocity and various critical volume fractions corresponding, for example, the "threshold" and gel-point concentrations [9]. A method for measuring such critical volume fractions is illustrated in Figure 8.
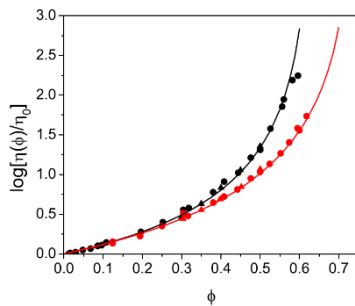
Figure 7: Relative viscosity at low and high shear rates as function of solids volume fraction. Lines correspond to predictions at ϕ = 0.63 (random close packing) and ϕ = 0.7404 (face-centred cubic) [8].
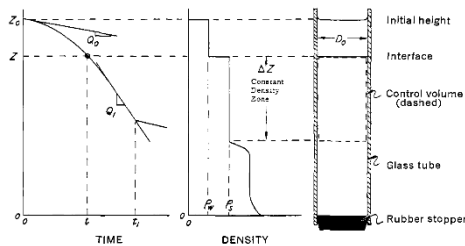
Figure 8: Control volume and time-height-density relationships. (a) Height of interface *vs.* time. (b) Height *vs.* density profile at time *t*. (c) Settling tube [10].

Test materials

Following discussions with industry partners, several nuclear-analogue test materials were used at volume fractions from 0.1% to 15% by volume, all in water as the carrier fluid: calcium carbonate, magnesium hydroxide and barium sulphate, as well as spherical glass and non-spherical plastic species for general engineering interest.

Results and discussion

The following results are/will be presented:

1. Pipe rheometry results using the Doppler velocimetry/pressure-drop method will be presented for a number of test materials: water, xanthan gum and glycerol for method validation and the test materials given above. Results will be fitted to a suitable rheological model and against conventional, off-line viscometry measurements.

Examples of velocity profiles at various solids fractions of magnesium hydroxide are shown in Figure 9, along with a comparison of in-line and off-line rheology curves for calcium carbonate at several solids fractions in Figure 10.
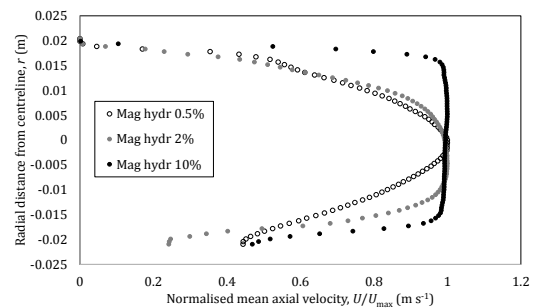

Figure 9: Laminar velocity profiles for magnesium hydroxide showing yield stress/plug behaviour. To be published.

2. Measurements of the critical deposition velocity for the test materials given above will be presented over the full range of volume fractions, and some example data are presented in Figure 11 for spherical glass particles.
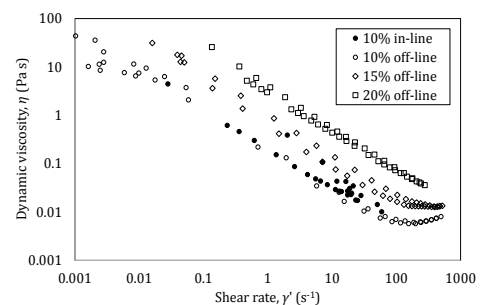

Figure 10: In-line and offline viscosity curves for calcium carbonate, preliminary analysis. To be published.

Conclusions and future work

Using the methods and results described here, the overall aim is to characterise settling and non-settling, intermediate- and high-concentration suspensions in

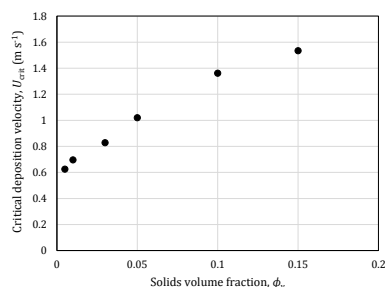terms of CDV at all flow rates and in-line rheometry at lower flow rates.

Figure 11: Critical deposition velocity *vs.* solids volume fraction for 77μm spherical glass particles. To be published.

A new laboratory containing multiple pipe flow loops with a range of diameters, as shown in Figure 12, is being commissioned that will allow for characterisation of suspensions and slurries with arbitrary concentrations and physical properties with the acoustic methods discussed above, in horizontal, vertical and inclined configurations, with the addition of laser-based particle image velocimetry (PIV) for high-resolution, near-wall measurements in pipe flow and other flow regimes.

Figure 12: New nuclear laboratory, new placement for pipe flow loop.

The laboratory facilities are to be supplemented with high-temperature and molten salt flow loops for energy storage and reactor-analogue flow applications.

Acknowledgements

References

[1] Wiklund J (2007), Chem. Eng. Sci. 62 (16) 4277-4293.

[2] Rice HP, Fairweather M, Peakall J, Hunter TN, Mahmoud B and Biggs SR (2015), Chem. Eng. Sci. 126 759-770.

[3] Rice HP, Fairweather M, Hunter TN, Mahmoud B, Biggs SR and Peakall J (2014), J. Acoust. Soc. Am. 136 (1) 156-169.

[4] Jacobson SA, Denbigh PN and Naudé DEH (1985), Ultrasonics 23 (3) 128-132.

[5] Dabak T and Yucel O (1987), Powder Technol. 52 193-206.

[6] Soepyan FB *et al.* (2014), AIChE J. 60 (1) 76-122.

[7] Parzonka W *et al.* (1981), Can. J. Chem. Eng. 59 291.

[8] Mendoza CI and Santamaria-Holek I (2009), J. Chem. Phys. 130 144904.

[9] Johnson M *et al.* (2016), Ind. Eng. Chem. Res. 55 9983-9993.

[10] Michaels AS and Bolger JC (1962), Ind. Eng. Chem. Fundam. 1 (1) 24-33.

Quartz Crystal Microbalance as a Tool to Measure Complex Suspension Rheology

J.A. Botha*[1], T.N. Hunter[1], G.A. Mackay[2], R. Cowley[4], S.E. Woodbury[3], and D.Harbottle[1]

*Correspondence: pm10jab@leeds.ac.uk
[1]School of Chemical and Process Engineering, University of Leeds, UK;
[2]NNL Workington Laboratory, Cumbria, UK;
[3]NNL Central Laboratory, Sellafield, Cumbria, UK
[4]Sellafield Analytical Services, Cumbria, UK

Abstract

The UK nuclear industry is currently entering a phase of post operational clean out, where the remediation of Sellafield, the largest nuclear site in the UK, is anticipated to cost £ 53 bn over the next 100 years. Substantial cost is associated with the clean-up and safe transfer of complex radioactive legacy waste sludge encountered in ponds, silos and highly active storage tanks across the site. To develop suitable design strategies for the mobilization and transfer of the sludge, its rheology should be accurately determined. This work demonstrates the use of a quartz crystal microbalance (QCM) to measure sludge rheology and compare the results to its shear yield stress. The device is simple to operate with no mechanical parts near the test material, is small and portable which allows for deployment into limited access areas and provides the user with in-situ rheological information on the test sample which eliminates the need for operator sampling. The measurement principle of the QCM relates to the changes in resonance frequency and motional resistance of a piezo-electric gold-coated quartz sensor as it is submerged into the desired test material. The air-to-sample frequency and resistance shifts are shown to correlate well with the shear yield stress of a suspension as measured by conventional vane viscometry.

Introduction

Sellafield is currently the largest nuclear site in Europe and globally contains one of the largest inventories of untreated waste. Effective treatment and clean-up of these waste inventories is therefore a significant challenge to the UK's nuclear decommissioning program where costs to turn the site into a greenfield site are estimated to be £53 bn over the next 100 years. A significant portion of these costs relate to the recovery and transport of legacy waste sludge to interim storage facilities. The First Generation Magnox Storage Pond (FGMSP) contains approximately 14,000 m^3 of contaminated water and approximately 1,200 – 1,500 m^3 of complex radioactive sludge formed by the corrosion of Magnox fuel rods due to lengthy storage times in water and organic material and dust entering the open air pond [1].

In order to best design suitable sludge handling processes, the rheological properties of the sludge must be characterised. Sampling is potentially hazardous and is a costly undertaking, and sampling of the sludge introduces history effects where the rheology of the sample changes due to pre-shearing of the sample. A technology that could therefore determine the rheological properties of the sludge *in situ* is an attractive alternative, especially if the new technology could be deployed at a number of locations around a pond or at another facility.

The current research investigates the use of a quartz crystal microbalance (QCM) to measure sludge rheology. The devices are small (sensor area typically less than 1 inch in diameter), portable and contain no electrical parts near the sensor, making their application to measure the rheological properties of complex fluids and sludge across a nuclear facility highly desirable.

The device is traditionally described as being an ultra-sensitive mass balance that have been widely applied in other scientific disciplines to measure the adsorption/desorption of surface active species (surfactants, polymers, biological molecules) at the sensor surface [2-6]. The QCM has also been used in liquid environments where changes in the bulk properties of the nonadsorbing fluid will result in characteristic shifts in the vibrational frequency and motional resistance across the quartz resonator [7, 8]. The objective is to expand the usability of the QCM to include yield stress suspensions. Previous results to the work have been demonstrated at the Waste Management 2016 Symposia [9].

Methodology Details

Materials: Samples used for the preparation of suspensions used throughout this study were as follows: Versamag A (high MgO content $MgOH_2$, Rohm and Haas) – aging tests. Versamag B (low MgO content $MgOH_2$, Martin Marietta) – concentration tests, aging tests. Titanium dioxide (ANX Type-N anatase grade, Degussa) – pH tests.

Initial suspension: A 200 g suspension was prepared to the desired concentration by addition of a known mass of deionised water (18 MΩ cm) to the required powder mass in a 250 mL glass beaker. The suspension was homogenised by hand using a metal spatula for 5 min until the suspension resembled a smooth paste. The suspension was sealed before sample analysis took place.

Solids concentration: A 44.2 vol% Versamag B suspension was left to hydrate for a period of at least 2 weeks with mixing taking place once every 2 days. The solids concentration of the suspension was altered via addition of deionised water followed by mixing as outlined before. The suspension was left for 10 mins to equilibrate before measurements took place.

Aging effects: Once the initial 22 vol% suspension had been prepared, a layer of mineral oil (Fisher Scientific) was gently poured on top of the suspension layer to prevent evaporation. Separate batches of the suspension were left until the required time had elapsed (up to 70 hrs) before sample analysis took place. For QCM measurements, the probe was submerged into the fresh suspension and left undisturbed until 70 hrs had elapsed. The suspension was maintained at a temperature of 30 ºC in a water bath heated by a hot plate.

pH effects: A 16.2 vol% suspension was made with a 10 mmol/L NaCl (Fisher Scientific, analar grade) background electrolyte. The suspension was left overnight to equilibrate. The pH of the suspension was changed using either NaOH (ACS reagent, Sigma Aldritch) or HCl (analar grade, VWR International) in separate batches and measured using a Hannah Instruments HI 8424 glass calomel pH probe and left for 30 min prior to measurements taking place.

Vane viscometry: The suspension shear yield stress was measured using a Brookfield DV II+ Viscometer. A four blade vane of the following dimensions was used: low yield stresses – Vane 71: D = 3.45 cm, L = 6.85 cm, average yield stresses – Vane 72: D = 2.17 cm, L = 4.33 cm, high yield stresses – Vane 73: D = 1.27 cm, L=1.25 cm. There is low variability introduced when vane dimensions are changed; several authors have reported good agreement between different results despite varying vane dimensions [10-13]. Previous tests for 15.5 vol% Versamag A have shown that at an aging time of between 3-4 hrs, the shear yield stress for vane 71 was 13.6 Pa and 12.6 Pa, whilst for vane 72 it was found to be 13.4 Pa, 13.1 Pa and 12.6 Pa. The vane was gently lowered into the particle suspension and rotated at 1 rpm. The resistance to vane rotation is measured as an increase in the torque. At the yield stress the torque passes through a maximum as the suspension begins to flow. To avoid any wall effects the vane-to-cylinder radii ratio was equal to at least

1:2. The sample beaker was clamped to avoid any rotation of the sample when measuring high yield stress suspensions. The yield stress (τ_y) can be calculated by Equation 4 [11].

$$T(max) = \frac{\pi D^3}{2}\left(\frac{H}{D} + \frac{1}{6}\right)\tau_y \qquad \text{(Eq. 4)}$$

Where $T(max)$ = maximum torque, D = vane diameter, H = vane height and τ_y = shear yield stress of the test material.

Quartz crystal microbalance: A 5 MHz AT-cut gold-coated quartz sensor (d = 25.4 mm) was cleaned by sonicating in 2 vol% Decon-90 solution for 5 min and rinsed thoroughly with deionised water and dried using nitrogen. The sensor was loaded into a Stanford Research Systems (SRS) QCM 200. The sensor was allowed to stabilize in air for 30 min. A stable sensor resonance was considered when both the frequency and resistance responses are less than 5 Hz/hr and 0.5 Ohm/hr, respectively. The suspension was prepared as previously outlined. The sensor probe was then submerged into the test material and mixed. Due to the dampening effect the oscillator compensation was adjusted to provide stable oscillation. The setup was left for at least 5 min to provide consistent frequency and resistance readings. The probe was mixed again and the process was repeated until at least three consecutively similar frequency and resistance readings were achieved.

Results and Discussion

Solids concentration: The QCM ΔR response in Figure 1 (A) closely resembles the increase in suspension yield stress in Figure 1 (B) where an Ln ΔR versus Ln yield stress plot for the same concentrations shows a direct correlation with R^2 = 0.993. This direct correlation suggests that the increasing number of particle-particle links with concentration is responsible for both the changes in suspension yield stress and ΔR. The particles adsorbed to the QCM surface will have an increase in their apparent stiffness due to additional link formation, resisting motion from the resonator surface. The resonator will therefore require more energy to move these particles, increasing its motional resistance.

The ΔF response initially closely resembles the ΔR and yield stress curves where ΔF becomes more negative with increasing concentration. This initially more negative response suggests effects that can be attributed to small film mass adsorption and bulk fluid effects described by Sauerbrey [14] and Kanazawa [15] respectively may be responsible. As the particle network stiffens, the QCM may detect larger particle clusters as single entities that grows with increasing concentration. The increase in the apparent size of these adsorbed particles will contribute to a larger mass adsorption and therefore a reduction in resonance frequency. Eventually the clusters detected by the QCM will have a natural frequency of vibration significantly lower than the resonator surface due to their size and stiffness and therefore appear stationary relative to the resonator [16]. The particles linked to the resonator surface will 'pull' the resonator back to its original position as it oscillates. This force acts to enhance the resonance frequency of the

oscillator and is termed elastic loading [16]. This phenomenon may describe the change in the ΔF response at ~ 23 vol%.
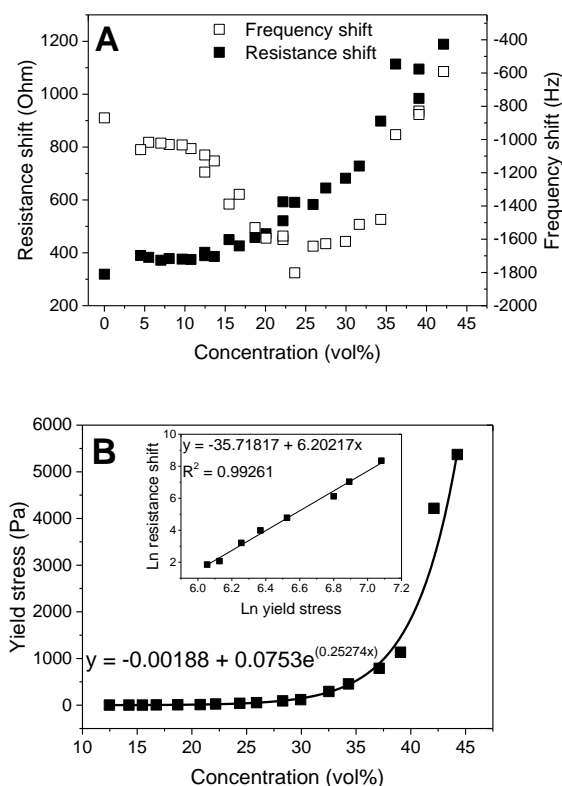

Figure 1 Comparison between (A) QCM ΔF and ΔR response and (B) yield stress as a function of Versamag B concentration.

Aging effects: The QCM ΔF and ΔR response closely resembles the increase in yield stress for Versamag A and B, with Versamag A showing a greater change after 70 hrs (Figure 2 A and B). Versamag A also shows a greater reduction in its MgO mass fraction between t = 0 – 16 hrs (Figure 2 C) which corresponds to the greatest change in yield stress and QCM response (Figure 1 A and B). DSC results (Figure 2 C) show that the samples aged to ~ 16 hrs absorbed the greatest amount of energy suggesting that a significant amount of Mg-OH bonds had to be broken per gram of sample upon heating. This suggests that the aging of Versamag is driven by the dissolution and reaction of MgO followed by the precipitation of Mg(OH)$_2$ onto existing surface sites, resulting in crystal growth and particle interlinking. This linking process between different clusters result in a stiffer network, increasing the yield stress of the suspension. The greater rate of reduction of MgO in Versamag A may be as a result of smaller crystallite sizes [17] and/or a greater proportion of the MgO being present at surface sites.

The increasingly more positive ΔF response may also be due to elastic loading. The larger clusters form stronger chemical links between each-other resulting in the particles linked to the resonator surface being stationary. This effect will enhance the QCM air - to - sample ΔF where it eventually reaches a value of +1000 Hz after ~70 hrs. The stiffer network

as a result of particle growth and interlinking will result in the particles resisting motion from the resonator surface to a greater extent, leading to an increase in ΔR.
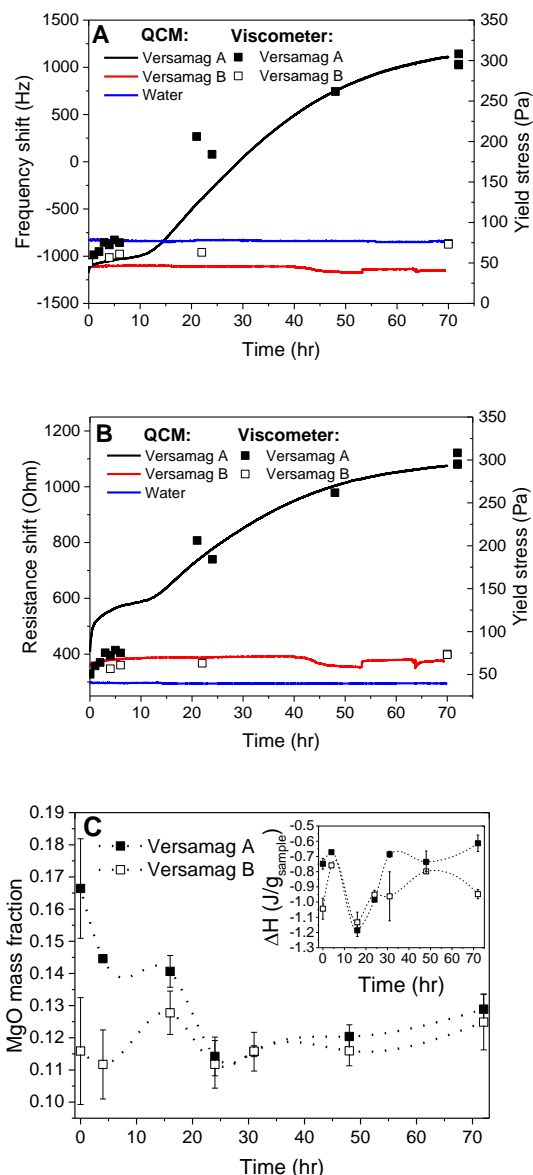

Figure 2 Comparison between the yield stress and QCM (A) ΔF, (B) ΔR and (C) TGA-DSC Mg(OH)$_2$ mass losses for Versamag A and B with aging time.

pH effects: The QCM frequency response appears to follow the shear yield stress of the suspension at low pH ranges (pH 4 – 6.5, Figure 3 A). At higher pH values beyond the isoelectric point of the suspension, this relationship breaks down where the frequency response remains relatively unchanged as the pH of the suspension is increased further. The QCM ΔR response showed a similar trend with ΔF ≈ 1/ΔR (data not shown). Atomic force microscopy measurements between a gold QCM surface and a TiO$_2$ sphere (Figure 3 B) revealed that at pH values above the isoelectric point for anatase, the interaction between gold and anatase becomes repulsive (zero attraction force). The ΔF reading is therefore dependent on the degree of attraction between the suspension particles and the resonator surface. Work investigating the relationship between the degree of attraction between the QCM surface and suspension

particles and the QCM ΔF and ΔR response by coating the resonator surface in different materials is ongoing.
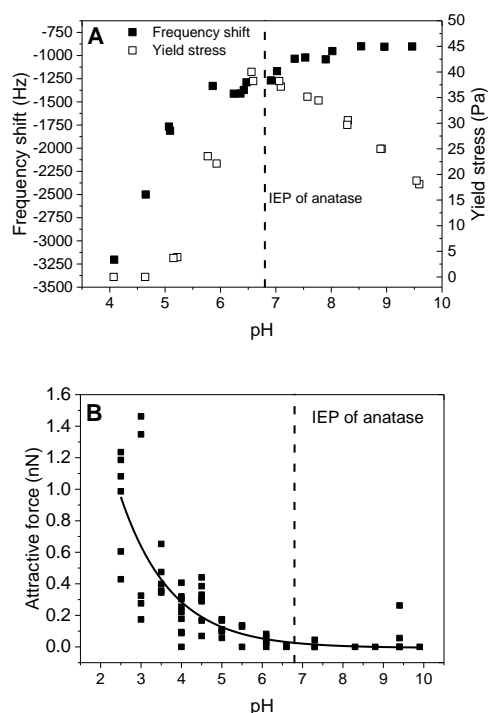

Figure 3 TiO$_2$ (A) QCM ΔF and yield stress comparison and (B) AFM attractive force to a gold coated QCM resonator surface as a function of pH.

Conclusions and Future Work

The applicability of using a quartz crystal microbalance to measure sludge rheology and compare the air-to-sample shifts in resonant frequency and motional resistance to the shear yield stress of a suspension has been demonstrated for a variety of different systems. Future work includes investigating the QCM response to changes in the strength of interaction between the suspension and resonator surface by coating the resonator surface in different materials. Differences in the QCM response will also be investigated for varied suspensions of a similar yield stress in order to isolate the factors that affect the QCM signal.

Acknowledgements

References

1. Gregson, C.R., et al., *Combined electron microscopy and vibrational spectroscopy study of corroded Magnox sludge from a legacy spent nuclear fuel storage pond.* Journal of Nuclear Materials, 2011. **412**(1): p. 145-156.
2. O'Sullivan, C.K. and G.G. Guilbault, *Commercial quartz crystal microbalances - theory and applications.* Biosensors & Bioelectronics, 1999. **14**(8-9): p. 663-670.
3. Keller, C.A. and B. Kasemo, *Surface specific kinetics of lipid vesicle adsorption measured with a quartz crystal microbalance.* Biophysical Journal, 1998. **75**(3): p. 1397-1402.
4. Hook, F., et al., *Variations in coupled water, viscoelastic properties, and film thickness of a Mefp-1 protein film during adsorption and cross-linking: A quartz crystal microbalance with dissipation monitoring, ellipsometry, and surface plasmon resonance study.* Analytical Chemistry, 2001. **73**(24): p. 5796-5804.
5. Caruso, F., et al., *Quartz-Crystal Microbalance and Surface-Plasmon Resonance Study of Surfactant Adsorption onto Gold and Chromium-Oxide Surfaces.* Langmuir, 1995. **11**(5): p. 1546-1552.
6. Marx, K.A., *Quartz crystal microbalance: A useful tool for studying thin polymer films and complex biomolecular systems at the solution-surface interface.* Biomacromolecules, 2003. **4**(5): p. 1099-1120.
7. Kanazawa, K.K. and J.G. Gordon, *Frequency of a Quartz Microbalance in Contact with Liquid.* Analytical Chemistry, 1985. **57**(8): p. 1770-1771.
8. Martin, S.J., V.E. Granstaff, and G.C. Frye, *Characterization of a Quartz Crystal Microbalance with Simultaneous Mass and Liquid Loading.* Analytical Chemistry, 1991. **63**(20): p. 2272-2281.
9. J.A. Botha, W.D., T.N. Hunter, S. Biggs, G.A. Mackay, R. Cowley, S.E. Woodbury and D. Harbottle, *A Novel Techynology for Complex Rheological Measurements.* Waste Management 2016 Symposia, 2016.
10. Alderman, N.J., G.H. Meeten, and J.D. Sherwood, *Vane Rheometry of Bentonite Gels.* Journal of Non-Newtonian Fluid Mechanics, 1991. **39**(3): p. 291-310.
11. Dzuy, N.Q. and D.V. Boger, *Direct Yield Stress Measurement with the Vane Method.* Journal of Rheology, 1985. **29**(3): p. 335-347.
12. Liddell, P.V. and D.V. Boger, *Yield stress measurements with the vane.* Journal of Non-Newtonian Fluid Mechanics, 1996. **63**(2-3): p. 235-261.
13. Johnson, S.B., et al., *Surface chemistry-rheology relationships in concentrated mineral suspensions.* International Journal of Mineral Processing, 2000. **58**(1-4): p. 267-304.
14. Sauerbrey, G., *Verwendung Von Schwingquarzen Zur Wagung Dunner Schichten Und Zur Mikrowagung.* Zeitschrift Fur Physik, 1959. **155**(2): p. 206-222.
15. Kanazawa, K.K. and J.G. Gordon, *The Oscillation Frequency of a Quartz Resonator in Contact with a Liquid.* Analytica Chimica Acta, 1985. **175**(Sep): p. 99-105.
16. Pomorska, A., et al., *Positive Frequency Shifts Observed Upon Adsorbing Micron-Sized Solid Objects to a Quartz Crystal Microbalance from the Liquid Phase.* Analytical Chemistry, 2010. **82**(6): p. 2237-2242.
17. Mullin, J.W., et al., *Aging of Precipitated Magnesium-Hydroxide.* Industrial & Engineering Chemistry Research, 1989. **28**(11): p. 1725-1730.

Application and theory of shear enhanced ultra-filtration with calcite suspension

K. Schou*, M.Dragosavac, R.G. Holdich[1]

*Correspondence: K.Schou@Lboro.ac.uk

[1] Affiliation (Loughborough University, Epinal Way, Loughborough LE11 3TU, United Kingdom, UK)

Abstract

By applying shear to the surface of a filter during micro- and ultra-filtration the flux across the filter increases. Typical reports are of 4x increases, but reports exist of up to 17.1x (Jaffrin et al. 2004). Oscillation has been demonstrated to have superior shear generating conditions over rotational systems (Zamani et al. 2015) due to the inertia of the fluid, and simplicity of seals. This work investigates the core principles at work. A calcite suspension was tested under enhanced shear conditions to determine the fundamentals of this effect. A standard ceramic filter and a slotted nickel filter were tested. The filters were oscillated both axially and azimuthally (up and down, and around the axis). The cake build-up under various applications of shear was investigated, and compared to the particle retention, and any change in the resistance of the filter in question. This work investigates a predictive model of flux, dependent on shear and the suspension properties. This work shows that the filter cake provides both the particle retention and the largest resistance to filtration. Filter cake at pseudo-steady state is dependent on the magnitude shear stress, not application of shear (azimuthal/axial), filter used or concentration of source suspension. The thickness of cake, permeability, applicability to currently used theory, initial stages, and specific shear stress have been investigated intensively and backed up with computational fluid dynamics. The overall aim of this work is to build a method of determining an approach to determining pseudo steady state flux (and appropriate particle retention) knowing the shear stress and particle size distribution of suspension.

Introduction

Ultrafiltration is used in many industries, In Sellafield's EARP an ultrafiltration step separates co-precipitate radionuclides from water. This currently uses cross flow ultra-filters, which is common in industry. In order to receive reasonable flux across the membrane the cross flow filtration requires constant recirculation of the suspension. By replacing the recirculating pump with directed shear at the membrane surface it may be possible to reduce energy usage and increase flux [1][2], [3][4]

The application of enhanced shear on filtration has been reported to increase the pseudo steady state flux as high as 17.1x [2].A significant amount of research has already been done on this effect, but there is a gap in knowledge on the fundamentals of these effects.[5], [6]. This enhancement in pseudo steady state flux is significant, prompting interest in the usage of shear enhanced filtration. The purpose of this project is to determine the specific mechanism behind the flux increase, to study the controlled shear at the surface of a filtering membrane and a fundamental understanding of a compact but efficient filtering system.

This technology can replace the current cross flow filtration methods, which require constant recycling of the suspension in order to receive reasonable fluxes, with a more efficient and compact filtration method.

Applying shear reduces cake formation but it is harder to remove cake once formed. [8]

Key research questions

The following are the main questions which this project aims to answer.

- Is there a significant effect to be applied?
- What is the effect of the filter being used?
- Does the application of the shear (azimuthal/axial) matter?
- What are the fundamental principles at work?
- How can these principles be used to advantage?
- What are the potential problems of using this technology?
- How does this technology apply to more used materials (ferric floc and magnesium hydroxide).
- Does the localised shear damage the suspension, creating a more difficult to filter suspension?

Methodology

Experimental Setup

A 1% w/w calcite suspension (calcium carbonate) was drawn through a filter while the filter was oscillated either axially (along axis) or azimuthally (around axis) until at equilibrium (usually 1 hour). The frequency and amplitude were controlled. The flowrate (from change in mass), trans-membrane pressure (TMP) and frequency of oscillation were logged. The filter cake that had formed was measured optically (photo & image analysis) and was sampled for concentration (gravimetric analysis) and particle size distribution (Malvern master-sizer).
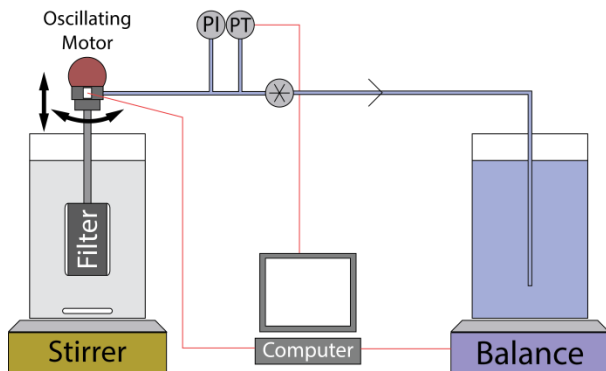
Figure 1, Experimental setup. System filters 1% w/w calcite suspension under applied shear until equilibrium is reached. An accelerometer, pressure transducer and balance were logged to find shear, trans-membrane pressure and flow rate respectively.

The Suspension

The suspension under test is a 1% w/w calcite suspension. The suspension has a sauter mean diameter (d332) of 2.74 μm and a 10% cumulative size of 0.95 μm.
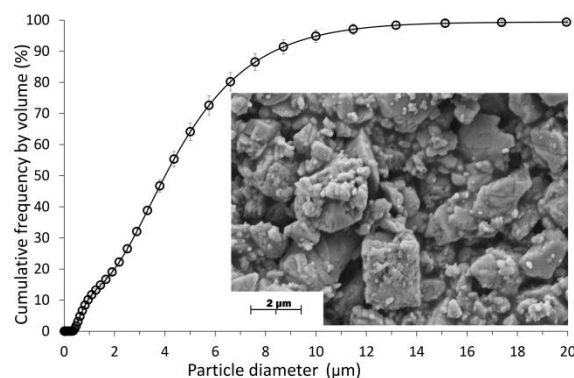
Figure 2, Particle Size distribution (PSD) of the 1% calcite suspension. (Malvern Mastersizer), SEM inset of calcite. Note the smaller particles atop the larger agglomerates. 10% of cumulative is a d_p of 0.955 μm, d_{32} is 2.7 μm.

Calcite was used a suspension medium due to its particle size range, inherent safety, availability & ease of cleaning the filter.
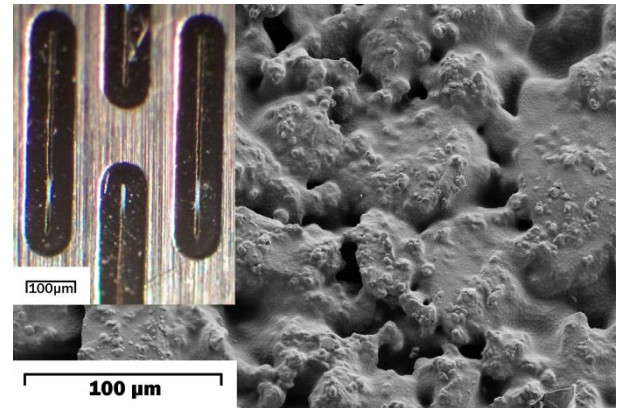
Figure 3 SEM of the surface of the ceramic filter, note the pore sizes are larger than the d_{32} of the calcite 100μm. nickel filter inset.

There are two types of filter used in this work. A ceramic depth filter and a slotted metal filter. Showed similar results once the cake had formed. The ceramic filter did not allow particles through during the cake formation stage (first 5 seconds), however the nickel filter did. The slots in the slotted filter are about 400 μm long and 7-8 microns wide. The nominal pore size for the ceramic filter is 1 μm however, the SEM clearly shows that the pores are in the region of 10-20 microns.
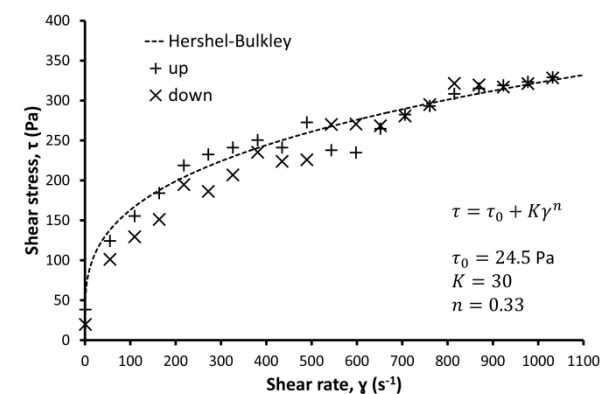

Figure 4. Rheogram of a 37% v/v calcite slurry, run (up and down) took 24.76 minutes. This fluid fits a Herschel Bulkley fluid

The filter cake which formed had consistently a concentration of 37% ±1.5% by volume, (gravimetric analysis) regardless of shear applied. The cake is a Herschel Bulkley fluid (shear thinning with a yield stress). Bulk viscosity of the suspension can be taken to be 0.001 Pas^{-1}.

Results and Discussion

Filter cake thickness

The thickness of the cake formed was measured by taking a photograph and analysing the image. The thickness is heavily affected by the shear applied
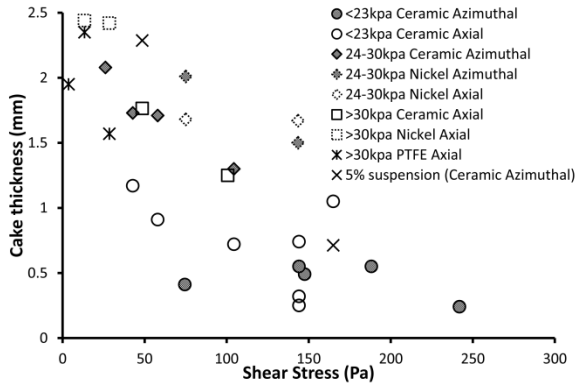

Figure 5, The thickness of the filter cake built up with axial and azimuthal oscillation at equilibrium

As the resistance of the filter is heavily dependent on the resistance due to cake, the reduction of filter cake is a significant finding.

By controlling the filter cake thickness, it is possible to directly control the resistance of the filter (and hence the flux). Applying so much shear that the cake is removed entirely with the shear reduces the particle retention. Therefore it is ideal to control the filter cake to a very thin layer. The power requirements in order to reduce the formation of the cake gets larger as the cake gets thinner so there are diminishing returns as the cake gets thinner.

Resistance

Due to cake formation the resistance over the filter will increase. High frequency sampling was taken during the initial sections of the cake formation (0-10 seconds). This was intended to determine accurately the resistance of a blocked filter. This was found not to be necessary as the tests with reverse osmosis (RO) water consistently showed a filter resistance of 5.4 $\times 10^{10}$ for the ceramic filter.
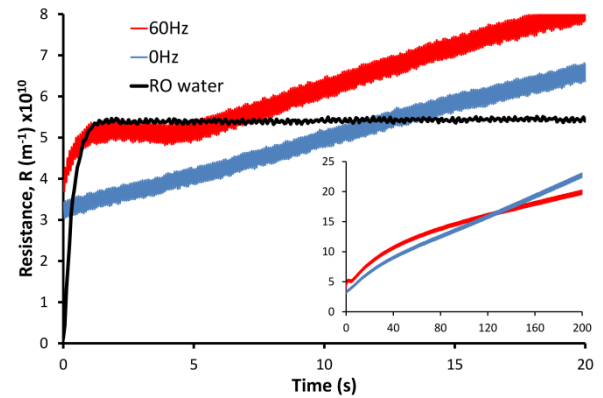

Figure 6, The resistance vs shear stress for with and without oscillation at the beginning of the run. Note that while R without shear is lower to begin with, it does increase past 60Hz after 120s.

This did show that there is a marked difference to the formation of the cake in the first couple of seconds of filtration. Interestingly the initial resistance of the system without shear is lower than with shear. While this is counter to the results from the equilibrium there is a cross over. The equilibrium resistance (and therefore the cake thickness and flux) was found to be independent of the filter type, application of oscillation and concentration.
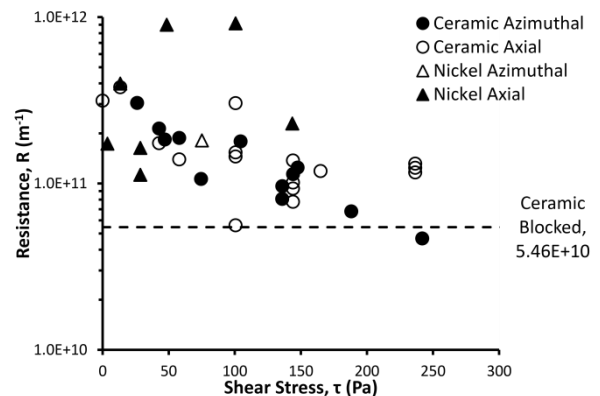

Figure 7. The total resistance vs shear stress at equilibrium

As the resistance for this system is dependent only on the magnitude of the shear, but not the type of filter, it can be determined that cake filtration is dominating this system. That it is independent of source concentration indicates that a geometry specific force balance will give the equations at the heart of this process. Resistance is found by Darcy's law:

$$R = \frac{A}{\mu_p} \frac{\Delta P}{Q}$$

Where A is filter area, μ_p is permeate viscosity, ΔP is transmembrane pressure and Q is volumetric flowrate
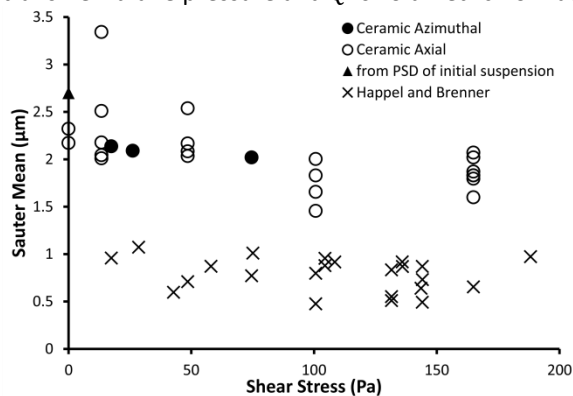

Figure 8, Sauter mean diameter of the filter cake at different shear stresses, (Malvern Mastersizer) and the calculated. Average of Happel and Brenner is 0.74 μm

Investigating the particle size distribution of the cake at increasing shears shows a small change in the d_{32}. Calculating the particle diameter using real permeability and Happel and Brenner's permeability model, The particles sizes which fit with this model of permeability fit with the 10% of cumulative particle size, which is consistent with literature.
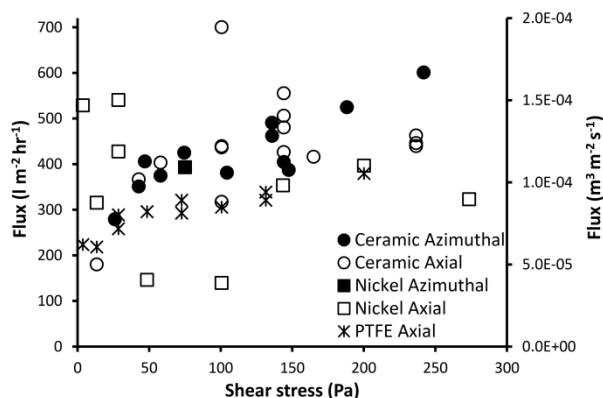
Figure 9 Flux vs shear stress with the different applications of shear and the filters. (PTFE filter is the nickel slotted filter with a PTFE coating)

By plotting flux against shear stress, it is possible to find the correlation of:

$$ J = K_1 \tau + K_0 $$

Which follows the friction model, and is consistent with other literature. K_1 and K_0 are empirical fits, which may be currently unknown variables/constants.

It is the intention of the authors to reduce these empirical fits into parameters from simple tests (i.e. PSD, cake concentration, etc.)
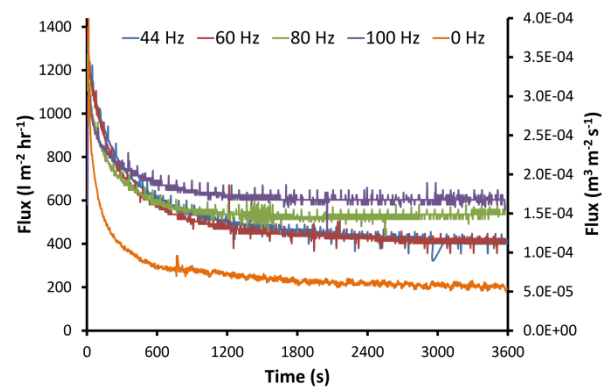

Figure 10. Flux over time compared with multiple frequencies (and hence shear stresses) in the azimuthal orientation with the ceramic filter. Orange line is when no shear is applied.

The graph above shows a simplified look at the flux over time in a few of the experiments. The line without shear (0Hz) does not reach equilibrium as it will continue to build up a cake. For the others there is a clear pattern of increased equilibrium flux with increase in frequency (and therefore shear). Enhancement of equilibrium flux is how this effect is typically reported. For just the lowest oscillations, there is approximately 2x increase in the flux. Note that a theoretical maximum of 8.5x exists due to the filter resistance.

CFD
Computational fluid dynamics (COMSOL) was used in order to check the shear stresses being calculated with this work. A low Re k-ε model was used with a 1mm cake with rheological properties found in the cake, and a 40mm cake-vessel wall section.

Conclusions and future work
Applying shear to the surface of the filter has shown to reduce the cake formation. This reduces the resistance to flow and therefore an increase in flux across the filter. There is a consistent cake size formed under specific shear conditions, regardless of suspension concentration, filter used and how the shear is applied. The testing to date has been done with calcium carbonate, future work with ferric floc and (used in the EARP) and magnesium hydroxide (used in SixEP). Will be done, using the knowledge and methods developed in this work to find how this shear enhanced filtration may be used with real world materials.

Acknowledgements

Feasibility of Ultrasonic Spectroscopy for Use In-Situ Sludge Characterisation

O.S. Ayoola*[1], S. Watson[1], B. Lennox[1] and G.X. Randall[2]

*Correspondence: olusola.ayoola@postgrad.manchester.ac.uk

[1] The University of Manchester, Dalton Cumbrian Facility, Cumbria, United Kingdom
[2] Sellafield Ltd, Risley, United Kingdom

Abstract

The aim of this study is to determine the feasibility of ultrasonic spectroscopy as a technique for in-situ measurements of particle size distribution of sludge. Current ex-situ techniques such as the laser diffraction method require a periodic collection of pond sludge samples and analysis in laboratories. In contrast, an in-situ solution is expected to improve data gathering efficiency, confidence in results and safety of sludge characterisation campaigns. Despite its suitability for high concentration sludge, the deployment of ultrasonic spectroscopy for analysing sludge in-situ may not be feasible. This is because of its dependence on a number of thermo-mechanical properties, a non-readily available data, particularly for legacy nuclear waste. Recent researches suggest this limitation could be by-passed if an analytical approach to data interpretation can be adopted, rather than the theoretically established mathematical approach. In furtherance, this paper suggests the use of existing mathematical theories to develop a series of training and testing data which may be used to develop an analytical model for data interpretation. Statistical analyses on arrays of related thermo-mechanical properties, resulting ultrasonic data and predicted particle size data will be employed. It is expected that the identification of a recurring pattern in the relationship between these data will be an addition to knowledge.

Introduction

If sludge analysis is performed directly inside the ponds, there will be immeasurable benefits. Benefits include; an improvement in safety, efficiency and confidence in results. It has been observed that ex-situ methods of sludge characterisation subjects samples to rigorous sample handling and variable treatment procedures thus affecting data quality.

Towards the decommissioning of nuclear legacy ponds, the interest is to measure and monitor the spatial distribution of particle size distribution (PSD), particle rheology and particle morphology amongst other properties across the sludge bed. Sludge characterisation is therefore useful in making decisions with respect to the design, requirement and suitability of waste transportation and processing facilities. Of particular interest to this paper is the measurement of particle size distribution (PSD).

The PSD of a sample refers to the statistics of the various sizes of particles that can be found in the given sample. Understanding that particles are not necessarily spherical, the international standards [ref] allows for the use of an "equivalent diameter" to characterise the size of any particle. The equivalent diameter of any particle is the diameter of a similar but spherical particle which will behave just as the particle

when analysed using the same technique. Table 1 shows a summary of the different techniques for particle size analysis.

Table 1 Comparative analysis of some PSD measurement techniques

Techniques	Applications	Advantages	Limitations
Image Analysis & Microscopy	Pharmaceuticals	Absolute information about the particles	Time consuming and subject to human error [1].
Laser Diffraction Method	Pharmaceuticals [2] and soil science [3]	Bulk analysis and improved accuracy	Sample preparation and Requires Optical parameters.
Sieving Analysis	Pharmaceuticals [2]	Simplest method [2].	Offline approach
Ultrasonic Spectroscopy	High particle concentrations [4].	High sample concentration (20 %) [4].	Thermo-mechanical parameters.

The current ex-situ approach involves the use of laser diffraction method. This requires sludge samples to be taken out of the ponds and diluted to a concentration of 1 %. However, with its applicability to samples of higher concentrations, even up to 50 % [5], ultrasonic spectroscopy may be considered a more suitable solution for in-situ particle size analysis of sludge.

There are challenges facing the deployment of ultrasonic spectroscopy for in-situ operations however. This report seeks to highlight these challenges and discuss solutions.

Ultrasonic Spectroscopy for Particle Size Distribution

Ultrasonic spectroscopy refers to the use of sound waves in the range of 100 kHz – 100 MHz [6] for the analysis of sample properties. The efficacy of this technique relies on the accurate detection of changes made to the properties of the sound waves which have interacted with the particulate sample. Also relied on is the successful interpretation of such changes made, in order to predict the particle size distribution present in the sample.

Figure 1 shows an example of an ultrasonic spectroscopy set-up. An impulse signal kδ(t) of appropriate width τ and amplitude k is generated and made to excite an appropriate transducer of known bandwidth. The signal then travels to the other end of the measurement chamber and bounces off the reflector, thus returning to the transducer at a time t, having travelled a total distance 2L; where L is the length of the measurement chamber. The received signal y(t) is then stored for FFT analysis. In order to eliminate background noise or errors due to unaccounted factors, this measurement is either performed a few more times at varying chamber lengths as can be achieved by conducting an initial test using only water or by using a moveable reflector [7],. For the purpose of in-situ, the set-up for an ultrasonic spectrometer for in-situ deployment will require a customised design as will later be proposed in the course of the research.
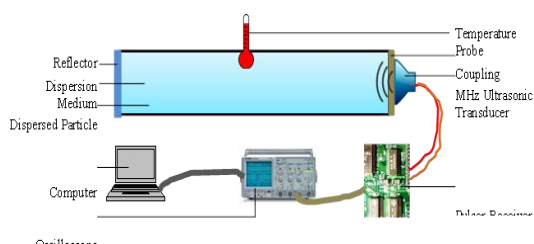

Figure 1: A schematic layout for ultrasonic spectroscopy using the pulse-echo approach

The idea of an impulse is based on knowledge that an impulse signal of width τ is one comprising of frequency components of bandwidth 1/τ. By conducting a Fast Fourier Transformation (FFT) on both the sent and received signal therefore, the impact of the particulate medium on the originally transmitted wave can be observed for each frequency component. The expectation is that there exist a relationship between the wavelength of the sound and the size of the interacting particle. Hence, at varying frequencies,

the attenuation observed will vary. The chosen bandwidth must however be commensurate with the range of particles suspected to be contained in the sample.

A number of theories have been postulated, explaining how and why particles affect sound properties during interaction. The ECAH [8] [9] and the Coupled-phase model [10] are however prominent in this regard. These theories are useful in applying mathematical analysis for data interpretation of PSD. While ECAH theory is valid for lower concentrations, Coupled-phase model deals with cases of extremely high concentrations. This paper will not go into details about these two theories. The major point to note however is that contributors to sound attenuation can be classified into four;

Scattering losses, intrinsic absorption losses, thermal dissipation losses and visco-inertial dissipation losses [11]. Scattering and absorption dominate as attenuation factors at high frequencies (short wavelength region) where λ<<r while visco-inertial and thermal losses dominate at low frequencies, (long wavelength region) when λ>>r. For simplicity, Hay and Mercer [12] focused on the Short Wavelength Region (SWR) where the ECAH theory could be conveniently deployed.

The Challenge

The challenge however is that in order to relate signal attenuation to PSD, a mathematical algorithm must be adopted which requires that th e operator supplies several thermomechanical parameters about the sample under test. These parameters include the specific heat capacities, bulk viscosities, temperature changes, bulk modulus amongst others. Having observed that these parameters are not readily available, particularly for unknown samples which are being analysed in-situ, researchers have sought a solution to this. It has however been observed that as long as these theories are applied, all the parameters required must be accurately known, as compromising them will invalidate the data interpretation. Against this background, it was suggested that an analytical solution may be most appropriate [12]. This involves the development of a statistical algorithm for converting attenuation data to PSD without recourse to the thermo-mechanical library. This will however involve a series of learning and testing data obtained experimentally. This research therefore seeks to further investigate the feasibility of ultrasonic spectroscopy to in-situ sludge characterisation in spite of the mathematical challenges. In the next section, an insight into this mathematical challenge is given as well as a proposed solution.

Methodology Details

How it currently works

Before commencement of measurements, it is necessary to have a library of thermo-mechanical parameters of the sample involved and temperature must be monitored and kept constant during the process. The following mathematical steps can then be employed:

Let $A(w,0)$ and $A(w,x_i)$ be the amplitude for frequency component w of the sent and received acoustic waves respectively, in a measurement chamber of variable length $0.5x_i$. The observed ultrasonic attenuation spectrum (UAS), is obtained as follows:

$$A_i(w,x_i) = A(w,0)\, e^{-\alpha(w)x_i}\, e^{\frac{jwx}{c(w)}} \quad (1)$$

$$\alpha(w) = \frac{1}{N}\sum_0^n \alpha_i(w) \quad (2)$$

$$\frac{w}{c(w)} + j\alpha(w) = k_c\left(1 + \frac{3\varphi}{jk_c^3 R^3}\right)(A_o + 3A_1 + 5A_2)^{0.5}$$
$$(3)$$

Where $A(w,x)$ is the amplitude of the sound wave after travelling distance x. $\alpha(w)$ is the attenuation coefficient, measured in nepers per meter. $c(w)$ is the velocity spectrum of sound, w refers to frequency. Also, R is the particle radius of dispersed sample, ф is the dispersed volume fraction, A_n is the partial wave coefficients that depend on thermo-mechanical properties. A_2 is negligible at less than 100 MHz. A_1 accounts for visco-inertial effects while A_0 includes other physical quantities.

In using this algorithm, having obtained a UAS, R should be the only unknown and can be solved to obtain the PSD.

A simpler algorithm was provided at and referred to as the principle of ultrasonic extinction:

$$\alpha(f) = C_{p.a}\Delta L\, K(x,f)dQ_2(r) \quad (4)$$

$\alpha(f)$ is the attenuation spectrum, $C_{p.a}$ is the projection area concentration, ΔL is the gap width, $K(x,f)$ is the Matrix of related extinction cross-section and $dQ_2(r)$ is the particle size distribution (PSD) of the particulate sample.

With this, $dQ_2(r)$ can be produced from α(f) directly (model independent) by attempting to solve the matrix operation or indirectly by simply characterising it by the mean and standard deviation of the measured PSD and predicting that it follows a mono-modal or bi-modal normal distribution [11].

Hay and Mercer [12] gave a simplified approach to the ECAH theory, focussing on the SWR only, to produce the equation below:

$$K_{i,j} = -\frac{4\pi}{K_c^2}\sum_0^n (2n+1)\left|A_n(r_i, f_j)\right|^2 \quad (5)$$

$$K_c = \frac{w}{c(w)} \quad (6)$$

$$A_n(r,f) = -j\sin(\eta_n(r,f))\cdot e^{-\eta_n(r,f)} \quad (7)$$

Where η_n is the phase shift of the partial scattered waves and $A_{n(r,f)}$ is the scattered amplitude coefficient. In all of the equations above, thermo-mechanical parameters such as $K(x,f)$ or A_n are relied upon.

Developing an analytical model

As earlier mentioned, an alternative solution, that seeks to eliminate the need for a thermo-mechanical properties library, is the development of an analytical model, particularly involving the use of statistics. This solution may be achieved by collecting a number of learning and testing data produced by existing analytical techniques. Data required are sets of UAS and their corresponding PSD at known sample conditions (and known thermo-mechanical properties). These data will be used to create a fingerprint library for test data that will be used.

It is not possible to gather an infinite set of fingerprints data required for an efficient library. More so, it is possible to have similar UAS-PSD fingerprints for samples that differ in material and thermo-mechanical properties. The task before this research is to identify any statistical pattern in the relationship between the UAS, the array of thermo-mechanical properties, and the corresponding PSDs.

Conclusions and Future Work

If a pattern is identified, then it may be concluded that the application of ultrasonic spectroscopy for in-situ characterisation of relatively unknown sludge samples is indeed feasible.

In obtaining the required UAS data, in the absence of an available ultrasonic spectroscopy experimental set-up, this research will make use of UAS data obtained by other researchers and will also develop some UAS data by back-substitution of PSD models into the earlier discussed equations.

Acknowledgements

References

[1] L. Beaubien and A. J. Vanderwielen, "Particle-Size Analysis of Pharmaceutical Powders," *Journal of Pharmaceutical Sciences,* vol. 69, no. 6, pp. 651-655, 1980.

[2] H. G. Brittain, "Characterization of Pharmaceutical Compounds in the Solid State," in *Handbook of Modern Pharmaceutical Analysis*, Second ed., vol. 10, S. Ahuja and S. Scypinski, Eds., NewYork, Elsevier Inc, 2011, pp. 11-49.

[3] M. Ryzak and A. Bieganowski, "Methodological Aspects of Determining Soil Particle-Size Distribution Using the Laser Diffraction Method," *J. Plant Nutr. Soil Sci,* vol. 174, pp. 624-633, 2011.

[4] U. Riebel, "Ultrasonic Spectrometry: On-line Particle Size Analysis at Extremely High Particle Concentrations," in *Particle Size Analysis*, Cambridge, Royal Society of Chemistry, 1992, pp. 488-497.

[5] F. Alba, "Acoustic Spectroscopy as a technique for the Particle Sizing of High Concentration Colloids, Emulsions and Suspensions," *Colloids and Surfaces A: Physiochemical and Engineering Aspects,* vol. 153, pp. 495-502, 1999.

[6] B. I. 20998-1:2006, Measurement and Characterization of Particles by Acoustic Methods — Part 1: Concepts and Procedures in Ultrasonic Attenuation Spectroscopy, British Standard, 2006.

[7] F. Peters and L. Petit, "A Broad Band Spectroscopy Method for Ultrasound Wave velocity and attenuation measurement in Dispersive Media," *Ultrasonics,* vol. 41, pp. 357-363, 2003.

[8] P. S. Epstein and R. R. Carhart, "The Absorption of Sound in Suspensions and. Emulsions I. Water Fog in Air," *The Journal of the Acoustical Society of America,* vol. 25, no. 3, pp. 553-565, 1953.

[9] J. Allegra and S. Hawley, "Attenuation of sound in Suspensions and Emulsions: Theory and Experiments," *The Journal of the Acoustical Society of America,* vol. 51, p. 1545, 1972.

[10] A. Dukhin and P. Goetz, "Acoustic Spectroscopy for concentrated Polydisperse Colloids with High Density Contrast," *Langmuir,* vol. 12, no. 21, pp. 4987-4997, 1996.

[11] D. McClements, "Ultrasonic Measurements in Particle Size Analysis," *Encyclopedia of analytical Chemistry,* 2006.

[12] A. E. HAY and D. G. MERCER, "On the theory of sound scattering and viscous absorption in aqueous suspensions at medium and short wavelengths," *Journal of Acoustical Society of America,* vol. 78, no. 5, pp. 1761-1771, 1985.

[13] F. Babick, M. Stintz and A. Richter, "Ultrasonic Particle Sizing of Disperse Systems with Partly Unknown Properties," *Particle & Particle Systems Characterization,* vol. 23, pp. 175-183, 2006.

[14] M. Sperazza, J. N. Moore and M. S. Hendrix, "High-Resolution Particle Size Analysis of Naturally Occuring Very Fine-Grained Sediment Through laser Diffractometry," *Journal of Sedimentary Research,* vol. 74, no. 5, pp. 736-743, 2004.

Irradiated Sludges

M. O'Leary*[1], C. Johnston[2], G. Tribello[2], J. Kohanoff[2], F. Currell[1]

*Correspondence: moleary05@qub.ac.uk

[1] Centre for Plasma Physics (Queen's University Belfast, University Road, Belfast, BT9 1NN , UK)
[2] Atomistic Simulation Centre (Queen's University Belfast, University Road, Belfast, BT9 1NN, UK)

Abstract

This project aims to identify production mechanisms of important radiolytic products, especially gaseous products for example molecular hydrogen gas, from Magnox sludges at Sellafield sites. We use irradiation platforms at the diamond light source, and Q14 in Queen's University Belfast, to irradiate sludge mimics, and then take measurements of the type and amount of different end products, like hydrogen gas, produced by irradiation. These results will then be compared to the predictions of simulations made by the Atomistic Simulation Centre, also at Queen's University Belfast.

Introduction

Sellafield site has one of the largest inventories of nuclear legacy waste in Europe. Sludge makes up a large amount of this waste, the Magnox Sludges are the most common form of sludge. Magnox sludge is the corroded nuclear fuel rod cladding from the early Magnox nuclear reactor; the cladding is made from alloy Magnox AL80[1], which is made mostly magnesium. Most of the sludge is in the Magnox Swarf Storage Silos. During the 1974 miner's strike, the Magnox Power plants, importantly Calder Hall located on the Sellafield site, had more fuel cycled, to make up for power lost from the coal burning plants. The buffer ponds at Calder Hall, where the fuel rods were stored before being moved for reprocessing, were overwhelmed by the increase in the amount of fuel used in such a short amount of time. The legacy of this is in the First Generation Storage Pond (seen in figure 1), the sludge in these ponds will soon be moved to the Sellafield Sludge Packaging Plant (SPP1, in Figure 2)[1]. The major safety issue in these sludges is the build up and retention of gases. Two main ways to produce gas are through radiolytic production of gases and through the corrosion of the fuel rod cladding. This project will investigate the ways that irradiating sludges affects gas produced in them.

In order to investigate the gases produced by the effects of irradiation on sludges: we will irradiate sludge mimics, and measure the quantity and types of gases produced. The irradiations will be done using Q14, a new irradiation platform at Queen's University Belfast (Figure 3). At the heart of Q14 is a mechatronic irradiation control apparatus, called MJOLNIR-2 that builds on the previously developed MJOLNIR; which was developed to be used as an end station for hanging drip irradiation experiments at the Diamond Light Source[2]. MJOLNIR-2 includes an integrated broad band x-ray source, with the capability to do vertical and horizontal irradiations of samples. Primary application of Q14 will be in the domain of nano-medicine, irradiating various nano-particle solutions.

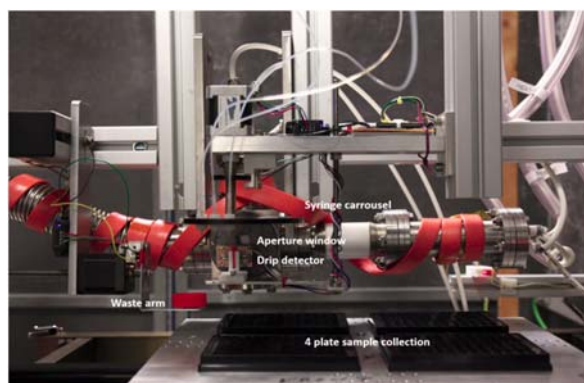**Figure 1** First Generation Storage Pond

Figure 2 SPP1, Under Construction

Figure 3 Inside Q14 (MJOLNIR-2)

Figure 4 Probe Experiment

Element	Min (% w/w)	Max (% w/w)
Aluminium	0.7	0.9
Beryllium	0.002	0.03
Cadmium	-	0.0002
Calcium	-	0.008
Cerium(1)	-	0.02
Copper	-	0.01
Iron	-	0.006
Lead	-	0.005
Magnesium	base	base
Manganese	-	0.015
Neodymium(1)	-	0.02
Nickel	-	0.005
Silicon	-	0.01
Silver(1)	-	0.01
Thorium(1)+Uranium(1)	-	0.0001
Zinc	-	0.01
Zirconium	-	0.025

Table 1 Composition of Magnox AL80

Methodology Details

The basic methodology, employed in this project, is to: irradiate sludge mimics; then after irradiation to measure the amount of a particular end product produced by irradiating the sample; then these results are compared to the predictions made by simulations, to validate physical reliability of the simulations or to investigate possible radiation induced mechanisms in the sludge.

Initial irradiation will be done on the newly developed Q14 irradiation platform. Q14 consists of MJOLNIR-2, its lead housing and a control station. MJOLNIR-2 has an inbuilt radiation source, an x-ray tube. The x-rays are produced by accelerating electrons at a truncated cylindrical piece copper, onto which pieces of other materials can be placed to produce different x-ray energy spectra. Below and to the side of the target there are beryllium windows, through which the x-rays are emitted.

The samples will be held in a sample container made out of stainless steel. The sample container will be a cylindrical chamber milled out of stainless steel. The top of the container will have a thin metal foil window through which will be x-ray-transparent, but also keep the container air tight. The side of the sample container will have gas fittings that allow for the removal and sampling of the headspace.

Before the irradiation of sludge mimics can begin the apparatus has to be calibrated, so that the results obtained can be properly interpreted. The aim will be to use chemicals that have well know G values, the amount of a particular end product produced by irradiation for an amount of energy absorbed by the medium. G value for molecular hydrogen from gamma irradiation is well

known for water, across the full range of pH [3]. Sludge mimics that will be used will start out as a mixture of water with Magnesium Hydroxide at the pH of the ponds; then materials of increasing similarity to the sludge in the ponds will be added.

The measurement of the end products involves the use of a variety of methods tailored for each specific end product. For gaseous end products use the gas chromatograph to measure the amount produced. With a thermal conductivity detector (TCD) the concentrations of the different chemicals in a gaseous sample can be measured. By sampling the headspace of the sample container, through the Gas Chromatograph, the amounts of different gaseous end products can be measured. The Hydrogen gas given off during irradiation can be directly measured by this method; and any gaseous products trapped in the sample can be measured by agitating the sample after taking a headspace sample and then repeating the above method.

Hydrogen dissolved in the sludge mimic is measured using hydrogen micro-probes, from Unisense. These are used to measure the local concentration of hydrogen dissolved. These probes are used to measure the diffusion coeffient of hydrogen through sludges. This is done using the diamond light source to irradiate a very localised region of the sludge. The concentration of hydrogen was measured at different distances from this region.

For aqueous end products we will use a variety of colorimetric assays in solution. Trapping assays are particularly useful in that they remove the particular end product from solution while also producing a noticeable change, acting as a scavenger and an assay.

When, using methods outlined above, the amount of an end product produced is measured; then to get a G-value for the end product one has to know how much energy was absorbed by the sample. Measuring the dose (energy absorbed per unit mass), dosimetry, is important to calculate how much energy was absorbed in the sample. For water many methods of dosimetry have been developed like the Fricke dosimeter, a chemical dosimeter that measures the production of Fe (III) from Fe (II) by irradiation [3]. But it will probable that other methods of dosimetry may have to be developed for sludge mimics, for example applying correction factors to the dose to water derived from Monte Carlo radiation Transport simulations.

Discussion and Future Work

Comparison of the results to the predictions of the simulations will help to calibrate those simulations. The mechanisms can be further investigation using scavengers to remove certain intermediary species from solution; thus cutting off certain pathways that were predicted produce a particular end product, then by comparing the yield of that end product with and

without the scavenger it will be possible to establish potential pathways for gas production, here using trapping assays will be useful because the amount of the intermediary species produced can also be measured.

Since Q14 was not designed to host experiments with long irradiations that may be necessary later in the project, and may not be capable of the high dose rates that will be needed to get a suitable stimulant of the sludge environment. Then for these longer irradiations and higher dose rates, we are considering the development of a newly designed dedicated radiation source, for this project, is underway. A design that uses an x-ray source that can perform irradiations in from many angles on a sample is being considered, currently.

Conclusions

This document outlines the proposed shape of this project over the next few years. The project will mainly look into the possible mechanisms for the production of gaseous end products from the irradiation of sludges, in particular the Magnox sludges. This will be done through the measurement of yields of a variety of end products produced in sludge mimics when they are irradiated; then comparing these results to the predictions of simulations.

References

[1] http://www.sellafieldsites.com

[2] C Polin et al. Rev. Sci. Instrum. **86** 035106 (2015)

[3] JWT Spinks, RW Woods, *An Introduction to Radiation Chemistry*, John Wiley and Sons, New York, 1990

Thermal treatment of plutonium contaminated materials (PCM) waste

L.Boast*[1], R.J.Hand[1], and N.C.Hyatt[1]

*lboast1@sheffield.ac.uk

[1] Immobilisation Science Laboratory, Department of Materials Science and Engineering, the University of Sheffield

Abstract

Key drivers for the application of thermal treatment processes include the reduced volume, improved passive safety, and superior long term stability, of the vitrified wasteform products. These advantages have led to a renewed interest in thermally treating various UK ILW streams. To support the increased investment in thermal treatment technologies a fundamental understanding of the processes and the impact of waste inventory needs to be established. The research described in this report aims to provide the evidence necessary to support a major investment in thermal treatment of plutonium contaminated materials. The report describes the use of laboratory scale waste simulants to develop an understanding of the waste and matrix interactions during thermal treatment of PCM waste. The report includes the thermal treatment process, characterisation and long term performance of the vitrified product.

Introduction

PCM waste is a subcategory of intermediate level waste, which is generated as a result of the handling of plutonium during nuclear fuel processing and other related activities. The amount of PCM waste in the UK is estimated to be over 31,000m³, with 70% of PCM waste stored at the Sellafield site [1]. The PCM waste, which can incorporate masonry, metal, organic or a mixture of each, are double bagged in heat sealed PVC linings before being stored in 200 L mild steel drums. The heterogeneous nature of the waste material presents a considerable materials science and engineering challenge for PCM waste immobilisation. A process is already in place at the Sellafield site for the treatment of some categories of PCM waste, centred on the Waste Treatment Centre (WTC). The general method of the WTC is compression of the 200 L drums containing the PCM waste, and the resulting crushed drums are grouted in cement and stored within 500 L steel storage containers [2]. There are however concerns regarding the reliability of the supercompaction and subsequent grouting process to deliver a consistent wasteform suitable for long-term storage and eventual disposal [3].

Thermal treatment is the main alternative technology available for the treatment of PCM waste. Key drivers for the application of thermal treatment processes include the reduced volume, improved passive safety, and superior long term stability, of the vitrified wasteform products. Proof of concept studies by the University of Sheffield, have demonstrated PCM compatibility with currently available thermal treatment technology platforms [4]. In this study [4] the authors successfully vitrified simulant PCM waste using ground granulated blast furnace slag (GGBS) which enabled a mixed slag/metal wasteform for high metal waste feeds. However, GGBS has a wide range of applications, combined with low levels of production in the steel industry, means that GGBS is a poor economic choice for the application of nuclear waste vitrification.

The study described in this report uses the same process and wasteform considerations, from the previous study [4] but with the use of recycled soda lime silica (SLS) glass cullet as the glass forming additive. Providing SLS glass cullet meets the required process and wasteform specifications for a vitrified wasteform, SLS will be more advantageous as a choice of additive based upon its unlimited availability. The project will determine the effectiveness of using SLS glass cullet as a glass forming additive.

More specifically the aims of the project are to develop an understanding of waste / matrix interactions during thermal treatment of PCM wastes. The project will contribute to accelerating the acquisition of knowledge and experience required to support NDA in deploying thermal technologies as a national asset for ILW treatment.

Methodology Details

Using Ce as a Pu surrogate laboratory scale experiments using simulant PCM drum mock ups, as shown in figure 1-4, have been performed. The PCM mock up drums include PVC waste, metal waste, mixed waste and

masonry waste ensuring a complete understanding of the various wastes streams expected from the PCM waste drums found at the Sellafield site.

Experimental Procedures

The compositions of the four PCM waste simulants are given in table 1.

Waste Type (wt %)	PVC Waste	Metal Waste	Masonry Waste	Mixed Waste
Mild Steel	44.44	20.00	30.00	30.00
PVC	55.56	10.00	10.00	10.00
Metal items	0	70.00	0	15.00
Masonry	0	0	60.00	40.00
Glass	0	0	0	5.00
Total	100.00	100.00	100.00	100.00

Table 1: Representative PCM waste simulants.

Fig1: PVC waste Simulant

Fig2: Metal waste simulant

Fig3: Masonry waste simulant

Fig4: Mixed waste simulant

Fig5: Simulant waste with addition of glass frit at 1:1 wt ratio

The upper estimated PuO_2 content of PCM wastes is the molar equivalent of 0.207 wt% CeO_2 [5]. All melts were doped with 1.043 wt% CeO_2 as a PuO_2 surrogate to allow for conservatism and to ensure detection during analytical studies post processing. Based upon the need for an oxidising material for waste streams with a higher

metal proportion to aid vitrification, a recycled glass frit (soda-lime-silica) was selected as an additive at a ratio of 1:1 (waste to additive) for all waste streams. Crucibles shown in figure 5, containing simulant waste and additive were heated overnight at 2 °C min to 1100° C; crucibles were subsequently transferred to a gas-fired furnace, which had been preheated to 1100°C, then ramped to 1450°C over a period of 90 min. The crucibles were held at 1450°C for 4 hours before being removed to cool in air to room temperature. It should be noted from figure 5 that a graphite clay crucible was required for the higher weight percentage metal waste feed. This was due to the corrosive nature of the molten metal with alumina crucibles.

Melting behaviour showed no violent reactions between the waste simulant and glass additive. As expected a substantial metallic fraction resulted for the vitrified metal type, as shown in figure 6(b).
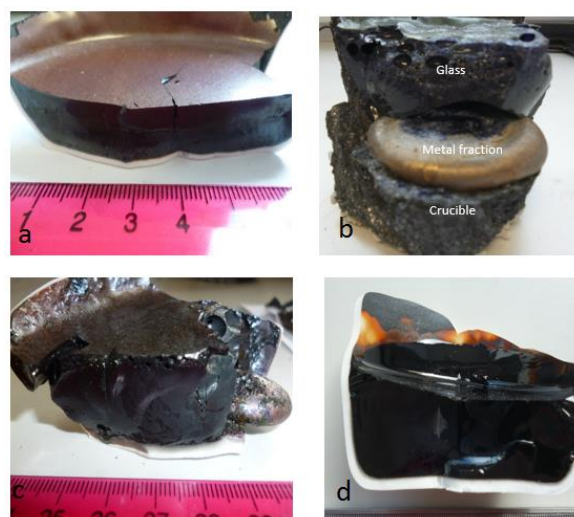

Fig6: Showing vitrified simulant PCM drum mock ups (a) PVC waste, (b) metal waste, (c) masonry waste, and (d) mixed waste

Wt %	PVC	Masonry	Metal	Mix
SiO_2	37.93	54.85	69.87	54.23
MgO	0.86	0.86	1.17	0.93
Al_2O_3	16.51	11.70	7.6	9.29
CaO	5.46	7.07	7.43	6.9
Na_2O	6.02	6.81	7.72	6.53
Fe_2O_3	30.38	17.65	0.82	18.13
CeO_2	0.42	0.33	0.60	0.43
Other	2.2	1.25	3.98	3.08
Sum	99.31	99.53	98.59	99.09

Table 2 Composition of wasteform (wt%) components via XRF

XRF determined composition of major elements in the glass waste form is shown in table 2. PuO_2 (CeO_2

surrogate) from the PCM is physically and chemically immobilised in the resulting materials, i.e. no residual PuO_2 (CeO_2) remains after processing. All of the analysis indicated that Ce was incorporated into the oxide phase in all samples. It is known that Pu is more thermodynamically favourable to partition within the slag phase; therefore, it may be possible to treat the resultant metallic waste as LLW if sufficient separation of the two phases can be achieved.

The overriding difference in slag fraction composition is the Fe_2O_3 content of the final oxide fraction of the wasteform which can be attributed to the type of crucible used and the resulting redox conditions on the melt. EDS analysis determined no measurable retention of Cl within the slag fraction of the wasteforms. It was therefore concluded that all Cl present in the organic waste was volatilised by the high temperature.

Masonry Waste

XRF and SEM/EDS studies demonstrated the glass wasteform to be composed of a $CaO–Fe_2O_3–Al_2O_3–SiO_2$ glass. XRD studies evidenced an amorphous structure with no undissolved material within the glass matrix.

PVC Waste

The XRD pattern of the vitrified PVC waste stream, Figure 7, showed reflections corresponding to spinel phase $Mg(Fe,Al)_2O_4$ (Magnesioferrite). Diffuse scattering corresponding to the presence of an amorphous component in the form of $CaO-Al_2O_3-SiO_2-Fe_2O_3$ glass. The SEM/EDS image in figure 8 show the dendritic crystal structure corresponding to the identified spinel phase.

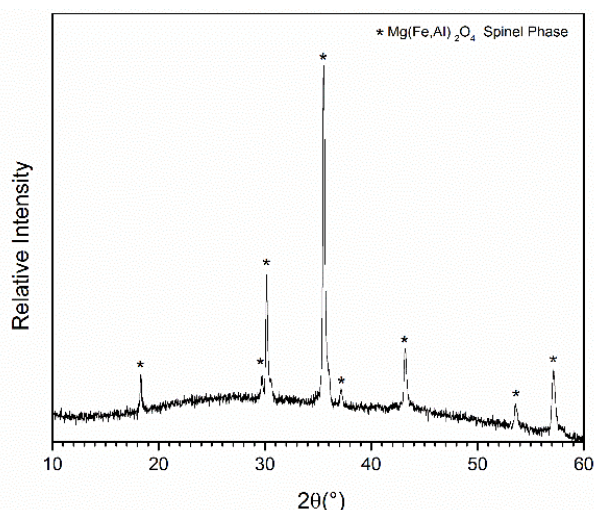**Fig8: BSE image showing microstructure of slag produced by vitrification of PVC waste type. S corresponds to identified spinel phase**

Metal Waste

The XRD pattern of the vitrified metal waste stream showed diffuse scattering corresponding to an amorphous component in the form of $CaO-Al_2O_3-SiO_2-Fe_2O_3$ glass. SEM / EDX analysis showed graphite inclusions were present from the corrosion of the crucible.

Mixed Waste

The XRD pattern of vitrified mixed waste stream, Figure 9, showed identified reflections corresponding to crystalline $Ca(Si,Al)_2O_6$ - diopside, and $(Cr,Fe,Al)_2O_4$ - spinel phases. Diffuse scattering corresponding to the presence of an amorphous component in the form of $CaO–Fe_2O_3–Al_2O_3–SiO_2$ glass was also observed. SEM / EDX analysis showed a dendritic structure (spinel phase) and diopside crystal phase within the glass.

Fig7: X-ray powder diffraction pattern showing identified reflections corresponding $Mg(Fe,Al)_2O_4$ spinel phase, together with diffuse scattering corresponding to the presence of an amorphous component, in the slag produced by vitrification of PVC waste type.
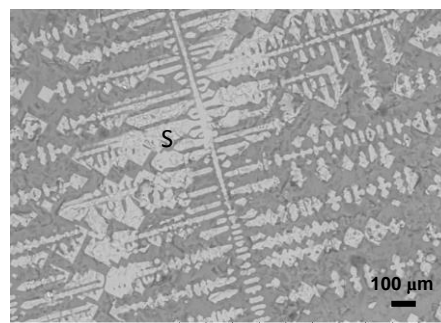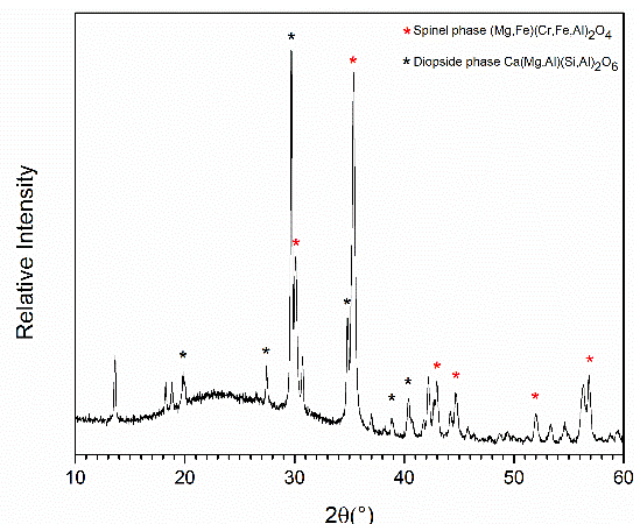

Fig9: X-ray powder diffraction pattern showing identified reflections corresponding $(Mg,Fe)(Cr,Fe,Al)_2O_4$ spinel phase (Red Stars) phases and $Ca(Si,Al)_2O_6$ diopside (black stars), together with diffuse scattering corresponding to the presence of an amorphous component, in the slag produced by vitrification of mix waste type.

Long term Durability tests

The project has also developed an understanding of the vitrified waste product in terms of stability with respect to generic ILW disposal concepts, through accelerated dissolution experiments. Figure 10 shows the controlled atmosphere experiment designed during the project.

Fig 10: Controlled nitrogen atmospheric chamber to avoid carbonation of samples and ensure high PH conditions to simulate the GDF environment.

PCT experiment of the vitrified waste types described in the project were be performed for 112 days. PCT is used to evaluate the chemical durability of a glass waste form by measuring the concentrations of the chemical elements released to a test solution, in this experiment the solution is a saturated $Ca(OH)_2$ solution to simulate the conditions expected within a GDF. Results show that the materials produced in this investigation are broadly comparable, in terms of durability, to other simulant UK ILW glass products considered potentially suitable for geological disposal. Therefore, the project has provided strong evidence that the glass wasteforms meet the defined waste acceptance criteria (WAC). Figure 11 shows the surface of the glass after being submerged in $Ca(OH)_2$ for 112 days.
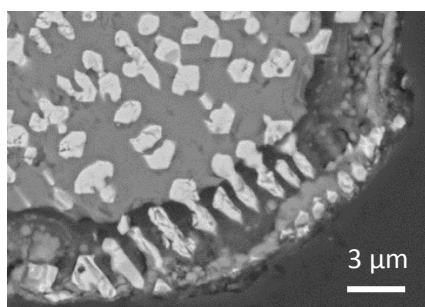

Fig 11: surface of the PVC wasteform after 112 days submerged in $Ca(OH)_2$

Ce XANES analysis

Using the light source at Brookhaven National Lab, X-ray absorption spectroscopy has been used to investigate the elemental speciation of Ce within the slag samples. Ce^{3+} was determined as the bulk speciation, which is comparable to the known speciation of Pu^{3+} in silicate glasses at high temperatures. The upper analysed Ce_2O_3 concentration in the slag is well below the solubility limits of Pu_2O_3 in borosilicate glasses. This provides strong evidence the glass developed here would incorporate Pu at the concentration expected from the PCM waste.

Conclusions

CeO_2 as a PuO_2 surrogate from PCM wastes is physically and chemically immobilised in the vitrified SLS products, i.e. no residual CeO_2 remains after processing. All of the analysis indicated that Ce was incorporated into the oxide phase in all samples. The investigation has demonstrated a strong case for vitrifying PCM waste based upon analytical studies showing a high quality glass produced for waste immobilisation with a substantial volume reduction resulting in lower disposal costs.

Acknowledgements

References

[1] "Treatment of Plutonium Contaminated Materials at Sellafield", Stakeholder Consultation Briefing Note - http://sellafieldsites.com/wp-content/uploads/2012/08/PCM-brochure-low-res.pdf

[2] "Plutonium Contaminated Materials (PCM) – A review of the status at Sellafield, Dounreay, Harwell and Aldermaston"- http://www.hse.gov.uk/aboutus/meetings/iacs/nusac/131005/p15.pdf

[3] "The management of higher activity radioactive waste on nuclear licensed sites" Scottish Environment Protection Agency to nuclear licensees – Nov (2011)

[4] "Thermal treatment of simulant plutonium contaminated materials from the Sellafield site by vitrification in a blast furnace slag" Hyatt N.C., Schwarz R.R., Bingham P.A – (2004) Journal of Nuclear Materials

[5] "Treatment of PCM at Sellafield: BPEO Sellafield" – M.Egan, A. Paulley, G.Towler – 2008 <http://www.sellafieldsites.com/wp-content/uploads/2012/08/PCM-BPEO-Study-QRS-1372A-1-Version-2_0.pdf>.

Simultaneous 3D reconstruction and

material/object recognition for nuclear wastes

Cheng Zhao*[1], Li Sun[1], and Rustam Stolkin[1]

*Correspondence: IRobotCheng@gmail.com

[1] *University of Birmingham (Extreme Robotics Lab,*
Edgbaston, Birmingham, West Midlands, UK, B15 2TT)

Abstract

This work focuses on the use of advanced computer vision methods for 3D characterization of buildings, scenes or objects, during nuclear decommissioning, especially decommissioning operations which rely on robotic interventions. Our work will address the problem of developing new computer vision methods for real-time, semantic, 3D reconstruction of nuclear waste scenes. This involves real-time 3D reconstruction of a scene, but also involves simultaneously recognising different types of materials or objects that are present in the scene, and using these material/object categories to "semantically" label all parts of the 3D scene model. Until now, three pieces of research have been completed: 1. the 2D-3D nuclear dataset and virtual camera system, 2. weakly-supervised DCNN for RGB-D object recognition in real-world applications which lack large-scale annotated training data, 3. a fully end-to-end deep learning approach for real-time simultaneous 3D reconstruction and material recognition.

Introduction

Our work focuses on the use of advanced computer vision methods for 3D characterization of buildings, scenes or objects, during nuclear decommissioning, especially decommissioning operations which rely on robotic interventions.

Decommissioning the UK's 4.9 million tonnes of legacy nuclear waste represents the largest environmental remediation project in the whole of Europe, expected to cost £90-220 billion over the next 100 years (with the cost estimates themselves expected to rise over time). It is expected that at least 20% of these costs (order £40billion) must be spent on robotic interventions inside radioactive zones which are too hazardous for humans to enter.

Before any decommissioning operations can begin, the facility or materials being decommissioned must be "characterised", which includes 3D mapping and modeling, as well as identifying types and severities of nuclear, chemical, thermal or other hazards. In particular it is very important to identify the kinds of materials which are present in a scene. 3D reconstruction may be needed for concrete-shielded rooms or "caves", containing legacy plant (e.g. pipes and vessels) which will need to be cut and dismantled by a robot and then packed into safe storage containers. Many such caves are many decades old, and their

content is uncertain. The RoMaNS project addresses a different problem of "sorting and segregation". Thousands of legacy waste containers (some extremely old) have uncertain contents. These must now be cut open and sorted through by robots. Real-time 3D modeling of these heaps of assorted objects is necessary to enable robotic grasping and manipulation. Furthermore, identification of types of materials is also critically important, so that low-level waste can be placed into relatively cheap containers and waste processing routes, while more dangerous waste can be identified and placed into much more expensive containers for longer-term storage. It is very important to avoid filling expensive high-level waste containers with low-level waste, at huge unnecessary cost to the tax-payer.

Therefore, our work will address the problem of developing new computer vision methods for real-time, semantic, 3D reconstruction of nuclear waste scenes. This involves real-time 3D reconstruction of a scene, but also involves simultaneously recognising different types of materials or objects that are present in the scene, and using these material/object categories to "semantically" label all parts of the 3D scene model.

The 2D-3D nuclear dataset and virtual camera system

In popular perception, nuclear waste is imagined to mainly comprise spent nuclear fuel rods. In reality, nuclear waste can include almost any type of object or material imaginable. For example, NNL estimates that on average 10,000 pairs of rubber gloves are used every day at just one (large) UK nuclear site. Most of these gloves become contaminated nuclear waste. Other kinds of waste materials include contaminated protective suits, respirator masks, leather coats (worn over airtight plastic suits to protect them from puncture during tool use), air hoses, tools, and all kinds of construction materials that have been removed from decommissioned nuclear facilities in a contaminated state.

After talking directly with nuclear decommissioning experts and obtaining the pictures of the real nuclear wastes, our 2D-3D nuclear waste database has been built. This dataset includes the metal, can, wood, bottle, brick, chain, pipe, sponge, glove, fabric and etc., as shown in Fig.1. It contains a large number of RGB images, depth images and 3D point cloud models. The 3D model of the nuclear object can be obtained from RGBD SLAM. Meanwhile the RGB and depth images of the key frame can be obtained. After getting the 3D object model, millions of labelled RGB-D image can be obtained from different viewpoints using our virtual camera system for deep learning training, as shown in Fig.2. A ground-truth 6DOF camera trajectories can also be provided by virtual camera system as a benchmark for 3D reconstruction.

Figure 1. Samples of 2D-3D nuclear material database.
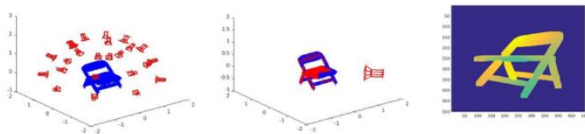

Figure 2. Millions of RGB and depth images can be obtained from different viewpoints using our virtual camera system.

This database can be employed for 3D Model Classification Challenge and 3D Reconstruction Challenge. Hundreds of object models are provided. 3D model classification challenge and 2.5D/3D model retrieval challenge can be established. This challenge is similar with Model-Net challenge, the difference is we use real object models rather than 3D CAD models. Objects are scanned with rich-textured background, which can be the benchmark of 3D object reconstruction. In reconstruction evaluation, rich-textured background is replaced by plain background.

Weakly-supervised DCNN for RGB-D object recognition in real-world applications which lack large-scale annotated training data[1]

The overview of the work

This paper addresses the problem of RGBD object recognition in real-world applications, where large amounts of annotated training data are typically unavailable. To overcome this problem, we propose a novel, weakly-supervised learning architecture (DCNN-GPC) which combines parametric models (a pair of Deep Convolutional Neural Networks (DCNN) for RGB and D modalities) with non-parametric models (Gaussian Process Classification). Our system is initially trained using a small amount of labeled data, and then automatically propagates labels to large-scale unlabeled data. We first run 3D- based objectness detection on RGBD videos to acquire many unlabeled object proposals, and then employ DCNN-GPC to label them. As a result, our multi-modal DCNN can be trained end-to-end using only a small amount of human annotation. Finally, our 3D-based objectness detection and multi-modal DCNN are integrated into a real-time detection and recognition pipeline. In our approach, bounding-box annotations are not required and boundary-aware detection is achieved. We also propose a novel way to pretrain a DCNN for the depth modality, by training on virtual depth images projected from CAD models. We pretrain our multi-modal DCNN on public 3D datasets, achieving performance comparable to state-of-the-art methods on Washington RGBS Dataset. We then finetune the network by further training on a small amount of annotated data from our novel dataset of industrial objects (nuclear waste simulants). Our weakly supervised approach has demonstrated to be highly effective in solving a novel RGBD object recognition application which lacks of human annotations.

The pipeline of the work

Our proposed pipeline has three steps: (1) a real-time 3D-based object detection approach is proposed to generate high-quality objectness proposals in RGBD video stream; (2) DCNN-GPC is proposed to propagate small-scale labeled data to moderate-scale in order to train the multi-modal DCNN end-to-end; (3) a real-time detection and recognition system is integrated.
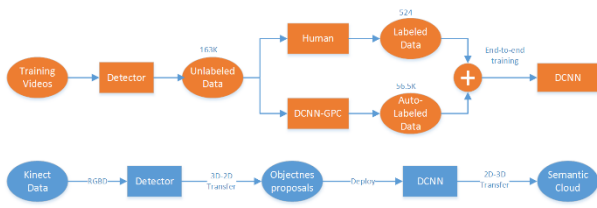
Figure 3. Flow chart of our proposed weakly-supervised DCNN method. Training is shown in orange and deployment in blue.
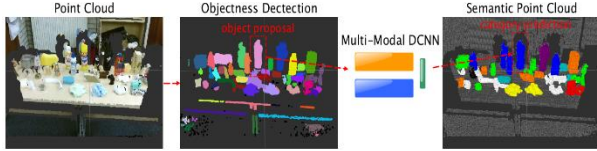

Figure 4. RGBD point cloud (left) yields objectness proposals (middle). For each such proposal, the multi-modal DCNN performs category recognition. The pixel-wise recognition result is projected to obtain a 3D semantic cloud.

The novel contributions of the work

This paper use a minimal amount of labeled data (0.3%) to train a classifier which then automatically labels large-scale unlabeled data to enable end- to-end DCNN learning, i.e. weakly-supervised deep learning.

The main contributions of this paper are as follows:

1) Previous RGBD object recognition methods have predominantly been fully-supervised, making them unsuitable for rapid deployment in new applications. In contrast, we propose a weakly supervised method, based on Gaussian Process Classification (GPC) combined with DCNN deep learning. Unlike previous work, our method does not require bounding box object annotation, and uses very little manually-labeled data (0.3%).

2) Our approach learns directly from raw depth images, in contrast to previous work which relies on extracting low-level features or color-mapping. We use a new approach to pretrain the depth DCNN by using many automatically generated synthetic depth images.

3) We introduce a new industrial dataset, comprising RGBD videos of realistic nuclear waste-like objects. A real-time detection and recognition system is implemented and significantly outperforms a fully-supervised method i.e R-CNN on this real-world data.

The related links of the work

The detail paper can be found here.

The video demo can be found here.

A fully end-to-end deep learning approach for real-time simultaneous 3D reconstruction and material recognition[2]

The overview of the work

This paper addresses the problem of simultaneous 3D reconstruction and material recognition and segmentation. Enabling robots to recognise different materials (concrete, metal etc.) in a scene is important for many tasks, e.g. robotic interventions in nuclear decommissioning. Previous work on 3D semantic reconstruction has predominantly focused on recognition of everyday domestic objects (tables, chairs etc.), whereas previous work on material recognition has largely been confined to single 2D images without any 3D reconstruction. Meanwhile, most 3D semantic reconstruction methods rely on computationally expensive post-processing, using Fully-Connected Conditional Random Fields (CRFs), to achieve consistent segmentations. In contrast, we propose a deep learning method which performs 3D reconstruction while simultaneously recognising different types of materials and labeling them at the pixel level. Unlike previous methods, we propose a fully end-to-end approach, which does not require hand-crafted features or CRF post-processing. Instead, we use only learned features, and the CRF segmentation constraints are incorporated inside the fully end-to-end learned system. We present the results of experiments, in which we trained our system to perform real-time 3D semantic reconstruction for 23 different materials in a real-world application. The run-time performance of the system can be boosted to around 10Hz, using a conventional GPU, which is enough to achieve real- time semantic reconstruction using a 30fps RGB-D camera. To the best of our knowledge, this work is the first real-time end- to-end system for simultaneous 3D reconstruction and material recognition.

The pipeline of the work

The pipeline of simultaneous 3D reconstruction and material recognition comprises three units as illustrated in Figure 5: a real-time 3D reconstruction unit based on RGB-D SLAM, a 2D material recognition unit based on FCN-8s with CRF-RNN, and a 3D semantic reconstruction unit based on Bayesian update. Firstly, the FCN-8s with CRF-RNN is employed for 2D material recognition using the RGB image from RGB-D camera. Then the semantically labeled RGB image, and the corresponding depth image, are combined together through back-projection to generate a semantic point cloud for each key frame. Finally, all semantic point clouds are combined incrementally using visual odometry, and Bayesian update is employed for label probability refinement
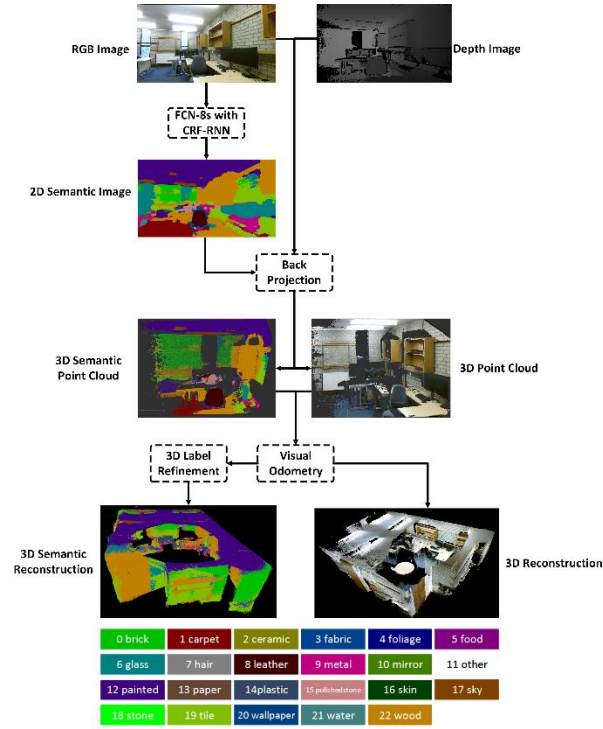
Figure 5. Pipeline of proposed simultaneous 3D reconstruction and material recognition system. Firstly, FCN-8s with CRF-RNN is employed for 2D material recognition using the RGB image from RGB-D camera. Then the semantically labeled RGB image, and the corresponding depth image, are combined together through back-projection to generate a semantic point cloud for each key frame. Finally, all semantic point clouds are combined incrementally using visual odometry, and Bayesian update is employed for label probability refinement

The novel contributions of the work

In this paper, we present a fully end-to-end system, which performs real-time 3D reconstruction while simultaneously recognizing and labeling each pixel according to its material. The main contributions of this paper can be summarized as follows:

1) To the best of our knowledge, this is the first system to perform simultaneous 3D reconstruction and material recognition.

2) Hand-crafted features or post-processing CRF optimization are not required. In contrast, the system is fully end-to-end learned, and this helps to deliver real-time performance, as well as generality for different applications.

3) The run-time performance of the whole system can be boosted, using a conventional GPU, to around 10Hz, which is enough to achieve real-time semantic reconstruction using a 30fps RGB-D camera.

4) We demonstrate our method in a real-world application, reconstructing a room while simultaneously recognizing and labelling 23 different materials.

The related links of the work

The detail paper can be found here.

The video demo can be found here.

References

[1] L. Sun, C. Zhao, and R. Stolkin, "Weakly-supervised DCNN for RGB-D Object Recognition in Real-World Applications Which Lack Large-scale Annotated Training Data," Mar. 2017.

[2] C. Zhao, L. Sun, and R. Stolkin, "A fully end-to-end deep learning approach for real-time simultaneous 3D reconstruction and material recognition," Mar. 2017.

Re-Use and Volume Reduction of Scabbled Contaminated Concrete from Nuclear Decommissioning

Toby Lord[1,2], Leon Black[2]

[1] School of Chemical and Process Engineering, University of Leeds, Leeds, LS2 9JT

[2] School of Civil Engineering, University of Leeds, Leeds, LS2 9JT

*Correspondence: cn10tl@leeds.ac.uk

Abstract

Around 50% of the UK's classified nuclear waste is building waste including concrete, cement and rubble. While research has gone into ways to minimise the volume of this waste, little has examined recycling of the materials. This research aims to investigate methods to reduce the burden on present and future storage and disposal facilities through re-use and volume reduction of conditioned contaminated concrete. Characterisation of ground, aged concrete has shown the possible presence of additional reactivity, while an investigation into the re-use of scabbled concrete within encapsulation grouts is ongoing. Laser Induced Breakdown Spectroscopy has been used to attempt to identify contamination products within a cement paste, with detection of a number of simulant radionuclides at inclusion rates as low as 0.1wt%.

Introduction

Over 40% of the UK's nuclear waste by volume is classified as building waste, including concrete, cement and rubble[1]. This places a significant load on the limited capacity for nuclear waste. As part of the decommissioning process, contaminated concrete is scabbled from the uncontaminated mass in an effort to reduce the volume of waste, yet still a significant volume of contaminated material remains for disposal.

Concrete on nuclear facilities can be contaminated with a number of radionuclides, depending on exposure and type of facility[2]. In many instances, the radiation levels are such that the scabbled material produced is classified as Intermediate Level Waste, with disposal costs of £14,500 per m³[3]. While research has gone into ways of minimising the volume of this waste, little has examined recycling of the materials. This project aims to investigate the re-use and recycling of materials, as well as methods of minimising the volume of scabbled material created, in order to reduce the overall volume of nuclear waste for disposal.

Methodology Details

This research can be split into two distinct areas; re-use and volume reduction. Re-use focusses on including the scabbled material within the grout encapsulation matrix for other nuclear waste, increasing the waste to container volume ratio.

Volume reduction focusses on using laser induced breakdown spectroscopy to identify radioactive contaminants within concrete, with the aim of helping to minimise the volume of concrete that requires scabbling.

Re-Use

Two concrete mixes were cast to mimic the concrete likely to be found on nuclear sites – a CEMI 50MPa and a CEMII 50MPa with 20% pulverised fuel ash (PFA). Both mixes were aged until at least 90 days, until they were strength tested to ensure conformability, then crushed and ground to the same particle size distribution (PSD).

The ground material was then used, at 10, 20 and 40% replacement levels, within a fresh grout mix to investigate the effect that replacement has on the overall properties of encapsulation grouts that have stringent specifications[4]. The properties to be investigated are overall heat of hydration, strength, degree of hydration, permeability, sorptivity, rheology and bleed. These tests have been, and will be, carried out at 1, 7, 28 and 90 days of age, with the material currently ageing.

Due to the depth of contamination and the age of the concrete being scabbled, a large proportion of the concrete is likely to be carbonated[5]. As such, some of the ground material will be carbonated before also being used, at the same replacement levels, as a filler within a fresh encapsulation grout. As nuclear encapsulation grouts contain high levels of blast-furnace slag (BFS), the reactions between this, the cement, and the calcium carbonate within the ground carbonated material will be examined, as this 'ternary' cement is known to produce additional reaction products to that of a standard cement mix[6].

Volume Reduction

Laser Induced Breakdown Spectroscopy (LIBS) uses a high intensity laser to breakdown a material, creating a plasma, on which light spectroscopy can be carried out, providing intensity vs wavelength data. By mapping the intensity peaks against a reference database, an elemental breakdown of the material can be found. As laser scabbling is one of the methods being investigated for contaminated concrete removal[7], this technique could be very appropriate for contamination investigation at nuclear sites.

Experimental work has been carried out to determine if this method is suitable for detecting radionuclide contaminants within a cement paste. Four non-active radioactive simulants were used at 0.1 and 1.0 weight percent; cobalt (cobalt sulphate), nickel (nickel chloride), caesium (caesium chloride) and strontium (strontium chloride) Eleven cement pastes were mixed with a 0.5 water to cement ratio; a reference mix, each contaminant at both weight percentage inclusions, and a combination of all simulants at the two weight percentages.

With laser intensity set to maximum in order to maximize the smaller peaks, larger peaks such as

calcium, silicon, nitrogen and others became saturated, but this wasn't an issue for this set of experiments. Comparing all samples back to the reference, a ratio of peak heights between samples was found and plotted, whereby large differences in peak heights between samples at the same wavelength were identified, and compared to the National Institute of Standards and Technology (NIST) Atomic Spectra Database, such that the element producing the discrepancies in peak heights could be identified.

Results and Discussion

A typical wavelength vs intensity plot for cement is shown in figure 1, with several large peaks dominating, and smaller peaks falling in between. The larger peaks can be seen to have the same intensity, at around 65,000, as saturation occurs for the more abundant elements, in order to maximise the smaller peaks.
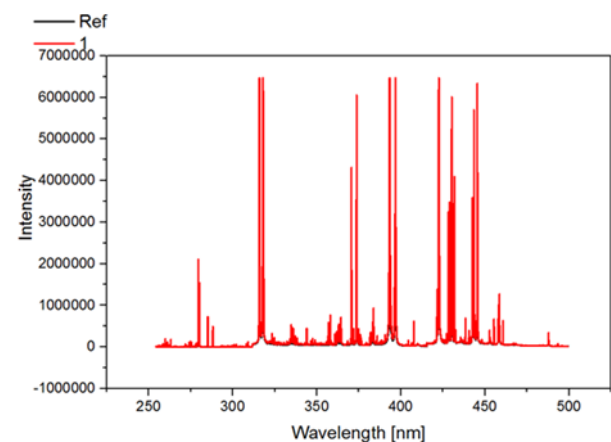

Figure 1 - Typical wavelength vs intensity plot for cement

Figure 2 shows a plot of original intensity data for a cobalt duped sample and a reference sample, with two peaks visible. Underneath this is a plot of the ratio of peaks from a number of cobalt samples, all clearly showing a difference in peak intensities between cobalt duped samples and a reference. On further inspection, the peaks can be matched precisely with the NIST data for cobalt, and known peaks at 340.512nm and 340.918nm. Such peaks were visible for all simulants used, with reduced peaks and increased analysis time required for the lower 0.1wt% however.
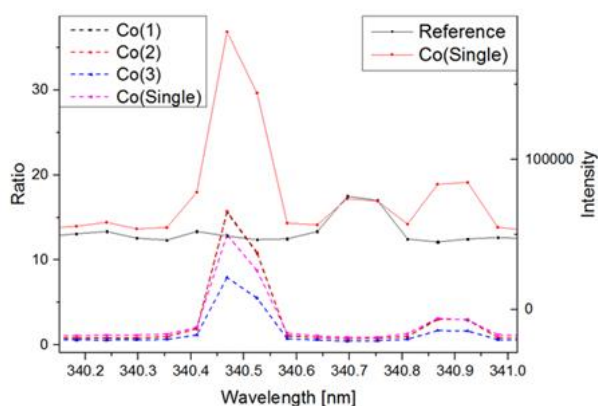
Figure 2 - Raw intensity data, and ratio plot, for cobalt vs reference samples

Conclusions and Future Work

Work on the re-use and recycling of the scabbled concrete is ongoing, with initial work showing possible signs of additional reactivity within the ground concrete, although full characterisation is required to further understand the reactivity of the ground material.

Contaminant investigation for volume reduction using LIBS has shown to be possible for the four simulants used, at weight percentages as low as 0.1%. Further work is required on sensitivity, in terms of at what level of inclusion can be spotted by the LIBS technique, and whether further simulant contaminants can be spotted. Additional work for LIBS investigation includes looking at different methods for contamination impregnation, and whether concrete contaminated after ageing, as opposed to contaminants being cast directly into fresh cement pastes, has any affect on the ability of LIBS to spot the contaminants.

Acknowledgements

References

1. Pöyry Energy Limited and Amec plc, *The 2013 UK Radioactive Waste Inventory*. 2014: Moor Row, Cumbria.
2. Bath, A., G. Deissmann, and S. Jefferis, *Radioactive Contamination of Concrete: Uptake and Release of Radionuclides*, in *The 9th International Conference on Radioactive Waste Management and Environmental Remediation*. 2003, ICEM: Oxford.
3. Department of Energy & Climate Change, *Waste Transfer Pricing Methodology for the Disposal of Higher Activity Waste from Nuclear Power Stations*. 2011, Department of Energy and Climate Change: London.
4. Collier, N.C. and N.B. Milestone, *The Encapsulation of Mg(OH)$_2$ Sludge in Composite Cement.* Cement and Concrete Research, 2010. **40**: p. 452-459.
5. Sisomphon, K. and L. Franke, *Carbonation Rates of Concretes Containing High Volume of Pozzolanic Materials.* Cement and Concrete Research, 2007. **37**: p. 1647-1653.
6. Menendez, G., V. Bonavetti, and E.F. Irassar, *Strength development of ternary blended cement with limestone filler and blast-furnace slag.* Cement & Concrete Composites, 2001. **25**: p. 61-67.
7. Peach, B., et al., *An experimental investigation of laser scabbling of concrete.* Construction and Building Materials, 2015. **89**: p. 76-89.

Investigating the effects of ionizing radiation on Calcium Silicate Hydrates using First-Principles Calculations

R. Kavanagh*[1], C. Johnston[1], K. Boukari[2], J. Kohanoff[1], G.A. Tribello[1], and A. Saúl[2]

*Correspondence: rkavanagh04@qub.ac.uk

[1] *Atomistic Simulation Centre, Queen's University Belfast, University Road, Belfast BT9 1NN, UK*
[2] *Aix-Marseille University, CINaM-CNRS UMR 7325 Campus de Luminy, 13288 Marseille cedex 9, France*

Abstract

The long-term storage of nuclear waste remains a significant challenge for the nuclear industry. One of the most vital materials employed in this storage process is cement – a complex, poorly understood calcium silicate hydrate mineral. *Ab initio* simulation of cement under the effects of ionizing radiation suggests that excess electrons can solvate in the water-rich cavities and form radicals that may result in the production of H_2 gas. Electron holes also tend to localise at electron rich oxygens found in the cement structure and may further contribute to gas formation. This gas is highly dangerous as it is flammable and may cause pressurisation that could result in dangerous radioactive materials being released into the environment. To safely and effectively store waste, a deep understanding of cement and the interactions between it and the radioactive materials it may encounter is essential.

Introduction

Cementitious materials such as Ordinary Portland Cement (OPC) and Blast Furnace Slag (BFS) are widely utilized by the nuclear industry in the UK. These materials are integral for the storage of intermediate-level wastes (ILW) such as plutonium contaminated materials (PCM) – waste items produced during the processing and handling of plutonium – and brucite sludges ($Mg(OH)_2$) found in storage ponds in nuclear sites such as Sellafield.

Typically, these hazardous materials are immobilized in a cement matrix inside a steel container. The combination of the porous, high pH cement, which traps the radionuclides, and the steel, which acts as a physical barrier, is ideal as cement pastes are cheap and easy to produce and possess a wide range of attractive thermal and mechanical properties.

A deep understanding of the structure and chemical properties of the components that make these cements is essential if we are to use this material for storing radioactive wastes. The main product formed in the making of OPC is Calcium Silicate Hydrate (CSH). CSH is a Ca-rich phase ($1.5 \leq Ca \leq 2$) gel composed of a highly variable mix of crystalline minerals and poorly ordered phases.[1] In the UK OPC is typically mixed with supplementary materials such as BFS to produce concretes with a wider range of tuneable properties such as enhanced durability and different chemical behaviours.[2]

The "white cements" that are widely used in the UK possess a Ca/Si ratio of around 1, which is much lower than typical OPC pastes. On the nanoscale these cements are thought to resemble tobermorite 11 Å – a crystalline calcium silicate hydrate mineral.[3] Tobermorite with no aluminium content can possess a variety of different chemical structures with a general formula of $Ca_{4+x}Si_6O_{15+2x}(OH)_{2-2x}\cdot 5H_2O$ where x represents the number of additional calcium atoms in the interlayer spacing.[4] Tobermorite is made of SiO_4 tetrahedral structures joined together in a repeating pattern of 2 "pairing" tetrahedra followed by a "bridging" tetraherdron. These bridging units lie out of plane with the pairing units to join adjacent chains via Si-O-Si cross-links. These linked chains then form circular pore-like structures that are known as the interlayer spacing. These regions contain a varying number of chemically bound water molecule and hydrated calcium species.[4] This "interlayer" is sandwiched between Ca-O polyhedral layers that are known as the intralayer spacing and which are responsible for the rigid structure and charge balancing of the chemical system. A representation of a tobermorite mineral can be found in Figure 1.

Due to the highly variable nature of CSH and tobermorite, the true structure of cement at the nanoscale is poorly understood. Furthermore, the effect of ionizing radiation on cement pastes remains a challenge as few studies have tackled this problem[5,6] It is known, however, the effect of radiation on water molecules trapped in cement is different to the effect of radiation on molecules in bulk water..[7]
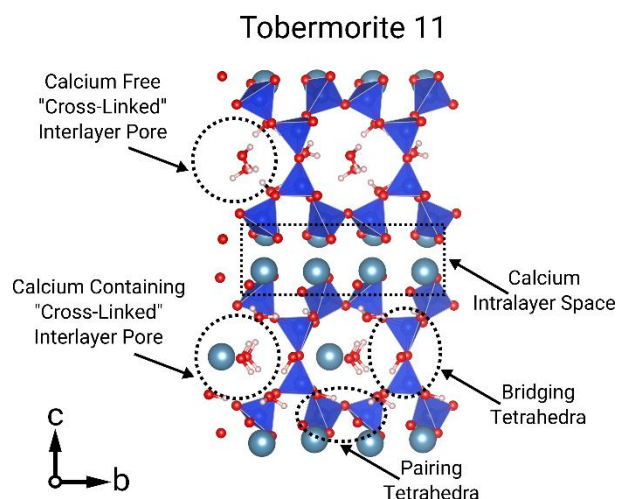
Tobermorite 11

Figure 1 Atomic structure model of tobermorite 11 with calcium, silicon, oxygen and hydrogen are represented in grey, dark blue, red and white respectively. The unit cell has been replicated for clarity.

This work aims to rationalise the behaviour of cement analogues under the influence of ionizing radiation by using *ab initio* calculations. By investigating the electronic properties of these materials, the study aims to provide insight into the cements that are used for nuclear applications.

Methodology Details

The two models employed in this study, which are seen as suitable representations of low Ca/Si cements were obtained from work by Merlino et. al.[3] CS-083 has the maximum possible Ca occupancy (x = 1) and a chemical composition of $Ca_{10}Si_{12}O_{34} \cdot 10H_2O$. The second structure is a model for the tobermorite that is found naturally in the Urals, Russia and has x = 0.5. This structure possesses the chemical formula $Ca_9Si_{12}O_{32}(OH)_2 \cdot 10H_2O$ and contains 2 hydroxyl groups attached to Si so as to preserve charge neutrality. CS-083 and CS-075 have Ca/Si ratios of 0.83 and 0.75 respectively. It is worth noting that 0.83 is the highest possible Ca/Si for a tobermorite 11 Å species. The unit cells contain 86 and 87 atoms respectively and possess the same monoclinic shape. The A, B and C cell vectors are 6.732, 7.369 and 22.680 respectively. The angles α, β and γ are 90°, 90°, and 123.18° and the cell is periodic in all 3 directions.

The Quantum ESPRESSO[8] code was used to determine the optimal positions for both the hydroxyl groups and the interlayer calcium atoms of CS-075. A 3x3x1 k-point grid was used with Vanderblit ultra-soft pseudopotentials.[9] The kinetic energy cutoffs for the wavefunctions and the charge density were set equal to 90 and 900 Ry respectively.

In all subsequent calculations in the study the CP2K open source electronic structure code was used.[10]

Three sets of calculations were performed as both structures were optimized in their neutral state and in their +1/-1 charged states (charged cells were generated by removing or adding electrons into the simulation cell). The calculations used the Quickstep[11] algorithm with the Gaussian and Plane Wave (GPW) method[12] and a molecularly optimized Gaussian atom-centered basis sets[13] with a planewave cutoff of 800 Ry. Initially the Perdew-Burke-Ernzerhof (PBE) functional[14] was used but all calculations were then repeated with the Minnesota hybrid M06-2X functional.[15] This functional was chosen for its enhanced accuracy as the Minnesota suite is well regarded in the main-group chemistry community. The simulations used a truncated Coulomb operator and the CP2K Auxiliary Density Matrix Method[16] to alleviate the computational costs of the Hartree-Fock exchange calculations. All calculations with a charge were performed using the spin-polarized unrestricted Kohn-Sham formalism.[17] Ab initio molecular dynamics calculations were carried out with CP2K at the M06-2X level. The NVT ensemble was used to simulate behaviour at 300K with a time step of 0.5 fs.

Results and Discussion

The manner in which the excess electron introduced upon irradiation localizes can be seen in Figure 2. The additional electron that was added into the unit cell occupies the LUMO of the spin channel and makes the total number of electrons uneven. As such we can examine where the excess electron localises by visualizing the spin density. The same technique can also be used to study the presence of holes, as once again the uneven electron count that results from the removal of an electron ensures that the system has a non-zero spin moment.

Figure 2 shows that the excess electron tends to locate in the interlayer spacing and that it is delocalised over the interlayer calcium and 5 nearby water molecules in both CS-083 and CS-075. In CS-075 (Figure 2b) where only half the interlayer regions are filled with calcium the electron preferentially locates in the region occupied by a calcium. This suggests that calcium can help "attract" free electrons that happen to be nearby. In both cases it is clear to see that free electrons will localise around water molecules and will likely be solvated as they tend not to reduce calcium despite being strongly reducing species.[18] We therefore assume that the solvated electron will act as a precursor to H_2 production via the formation of radicals in the water.
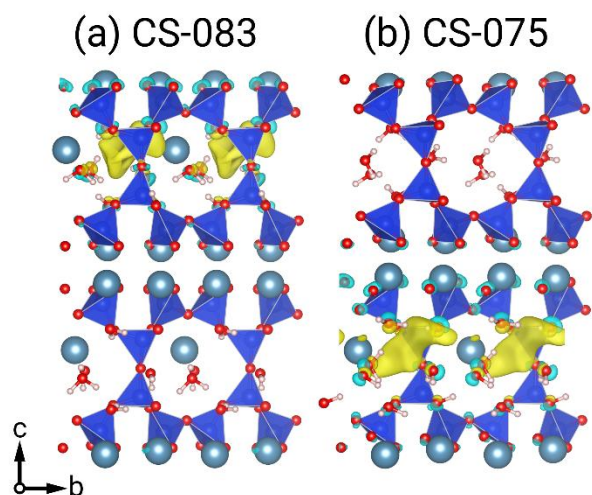
(a) CS-083   (b) CS-075

Figure 2 (a) Representation of the spin density of CS-083 with an excess electron. (b) Spin density of CS-075 with an excess electron. The yellow and blue surfaces show isocontours where the spin density are positive and negative respectively. Both models have been optimized at the M06-2X level. The isosurfaces are drawn at $\pm$ 0.002 eÅ^{-3}.
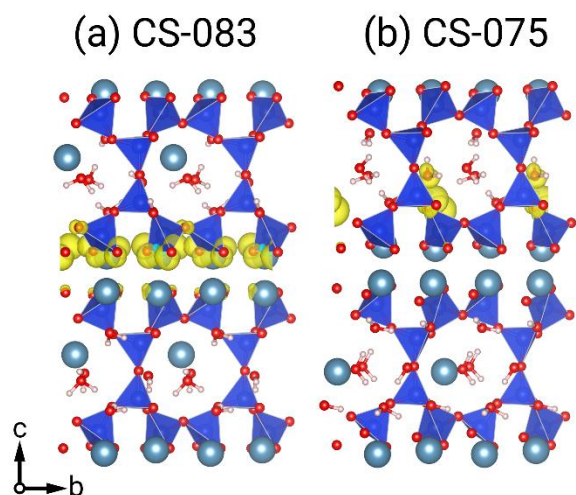

(a) CS-083   (b) CS-075

Figure 3 (a) Representation of the spin density of CS-083 with an electron removed (hole). (b) Spin density of CS-075 with a hole. The yellow and blue surfaces show isocontours where the spin density are positive and negative respectively. Both models have been optimized at the M06-2X level. The isosurfaces are drawn at $\pm$ 0.002 eÅ^{-3}.

The spin densities of structures containing holes produced are shown in Figure 3a for the Ca-rich case (CS-083) and 3b for the reduced Ca content structure (CS-075). When CS-083 is ionized the hole sits on the oxygens of an SiO_4 that points towards the calcium in the oxygen rich intralayer space. In other words, in the Ca-rich case the hole appears to delocalise over the intralayer oxygens. In this structure it thus seems unlikely that the hole will react with water and produce hydrogen gas.

The results for CS-075 provide an alternative insight into the behaviour of holes in tobermorite structures. Figure 3b shows that the hole strongly localises on a single

oxygen that is part of an SiO_4 species. This oxygen points towards the interlayer space and a small amount of the spin (6%) can even be found on a nearby water molecule. This suggests that in CS-075 the hole could react with water molecules to form H^+ leading to a cascade of reactions that might ultimately produce H_2 gas.

The results presented show that the excess electrons will typically solvate in the interlayer spacing and suggest that they are "directed" to these regions by the positive calcium atoms found there. Holes tend to locate on SiO_4 oxygen atoms where there is a large amount of electron density. These holes are usually caught in the water-free regions of the tobermorite crystal and are thus unlikely to induce radical cascades.

Conclusions and Future Work

The production of radicals due to electronic defects in cement analogues was investigated. Our results demonstrate that excess electrons are more likely to be involved in these radical formation reactions as they locate near the interlayer water. For the most part, however, cements appear robust to holes as they locate in water-free regions and thus cannot react with water. This behaviour seems particularly prevalent in samples with higher calcium contents. In fact the presence of interlayer calcium atoms appears to not only affect the geometry of the system but also the behaviour and susceptibility of cement materials to the effects of irradiation. In general, ionizing radiation is a concern as both adding and removing electrons can introduce radicals into the material. These reactive species can then either damage the SiO_4 framework, which induces microcracking,[19] or react with water to form H_2 gas.

The next stage of this project involves examining tobermorite systems with defects such as aluminium. Such compositions more closely resemble those of the cements used in the UK.[19] In addition, radionuclide substitutions such as ^{90}Sr[20] will be investigated. Studying the effects of ageing in cements is of vital importance to the fidelity and longevity of cements for nuclear storage as the size, geometry and properties of cement pastes change with age.[21]

Acknowledgements

References

[1] I.G. Richardson, The calcium silicate hydrates *Cem. Concr. Res.* 38, **2008,** 137-158

[2] M.C.G. Juenger, F. Winnefeld, J.L. Provis, Advances in alternative cementitious binders *Cem. Concr. Res.* 38, **2011,** 1232-1243

[3] S. Merlino, E. Bonaccorsi, T. Armbruster, The real structure of tobermorite 11 Å: Normal and anomalous forms *Am. Mineral* 88, **1999,** 1613-1621

[4] C. Biagioni, S. Merlino, E. Bonaccorsi, The tobermorite supergroup: a new nomenclature *Mineral Mag* 79(2), **2015,** 485-495

[5] M. Lainé, E.A. Balan, F. Martin, H.J. von Bardeleben, J.L Robert, S. Le Caër, Reaction mechanisms in talc under ionizing radiation: Evidence for a high stability of H˙ atoms *J. Phys. Chem. C.* **2016,** 120

[6] J.K. Thomas, Physical aspects of photochemistry and radiation chemistry of molecules absorbed on SiO_2, γ-Al_2O_3, zeolites and clays *Chem. Rev.* 93, **1993,** 301-320

[7] J.W.T Spinks, R.J. Woods An introduction to radiation chemistry; 3rd ed.; *Wiley-Interscience Publication* New York, USA, **1990**

[8] P.B. Giannozzi, N. S. Bonini, M. Calandra, R. Car, C. Cavazzoni, D. Ceresoli, G.L. Chiarotti, M. Cococcioni, I. Dabo, A.D. Corso, S. de Gironcoli, S. Fabris, G. Fratesi, R. Gebauer, U. Gerstmann, C. Gougoussis, A. Kokalj, M. Lazzeri, L. Martin-Samos, N. Marzari, F. Mauri, R. Mazzarello, S. Paolini, A. Pasquarello, L. Paulatto, C. Sbraccia, S. Scandolo, G. Sclauzero, A.P. Seitsonen, A. Smogunov, P. Umari, R.M. Wentzcovitch, QUANTUM ESPRESSO: a Modular and Open-Source Software Project for Quantum Simulations of Materials. *J. Phys.: Condens. Matter* **2009,** 21, 395502.

[9] D. Vanderbilt Soft self-consistent pseudopotentials in a generalized eigenvalue formalism *Phys. Rev. B* 41, **1990,** 7892

[10] J. Hutter, M. Iannuzzi, F. Schimann, and J. VandeVondele. cp2k: atomistic simulations of condensed matter systems. *Comput. Mol . Sci*, 4, **2014**

[11] J. VandeVondele, M. Krack, F. Mohamed, M. Parrinello, T. Chassaing, and J. Hutter. Quickstep: Fast and accurate density functional calculations using a mixed Gaussian and plane waves approach. *Comp. Phys. Commun*, 167, **2005**

[12] G. Lippert, J. Hutter, M. Parrinello. A hybrid Gaussian and plane wave density functional scheme. *Molecular Physics*, 92, 1**997**

[13] J. VandeVondele, J. Hutter. Gaussian basis sets for accurate calculations on molecular systems in gas and condensed phases. *J. of Chem. Phys.*, 127, **2007**

[14] J. P. Perdew, K. Burke, M. Ernzerhof. Generalized Gradient Approximation Made Simple. *Phys. Rev. Lett.*, 77, **1996**

[15] Y. Zhao, D. G. Truhlar The M06 suite of density functionals for main group thermochemistry, thermo-chemical kinetics, non-covalent interactions, excited states and transition elements: two new functionals and systematic testing of four M06-class functionals and 12 other functionals, *Theor. Chem. Account,* 120, **2008,** 215-241

[16] M. Guidon, J. Hutter, J. VandeVondele, Auxiliary density matrix methods for Hartree-Fock exchange calculations, *J. Chem. Theory Comput.* 6, **2010,** 2348-2364

[17] O. Gunnarsson, B.I. Lundqvist, Exchange correlation in atoms, molecules and solids by the spin-density-functional formalism, *Phys. Rev. B.* 13, **1976,** 4274-4298

[18] C. Fourdrin, H. Aarrachi, C. Latrille, S. Esnouf, f. Bergaya, S. Le Caër, Water radiolysis in exchanged-montmorillonites: the H_2 production mechanisms. *Environ. Sci. Technol.* 47, **2013,** 9530-9537

[19] N. Mobasher, S.A. Bernal, H. Kinoshita, C.A. Sharrad, J.L. Provis, Gamma irradiation resistance of an early age slag-blended cement matrix for nuclear waste encapsulation *J. Mater. Res.* 9, **2015,** 1563-1571

[20] L. Dezerald, J. J. Kohanoff, A. A. Correa, A. Caro, R. J.M. Pellenq, F. J. Ulm, A. Saul, Cement as a wasteform for nuclear fission products: the case of Sr^{90} and its daughters *Environ. Sci. Technol.*, 49, **2015,** 13676-13683

[21] H. Manazo, J. Dolado, A. Ayuela, Elastic properties of the main species present in Portland cement pastes *Acta. Mater.* 84 **2009,** 411-429

Production of biogenic phosphate minerals and applications for the remediation of radionuclides

T.K Mullan*[1], R. Lunn[1], and J.C. Renshaw[1]

*Correspondence: thomas.mullan@strath.ac.uk

[1] Department of Civil & Environmental Engineering, University of Strathclyde, Glasgow, G1 IXJ, UK

Abstract

The microbial production of phosphate minerals has gained attention as a promising mechanism of *in situ* groundwater remediation. To date, most research has focused on the immobilisation of contaminants by the induced precipitation of insoluble contaminant-phosphate minerals (e.g. uranyl phosphates); however, it is also possible to use this technique to manufacture materials such as calcium phosphates that can incorporate and immobilise a range of contaminants within their structure. These calcium phosphates can be utilised for the long-term, passive remediation of groundwater flow. This project investigates the use of fungi to induce the formation of calcium phosphate minerals *via* the enzymatic hydrolysis of an organic phosphate substrate (phytate). Attention is given to the factors influencing phytate degradation, biomineral formation, composition and characteristics, and this knowledge used to optimise biomineral production.

Introduction

Groundwater contamination is a problem that can arise at all stages of the nuclear fuel cycle, from mining to plant operation to decommissioning and disposal [1].

Treatment of this contamination is required to prevent further spread into the environment and to avoid the potential for contamination to reach public water supplies. One remediation option is *in situ* immobilisation of contaminants within the subsurface, using, for example permeable Reactive Barriers (PRBs). This approach, limits contamination migration into the wider environment while efforts are ongoing to address the contaminant source. It can also aid removal of the contaminated material if it is decided that that is the most suitable final solution. Immobilisation techniques may rely on physical, chemical or biological, mechanisms.

A wide range of materials can be used in PRB construction, for example zerovalent iron or zeolite minerals [2]. Within the context of the nuclear industry phosphate minerals (particularly members of the apatite group such as hydroxyapatite [$Ca_{10}(PO_4)_6(OH)_2$]) are considered to be a promising option [3]. This is due to their ability to immobilise and incorporate a range of relevant contaminants into their structure, including] U, Sr, Co, trivalent lanthanides and actinides], Th, Ra, and Pb [6], and their stability towards degradation by geochemical processes and ionising radiation [3]. Phosphate biominerals (i.e. minerals produced as a result of biological activity), include the teeth and bones of animals, or precipitates formed as a result of microbial activity. These biominerals are currently an active area of research as they may possess superior physicochemical properties to aid the immobilisation of contaminants compared to geologically sourced or synthetically prepared forms. They may also be a more sustainably sourced material compared to options that rely on the relatively limited resources of geologically-sourced phosphate [3].

The microbially induced precipitation of phosphate minerals is of particular interest not only due to the intrinsic properties of the produced mineral but also because microorganisms provide a range of novel opportunities for the deployment and engineering of the remediation solution. For example, biominerals may be produced in *ex situ* bioreactors, or *in situ* by injecting suspended solutions of microorganisms and mineral constituents into the subsurface, or potentially, by allowing multicellular fungi to grow into contaminated media and subsequently induce mineralisation.

Microorganisms are able to induce phosphate biomineralisation through the action of phosphatase enzymes (Figure 1). These enzymes hydrolyse organic phosphate (P_o) compounds and release inorganic phosphate (P_i) into solution, which can then form precipitates with other ions present, for example contaminants in the environment or a supplied source of calcium [5], [7]. The microbial cell may also provide a nucleation point for mineralisation, further supporting the process [7].

Most research to date has focused on using this process to immobilise contaminants directly *via* the

formation of insoluble metal phosphates [8]–[12]. However, the concentration of some contaminants (for example, Np and Pu) will often be too low for the metal-phosphate to precipitate out of bulk solution; in cases such as this, a manufactured biomineral (e.g. calcium phosphates) can be used to support immobilisation of such contaminants [7].
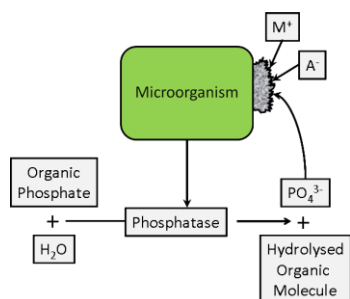

Figure 1 Schematic of phosphate biomineral formation; M+ and A- represent other cations and anions involved in biomineral precipitation

Research into biogenic hydroxyapatite (BHAP), amorphous calcium phosphate produced by a strain of *Serratia* sp. bacterium, showed the biomineral to have a higher sorption capacity for Sr^{2+}, Co^{2+}, Eu^{3+}, and UO_2^{2+} as compared to a synthetically produced hydroxyapatite. This was attributed to the more amorphous nature of the material, smaller crystallite size, and higher specific surface area [5], [13]. Additionally, when compared to synthetic hydroxyapatite and clinoptilolite (a zeolite mineral), BHAP maintained high uptake values for Sr^{2+} and Co^{2+} in the presence of competing cations (Na^+, Mg^{2+}, Ca^{2+}) found in some groundwaters and seawater; an important property due to potential for saline intrusion and/or groundwaters at sites such as Sellafield and Fukushima [14].
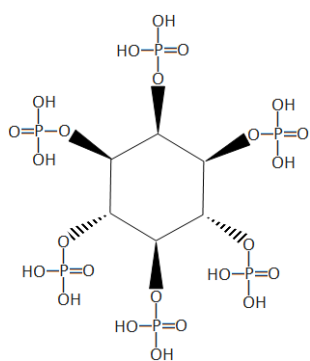

Figure 2 Structure of phytic acid, which mostly occurs in nature as a mixed magnesium/potassium salt [15]

In laboratory scale, proof-of-principle studies, glycerol phosphate compounds have typically been used as a P_o donor molecule. However, the high cost of this compound has been recognised as the main cost-limiting factor in the practical deployment of the technique [7], [16]. An alternative source of phosphate is *myo*-inositol hexakisphosphate ($C_6H_{18}O_{24}P_6$; Figure 2), commonly referred to as 'phytic acid' (as a free acid) or 'phytate' (in salt form); this is a widespread component of plant tissues, particularly seeds and grains [7], [15], [16]. Phytate extracted from plant waste products may be able to provide a readily available and low-cost source of phosphate. Research into phytate degradation has mostly occurred within agricultural sciences [17] and it is only in the past decade that the use of phytate as a substrate for phosphate biomineralization has been studied [9], [10], [16], [18].

Phosphatase enzymes that hydrolyse phytate are commonly known as 'phytases' and are produced by many microorganisms [17], [19], [20]. Two species of fungi have been chosen as promising options for investigating and developing the microbially induced phosphate precipitation technique as a remediation solution.

Aspergillus niger

Aspergillus niger is a species of filamentous fungi commonly found in the environment (Figure 3). *A. niger* is an industrially important organism that is widely used for the production of citric acid, and has also been used commercially for the production of phytase enzymes to enhance animal feed [19]. Recent research has demonstrated the ability of *A. niger* to induce the precipitation of uranyl phosphates [8]. However, the species is also known for its high production of organic acids, particularly oxalic and citric acid [21], [22]. These acids may solubilise minerals, leading to the (re)mobilisation of contaminants, or may form complexes with metals at the expense of phosphate precipitation [7], [21]–[23]. Alternatively, the presence of citrate in the system during biomineralization has been shown to improve subsequent metal uptake values [13] while the formation of insoluble oxalates may be able to support contaminant immobilisation [24].

Figure 3 Colonies of *Aspergillus niger* ATCC 201373 grown on malt extract agar

Blastobotrys adeninivorans

Blastobotrys adeninivorans (Figure 4) is a species of yeast that has been described as having "great

biotechnological potential" due to its production of various important enzymes and ability to grow under a wide range of conditions [25]. Phytase activity appears to be a uniform property for the species, which has also been shown to be capable of using phytate as a source of carbon [26]. *B. adeninivorans* has been successfully used to induce calcium phosphate precipitation *via* the degradation of phytate [18].

Figure 4 Colonies of *Blastobotrys adeninivorans* CBS 8335 grown on yeast-mold agar

A range of factors influence the production and activity of phytase enzymes with phosphate concentration and source, C source, presence/absence of O_2, presence of other chemical species, initial pH, and temperature all known to be important [17], [19], [20], [26]. The effect these factors have differs between microbial species and, while an in-depth study of enzyme regulation is beyond the scope of this work, a basic understanding of these processes is required as they will influence mineral precipitation and determine which environments particular microorganisms are best suited to be deployed in.

Methodology Details

Phytate degradation

Experiments are currently investigating the ability of model microorganisms to degrade phytate under varying growth conditions. Initial studies have focused on the effect of P concentrations on phytase enzyme production. The amount of P_i available is particularly critical as many organisms only display appreciable phytase activity when grown in phosphate-limited media. Cultures grown under a range of conditions, including phosphate-rich and phosphate depleted media, are being investigated for phytase activity either by subculturing cells into new media containing phytate or by filtering cultures and mixing the supernatant with phytate solution to investigate the activity of any extracellular phytase secreted into solution.

Phytase activity is assessed by measuring the amount of P_i released into solution using a colorimetric assay. A 0.5 mL sample (diluted to a theoretical P_i concentration of 0–30 mg/L) is mixed with 0.9 mL of 0.17 M sodium dodecyl sulfate, 1.0 mL of 0.01 M ammonium heptamolybdate in 2 M hydrochloric acid, and 0.1 mL of 0.01M ascorbic acid. The spectrophotometric

absorbance of the assay samples is then measured at 700nm. The absorbance at this wavelength is proportional to P_i concentration. Standards with known concentrations of P_i (0–30 mg/L) were also measured to generate a standard calibration curve .

Results and Discussion

Initial experiments involved pre-growth of cultures in rich growth media containing P_i followed by subculturing of cells into solution containing phytate at a concentration of 5 mM. Solutions were placed on an orbital shaker at room temperature for a week with samples taken and various time points (Figure 5).
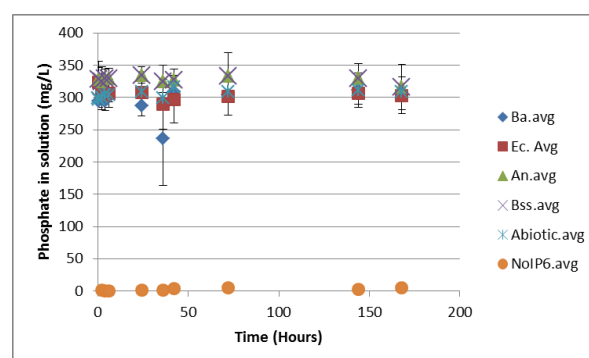

Figure 4 Results of phosphate assay from initial experiments. Ba = *B. adeninivorans*; An = *A. niger*; Ec and Bss represent *Escherichia coli* and *Bacillus subtilis* subsp. *spizizenii*, two species of bacteria that have also been investigated; Abiotic = phytate with no cells; NoIP6 = cells incubated in solution without phytate present. Error bars represent one standard deviation of triplicate samples.

Results showed that the phytate stock used contains a P_i impurity of ~ 10% of the phytate content and that, for all organisms tested, there was no change in P_i content over time. Therefore there was no degradation of phytate by the microorganisms, This suggests that the Pi content in either the test solution or the initial growth cultures was high enough to suppress phytase production. This demonstrates the importance of optimising pre-growth conditions to induce phytase activity, and experiments are ongoing to further understand and characterise this.

Acknowledgements

References

[1] B. J. Merkel and M. Hoyer, '16 - Remediation of sites contaminated by radionuclides', in *Radionuclide Behaviour in the Natural Environment*, C. Poinssot and H. Geckeis, Eds. Woodhead Publishing, 2012, pp. 601–645.

[2] M. M. Scherer, S. Richter, R. L. Valentine, and P. J. J. Alvarez, 'Chemistry and Microbiology of Permeable Reactive Barriers for In Situ

Groundwater Clean up', *Crit. Rev. Environ. Sci. Technol.*, vol. 30, no. 3, pp. 363–411, Jul. 2000.

[3] J. F. Rakovan and J. D. Pasteris, 'A Technological Gem: Materials, Medical, and Environmental Mineralogy of Apatite', *Elements*, vol. 11, no. 3, pp. 195–200, Jun. 2015.

[4] J. M. Hughes and J. F. Rakovan, 'Structurally Robust, Chemically Diverse: Apatite and Apatite Supergroup Minerals', *Elements*, vol. 11, no. 3, pp. 165–170, Jun. 2015.

[5] S. Handley-Sidhu *et al.*, 'Bacterially Produced Calcium Phosphate Nanobiominerals: Sorption Capacity, Site Preferences, and Stability of Captured Radionuclides', *Environ. Sci. Technol.*, vol. 48, no. 12, pp. 6891–6898, Jun. 2014.

[6] J. L. Conca and J. Wright, 'An Apatite II permeable reactive barrier to remediate groundwater containing Zn, Pb and Cd', *Appl. Geochem.*, vol. 21, no. 12, pp. 2188–2200, Dec. 2006.

[7] L. E. Macaskie, P. Yong, and M. Paterson-Beedle, 'Bacterial precipitation of metal phosphates', in *Phosphorus in Environmental Technologies: Principles and Applications*, E. Valsami-Jones, Ed. IWA Publishing, 2004, pp. 549–581.

[8] X. Liang, S. Hillier, H. Pendlowski, N. Gray, A. Ceci, and G. M. Gadd, 'Uranium phosphate biomineralization by fungi', *Environ. Microbiol.*, vol. 17, no. 6, pp. 2064–2075, 2015.

[9] X. Liang, M. Kierans, A. Ceci, S. Hillier, and G. M. Gadd, 'Phosphatase-mediated bioprecipitation of lead by soil fungi', *Environ. Microbiol.*, p. n/a-n/a, 2015.

[10] X. Liang, L. Csetenyi, and G. M. Gadd, 'Uranium bioprecipitation mediated by yeasts utilizing organic phosphorus substrates', *Appl. Microbiol. Biotechnol.*, pp. 1–11, 2016.

[11] L. Newsome, K. Morris, and J. R. Lloyd, 'The biogeochemistry and bioremediation of uranium and other priority radionuclides', *Chem. Geol.*, vol. 363, pp. 164–184, Jan. 2014.

[12] L. Newsome, K. Morris, and J. R. Lloyd, 'Uranium Biominerals Precipitated by an Environmental Isolate of Serratia under Anaerobic Conditions', *PLOS ONE*, vol. 10, no. 7, p. e0132392, Jul. 2015.

[13] S. Handley-Sidhu *et al.*, 'Uptake of Sr2+ and Co2+ into Biogenic Hydroxyapatite: Implications for Biomineral Ion Exchange Synthesis', *Environ. Sci. Technol.*, vol. 45, no. 16, pp. 6985–6990, Aug. 2011.

[14] S. Handley-Sidhu, T. K. Mullan, Q. Grail, M. Albadarneh, T. Ohnuki, and L. E. Macaskie, 'Influence of pH, competing ions, and salinity on the sorption of strontium and cobalt onto biogenic hydroxyapatite', *Sci. Rep.*, vol. 6, p. 23361, Mar. 2016.

[15] S. B. Shears and B. L. Turner, 'Nomenclature and terminology of inositol phosphates: clarification and a glossary of terms.', in *Inositol phosphates: linking agriculture and the environment*, B. L. Turner, A. E. Richardson, and E. J. Mullaney, Eds. Wallingford: CABI, 2007, pp. 1–6.

[16] M. Paterson-Beedle, J. E. Readman, J. A. Hriljac, and L. E. Macaskie, 'Biorecovery of uranium from aqueous solutions at the expense of phytic acid', *Hydrometallurgy*, vol. 104, no. 3–4, pp. 524–528, Oct. 2010.

[17] J. Dvořáková, 'Phytase: Sources, preparation and exploitation', *Folia Microbiol. (Praha)*, vol. 43, no. 4, pp. 323–338, Aug. 1998.

[18] G. Roeselers and M. C. M. Van Loosdrecht, 'Microbial phytase-induced calcium-phosphate precipitation — a potential soil stabilization method', *Folia Microbiol. (Praha)*, vol. 55, no. 6, pp. 621–624, Nov. 2010.

[19] J. E. Hill and A. E. Richardson, 'Isolation and assessment of microorganisms that utilize phytate.', in *Inositol phosphates: linking agriculture and the environment*, B. L. Turner, A. E. Richardson, and E. J. Mullaney, Eds. Wallingford: CABI, 2007, pp. 61–77.

[20] R. Greiner, 'Phytate-degrading enzymes: regulation of synthesis in microorganisms and plants.', in *Inositol phosphates: linking agriculture and the environment*, B. L. Turner, A. E. Richardson, and E. J. Mullaney, Eds. Wallingford: CABI, 2007, pp. 78–96.

[21] M. M. Gharieb and G. M. Gadd, 'Influence of nitrogen source on the solubilization of natural gypsum (CaSO4.2H2O) and the formation of calcium oxalate by different oxalic and citric acid-producing fungi', *Mycol. Res.*, vol. 103, no. 04, pp. 473–481, Apr. 1999.

[22] A. Ceci *et al.*, 'Transformation of vanadinite [Pb5(VO4)3Cl] by fungi', *Environ. Microbiol.*, vol. 17, no. 6, pp. 2018–2034, 2015.

[23] X. Liang, M. Kierans, A. Ceci, S. Hillier, and G. M. Gadd, 'Phosphatase-mediated bioprecipitation of lead by soil fungi', *Environ. Microbiol.*, vol. 18, no. 1, pp. 219–231, Jan. 2016.

[24] G. M. Gadd *et al.*, 'Oxalate production by fungi: significance in geomycology, biodeterioration and bioremediation', *Fungal Biol. Rev.*, vol. 28, no. 2–3, pp. 36–55, Oct. 2014.

[25] E. Böer, G. Steinborn, K. Florschütz, M. Körner, G. Gellissen, and G. Kunze, 'Arxula adeninivorans (Blastobotrys adeninivorans) — A Dimorphic Yeast of Great Biotechnological Potential', in *Yeast Biotechnology: Diversity and Applications*, T. Satyanarayana and G. Kunze, Eds. Dordrecht: Springer Netherlands, 2009, pp. 615–634.

[26] K. Sano, H. Fukuhara, and Y. Nakamura, 'Phytase of the yeast Arxula adeninivorans', *Biotechnol. Lett.*, vol. 21, no. 1, pp. 33–38, Jan. 1999.

USE OF COLLOIDAL SILICA GROUT FOR

GROUND BARRIERS IN DECOMISSIONING:

INJECTION EXPERIMENTS AND NUMERICAL SIMULATIONS

M. Pedrotti*[1], C. Wong[1], P. Bots[1], G. El Mountassir[1] and R. Lunn[1]

*matteo.pedrotti@strath.ac.uk

[1] Department of Civil and Environmental Engineering (University of Strathclyde, Glasgow, UK)

Abstract

Over the last three decades, colloidal silica has been investigated and more recently adopted as a low viscosity grouting technology (e.g. for grouting rock fractures within geological disposal facilities nuclear waste). The potential of colloidal silica as a favourable grouting material exists due to: its initial low viscosity; its low hydraulic conductivity after gelling (of the order of 10^{-7} cm/s); the very low injection pressures required; its controllable set/gel times (from minutes to several days); the fact it is environmentally inert; its small particle size (less than hundreds of nanometres) and its cost-effectiveness. Colloidal silica can be destabilised by the addition of a salt accelerator compound and a change to pH, resulting in a rapid increase in viscosity (i.e. gelation) and formation of a rigid solid gel. This behaviour allows for low injection pressures to be used during the grouting process due to the initial low viscosity; with the resulting gel forming the contaminant ground barrier. This study aims to investigate the use of colloidal silica based grouts for formation of ground barriers at the Sellafield site. Potential applications include pre-treatment of the ground beneath, and surrounding, legacy structures prior to the retrieval of hazardous wastes and the formation of horizontal and vertical barriers surrounding unlined waste disposal trenches. In this summary some preliminary results on lab-scale injection experiments and finite element simulation are compared.

Why colloidal silica?

Groundwater control at contaminated sites is often controlled via the use of low permeability barriers created using excavation and replacement or grouting techniques. Soil-bentonite slurry trenches are a commonly employed method. They are constructed by excavating a continuous narrow trench under a bentonite slurry that stabilizes the excavation. The trench is backfilled subsequently with a blend of natural soil and bentonite, thereby displacing the slurry [1]. The completed wall acts as a barrier to lateral flow of water and most fluid pollutants. The main issues with the deployment of this technique on a nuclear decommissioning site relate to worker exposure and the challenge of accessing and excavating contaminated soil.

Jet grouting and permeation grouting are two general categories usually suitable for hydraulic barriers. Jet grouting uses high-energy emplacement of cement or chemical grouts whereby the sediment is displaced and mixed with the grouting material. Permeation

grouting is the injection of a liquid grout (low viscosity) that fills the natural porosity and then sets or gels to form a solid void-filling material [2].

The most commonly used grouts are cement grouts where Portland cement is the primary component. The particle size distribution of the cement particles controls the ability of the grout to penetrate small pores or openings. For cement grouts, emplacement is often an issue for finely textured regions. Microfine or ultrafine cement grouts incorporate micron-scale solids in the mix. However grout penetration for cement grouts would only be appropriate for coarse sand or gravel layers, with no fine sediments less than about 0.1 mm diameter [2]. Cement grouts are also not suitable for injection near surface due to the potential for ground heave under the necessary high injection pressures.

Chemical grouts are easier to inject than cement grouts because they are stable solutions, they have lower viscosity and can be injected into smaller pore sizes. However, chemical grouts are often expensive, exhibit syneresis and may contain toxic components [3], colloidal silica represents an exception.

Colloidal silica as grouting material

Colloidal silica as a grouting material has been successfully adopted as a fluid-flow control system within the petroleum industry since the late 1980s [4]. Consolidated core plugs of fully cured colloidal silica were observed to withstand applied pressure gradients of more than (56 MPa/m) before exhibiting any permeability change. Passive site remediation proposed by Gallagher [5] studied the application of colloidal silica as a non-disruptive mitigation technique to sites susceptible to liquefaction. Desirable characteristics were long injection periods up to 100 days for low concentration solutions of approximately 10 to 20% colloidal silica concentration. Du Pont Chemicals R & D

initiated work examining the feasibility of colloidal silica grout as a soil remediation technique through a series of bench-scale laboratory studies. Gelled colloidal silica was seen to prevent leaching of fluids containing metals through permeability reduction. Further, high affinities for the adsorption of metals from solution were seen by the colloidal silica gel itself [6]. Similarly, the stabilization process of chromium contaminated soils using colloidal silica was investigated by Yossapol and Meegoda [7].

In the 90s, Lawrence Berkley National Laboratory and Brookhaven National Laboratory carried out in-situ [8-12] and laboratory [13-15] tests to demonstrate the use of silica colloids for permeation grouting for containment technology.

Researchers at Chalmers University of Technology have investigated the application of colloidal silica grout to minimise water ingress during the construction and operation of a nuclear waste repository in hard rock at great depth. In order to evaluate penetrability, laboratory mechanical tests on colloidal silica [16, 17] and field tests [18, 19] were performed. More recently, colloidal silica has been adopted in the tunnelling and underground construction industry for preventing water ingress, mainly as a secondary injection grout during the pre-injection stage (i.e. injecting in advance of the tunnel face during excavation) (e.g. Butrón, Gustafson [20], Bahadur, Holter [21]).

Colloidal silica gelling

Colloidal silica is a stable aqueous suspension of microscopic silica particles (SiO_2). In alkaline solutions and low electrolyte concentration colloidal silica is stable. Destabilization of the solution and subsequent gelation can be induced by destabilization of the particle repulsive forces through the addition of an accelerator electrolyte compound. This process, shown in Figure 1, results in a rapid viscosity increase

after a given period of time (gel time). Gel time has been proven to depend on colloidal particle size, colloidal particle concentration, electrolyte concentration, cation valency, cation atomic mass and temperature (which is not considered here) [22].
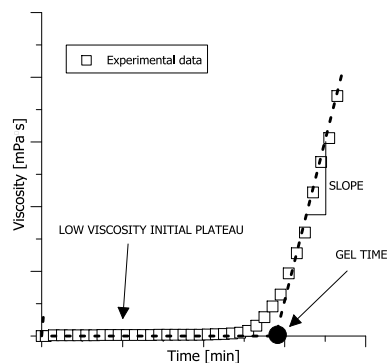

Figure 1. Viscosity trend and gel time

Grout injection – Experimental setup

An injection tank (1.3m x 0.4m x 0.1m) has been set up to investigate grout injection. These experiments will test our capability to accurately predict grout penetration within different soils, using a variety of ground water compositions.

Leighton Buzzard sand with d_{50} 1.2 mm, specific gravity 2.65 and coefficient of conformity 1.26 was used for this test. The final porosity of the sand within the tank was estimated to be about 0.36.

The tank was filled with about 72 kg of sand and 17 litre of water. On the top layer a layer of clay was made in order to guarantee an horizontal upon injection.
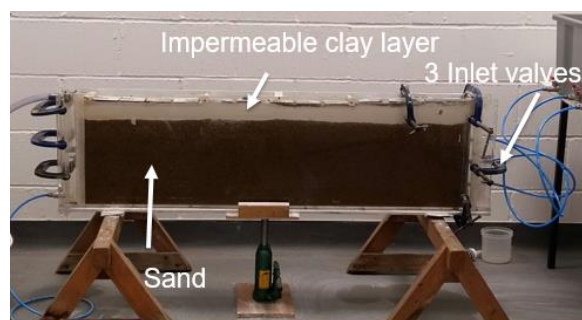

Figure 2. Experimental setup

Injection was performed from three lateral valves connected to a constant-head reservoir (Figure 2).

As preliminary injections water and fluorescein first and colloidal silica without any accelerant, later, were injected. Subsequently, colloidal silica with NaCl accelerant (gel time 1 hour) was injected and let to gel inside the tank, during the injection (Figure 3).

Figure 3. Grouted sand after colloidal silica injection

A fourth injection was performed by injecting the colloidal silica grout in a tank where the water was saline water (35g/L NaCl). For this injection accelerant was designed in order to get a gel time of 1 hour. The accelerant was designed by mixing the tank saline water with KCl. The required amount of KCl to achieve a 1 hour gel time was calculated by means of the analytical model previously developed [22].

Another last injection was performed in a tank that was filled by a mixture of Leighton Buzzard sand and commercially available washed building sand (by a ratio of 9 to 1 by volume) in order to reduce the hydraulic conductivity within the tank. For this experimental setup, injection was performed with a colloidal silica grout having a gel time of about 2 hours.

Grout injection – Finite Element modelling

The numerical model was developed with COMSOL Multiphysics ®.

The model was created by implementing the generalised form of Darcy's equation for the velocity profile of the injected fluid. This equation was coupled with a transport model implementing two different species. One species to simulate the concentration of colloidal silica and the other to simulate the accelerant concentration.

At each time-step and for any given spatial point, the model computed the viscosity of the colloidal silica via the viscosity analytical equation [22], according to the elapsed time, the accelerant concentration and the colloidal silica concentration

Preliminary results

In Figure 4 and Figure 5 two preliminary results are shown. Figure 4 shows the experiment and simulation comparison of fluorescein injection for a given time. Figure 5 shows the experiment and simulation comparison of colloidal silica injection.
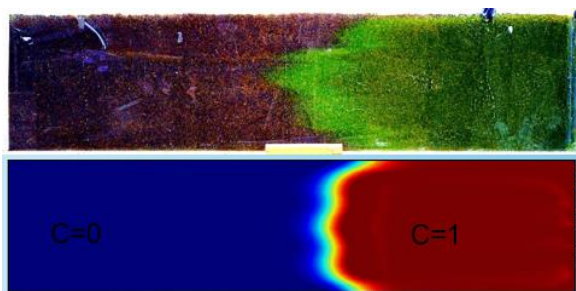

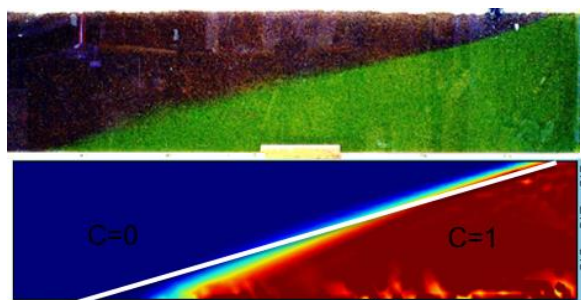**Figure 4. Fluorescein injection. Experiment and simulation comparison**

Figure 5. Colloidal silica injection (no accelerant). Experimen and simulation comparison

References

1. Tallard, G., *Slurry trenches for containing hazardous wastes.* Civil Engineering—ASCE, 1984. **54**(2): p. 41-45.
2. Truex, M.J., et al., *Evaluation of In Situ Grouting as a Potential Remediation Method for the Hanford Central Plateau Deep Vadose Zone.* Pacific Northwest National Laboratory, 2011.
3. Gallagher, P.M., S. Spatari, and J. Cucura, *Hybrid life cycle assessment comparison of colloidal silica and cement grouted soil barrier remediation technologies.* Journal of Hazardous Materials, 2013. **250**: p. 421-430.
4. Jurinak, J. and L. Summers, *Oilfield applications of colloidal silica gel.* SPE production engineering, 1991. **6**(04): p. 406-412.
5. Gallagher, P.M., *Passive Site Remediation for Mitigation of Liquefaction Risk*, in *Civil and Environmental Engineering*. 2000, Virginia Polytechnic Institute and State University.
6. Noll, M.R., C.L. Bartlett, and T.M. Dochat. *In situ permeability reduction and chemical fixation using colloidal silica*. in *Proceedings of the Sixth National Outdoor Action Conference*. 1992.
7. Yossapol, N. and J. Meegoda, *Remediation of Heavy Metal Contaminated Soil with Colloidal Silica.* Hazardous and industrial wastes, 2000. **32**: p. 787-798.
8. Persoff, P., et al., *Injectable barriers for waste isolation*. 1995, Lawrence Berkeley Lab., CA (United States).
9. Moridis, G., et al., *A field test of permeation grouting in heterogeneous soils using a new generation of barrier liquids.* Committed To Results: Barriers for Long-Term Isolation. ER, 1995. **95**.
10. Moridis, G., et al. *A field test of a waste containment technology using a new generation of injectable barrier liquids*. 1996.

11. Moridis, G., A. James, and C. Oldenburg, *Development of a design package for a viscous barrier at the Savannah River site.* 1996, Lawrence Berkeley National Lab., CA (United States). Funding organisation: USDOE Office of Environmental Restoration and Waste Management, Washington, DC (United States).

12. Moridis, G.J., S. Finsterle, and J. Heiser, *Evaluation of alternative designs for an injectable barrier at the Brookhaven National Laboratory Site, Long Island, New York.* Water Resources Research, 1999. **35**(10): p. 2937-2953.

13. Hakem, N., et al. *Sorption of cesium and strontium on Savannah River soils impregnated with colloidal silica.* in *International Containment Technology Conference.* 1997. Petersburg:[sn].

14. Manchester, K., et al. *Grout selection and characterization in support of the colloidal silica barrier deployment at Brookhaven National Laboratory.* in *Proc. 2001 International Contain. and Remed. Technol. Conf. and Exhib., 10-13 June, 2001. Orlando, FL.* 2001.

15. Persoff, P., et al., *Effect of dilution and contaminants on sand grouted with colloidal silica.* Journal of geotechnical and geoenvironmental engineering, 1999. **125**(6): p. 461-469.

16. Axelsson, M., *Mechanical tests on a new non-cementitious grout, silica sol: A laboratory study of the material characteristics.* Tunnelling and underground space technology, 2006. **21**(5): p. 554-560.

17. Butrón, C., M. Axelsson, and G. Gustafson, *Silica sol for rock grouting: Laboratory testing of strength, fracture behaviour and hydraulic conductivity.* Tunnelling and underground space technology, 2009. **24**(6): p. 603-607.

18. Funehag, J. and Å. Fransson, *Sealing narrow fractures with a Newtonian fluid: Model prediction for grouting verified by field study.* Tunnelling and underground space technology, 2006. **21**(5): p. 492-498.

19. Funehag, J. and G. Gustafson, *Design of grouting with silica sol in hard rock–New design criteria tested in the field, Part II.* Tunnelling and underground space technology, 2008. **23**(1): p. 9-17.

20. Butrón, C., et al., *Drip sealing of tunnels in hard rock: A new concept for the design and evaluation of permeation grouting.* Tunnelling and underground space technology, 2010. **25**(2): p. 114-121.

21. Bahadur, A., K. Holter, and A. Pengelly. *Cost-effective pre-injection with rapid hardening microcement and colloidal silica for water ingress reduction and stabilisation of adverse conditions in a headrace tunnel.* in *Underground Space– The 4th Dimension of Metropolises, Three Volume Set+ CD-ROM: Proceedings of the World Tunnel Congress 2007 and 33rd ITA/AITES Annual General Assembly, Prague, May 2007.* 2007. CRC Press.

22. Pedrotti, M., et al., *An analytical model for the control of silica grout penetration in natural groundwater systems.* Tunnel and underground space technology, 2016 (under revision).

Characterization of cement based material through Atomic Force Microscopy

PhD Student **Luca Rizzo**

University of Strathclyde – 2017

Concrete is the most widely used construction material and the most produced in the world with over 2.5 billion tons produced each year [Hartsock2015], and its first use is estimated around 300 BC by Romans, but its properties are not yet well investigated due to the complexity of its matrix. In particular, is a nanostructured, multi-phases, composite material that ages over time. It is composed of an amorphous phase, nanometer to micrometer size crystals, and bound water [Sanchez2010].

Scanning probe microscopy (SPM), invented in 1980, is widely applied to the study of materials surfaces down to the atomic scale [Sharif2016]. Between all the SPMs available today, the atomic force microscope is by far the most widely employed, mainly due to its versatility in terms of materials to which it may be applied regardless of electrical conductivity (metals, metal oxides, semiconductors, etc.) as well as the variability in operating environments, ranging from ambient and liquids to ultrahigh vacuum (UHV)[Baykara2016] . It provides spatial resolution of a fraction of a nanometer, depending on the surface roughness and the type of specimen, with a sharp-ended probe typically less than 10 nm in diameter [Zhong1993,Magonov1997]. The AFM is one of the foremost tools for imaging, measuring, and manipulating matter at the nanoscale. The information is gathered by "feeling" the surface with a mechanical probe, and monitoring the consequent deflection of the cantilever attached to the tip, versus its position on the sample. Related to cement, AFM is recognized as an important device to study its hydration mechanism, its cohesion forces [Sanchez2010], the carbonation of its phases and the evolution of cement pastes surface morphology when exposed to different RH values.

My PhD project involved a deep insight on the literature to understand how to enrich data and experiments about cement related materials that can be investigated through the AFM technique. Cement pastes surface inspection at micro-nano scale is of great interest to understand the nature of its cohesion and the atomic structure, but the porous nature of this material doesn't allow a simple and straightforward procedure with an atomic force microscope.   A meticulous procedure to try to improve the quality of the surface of cement pastes had been carried out, finding out the best water/solid ratio in the mixing phase (calcium hydroxide-nanosilica-water), the best substrate to

replicate a flat surface by depositing the cement paste during its curing, and how thermodynamic parameters as temperature and pressure affect the preparation. The MICA replication method seems the most reliable one, using a W/S ratio of 0.5 and by slowing spreading the cement during its early steps of curing /hydration.

Applying pressure to spread the cement onto the mica doesn't produce better results it rather can alter the surface of the substrate. Higher/lower temperature relatively to normal conditions doesn't seem to change significantly surface conditions, but we recently implemented a hydrothermal chamber/vessel which will be used to quantitatively determine temperature effects on the roughness.

We managed to obtain some nice resolution frames at the microscale with our improvements as shown below, to qualitatively evaluate the reactivity difference between nanosilica and silica fume with respect to calcium hydroxide to produce cement.
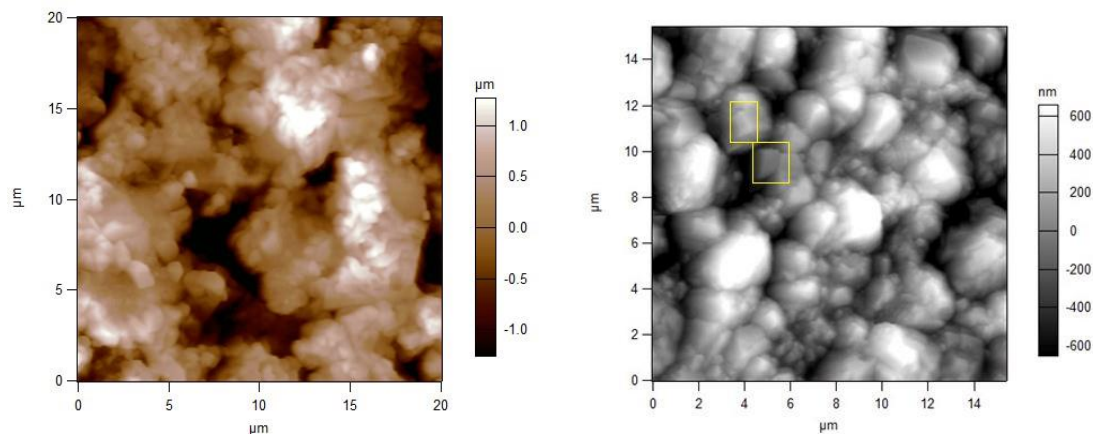

Figure : AFM images of CH-NS(left) and CH-SF(right) samples. Silica Fume is less reactive than Nano Silica, so there could be traces of unreacted Calcium Hydroxide (Portlandite) visible in the marked areas.   No CH crystals detected in CH-NS sample.

Afm will be used to study surface properties of cement pastes in different environments (CO2, Humidity, Solutions) through force distance curves (using standard colloidal probes),and eventually verifying evidences in imaging.

After an appropriate literature review, calcite portlandite and ettringite became object of our research as well, since AFM provides a unique tool to investigate interactions with respect to different species by crystal growth and dissolution in situ: in particular, incorporation of different ions in the crystal structure leads to inhibition of growth. Moreover, ionic strength, pH and other parameters can be changed to see their effects during the reactions. Calcite crystals are abundant and easily available; their surface is one of the most studied one as AFM substrates considering the surface is easy to cleave and to scan. We implemented a dual syringe pump system (one injects-one withdraws) with a fluid environmental cell which allow our chamber to have a controlled pressure

and amount of liquid during the scan above the surface. Since AFM is very sensitive to environmental effects having such a system allow to improve reproducibility and reliability of the experiments.

To improve my skills and familiarity with the AFM, I had been monitoring dissolution of calcite in the first stages to correlate the dissolution rate with the flow rate, in presence of DI water. We are right now getting real data about the inhibition of calcite growth in presence of Strontium Chloride in a range of concentrations (0.2 mM to 2mM) (check pictures) which will be available after proper data analysis. The same experiment will be tried in presence of other radionuclide analogues such as: Zinc Chloride, Cesium Chloride and Europium chloride to figure out if calcite can incorporate these cations in its crystal structure or to determine eventual interactions. Portlandite and Ettringite are other 2 important phases contained in Portland cement, and they will be object of our studies too. For this purpose we had been trying their synthesis (since they are hardly available in the market). For the synthesis of portlandite we had been trying many different recipes but the slow counter-diffusion method suggested by Ruiz-Agudo(2013) is the one which produced the best results so far. We got some clear crystals millimetre sized as well, and we are waiting for data analysis of XRD to understand if is pure portlandite or if they partially carbonated by atmospheric carbon dioxide. Portlandite will be studied to explore its reactivity with respect to magnesium hydroxide (magnox). Considering the lower solubility of the brucite we aim to study an epitaxial growth of brucite above the portlandite crystals. We managed to obtain some ettringite small crystals by mixing specific quantities of aluminium sulfate and calcium hydroxide with water to obtain a supersaturated solution of ettringite, stored at low temperature for weeks. Our crystals are millimetre sizes and we are trying to increase their size by seeding crystals technique.

Ettringite growth in the cement is known as the cancer of the cement, since its growth involves a great volume expansion in the concrete causing tensions and cracks; this mineral is very challenging to growth and that's why a characterization would lead to interesting data about its properties.

Smart cements for chloride / moisture sensing in nuclear concrete assets

L. Biondi*[1], M. Perry[1], A. Hamilton[1]

*lorena.biondi@strath.ac.uk

[1]Department of Civil and Environmental Engineering (University of Strathclyde, Glasgow, UK)

Abstract

Chlorides and moisture are two leading causes of reinforced concrete degradation. The issue is particularly important in a nuclear context, where concrete assets are usually coastal and may underpin safety-critical structures and radiation barriers. The goal of this research work is to develop an affordable, non-destructive, and combined monitoring and maintenance technology to support concrete integrity during operation and decommissioning in the presence of chlorides, water and radiation. We are developing novel "smart cements" coupled with an electrical system for use as a) chloride / moisture sensors and b) surface repairs for concretes at Sellafield. The project's objectives are to: i) develop field-applicable sensors, ii) assess their sensing and repair performance under beta and gamma radiation, moisture and chloride contamination and iii) develop their associated EIS (Electrical Impedance Spectroscopy) interrogation and data processing systems. In this paper we present the first results of making geopolymer binders, putting them on concrete samples and curing them, for the particular application of monitoring.

Introduction

Intelligent monitoring of concrete structures consists of automated measurement of the status of a structure and its components, by means of surface mounted or embedded sensors. These measurements may be performed by 'smart' structures and sensors, consisting of smart materials, which change their state in response to environmental conditions [1]. One of the main factors which cause corrosion of reinforcing rebars is the presence of chloride ions and moisture in concrete [2]. A very important technological challenge is developing new low-cost, effective non-destructive methods to monitor their concentrations in concrete. The issue is important for all types of buildings, and even more for special structures, such as concrete structures in a nuclear context. This work proposes a novel solution for both moisture and chloride monitoring, providing also repair and protection to concrete. This project will develop sensors based on novel "smart cements", which are fly-ash geopolymers, a class of highly-adhesive binders which cure to a durable, chemically-resistant, electrically conductive shell. This electrical conductivity has previously allowed geopolymer surface layers to be used as strain and temperature sensors [3]. Here, we will use the Electrical Impedance Spectroscopy (EIS) technique to monitor chlorides and moisture. The sensor that we will develop consists in a geopolymer layer put on a concrete surface, with electrodes linked to interrogation hardware, by means of which we can do EIS analysis (as shown in Fig. 1).
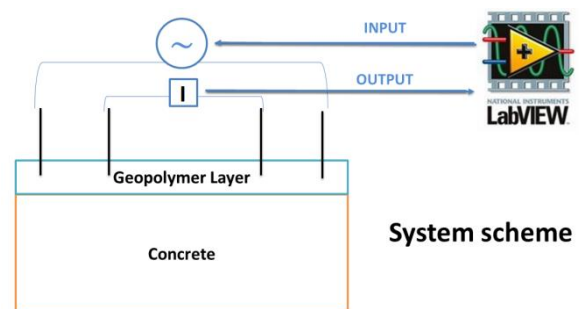

Figure 1 - Scheme of the system

This work is related to the first part of the project that consists of making a suitable geopolymer binder, putting it on a concrete surface, and curing it at certain humidity and temperature conditions, in order to achieve an uncracked and uniform layer.

Theory

In the normal highly alkaline environment of concrete, pH > 11.5, and without chloride, the surface of steel rebars is covered with a thin passive oxide film, which protects the steel from corrosion. Under certain

conditions, the passive film becomes unstable leading to corrosion. This results in cracking and spalling of concrete, since the products of corrosion swell creating internal stress [1]. *Depassivation* happens for two main reasons: *carbonation* and *chloride contamination* of concrete. *Carbonation* is due to a reduction of the pH in the concrete pore solution. CO_2 comes from the atmosphere and dissolves in the pore solution, neutralizing alkaline components and reducing the pH value. The speed of carbonation depends on the *moisture* content of the concrete: transport of CO_2 in concrete is very slow in pores filled with water, but the carbonation process can't take place without water. For this reason, the most dangerous range of moisture for carbonation is between 50 % and 80 % [4]. *Chloride* may come from internal sources, for instance the mix ingredients, or from external sources, such as de-icing salts and sea water. The corrosive attack of steel from chloride takes place only when the concentration of chloride in the region of concrete in contact with rebars reaches a suitable value, in the presence of a particular value of rebar electric potential. Moisture plays an important role also in this process, since it can happen only for chloride ions dissolved in the water contained in the pores of concrete [4].

Chloride content monitoring is challenging, since embedded sensors should be placed within concrete and not only on its surface. One developed and quite successful method is based on ion selective electrodes embedded in concrete, and another successful method is based on the use of fibre optic sensors. Numerous different methods are available to monitor moisture and humidity in concrete, most of them based on the measurement of a property of the material related to the moisture content [1]. The most suitable methods used to monitor moisture are h*umidity sensors* (dew point, thermal conductivity humidity electrochemical cell, wood/brick, or fibre optic sensors), e*lectrical resistance moisture sensors* and *dielectric permittivity sensors* (time domain reflectometer, capacitance and microwave sensors). The issue of all these methods is that they are not suitable for a long term monitoring, some of them are not accurate, and they don't provide repair and protection to concrete [1].

The novel method proposed here is based on the use of geopolymer binders, first described by Davidovits as cementitious materials obtained by the reaction between inorganic materials, rich in Silicium (Si), Aluminium (Al) and oxygen, with alkaline activators, which accelerate the polymerization reaction [5]. The most common alkaline activator is a combination of sodium hydroxide and sodium silicate, due to cost and availability [6]. We use fly ash as inorganic material for making geopolymers. Fly ash is a readily available and cheap resource, since it is a waste product of coal power plants. Fly ash includes substantial amounts of silicon dioxide (SiO_2), calcium oxide (CaO) and aluminium oxide (Al_2O_3) [5]. Calcium ions provide a faster reactivity, and allow a good hardness in a shorter curing time. Moreover the good electrolytic conductivity of fly ash geopolymers is suitable for EIS application. In the USA, Fly ash is divided into two distinct classes: Class F, Low-calcium fly ash, with CaO content less than 10%; class C, high-calcium class, with CaO content greater than 10%. In the UK all fly ash belongs to class F [5].

Methodology Details

Geopolymer synthesis

The mixing procedure for geopolymers consists of mixing fly ash with an alkali activator solution made of sodium hydroxide solution and sodium silicate solution (Fig. 2).

Figure 2 - Mixing procedure

Sodium Hydroxide solution is 10 Molar. Sodium silicate solution is made with $Na_2O \sim 10.6\%$ and $SiO_2 \sim 26.5\%$. The alkali activator solution was made at least 24 hours before making the binder, since the reaction between the two solutions is exothermic. The quality of the fly ash geopolymer layer depends on the following variables: a) the mass ratio L/A between the alkaline solution (L) and the fly ash powder (A) [5]; b) the mass ratio SH/SS between Sodium Hydroxide (SH) and Sodium Silicate (SS) solutions [5]; c) the molarity of the Sodium Hydroxide Solution [7]. Changing all these variables, we could find a suitable geopolymer layer for the sensor. Until now we used only one value of molarity for the NaOH solution, 10 M, and only one combination of the two ratios L/A and SH/SS, respectively: 0.50 and 0.40.

Sample preparation and curing

After mixing a geopolymer binder, we put it as a layer on concrete samples. We used concrete samples of different ages:
o small concrete cubes less than 3 months old;
o small concrete cubes over 3 months old;
o small concrete cubes over 6 months old;
o 3 years old concrete slabs;

o over 4 years old concrete slabs.

In some samples we put electrodes. We used copper electrodes with different thicknesses: 0.1 and 0.05 mm. The samples were cured in the following conditions:

- some at room temperature (23 °C) for about 28 days;
- some in the environmental chamber (EC) at 40°C for 3 days.

Results and Discussion

The main task of the experiment was to obtain uncracked geopolymer layers. In the following figures, we can see the difference between old and young concretes in curing geopolymers.
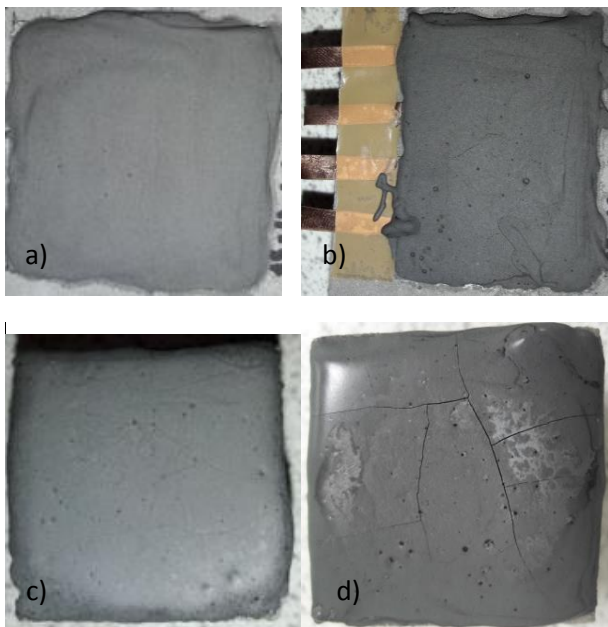

Figure 3 – The images a) and b) show geopolymer layers cured at 23°C for 28 days, on a 3 years old slab, respectively with and without electrodes. The images c) and d) show geopolymer layers cured at 23°C for 28 days, respectively on over six months old concrete sample and less than 3 months old concrete sample.

Looking at Fig. 3, we can see an evident difference between geopolymer layer put on over 4 years old concrete and geopolymers put on younger concretes, even if they were cured at the same conditions (23°C, for 28 days). In fig. 3, the images a) and b) show samples made on 4 years old concretes. The image a) shows a geopolymer layer without cracks; the image b) shows only some very slight cracks, probably due to the presence of copper electrodes with a thickness of 0.1 mm. The image 3 c) shows a geopolymer put on more than 6 months old concrete sample, and it has got a slightly evident network of cracks. The image 3 d), at the end, is related to the youngest concrete sample, less than 3 months old, and it shows a geopolymer with

marked and deep cracks. The cracks on samples which look cracked started to be visible from the 5th to the 10th day of curing. An explanation to these results can be find in the hydration process of concrete. Concrete is achieved by mixing sand, aggregates, cement and water. The water causes the hardening of concrete through a process called hydration, that is a chemical reaction in which the major compounds in cement form chemical bonds with water molecules and become hydrates. The overall progress of the hydration reactions is described by the degree of hydration, which is simply the ratio between the cement that has reacted and all the initial amount of cement. Complete hydration of all the cement gives a degree of hydration = 1. [8] Conventional Portland cement reaches a value of 1 (complete hydration) after one year, but this will not always be the case, as many cement pastes will never reach full hydration. The final degree of hydration will depend on the water/cement of the paste, the cement particle size, and the curing conditions. [9] Once put the geopolymer layer on concrete surface, the curing process of geopolymer may be affected by the hydration happening in concrete, since the aqueous solution in concrete pores reaches and interacts with the still fresh geopolymer binder. In support of this, we found that the samples where the geopolymer binder was put when it was already a bit hardened (more than 20 minutes after the mixing) look without evident cracks, even on young concrete, as shown in fig. 4. The explanation could be that a more hardened geopolymer binder interacts less with the pore solution of concrete.

Figure 4 – Geopolymer binder put on less 3 months old concrete after more than 20 minutes that it was mixed.

The same results were found on samples cured in the environmental chamber at 40°C for 3 days. Looking at fig. 5 below, we can see that the sample made on young concrete (on the left) is slightly cracked, instead the sample made on over 4 years old concrete is not cracked at all. Moreover, by compare the image d) of fig. 3 with the left image of fig. 5, we can see that the sample cured at room temperature is more cracked than the sample cured in the environmental chamber at 40°C, even if they are both made on young concrete. One explanation may be that the sample shown in fig. 3 was made on a concrete made about 40 days before, instead sample in fig. 5 was made after more than 3 months. Another explanation can be the use of environmental chamber in the second case, which

ensures the insulation of the samples from the external environment and allows to maintain more stable conditions during the curing time. For this reason in the future we will vary curing conditions, as temperature, time, and even humidity, using the environmental chamber.
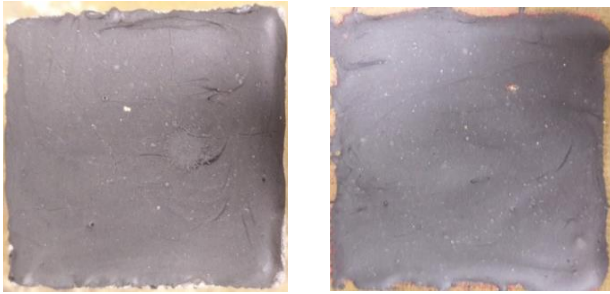

Figure 5 - On the left, geopolymer on a young concrete sample, over 3 years old; on the right, geopolymer on a concrete sample over 4 years old. Both cured in the environmental chamber at 40°C for 3 days.

At the end, fig. 6 shows samples made with and without electrodes embedded in the geopolymer layers, on a concrete slab (more than 4 years old).
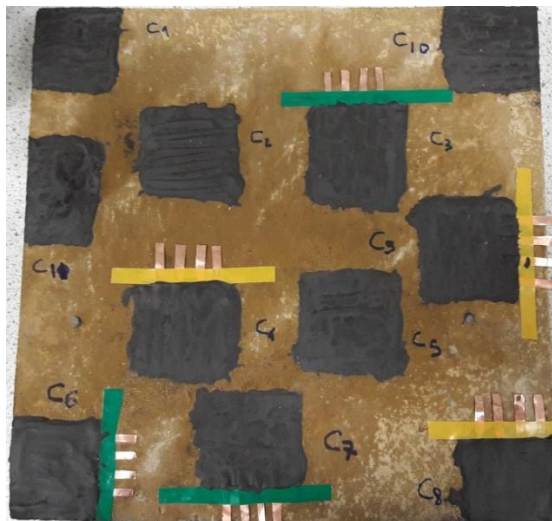

Figure 6 – Samples made on a concrete slab more than 4 years old. Samples with the green insulating tape are made with copper electrodes 0.05 mm thick, and samples with the yellow insulating tape are made with copper electrodes 0.1 mm thick. The slab was cured in the environmental chamber at 40°C for 3 days.

As we can see, the thickness of the electrodes doesn't change the result. There are only very slight cracks in some samples with electrodes, and in particular in samples in the corner of the slab.

Conclusions and Future Work

The results of this work are optimistic, as we have achieved uncracked geopolymer surface layers on concretes greater than 3 years old, in both curing conditions, 40°C in the environmental chamber and at room temperature (23°C). This represents an advantage since the sensing system may be applied to the monitoring of existing structures. However, this work is preliminary. More tests will be done, varying: the ratios L/A and SH/SS, the molarity of NaOH solution, the curing temperature, humidity level and time, and the hardness of the geopolymer binder in putting it on concrete surface. Moreover, in addition to the simple qualitative analysis done in this work, it is important to do also quantitative measurements as: electrical conductivity, porosity, absorptivity, strength and adhesion measurements. Also imaging may be useful to detect micro-cracks. All of these tests and measurements will help us to identify the most suitable geopolymer binders for this specific application.

References

[1] Davies R. D. and Buenfield N. R., Intelligent Monitoring of the Deterioration of Concrete Structures, DTI/CIRIA Report.

[2] Legat A. (2007). Monitoring of steel corrosion in concrete by electrode arrays and electrical resistance probes. Electrochemical Acta.

[3] Saafi M., Piukovics G., J Y. (2016). Hybrid grapheme/geopolymeric cement as a superionic conductor for structural health monitoring applications, Smart materials and structures. IOP Publishing.

[4] Bertolini L., Elsener B., Pedeferri P., Redaelli E., Polder R. (2013). Corrosion of steel in concrete: prevention, diagnosis, repair. 2nd edition, Wiley.

[5] Davidovits J. (2015). Geopolymer chemistry and applications. 4th edition. Institut Géopolymère.

[6] Turner L. K., Collins F. G. (2013). Carbon dioxide equivalent (CO2-e) emissions: A comparison between geopolymer and OPC cement concrete. Constructions and building materials.

[7] Hanjitsuwan S. (2014). Effects of NaOH concentrations on physical and electrical properties of high calcium fly ash geopolymer paste. Cement &concrete composites.

[8] A. van Beek, Hilhorst M.A. (1999). Dielectric measurements to characterize the microstructural changes of young concrete. HERON, vol. 44, No. 1.

[9] Jennings H., Thomas J. J. Materials Science of Cement Primer. TEA-21 Year 5 Final Report.

The effects of colloidal silica based grouts on Sr and Cs speciation – present and future research

P. Bots[*1], R.J. Lunn[1], G. El Mountassir[1], M. Pedrotti[1], T.E. Payne[2], J.L., J.C. Renshaw[1]

*Correspondence: pieter.bots@strath.ac.uk

[1] Department of Civil and Environmental Engineering, University of Strathclyde, Glasgow, G1 1XJ, UK
[2] Australian Nuclear Science and Technology Organisation, Kirrawee DC, New South Wales 2232, Australia

Abstract

This study aims to investigate the use of colloidal silica based grouts for formation of ground barriers at the Sellafield site (Cumbria, UK) and for in-situ encapsulation of low-level wastes at the Little Forest Legacy Site (New South Wales, Australia). Here we summarise results on the interactions of radionuclides (Sr and Cs) with soil and waste materials. Finally, we summarize the pathways to obtain detailed information on the effects of colloidal silica based grouts on these interactions and the behaviour of colloidal silica based grouts during their injection.

Introduction

Historical disposal of radioactive wastes by shallow burial in unlined trenches has left a legacy of contaminated wastes [1]. These waste trenches typically contain very complex mixed wastes, including radioactive contaminants, steel, plastics and organic materials such as solvents, clothing and paper, and geological materials from backfilling and the local environment. One such problematic site is Little Forest Legacy Site (LFLS), in Lucas Heights, Sydney, Australia. From 1960 until 1968 the site was used for the shallow burial of long-lived radioactive wastes produced during the short-lived nuclear energy research program of Australia. It is at present managed by ANSTO [2, 3]. The LFLS burial trenches contain a mix of contaminants, including: relatively short-lived fission products (e.g. Sr-90, Cs-137), long-lived radionuclides (e.g. Pu, U and Th), and non-radioactive, toxic elements (e.g. Be) [2]. Although the levels of radioactivity are relatively low compared to other legacy sites such as Sellafield (Cumbria, UK [4, 5]), Hanford (WA, USA [6]), and Savannah River (SC, USA [7]); contaminants (e.g. Tritium, Cs, Sr, U & Pu) have been found at the LFLS in the surface soils and groundwater [3, 8, 9] and a long-term management strategy is required in order to comply with national (ARPANSA) and international (IAEA) nuclear authorities. At present, in-situ immobilization of radioactive toxic wastes is preferred over retrieving the contaminated wastes (combined with reconditioning for further (geo)disposal) due to high cost and increased potential spreading of radioactive contamination. The use of several materials have been proposed to immobilize wastes in-situ, including cementitious materials [6, 10], phosphate (bio)minerals [6, 11] and colloidal silica grout [7]. Because of its low viscosity (easy to inject), non-toxic property, and high control over the gelling time (through varying accelerant type (e.g. KCl, NaCl, CaCl2) and concentration [7, 12]) colloidal silica grouts are considered ideal materials to immobilize radwastes in-situ [12]. The only potential disadvantage of colloidal silica grouts is that only ~33% of the gelled grout is solid and the remaining ~67% is interstitial water (including elevated concentrations of the accelerant salt) through which radionuclides could migrate.

Sr and Cs have been shown to interact with soil matrices dominantly through adsorption and cation exchange processes [13-17]. Strontium interacts strongly with metal oxide phases (e.g. anatase and goethite), sheet silicates and with cementitious materials through surface complexation [14, 16] while caesium dominantly interacts with clay minerals such as illite through cation exchange at frayed edges and/or through the diffusion into the hydrated interlayers [13, 17]. However, limited information is available on the interaction of Sr and Cs with waste materials and on the effects of colloidal silica grouts (and the different types of accelerant) on the geochemistry of Sr and Cs and their interactions with (complex) soils and wastes (i.e. desorption from soil and waste materials, dissolution, adsorption to colloidal silica, diffusion through gelled colloidal silica). Finally, during grouting, colloidal silica gelation is

triggered through the addition of cations in solution. Whilst several researchers have investigated colloidal silica penetration and gelation in uniform clean sands, no researchers have studied the gelation of colloidal silica in complex, heterogeneous soil matrices and where cations are already present in their pore waters.

Methodology Details

Adsorption of strontium and caesium to soil and wastes

Adsorption experiments were performed to a variety of single phases and mixtures based on XRD of the soil at the LFLS [8] and on the historical disposal records [2]. The phases studied were: illite-smectite mixed layer (Clay Mineral Society: ISCz-1), kaolinite, quartz, goethite, anatase, μ-crystalline cellulose, PVC, magnetite (Sigma Aldrich) and gibbsite (VWR). Additionally, mixtures to represent the soil and waste at the LFLS were also used. The solids were equilibrated with 40 ml 10 mM NaCl (to mimic groundwater at the LFLS [8]) at 10 g/L until the pH value (4 – 8) was stable. Once the pH was stable, 0.1 ml of a 10 mM NaOH and 0.1 ml of a 10,000 ppm Sr and/or Cs stock solutions were added (10 mM HCl) to the experiments to create experiments with 25 ppm Sr and/or Cs. After 24 h of equilibration, aliquots of the solutions were filtered through 0.2 μm PVDF syringe filters and analysed using ion chromatography (IC, Metrohm 850/858) and the pH values of all experiments were reanalysed.

Results and Discussion

Adsorption of strontium and caesium to soil and wastes

The results from the experiments on the adsorption of Sr and Cs to the single phases indicate that at pH 4 – 8, Sr and Cs interact strongly with kaolinite and illite and Sr also with anatase in the soils at LFLS. Cs does not appear to interact with any of the tested waste materials, while Sr dominantly interacts with cellulose (to simulate e.g. disposed paper and clothes) and magnetite (to simulate corroded steel). The presence of Cs did not appear to significantly affect the removal of Sr from solution, while the presence of Sr did have a (small but) significant effect on the removal of Cs from solution. This suggests that Sr interacts more strongly with the tested phases and competes for adsorption site with Cs. The specifics of these interactions and competition between Sr and Cs cannot be extracted from this information.

The results of the IC analyses of the experiments on Cs and Sr adsorption to simulated soil and waste mixtures are plotted in figure 1. These results show that the adsorption of Sr and Cs to soil and waste materials is pH dependent, and up to 12 ppm Sr and up to 10 ppm Cs were removed from solution during the experiments on Sr and Cs adsorption to the soil mixtures and up to 3 ppm Sr and negligible Cs was removed from solution during the experiments on Sr and Cs to the waste mixtures. The dashed lines in Figure 1 represent the weighted average of the IC results from the Sr and Cs adsorption experiments to the single phases. The discrepancy between the estimated and measured concentrations indicate that more information is needed to be able to correctly model and predict the speciation of Sr and Cs to these mixtures and thus also to the natural soils and wastes at contaminated sites like the LFLS, Sellafield and Hanford.
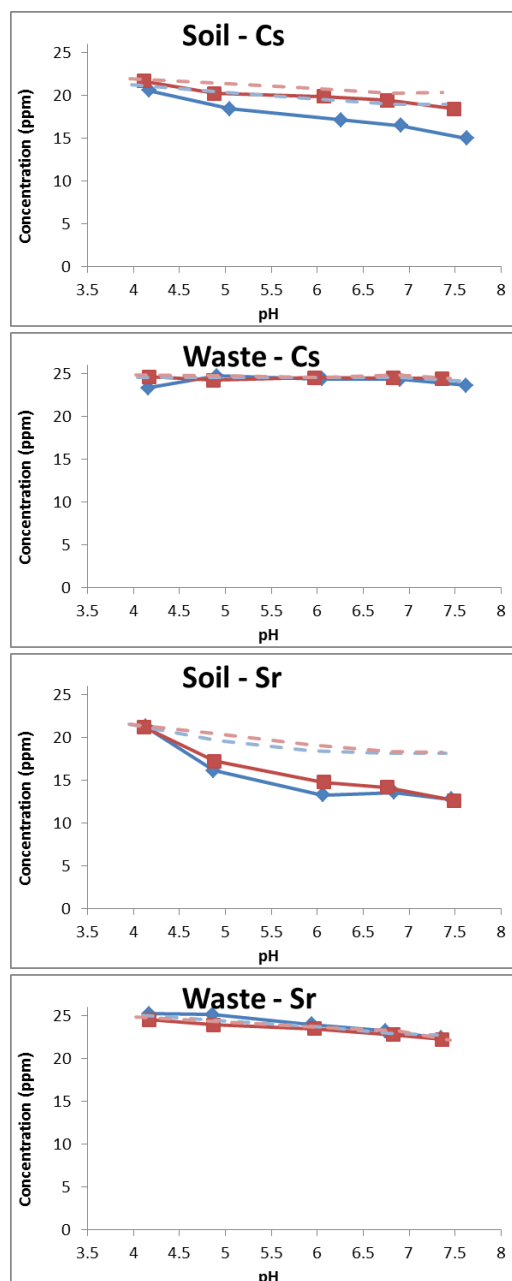
Figure 1 the measured Sr and Cs concentrations in solution after 24 h equilibration with the simulated soil and waste matrices. The dashed lines were calculated by taking the weighted average of the Sr or Cs concentration measured from the adsorption experiments on single phases. The blue lines and symbols represent the experiments with only Sr or Cs, and the red lines represent the experiments where both, Sr and Cs, were present.

Conclusions and Future Work

Through performing a comprehensive set of adsorption experiments we were able to determine that Sr and Cs interact with soil and waste materials. However, the details on these interactions are not yet understood as well as the influence of injected colloidal silica based grouts and the influence of the different types and concentrations of accelerant to be used.

Desorption of Sr and Cs as a function of accelerant concentration and type (NaCl, CaCl₂, KCl)

To determine the influence of the accelerant type and concentration, desorption experiments are ongoing. In these experiments, soil and waste materials pre-equilibrated with Sr and Cs at pH 7 will be separated from solution through centrifugation. The resulting solids will then be equilibrated with Sr- and Cs-free solutions with varying concentrations of NaCl (46.7 – 233 mM), CaCl₂ (6.67 – 33.3 mM) and KCl (27.5 – 138 mM) based on accelerants to obtain a gel time of approximately 3h [12]. During these experiments solution samples will be taken and filtered through 0.2 µm PVDF syringe filters and analysed using IC, to obtain information on the rate and extend of desorption of Sr and Cs through their competition with the cations present in the accelerant.

Synchrotron based X-ray CT experiments

Work has commenced on a small grant on the development of synchrotron based techniques in environmental radiochemistry (funded by: Env-Rad-Net). This project includes two objectives as described below, and the development of a flow-through experimental set-up to perform in-situ time resolved X-ray CT experiments at the Diamond-Manchester Branchline (13-2) at Diamond Light Source (Figure 2).
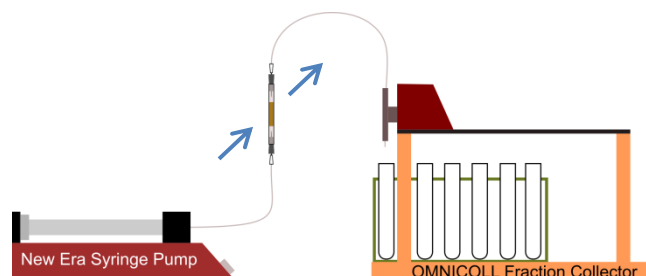

Figure 2 schematic of the experimental design for the in-situ time resolved X-CT experiments at the Diamond-Manchester Branchline (I13-2) at Diamond Light Source. The arrows represent the position and direction of the synchrotron X-rays during the experiments.

(1) In-situ time resolved X-ray CT experiments on the injection of colloidal silica based grouts.

These experiments will utilize the density difference between colloidal silica based grouts (1.2 – 1.3 g/cm³), pore water (1 g/cm³) and the solid phases (1.5 – 5.2 g/cm³) during the experiments. The differences in density between the components in these X-ray CT experiments allow us to track the injected colloidal silica based grout during the injection itself. These experiments will be performed to determine the effects of the pore water composition (0 – 100 mM NaCl) and the solid phases present during the injection of the colloidal silica based grouts.

(2) Element distribution through grouted and ungrouted matrices.

Due to the high performance of synchrotron based X-ray CT we can obtain information on the mineralogical distribution throughout samples up to 5mm in diameter. Additionally, by analysing the fluorescence above and below the absorption edges of Sr, Cs and U, we will be able to obtain a detailed picture on the elemental distribution throughout these samples. The samples that will be analysed for the mineralogical and elemental distribution will include both, grouted and ungrouted samples. This will allow us to determine the effect of the injection of colloidal silica on the distribution of Sr, Cs and U through (simulated) sediments and wastes.

X-ray Absorption Spectroscopy

Following the results from the adsorption experiments we aim to perform X-ray Absorption Spectroscopy (XAS) at beamline B18 at Diamond Light Source. XAS is an element specific analytical technique which allows for the determination of the "local coordination environment" of Sr and Cs. This will provide detailed information on the Sr and Cs speciation soil and wastes and specifically, on potential desorption of Sr and Cs within gelled colloidal silica grout. Thus, in order to acquire a full picture of the effects of colloidal silica grouts on the geochemistry and speciation of Sr and Cs we will aim to perform analyses on samples with and without gelled colloidal silica grout. This will complement the information obtained from the adsorption experiments and the ongoing desorption and synchrotron based X-ray CT experiments.

Acknowledgements

References

[1] Upgrading of near surface repositories for radioactive waste. Technical Report Series No. 433. 2005, IAEA: Vienna.

[2] Payne, T.E., Background Report on the Little Forest Burial Ground Legacy Waste Site. 2012, ANSTO.

[3] Payne, T.E., et al., Trench 'Bathtubbing' and surface plutonium contamination at a legacy radioactive waste site. Environmental Science and Technology, 2013. 47(23): p. 13284-13293.

[4] Morris, K., J.C. Butterworth, and F.R. Livens, Evidence for the remobilization of Sellafield waste radionuclides in an intertidal salt marsh, West Cumbria, U.K. Estuarine, Coastal and Shelf Science, 2000. 51(5): p. 613-625.

[5] Wallace, S.H., et al., Effect of groundwater pH and ionic strength on strontium sorption in aquifer sediments: Implications for 90Sr mobility at contaminated nuclear sites. Applied Geochemistry, 2012. 27(8): p. 1482-1491.

[6] Cantrell, K.J., et al., Chemical stabilization of Hanford tank residual waste. Journal of Nuclear Materials, 2014. 446(1-3): p. 246-256.

[7] Hakem, N., et al., Sorption of fission product radionuclides, 137Cs and 90Sr, by Savannah River Site sediments impregnated with colloidal silica. Radiochimica Acta, 2004. 92(7): p. 419-432.

[8] Cendón, D.I., et al., Identification of sources and processes in a low-level radioactive waste site adjacent to landfills: groundwater hydrogeochemistry and isotopes. Australian Journal of Earth Sciences, 2015. 62(1): p. 123-141.

[9] Ikeda-Ohno, A., et al., Solution speciation of plutonium and americium at an Australian legacy radioactive waste disposal site. Environmental Science and Technology, 2014. 48(17): p. 10045-10053.

[10] Oji, L.N., W.R. Wilmarth, and D.T. Hobbs, Loading capacities for uranium, plutonium, and neptunium in high caustic nuclear waste storage tanks containing selected sorbents. Nuclear Technology, 2010. 169(2): p. 143-149.

[11] Handley-Sidhu, S., et al., Influence of pH, competing ions, and salinity on the sorption of strontium and cobalt onto biogenic hydroxyapatite. Scientific Reports, 2016. 6.

[12] Pedrotti, M., et al., An analytical model for the control of silica grout penetration in natural groundwater systems. Tunnelling & Underground Space Technology, in review.

[13] Fuller, A.J., et al., Caesium incorporation and retention in illite interlayers. Applied Clay Science, 2015. 108: p. 128-134.

[14] Fuller, A.J., et al., EXAFS Study of Sr sorption to Illite, Goethite, Chlorite, and Mixed Sediment under Hyperalkaline Conditions. Langmuir, 2016. 32(12): p. 2937-2946.

[15] Trivedi, P. and L. Axe, A comparison of strontium sorption to hydrous aluminum, iron, and manganese oxides. Journal of Colloid and Interface Science, 1999. 218(2): p. 554-563.

[16] Bower, W.R., et al., Characterising legacy spent nuclear fuel pond materials using microfocus X-ray absorption spectroscopy. Journal of Hazardous Materials, 2016. 317: p. 97-107.

[17] Fan, Q., et al., Relationship between the adsorption species of cesium and radiocesium interception potential in soils and minerals: An EXAFS study. Journal of Environmental Radioactivity, 2014. 138: p. 92-100.